PROBLEMS OF MASKING AND ANTI-REFLECTIVE SiO₂ IN SILICON TECHNOLOGY†

🔴**Mykola S. Kukurudziak**[a,b]

ªRhythm Optoelectronics Shareholding Company, Holovna str. 244, 58032, Chernivtsi, Ukraine
ᵇYuriy Fedkovych Chernivtsi National University, Kotsyubyns'kogo str. 2, 58012, Chernivtsi, Ukraine
E-mail: mykola.kukurudzyak@gmail.com
Received April 24, 2023; revised May 7, 2023 accepted May10, 2023

The article examines the problems of thermal oxidation of silicon. Oxidation plays an important role in planar technology, which in turn is the basis of the technology of silicon integrated circuits, photodetectors and other solid-state electronics. During our production of silicon *p-i-n* photodiodes, a number of systematic types of defects and deterioration of product parameters caused by the degradation of masking or anti-reflective coatings during the manufacturing process were observed. A decrease in the insulation resistance of responsive elements in multi-element photodiodes was observed, which contributed to the increase of dark currents. A decrease in the responsivity of the products due to the degradation of the thickness or structure of the anti-reflective coating during technological operations, etc., was also revealed. It was established that the reason for the decrease in insulation resistance is the formation of inversion layers at the Si-SiO₂ interface, the presence of which can be detected when measuring *CV*-characteristics. It was also established that chemical treatment of substrates with SiO₂ in boiling acid solutions helps to reduce the thickness of the oxide. To avoid deviation of the thickness of the film from the condition of minimum reflection, it is necessary to grow a thicker layer of anti-reflective coating. It is noted that when etching the oxide during photolithography or when removing the PSG/BSG in hydrofluoric acid, it is not permissible to remove the cassette with plates from the solution for a long time, as this leads to uneven etching of the film due to the flow of the herb on the surface of the substrate. The causes of defect formation in Si and SiO₂ during oxidation are given. Thus, with improper mechanical and chemical processing of the plates, cristobalite inclusions may form in the film during oxidation. Cristobalite has a higher density than quartz glass, and the boundaries between amorphous regions and denser crystalline regions represent voids, which can be filled both by impurities from the surface and by the diffusant in the diffusion process. Also, during oxidation in silicon, packing defects are often formed. Centers of defect genesis can be mechanical damage to the plate surface or growth defects.

Keywords: *silicon; photodiode; oxidation; silicon oxide; volt-farad characteristic; transparent film*
PACS: 61.72.Ji , 61.72.Lk, 85.60.Dw

Oxidation plays an important role in planar technology, which in turn is the basis of the technology of silicon integrated circuits, photodetectors and other solid-state electronics [1]. At the initial stages of the development of planar technology, oxidation was used only for the manufacture of masking coatings that prevented the penetration of impurities into certain areas of the crystals during diffusion, as well as for the creation of a protective passivating layer after the device was manufactured. Recently, SiO₂ began to be used as active and passive elements in silicon functional blocks [2], as well as anti-reflective coatings (ARC) in photoreceiving devices [3]; this led to a new intensive study, it would seem, of the oxidation process and the properties of the oxide layer. In particular, conditions for the growth of nanometer films of silicon oxide are actively studied and modeled, which is relevant for miniaturization and increasing the speed of electronic elements [4, 5].

To date, a large number of methods have been developed, which have become standard, and allow obtaining high-quality oxide films, in particular, uniform in thickness, perfect in structure, and possessing high insulating properties. To a greater extent, these methods were developed empirically and are based on various processes: from thermal or anodic oxidation to deposition of a film from an external source [6]. Of course, to obtain oxide films with specified electrical properties, it is necessary to strictly control the behavior of impurities in the process of film formation, which is an urgent scientific and technical task.

During our production of silicon *p-i-n* photodiodes (PDs), a number of systematic types of defects and deterioration of product parameters caused by the degradation of masking or anti-reflective coatings during the manufacturing process were observed. A decrease in the insulation resistance of responsive elements (RE) in multi-element PDs was observed, which contributed to the increase of dark currents (I_d). A decrease in the responsivity of products (S_{pulse}) due to the degradation of the thickness or structure of the ARC during technological operations, etc., was also revealed. The described types of defects required a detailed study to establish the causes of their occurrence and methods of their avoidance.

When reviewing literary sources, it is seen that many works are devoted to the electrical properties of SiO₂. In particular, in a number of studies, the deterioration of the reverse characteristics is associated with the presence of positive fixed or mobile charges in the oxide film [7, 8]. Thus, a quantitative model of the formation of a fixed charge in silicon dioxide during thermal oxidation was developed in [7]. It was established that the amount of charge determines the number of internodal silicon atoms near the Si-SiO₂ interface, and an increase in the oxidation temperature contributes to a decrease in the value of the fixed charge due to an increase in the diffusion coefficient of internodal silicon atoms in SiO₂.

In [8], the effect of isothermal annealing in an inert atmosphere of structures with silicon oxide was investigated, and it was established that annealing allows reducing the amount of charge in the oxide. Note that in the case of silicon *p-i-n* PDs technology (and other electronic elements) there is no possibility of increasing the oxidation temperature due to the increase in the rate of degradation of the resistivity of the original material (ρ) and the life time of minor charge carriers (τ) [9]. This degradation is caused by an increase in the diffusion coefficients of the ions of uncontrolled impurities (Li^+, Na^+, K^+), which diffuse into the substrate during oxidation (which can also be the reason for the increase in the amount of mobile charge). It is worth noting that metals contribute to the amount of charge by changing (disrupting) the structure of the oxide. For the same reason, there is no possibility of introducing additional thermal operations into the technological production routes for annealing, as well as to avoid an increase in the number of thermal shocks.

Information about the degradation of oxide films and the influence of these factors on the responsivity of the PDs was not found in the literature. There are also no technological recommendations for avoiding the degradation of the insulation resistance of REs in multi-elements PDs. Accordingly, the study of the causes of the appearance and methods of avoiding the degradation of the masking and anti-reflective oxide films in the technology of silicon *p-i-n* PDs is the purpose of this work.

EXPERIMENTAL

The research was carried out on silicon four-element *p-i-n* PDs with a guard ring (GR) designed to detect radiation with a wavelength of $\lambda=1064$ nm. The production was carried out by diffusion-planar technology according to the technological regimes given in [10]. The starting material was single-crystal dislocation-free p-type silicon with orientation [111], $\rho\approx18\text{-}22$ k$\Omega\cdot$cm and $\tau\approx1.8\text{-}2.2$ ms. The technological process consisted of a complex of thermal operations and photolithography: semiconductor substrates were oxidized; photolithography was carried out to create windows for phosphorus diffusion; diffusion of phosphorus (predeposition) to the front side to create n^+-type REs and GR; drive-in of phosphorus in an oxygen atmosphere to redistribute the alloying impurity, increase the depth of the n^+-p-transition and form a anti-reflective coating; diffusion of boron to the reverse side of the substrate to create a p^+-type ohmic contact; photolithography for creating contact windows; sputtering of Cr-Au on the front and back sides.

Masking SiO_2 was formed during the first thermal operation at a temperature of $T=1423$ K according to the principle of dry-wet-dry oxidation [5]. Considering that the thickness of silicon oxide, which completely masks from the long-term diffusion of phosphorus at $T=1323$ K, reaches 0.3-0.4 μm [11], the thickness of the masking SiO_2 reached $d_{SiO2}\approx0.6\text{-}0.7$ μm. This thickness is also chosen taking into account the redistribution of phosphorus in the oxide during subsequent thermal operations.

Anti-reflective silicon oxide was formed during the drive-in of phosphorus in an atmosphere of dry oxygen at a temperature of $T=1423$ K. The thickness of SiO_2 was 0.18-0.19 μm, which corresponds to the minimum reflection condition [12]:

$$\frac{\lambda}{4} = nd_{SiO_2} \tag{4}$$

where λ is the working wavelength; *n* the refractive index of SiO_2; d_{SiO_2} is the thickness of the anti-reflective film.

To study the structural perfection of the surface of the substrates after thermal operations, selective etching was carried out in Sirtle's etchant [13].

After oxidation and each subsequent thermal operation, the high-frequency volt-farad (*CV*) characteristics of the metal-oxide-semiconductor-structures (MOS) were measured at a frequency of 30 kHz, which made it possible to predict the final parameters of the products.

The level of pulsed monochromatic sensitivity of PDs was determined at $\lambda=1064$ nm, bias voltage $U_{bias}=120$ V and pulse duration $\tau_i=500$ ns.

An important parameter of multi-element PDs with GR is the resistance of the isolation of the REs between themselves and the insulation resistance of the REs and the GR, the decrease of which leads to an increase in the photocoupling coefficient and dark currents. Determination of insulation resistance of REs and GR (R_{con}) was carried out according to the method given in [14] with $U_{bias}=2$ V and load resistance $R_l=10$ kΩ.

The thickness of the oxide films was measured by the ellipsometric method.

RESULTS OF THE RESEARCH AND THEIR DISCUSSION
A) Study of *CV*-characteristics

Measuring the *CV* characteristics of MOS structures at the initial stages of manufacturing makes it possible to estimate the final parameters of the products. Thus, in the case of *p-i-n* PDs manufacturing, the technological route consisted of 4 thermal operations, after each of which (except for phosphorus predeposition) *CV*-characteristics were measured. From the volt-farad characteristics, it is possible to determine the charge level in the oxide and detect the presence of inversion layers (IL) at the Si-SiO_2 interface. A typical *CV*-characteristic of the MOS structure for *p*-type silicon is shown in Fig. 1 (curve 1). When the number of charged states at the interface of two phases increases, the curve may shift to the left relative to the ordinate axis. As mentioned above, this leads to an increase in dark currents. But sometimes the formation of inversion layers at the Si-SiO_2 interface is observed, which form surface conductive leakage channels and reduce the insulation resistance between the REs.

The formation of ILs is possible both during the formation of a masking coating and during subsequent thermal operations. On Fig. 1 shows typical curves of volt-farad characteristics of MOS structures with inversion layers (curves 2-4). Curve 3 describes the case of doping of the silicon surface with uncontrolled impurities during oxidation, which led to a change in the conductivity type of the silicon surface to the opposite. Such a case is also possible in the presence of hydrochloric acid residues after purging quartz reactors for the purpose of cleaning from alkali metals. Curves 2 and 4 describe the case of the formation of inversion layers during the phosphorus dispersal and boron diffusion operations.
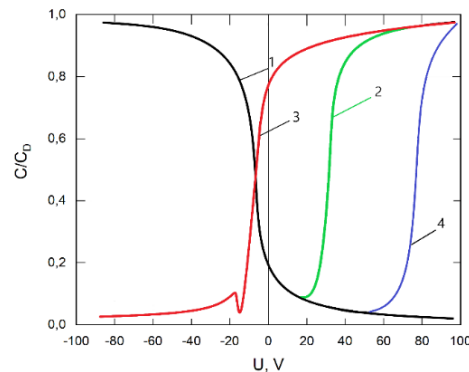
Figure 1. *CV*-characteristics of MOS structures: 1 – typical characteristic for *p*-type silicon; 2-4 – inverted characteristics

In the case of the formation of ILs during oxidation, it is necessary to etch the oxide and doing re-oxidation. The insulation resistance of REs and GR in samples with *CV*-characteristics of the Curve 2 type (Fig. 1) reached $R_{con} \approx$1-10 kΩ at $R_{con} \approx$5-15 MΩ for serial PDs. And dark current of GR $J_{GR} \approx$7-36 mA/cm^2 at $J_{GR} \approx$3.6-36 µA/cm^2 (U_{bias}=120 V) for serial products. It is impossible to accurately measure the REs of defective PDs, since it constantly increases due to the flow of charge carriers from the GR. It is possible to fix only the initial value, which reaches $J_d \geq$26 µA/cm^2 at J_d = 65-130 nA/cm^2 for serial samples. In the case of SiO$_2$ etching and re-oxidation, a decrease in dark currents is observed, but as experiments show, after re-oxidation, the values of I_d and I_{GR} are slightly higher than in serial products. This indicates the presence of residual inversion layers on the surface of the substrate, they can be eliminated by plasma-chemical or chemical-dynamic methods.

The insulation resistance of samples with *CV*-characteristics of the Curve 4 type (Fig. 1) reached $R_{con} \approx$ 200-600 kΩ, and $J_{GR} \approx$50-100 µA/cm^2. From the above, it is possible to conclude that it is possible to estimate the conductivity of surface inversion channels based on the volt-farad characteristics.

The causes of ILs are known and studied [15]. The key factor in their formation is an increase in the resistivity of the substrate, since with an increase in ρ of the material, a smaller amount of impurities is needed to change the surface conductivity to the opposite [16]. In most cases, an inversion layer is already present on *p*-type silicon with ρ=1-10 Ohm·cm [17]. In the case of a thermal oxidation operation, the possible technological reasons for the appearance of inversion are improper chemical treatment of substrates, the presence of alkali metal impurities in deionized water, quartz vessels, or a quartz reactor, and carrier gases. However, the appearance of ILs during boron diffusion is caused by the redistribution of impurities in SiO$_2$ and their diffusion to the Si-SiO$_2$ interface [18]. These impurities were introduced into the oxide during previous thermal operations and diffused into the surface layer of silicon due to the high total duration of thermal treatments. Another factor that contributes to the formation of ILs with a high total duration of thermal operations is the diffusion of boron atoms from the near-surface layers of silicon into the oxide, since the segregation coefficient of boron is below unity [19].

The probability of the appearance of inversion layers can be minimized by careful control of carrier gases, deionized water for the presence of alkali metals, and periodic purging of quartz reactors with hydrochloric acid vapors. It is possible to increase the resistance of the insulation of REs and GR by forming regions of restriction of leakage channels in the gaps between active elements of the PD isotype with the substrate material [14]. It is possible to reduce the influence of the inversion layers of the periphery of photodiode crystals on the level of dark currents of the GR when the masking oxide is etched from the periphery and new film is formed in the dry oxygen atmosphere during the operation of drive-in of phosphorus [20].

B) Reduction of the thickness of anti-reflective SiO$_2$ in the process of PDs manufacturing.

During the serial production of silicon *p-i-n* PDs, a decrease in the thickness of the ARC was noticed in the process of technological operations after its formation, this factor led to a decrease in responsivity, since the responsivity of the PD is directly proportional to the reflection coefficient of the anti-reflective film [21]:

$$S_\lambda = (1 - R)TQ\alpha_{p-n}\frac{\lambda}{1.24} \qquad (2)$$

where R is the ARCs reflection coefficient; T is the transmission coefficient of the input window or optical filter; Q is the quantum output of the internal photoeffect; α_{p-n} is the collection coefficient of minor charge carriers generated by radiation in the active region of the photodiode.

When studying what was described, it was seen that the reason for the decrease in d_{SiO2} is chemical treatment (CT). Accordingly, it was decided to study the influence of CT on the thickness of SiO_2.

To clean the substrates, we used CT in boiling solutions of acids with the composition indicated in Table 1, the treatment duration was 10 minutes. To study the change in d_{SiO2} in the process of washing before and after operations, the thickness of this coating was measured.

Table 1. The composition of acid solutions for CT of silicon substrates and the change in d_{SiO2} during the operation

| Solution	Composition	Δd_{SiO2}, nm
$H_2SO_4:H_2O_2:H_2O$	4:1:1	6-7
$HNO_3:H_2O_2:H_2O$	1:1:1	8-9
$NH_4OH:H_2O_2:H_2O$	5:1:1	16-17

Taking into account that after the formation of the anti-reflective oxide, according to the technological route, three more 3-stage washings are carried out, which will reduce d_{SiO2} by 90-100 nm, it is necessary to increase the duration of drive-in of phosphorus, and, accordingly, the thickness of ARC.

To be able to estimate the drop in responsivity (ΔS_{pulse}) of the PD as a result of d_{SiO2} reduction, a graph of the dependence of ΔS_{pulse} on the ARC thickness was obtained (Fig. 2). The initial responsivity of the PD crystal was measured at $d_{SiO2} \approx 0.18$ μm and the oxide was digested layer by layer in a slow etchant HF: H2O=1:10. After each etching process, S_{pulse} measurements were also performed.

Reflectance spectra of PDs were obtained at $d_{SiO2} \approx 0.170$-0.175 μm and PDs without ARC (Fig. 3).
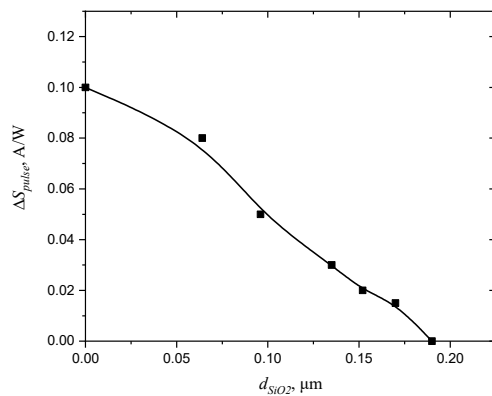
Figure 2. Experimental graph of the dependence of the drop in responsivity on the thickness of the anti-reflective coating
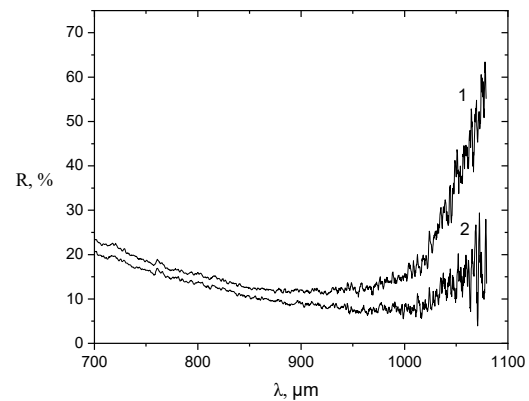

Figure 3. PDs reflection spectra: 1 - without ARC; 2 - $d_{SiO2} \approx 0.17$-0.175 μm

From Fig. 3, it can be seen that the reflection minimum of the investigated film is at $\lambda \approx 1.01$-1.02 μm due to the deviation of the film thickness from the optimized for $\lambda \approx 1.064$ μm. The reflection coefficient of PD without ARC is $R \approx 45$-50% at the working wavelength, and with a thickness of anti-reflective silicon dioxide of 0.17-0.175 μm, $R \approx 15$-20%. At $d_{SiO2} = 0.18$-0.19 μm at $\lambda \approx 1.064$ μm, $R = 5$-7%.

Changing the thickness of the masking and brightening coatings is also possible during photolithography, removal of phosphorosilicate (PSG) or borosilicate (BSG) glasses, and chemical dynamic polishing (CDP).

In particular, when etching the oxide during photolithography or when removing PSG/BSG in hydrofluoric acid, it is not permissible to remove the cassette with plates from the solution for a long time, as this leads to uneven etching of the surface (Fig. 4) due to the flow of the etchant on the surface of the substrate. Accordingly, non-uniformity of the film thickness can lead to scattered responsivity or uneven etching of the oxide during subsequent photolithography.

a)   b)
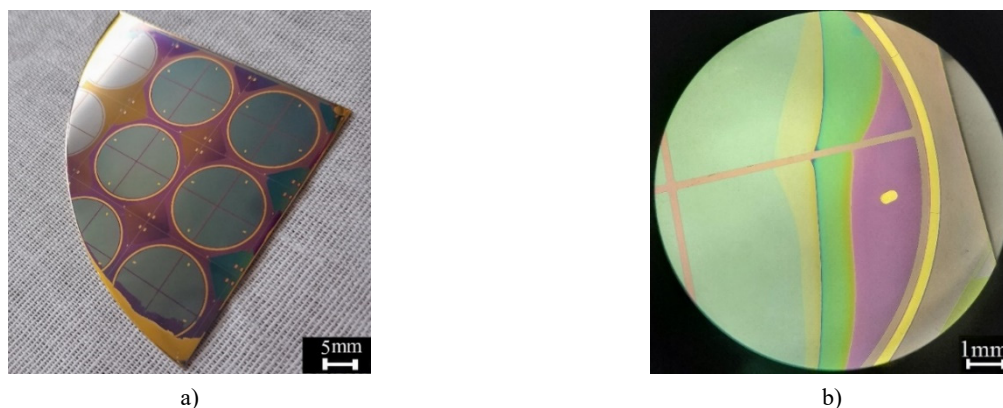
Figure 4. Image of uneven thickness of masking (a) and anti-reflective (b) SiO_2

In order to carry out the CDP of the reverse side of the substrate, the front side is covered with a chemically resistant varnish [22]. If the thickness of the varnish is insufficient during drying, it is possible to form thinnings or punctures through which undesirable etching of the working surface of the crystal occurs. The consequence of thinning is spot etching of the oxide over the entire surface of the RE (Fig. 5 a), and in the case of punctures, the seepage of the etchant under the varnish and local etching of SiO₂ (Fig. 5, b) or even silicon, which can lead to a breakdown of the *p-n* junction. To avoid the described situation, it is worth applying a double layer of varnish with intermediate drying.


a)   b)
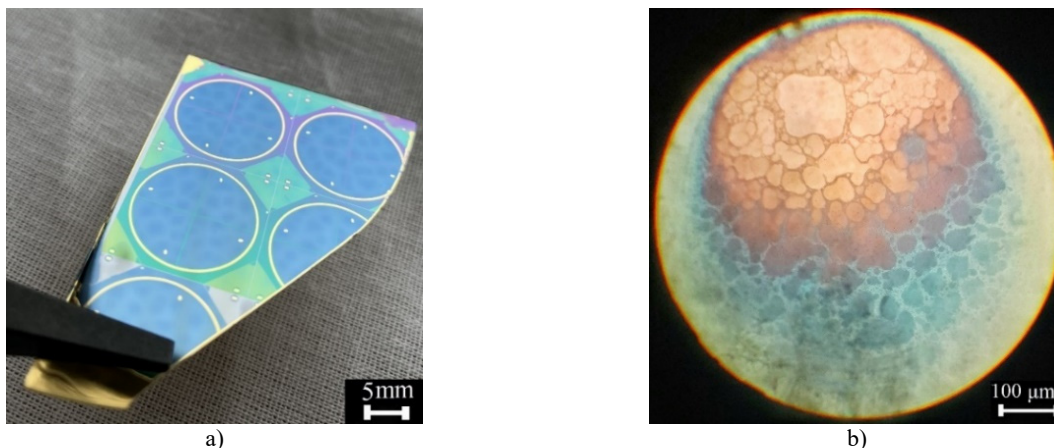
Figure 5. Image of the dispersion of the thickness of the oxide film after CDP due to the thinning of the varnish (a) and punctures (b)
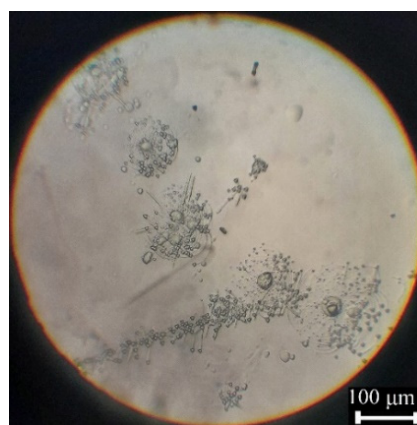
B) Defect formation during thermal oxidation

The most important condition for obtaining high-quality silicon oxide is the cleanliness of the plate before oxidation. The presence of impurities on the surface of silicon before oxidation or during the process of oxide growth negatively affects the uniformity of the film and the electrical properties of the interface.

On an uneven, contaminated surface, the grown or applied oxide contains inclusions of cristobalite (Fig. 6), which are undesirable in all classic cases of using oxide films of silicon technology. Cristobalite has a higher density than quartz glass, and the boundaries between amorphous regions and denser crystalline regions represent voids, which can be filled both with impurities from the surface and with a diffusant in the diffusion process [23]. A necessary condition for obtaining high-quality SiO₂ is the polishing of the surface of the substrates followed by chemical treatment. Ultrasonic cleaning is also possible.

Packing defects are often formed during oxidation in silicon [24]. The formation of these defects on the surface of the plates occurs for several reasons. The first is mechanical damage to the surface of the substrate during cutting or grinding. If such damages, for example, scratches or cutting marks, are not removed by subsequent chemical polishing, then they can become local areas of nucleation of packaging defects (Fig. 7a).

a)   b)
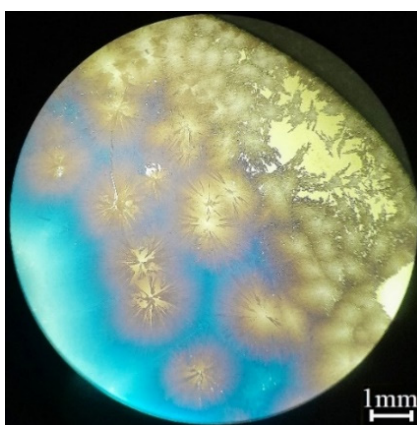
Figure 6. Image of silicon oxide with cristobalite inclusions   **Figure 7.** Image of structural defects in the areas of mechanical disturbances (a) and swirl defects (b) on the surface of plates (plates after selective etching)
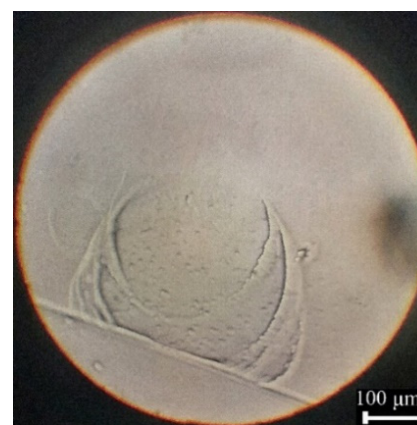
The second reason for the formation of packing defects (in the absence of mechanical damage on the surface) is related to the presence of growth and so-called swirl defects in the plates [25], since complexes of point defects with a swirl distribution are the seeds for packing defects during oxidation (Fig. 7b). Note that the defects formed during oxidation have an internodal nature and are associated with the accumulation and condensation of excess silicon atoms generated as a result of oxygen diffusion in silicon. It is the internodal silicon atoms that form point defect clusters in the areas of mechanical surface disturbances.

Another mechanism for the formation of structural defects during oxidation can be mechanical stresses introduced as a result of the difference in the thermal expansion coefficients of Si and SiO_2 [26]. But we did not observe the formation of defects by this mechanism.

It is worth noting that during the diffusion of phosphorus, clusters of packing defects are areas of dislocation generation. A high density of structural defects on the plate surface negatively affects the dark currents of photodiodes [27,28]. In order to avoid defect formation, it is worth using dislocation-free silicon, performing the CDP operation after mechanical processing of the wafers, and clearly controlling the substrates before thermal operations.

CONCLUSIONS

1. The problems of masking and anti-reflective SiO_2 in the technology of silicon *p-i-n* photodiodes were investigated.

2. The reason for the decrease in the insulation resistance of photosensitive elements in multi-element photodiodes is caused by the presence of surface inversion channels at the Si-SiO_2 interface. Inversion layers can be detected by measuring *CV*-characteristics.

3. Chemical treatment of oxidized substrates in boiling acid solutions helps to reduce the thickness of the oxide film.

4. When removing the cassette with oxidized plates from the solution during SiO_2, BSG or PSG etching, uneven etching of the film is possible due to the flow of the etchant on the plate.

5. Oxidation of contaminated or uneven substrates can be accompanied by the formation of oxide with the inclusion of cristobalite.

6. Defect formation during thermal oxidation occurs in areas of mechanical disturbances or growth defects.

ORCID ID

Mykola S. Kukurudziak, https://orcid.org/0000-0002-0059-1387

REFERENCES

[1] M. McClish, R. Farrell, R. Myers, F. Olschner, G. Entine, and K.S. Shah, Nuclear Instruments and Methods in Physics Research Section A: Accelerators, Spectrometers, Detectors and Associated Equipment, **567**(1), 36 (2006). https://doi.org/10.1016/j.nima.2006.05.055

[2] A. Rahim, J. Goyvaerts, and B. Szelag, IEEE Journal of Selected Topics in Quantum Electronics, **25**(5), 1 (2019). https://doi.org/10.1109/JSTQE.2019.2915949

[3] S. Zhang, Y. Yao, and D. Hu, Energies, **12**(6), 1168 (2019). https://doi.org/10.3390/en12061168

[4] G. Gerlach, and K. Maser, Advances in condensed matter Physics, **2016**, 7545632 (2016). https://doi.org/10.1155/2016/7545632

[5] S.W. Glunz, F. Feldmann, Solar Energy Materials and Solar Cells, **185**, 260 (2018). https://doi.org/10.1016/j.solmat.2018.04.029

[6] A.A. Prishya, L. Chopra, Materials Today: Proceedings, **72**, 1471 (2023). https://doi.org/10.1016/j.matpr.2022.09.348

[7] O.V. Aleksandrov, and A.I. Dus, Physics and technology of semiconductors, **45**(4), 474 (2011). (in Russian)

[8] H. Mizobata, Y. Wada, M. Nozaki, Applied Physics Express, **13**(8), 081001 (2020). https://doi.org/10.35848/1882-0786/aba320

[9] J. Vanhellemont, and E. Simoen, Journal of the electrochemical society, **154**(7), H572 (2007). https://doi.org/10.1149/1.2732221

[10] M.S. Kukurudziak, Physics and Chemistry of Solid State, **23**(4), 756 (2022). https://doi.org/10.15330/pcss.23.4.756-763

[11] C.T. Sah, H. Sello, and D.A. Tremere, J. Phys. Chem. Solids, **11**, 288 (1959). https://doi.org/10.1016/0022-3697(59)90229-X

[12] S.B. Khan, S. Irfan, Z. Zhuanghao, and S.L. Lee, Materials, **12**(9), 1483 (2019). https://doi.org/10.3390/ma12091483

[13] F.A. Abdullin, V.E. Pautkin, E.A. Pecherskaya, A.V. Pecherskiy, D.V. Artamonov, and K.O. Nikolaev, in: *2019 International Seminar on Electron Devices Design and Production (SED), IEEE,* (2019), pp. 1-4. https://doi.org/10.1109/SED.2019.8798467

[14] M. Kukurudziak, Radioelectronic and Computer Systems, **105**(1), 92 (2023). https://doi.org/10.32620/reks.2023.1.07

[15] V.M. Lytvynenko, I.M. Vikulin, Bulletin of the Kherson National Technical University, (1), 46 (2018). (in Ukrainian)

[16] Yu. O. Kruglyak, and M.V. Strikha, Sensor Electronics and Microsystem Technologies, **16**(2), 5 (2019). https://doi.org/10.18524/1815-7459.2019.2.171224 (in Ukrainian)

[17] M.M. Atalla, E. Tannenbaum, and E.J. Scheibner, Bell System Tech. J. **38**, 749 (1959).

[18] M.S. Kukurudziak, and E.V. Maistruk, in: *2022 IEEE 3rd KhPI Week on Advanced Technology (KhPIWeek) (IEEE, Kharkiv, 2022),* pp. 1-6. https://doi.org/10.1109/KhPIWeek57572.2022.9916420

[19] H. Chen, K. Morita, X. Ma, Z. Chen, and Y. Wang, Solar Energy Materials and Solar Cells, **203**, 110169 (2019). https://doi.org/10.1016/j.solmat.2019.110169

[20] M.S. Kukurudziak, Journal of nano- and electronic physics, **14**(1), 01023 (2022). https://doi.org/10.21272/jnep.14(1).01023

[21] A.V. Fedorenko, Technology and design in electronic equipment, **17**(3–4), 17 (2020). https://doi.org/10.15222/ TKEA2020.3-4.17 (in Ukrainian)

[22] M.S. Kukurudziak, Surface Chemistry, Physics and Technology, **14**(1), 42 (2023). https://doi.org/10.15407/hftp14.01.042 (in Ukrainian)

[23] K.L. Milton, T.R. Durrant, T. Cobos Freire, and A.L. Shluger, Materials, **16**(4), 1382 (2023). https://doi.org/10.3390/ma16041382

[24] F. Dai, and L. Zhang, Materials Science in Semiconductor Processing, **153**, 107187 (2023). https://doi.org/10.1016/j.mssp.2022.107187

[25] R. Tognato, Physica Status Solidi, **98**(2), 681 (2022). https://doi.org/10.1515/9783112501825-048

[26] T. Middelmann, A. Walkov, G. Bartl, and R. Schödel, Physical Review B, **92**(17), 174113 (2015). https://doi.org/10.1103/PhysRevB.92.174113

[27] B. Son, Y. Lin, K.H. Lee, Q. Chen, and C.S. Tan, Journal of Applied Physics, **127**(20), 203105 (2020). https://doi.org/10.1063/5.0005112

[28] M.S. Kukurudziak, Journal of nano- and electronic physics, **14**(4), 04015 (2022). https://doi.org/10.21272/jnep.14(4).04015

ПРОБЛЕМИ МАСКУЮЧОГО ТА ПРОСВІТЛЯЮЧОГО SiO$_2$ В КРЕМНІЄВІЙ ТЕХНОЛОГІЇ

Микола С. Кукурудзяк[a,b]

[a]*АТ «Центральне конструкторське бюро Ритм», 58032, м. Чернівці, вул. Головна, 244, Україна*
[b]*Чернівецький національний університет імені Юрія Федьковича, 58002, м. Чернівці, вул. Коцюбинського, 2, Україна*

В статті досліджено проблематику термічного окиснення кремнію. Окиснення відіграє важливу роль в планарній технології, яка в свою чергу є основою технології кремнієвих інтегральних мікросхем, фотоприймачів та інших твердотільних засобів електроніки. При виготовленні нами кремнієвих *p-i-n* фотодіодів побачено ряд систематичних видів браку та погіршень параметрів виробів спричинених деградацією маскуючого чи просвітляючого покриттів в процесі виготовлення. Спостерігалось зниження опору ізоляції фоточутливих елементів в багатоелементних фотодіодах, що сприяло зростанню темнових струмів. Також виявлено зниження чутливості виробів внаслідок деградації товщини чи структури просвітляючого покриття під час технологічних операцій та ін. Встановлено, що причиною зниження опору ізоляції є утворення інверсійних шарів на межі розділу Si-SiO$_2$, наявність яких можна виявити при вимірюванні *CV*-характеристик. Також встановлено, що хімічна обробка підкладок із SiO$_2$ в кип'ячих розчинах кислот сприяє зменшенню товщини оксиду. Для уникнення відхилення товщини плівки від умови мінімуму відбивання варто вирощувати товстіший шар просвітляючого покриття. Зауважено, що при травленні оксиду під час фотолітографії чи при зніманні ФСС/БСС в плавиковій кислоті не припустимо виймати касету з пластинами із розчину на тривалий час, оскільки це призводить до нерівномірного травлення плівки внаслідок стікання травника по поверхні підкладки. Наведено причини дефектоутворення в Si та SiO$_2$ під час окиснення. Так, при неналежній механічній та хімічній обробці пластин можливе утворення включень кристобалітів в плівку під час окиснення. Кристобаліт володіє вищою густиною ніж кварцове скло, а межі між аморфними областями і більш щільними кристалічними областями представляють порожнечі, які можуть бути заповнені як забрудненнями з поверхні так і дифузантом в процесі дифузії. Також під час окиснення в кремнію часто утворюються дефекти упаковки. Центрами зародження дефектів можуть бути механічні пошкодження поверхні пластини чи ростові дефекти.

Ключові слова: *кремній; фотодіод; окиснення; оксид кремнію; вольт-фарадна характеристика; просвітляюча плівка*

OSCILLATORY POROUS MEDIUM FERROCONVECTION IN A VISCOELASTIC MAGNETIC FLUID WITH NON-CLASSICAL HEAT CONDUCTION[†]

Naseer Ahmed[a]*, S. Maruthamanikandan[b†], B.R. Nagasmitha[b§]

[a]Department of Mathematics, Presidency College, Kempapura, Hebbal, Bengaluru 560024, India
[b]Department of Mathematics, School of Engineering, Presidency University, Bengaluru 560064, India
*Corresponding Author: naseerahmed.ar2023@gmail.com
[†]E-mail: maruthamanikandan@presidencyuniversity.in
[§]E-mail: nagasmitha.br@presidencyuniversity.in
Received March 25, 2023; revised May 10, accepted May 11, 2023

The classical stability analysis is used to examine the combined effect of viscoelasticity and the second sound on the onset of porous medium ferroconvection. The fluid and solid matrix are assumed to be in local thermal equilibrium. Considering the boundary conditions appropriate for an analytical approach, the critical values pertaining to both stationary and oscillatory instabilities are obtained by means of the normal mode analysis. It is observed that the oscillatory mode of instability is preferred to the stationary mode of instability. It is shown that the oscillatory porous medium ferroconvection is advanced through the magnetic forces, nonlinearity in magnetization, stress relaxation due to viscoelasticity, and the second sound. On the other hand, it is observed that the presence of strain retardation and porous medium delays the onset of oscillatory porous medium ferroconvection. The dual nature of the Prandtl number on the Rayleigh number with respect to the Cattaneo number is also delineated. The effect of various parameters on the size of the convection cell and the frequency of oscillations is also discussed. This problem may have possible implications for technological applications wherein viscoelastic magnetic fluids are involved.
Keywords: *Convection; Maxwell equations; Navier-Stokes equations for incompressible viscous fluids; Porous media; Viscoelastic fluids, Ferroconvection*
PACS: 47.55.P-, 46.25.Hf, 77.84.Nh, 77.22.-d, 41.20.-q

1. INTRODUCTION

Ferroconvection is a transfer of heat from one place to another in ferromagnetic liquids and its importance is due to the applications suggested by several authors [1-3] and many more. Ferrofluids, also known as magnetic fluids, are colloidal suspensions of nanosized ferromagnetic particles stably dispersed in organic or non-organic carrier fluids such as kerosene, water, and hydrocarbon. When exposed to an external magnetic field, they behave paramagnetically with susceptibility usually large for magnetic liquids [4]. Ferrofluids have commercial applications like vacuum feed-throughs for manufacturing semi-conductors [5]. Ferrofluid is also used in taking the drug in a human body to a target site by applying a magnetic field [6]. However, we can find many applications in different fields [7]. Finlayson [8] studied the convective instability of ferromagnetic fluids due to Bénard in the presence of a uniform vertical magnetic field and explained the thermomechanical interaction concept of ferromagnetic fluids. Lalas and Carmi [9] studied the thermoconvective stability of ferrofluids in the absence of buoyancy effects. Non-Darcy ferroconvection problem with gravity modulation using regular perturbation has been addressed by Nisha Mary and Maruthamanikandan [10]. Darcy-Brinkman ferroconvection with temperature-dependent viscosity has been studied by Soya Mathew and Maruthamanikandan [11] and thermorheological and magnetorheological effects on Marangoni-ferroconvection with internal heat generation has been investigated by Maruthamanikandan et al. [12]. Effect of MFD viscosity on ferroconvection in a fluid saturated porous medium with variable gravity has been examined by Vidya Shree et al. [13].

A good amount of attention is honoured to Rayleigh–Bénard convection (RBC) problems in Newtonian liquids with respect to heat transfer and other engineering applications as referred above. On the other hand, at shallow depths of the reservoirs, oil sands contain waxy crude which are viscoelastic fluids. They exhibit both liquid and solid properties and have many applications to the nuclear, petroleum, and chemical industries. They also have applications in cooling electronic devices, crystal growth, and material processes. In the study of viscoelastic fluids, the rheological equation involves one or two relaxation times (Bird et al. [14] and Joseph [15]) and also oscillatory convection is witnessed which is not noticed in Newtonian fluids. The Oldroyd model [16] is used for describing the viscoelastic properties of dilute polymers. The fact that principle of exchange of stabilities is not valid was shown by Green [17]. Recently, the onset of Darcy-Brinkman convection in a binary viscoelastic fluid saturated porous layer has been addressed studied by Swamy et al. [18].

The equation governing temperature (heat transport equation) in classical theory assumes a parabolic-type partial differential equation that admits thermal signals at an infinite speed, which is unrealistic. The new theories modified the classical Fourier's law of heat conduction and hence contain a hyperbolic-type heat transport equation that admits the thermal signals at a finite speed. As per this theory, heat propagates as a wave phenomenon rather than a diffusion phenomenon and the wavelike thermal disturbance is referred to as second sound (Chandrasekharaiah [19]). Gurtin and

---

Pipkin [20] investigated a general principle of thermal conduction in nonlinear analysis, including memories, a concept having a finite propagation speed. Straughan and Franchi [21] addressed the Bénard advection problem when the Maxwell-Cattaneo heat flow law is utilized in place of the ordinary Fourier theory of thermal conductivity. Soya Mathew and Maruthamanikandan [22] investigated oscillatory porous medium ferroconvection with Maxwell-Cattaneo law of heat conduction where they showed that the oscillatory mode of convection is preferred to stationary mode for large values of Prandtl and second sound parameter.

Under these conditions, the present paper is dedicated to examining convective instability in a Cattaneo viscoelastic ferrofluid saturated sparsely packed porous medium. The influence of various parameters is explored that perhaps direct us to oscillatory convection.
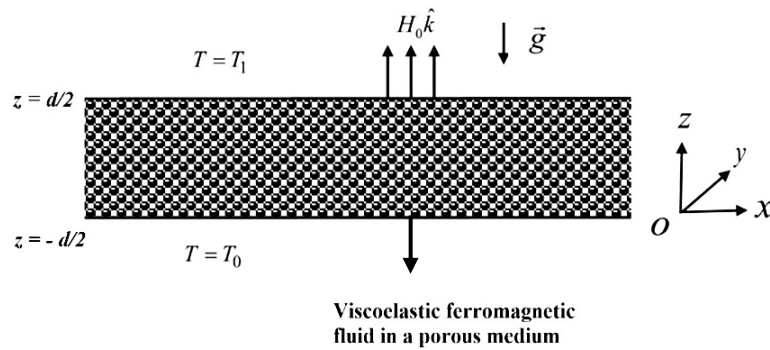

Figure 1. Physical Configuration

2. MATHEMATICAL FORMULATION

Let us consider an incompressible Cattaneo viscoelastic ferromagnetic fluid saturated porous medium confined between the two surfaces of non-finite length horizontally of finite thickness d. We consider Oldroyd's model to characterize the viscoelastic behaviour which is a non-Newtonian one. The lower surface at $z = -d/2$ and upper surface at $z = d/2$ are maintained at temperatures T_1 and T_0 respectively with $T_1 > T_0$ and $\Delta T = T_1 - T_0$ (see **Fig. 1**). It is assumed that at a quiescent state the temperature varies linearly across the depth. When the magnitude of ΔT become larger than the critical one, thermal convection will set in due to buoyancy force.

The fluid layer is exposed to a magnetic field $\vec{H}_0$ acting parallel to the vertical z-axis and the gravity force acting vertically downwards. We assume that Oldroyd's model is sufficient to characterize the viscoelastic behaviour which is simple enough to be tractable analytically. The governing equations supporting the Boussinesq approximation are written as follows.

$$\nabla \bullet \vec{q} = 0 \tag{2.1}$$

$$\left(1 + \lambda_1 \frac{\partial}{\partial t}\right)\left[\frac{\rho_0}{\varepsilon} \frac{\partial \vec{q}}{\partial t} + \frac{\rho_0}{\varepsilon^2}\left(\vec{q} \bullet \nabla\right)\vec{q} + \nabla p - \rho \vec{g} - \nabla \bullet \left(\vec{H}\,\vec{B}\right)\right] = \left(1 + \lambda_2 \frac{\partial}{\partial t}\right)\left[-\frac{\mu_f}{k}\vec{q} + \overline{\mu_f}\,\nabla^2 \vec{q}\right] \tag{2.2}$$

$$\varepsilon\left[\rho_0\, C_{V,H} - \mu_0 \vec{H} \bullet \left(\frac{\partial \vec{M}}{\partial T}\right)_{V,H}\right]\left[\frac{\partial T}{\partial t} + \vec{q} \bullet \nabla T\right] + (1-\varepsilon)\left(\rho_0\, C\right)_s \frac{\partial T}{\partial t}$$

$$+\mu_0\, T\left(\frac{\partial \vec{M}}{\partial T}\right)_{V,H} \bullet \left[\frac{\partial \vec{H}}{\partial t} + \left(\vec{q} \bullet \nabla\right)\vec{H}\right] = -\nabla \bullet \vec{Q} \tag{2.3}$$

$$\tau\left[\frac{\partial \vec{Q}}{\partial t} + \left(\vec{q} \bullet \nabla\right)\vec{Q} + \vec{\omega} \times \vec{Q}\right] = -\vec{Q} - k_1 \nabla T \tag{2.4}$$

$$\rho = \rho_0\left[1 - \alpha\left(T - T_a\right)\right] \tag{2.5}$$

$$M = M_0 + \chi_m\left(H - H_0\right) - K_m\left(T - T_a\right) \tag{2.6}$$

where λ_1 is the stress relaxation time, λ_2 is the strain retardation time ($0 \leq \lambda_2 < \lambda_1$), $\vec{q} = (u, v, w)$ is the fluid velocity, ρ_0 is the reference density, ε is the porosity, t is the time, p is the pressure, $\vec{g}$ is the acceleration due to gravity, ρ is the fluid density, μ_f is the dynamic viscosity, $\overline{\mu_f}$ is the effective viscosity, k is the permeability of the porous medium, $\vec{H}$ is the magnetic field, $\vec{B}$ is the magnetic induction, T is the temperature, μ_0 is the magnetic permeability, $\vec{M}$ is the magnetization, k_1 is the thermal conductivity, α is the thermal expansion coefficient, $C_{V,H}$ is the specific heat at constant volume and magnetic field, χ_m is the magnetic susceptibility, K_m is the pyromagnetic coefficient, $\vec{Q}$ is the heat flux, τ is a constant with the dimensions of time and $\vec{\omega} = \frac{1}{2} \nabla \times \vec{q}$.

Maxwell's equations for a non-conducting fluid with no displacement currents become (Finlayson [8])

$$\nabla \bullet \vec{B} = 0, \qquad \nabla \times \vec{H} = \vec{0}, \qquad \vec{B} = \mu_0 \left(\vec{H} + \vec{M} \right). \tag{2.7}$$

Equations characterizing the basic state are introduced in the form

$$\left.\begin{array}{l} \dfrac{\partial}{\partial t} = 0, \ \vec{q}_b = (0,0,0), \ T = T_b(z), \\[2mm] p = p_b(z), \ \rho = \rho_b(z), \ \vec{H} = H_b(z), \\[2mm] \vec{M} = M_b(z), \ \vec{B} = B_b(z), \ \vec{Q} = \vec{Q}_b(0,0,k_1\beta) \end{array}\right\} \tag{2.8}$$

where $\beta = \dfrac{T_1 - T_0}{2}$. The solution pertaining to the basic state reads

$$\rho_b = \rho_0[1 + \alpha\beta z] \tag{2.9}$$

$$\vec{H}_b = \left[H_0 - \frac{K_m \beta z}{1 + \chi_m} \right] \hat{k} \tag{2.10}$$

$$\vec{M} = \left[M_0 + \frac{K_m \beta z}{1 + \chi_m} \right] \hat{k} \tag{2.11}$$

$$\vec{B} = \mu_0 \left[\vec{H} + \vec{M} \right] \hat{k} \ . \tag{2.12}$$

3. STABILITY ANALYSIS

We shall obtain the dimensionless equations following the small perturbation stability analysis enveloping normal modes (Finlayson [8], Soya Mathew and Maruthamanikandan [11]). The perturbed state equations involving infinitesimally small perturbations are

$$\left.\begin{array}{l} \vec{q} = \vec{q}_b + \vec{q}\,', \ T = T_b + T', \ p = p_b + p', \\[2mm] \rho = \rho_b + \rho', \ \vec{H} = \vec{H}_b + \vec{H}', \vec{M} = \vec{M}_b + \vec{M}', \\[2mm] \vec{B} = \vec{B}_b + \vec{B}', \ \vec{Q} = \vec{Q}_b + \vec{Q}', \ \phi = \varphi_b + \phi' \end{array}\right\} \tag{3.1}$$

where the primes indicate perturbed quantities. The perturbed governing linearized equations take the form

$$\left(1 + \lambda_1 \frac{\partial}{\partial t}\right)\left[\frac{\rho_0}{\varepsilon}\frac{\partial}{\partial t}\left(\nabla^2 w'\right) - \alpha g \rho_0 \nabla_1^2 T' + \mu_0 K_m \beta \frac{\partial}{\partial z}\left(\nabla_1^2 \phi'\right) - \frac{\mu_0 K_m^2 \beta \nabla_1^2 T'}{1 + \chi_m}\right]$$
$$= \left(1 + \lambda_2 \frac{\partial}{\partial t}\right)\left[-\frac{\mu_f}{k}\nabla^2 w' + \overline{\mu_f} \nabla^4 w'\right] \tag{3.2}$$

$$(\rho_0 C)_1 \frac{\partial T'}{\partial t} - \mu_0 T_a K_m \frac{\partial}{\partial t}\left(\frac{\partial \phi'}{\partial z}\right) = -\nabla.\vec{Q}' + \left[(\rho_0 C)_2 - \frac{\mu_0 T_a K_m^2}{1 + \chi_m}\right]\beta w' \tag{3.3}$$

$$\left(1+\tau\frac{\partial}{\partial t}\right)\vec{Q}'=-\frac{\tau k_1 \beta}{2}\left(\frac{\partial \vec{q}'}{\partial z}-\nabla w'\right)-k_1 \nabla T' \tag{3.4}$$

$$\left(1+\chi_m\right)\frac{\partial^2 \phi'}{\partial z^2}+\left(1+\frac{M_0}{H_0}\right)\nabla_1^2 \phi'-K_m\frac{\partial T'}{\partial z}=0 \ . \tag{3.5}$$

We take divergence on both sides of equation (3.4) and substitute in equation (3.3) to eliminate $\vec{Q}'$ from equation (3.3). The resulting system of linearized perturbed equations are as follows

$$\left(1+\lambda_1\frac{\partial}{\partial t}\right)\left[\frac{\rho_0}{\varepsilon}\frac{\partial}{\partial t}\left(\nabla^2 w'\right)-\alpha g\rho_0\nabla_1^2 T'+\mu_0 K_m\beta\frac{\partial}{\partial z}\left(\nabla_1^2 \phi'\right)-\frac{\mu_0 K_m^2\beta\nabla_1^2 T'}{1+\chi_m}\right]$$
$$=\left(1+\lambda_2\frac{\partial}{\partial t}\right)\left[-\frac{\mu_f}{k}\nabla^2 w'+\overline{\mu_f}\nabla^4 w'\right] \tag{3.6}$$

$$\left(1+\tau\frac{\partial}{\partial t}\right)\left[\left(\rho_0 C\right)_1\frac{\partial T'}{\partial t}-\mu_0 T_a K_m\frac{\partial}{\partial t}\left(\frac{\partial \phi'}{\partial z}\right)\right]-\left[\left(\rho_0 C\right)_2-\frac{\mu_0 T_a K_m^2}{1+\chi_m}\right]\beta w'=-k_1\nabla^2 T'-\frac{\tau k_1\beta}{2}\nabla^2 w' \tag{3.7}$$

$$\left(1+\chi_m\right)\frac{\partial^2 \phi'}{\partial z^2}+\left(1+\frac{M_0}{H_0}\right)\nabla_1^2 \phi'-K_m\frac{\partial T'}{\partial z}=0 \tag{3.8}$$

where

$$\left(\rho_0 C\right)_1=\varepsilon\rho_0 C_{V,H}+\varepsilon\mu_0 H_0 K_m+\left(1-\varepsilon\right)\left(\rho_0 C\right)_s \ , \quad \left(\rho_0 C\right)_2=\varepsilon\rho_0 C_{V,H}+\varepsilon\mu_0 H_0 K_m \ , \quad \nabla_1^2=\frac{\partial^2}{\partial x^2}+\frac{\partial^2}{\partial y^2}, \ \nabla^2=\nabla_1^2+\frac{\partial^2}{\partial z^2} \ ,$$

$$K_m=-\left(\frac{\partial M}{\partial t}\right)_{V,H} \text{ and } \chi_m=\left(\frac{\partial M}{\partial H}\right)_{H_0,T_a} \text{ with } \phi' \text{ being the magnetic potential.}$$

The normal mode solution is accessible and the same has the form

$$\begin{bmatrix} w' \\ T' \\ \phi' \end{bmatrix}=\begin{bmatrix} W(z) \\ \Theta(z) \\ \Phi(z) \end{bmatrix}e^{i(lx+my)+\sigma t} \tag{3.9}$$

where l and m are respectively the wave numbers in the x and y directions and σ is the growth rate. Substitution of (3.9) into equations (3.6) to (3.8) leads to

$$\left(1+\lambda_1\sigma\right)\left[\frac{\rho_0}{\varepsilon}\sigma\left(D^2-K_h^2\right)W+\alpha\rho_0 gK_h^2\Theta-\mu_0 K_m\beta K_h^2 D\Phi+\frac{\mu_0 K_m^2\beta K_h^2\Theta}{1+\chi_m}\right]$$
$$=\left(1+\lambda_2\sigma\right)\left[-\frac{\mu_f}{k}\left(D^2-K_h^2\right)W+\overline{\mu_f}\left(D^2-K_h^2\right)^2 W\right] \tag{3.10}$$

$$\left(1+\tau\sigma\right)\left[\left(\rho_0 C\right)_1\sigma\Theta-\mu_0 T_a K_m\sigma D\Phi\right]$$
$$-\left[\left(\rho_0 C\right)_2-\frac{\mu_0 T_a K_m^2}{1+\chi_m}\right]\beta W=k_1\left(D^2-K_h^2\right)\Theta-\frac{\tau k_1\beta}{2}\left(D^2-K_h^2\right)W \tag{3.11}$$

$$\left(1+\chi_m\right)D^2\Phi-\left(1+\frac{M_0}{H_0}\right)K_h^2\Phi(z)-K_m D\Theta=0 \tag{3.12}$$

where $D=\frac{d}{dz}$ and $K_h^2=l^2+m^2$ is the overall horizontal wave number. Non-dimensionalizing equations (3.10) through (3.12) using the scaling

$$W^* = \frac{Wd}{\kappa}, \quad \Theta^* = \frac{\Theta}{\beta d}, \quad \Phi^* = \frac{\Phi}{\frac{K_m \beta d^2}{1+\chi_m}},$$

$$a = K_h d, \quad z^* = \frac{z}{d}, \quad \sigma^* = \frac{\sigma}{\frac{\kappa}{d^2}}$$

$$\tag{3.13}$$

we obtain the following dimensionless equations (asterisks are neglected for simplicity)

$$\left(1 + F_1 \sigma\right)\left[\frac{\sigma}{\text{Pr}}\left(D^2 - a^2\right)W + (R+N)a^2\,\Theta - Na^2 D\Phi\right] = \left(1 + F_2 \sigma\right)\left[-Da^{-1}\left(D^2 - a^2\right)W + \Lambda\left(D^2 - a^2\right)^2 W\right] \tag{3.14}$$

$$\left(1 + 2G\sigma\right)\left[\lambda\sigma\Theta - M_2\,\sigma D\Phi - (1-M_2)\,W\right] = \left(D^2 - a^2\right)\Theta - G\left(D^2 - a^2\right)W \tag{3.15}$$

$$\left(D^2 - M_3 a^2\right)\Phi - D\Theta = 0 \tag{3.16}$$

where $\lambda = \dfrac{(\rho_0 C)_1}{(\rho_0 C)_2}$ and $M_2 = \dfrac{\mu_0 K_m^2 Ta}{(1+\chi_m)(\rho_0 C)_2}$. The parameter M_2 is neglected as it is of very small order (Finlayson [8]). When $\lambda = 1$, we obtain the following equations

$$\left(1 + F_1\sigma\right)\left[\frac{\sigma}{\text{Pr}}\left(D^2 - a^2\right)W + (R+N)a^2\Theta - Na^2 D\Phi\right] = \left(1 + F_2\sigma\right)\left[\Lambda\left(D^2 - a^2\right)^2 W - Da^{-1}\left(D^2 - a^2\right)W\right] \tag{3.17}$$

$$\left(1 + 2G\sigma\right)\left(\sigma\Theta - W\right) - \left(D^2 - a^2\right)\Theta + G\left(D^2 - a^2\right)W = 0 \tag{3.18}$$

$$\left(D^2 - M_3 a^2\right)\Phi - D\Theta = 0 \tag{3.19}$$

where $F_1 = \dfrac{\lambda_1 \kappa}{d^2}$ is the non-dimensional stress relaxation parameter, $F_2 = \dfrac{\lambda_2 \kappa}{d^2}$ is the non-dimensional strain retardation parameter, $\text{Pr} = \dfrac{\varepsilon\mu_f}{\rho_0\kappa}$ is the Prandtl number, $R = \dfrac{\rho_0\alpha g\beta d^4}{\mu_f\,\kappa}$ is the thermal Rayleigh number, $N = \dfrac{\mu_0 K^2\beta^2 d^4}{\mu_f\,(1+\chi_m)\kappa}$ is the magnetic Rayleigh number, $Da^{-1} = \dfrac{d^2}{k}$ is the inverse Darcy number, $\Lambda = \dfrac{\overline{\mu_f}}{\mu_f}$ is the Brinkman number, $G = \dfrac{\tau\kappa}{2d^2}$ is the Cattaneo number and $M_3 = \left(\dfrac{1+\dfrac{M_0}{H_0}}{1+\chi_m}\right)$ is the non-buoyancy-magnetization parameter. The boundary conditions encompassing free and isothermal surfaces are $W = D^2 W = \Theta = D\Phi = 0$ at $z = \pm 1/2$ (Finlayson [8]).

3.1. Stationary Instability

As for the stationary mode, equations (3.17) - (3.19) turn out to be the following

$$\Lambda\left(D^2 - a^2\right)^2 W - Da^{-1}\left(D^2 - a^2\right)W - (R+N)a^2\Theta + Na^2 D\Phi = 0 \tag{3.20}$$

$$\left[G\left(D^2 - a^2\right) - 1\right]W - \left(D^2 - a^2\right)\Theta = 0 \tag{3.21}$$

$$\left(D^2 - M_3 a^2\right)\Phi - D\Theta = 0 \;. \tag{3.22}$$

Equations (3.20) through (3.22) along with the boundary conditions embrace an eigenvalue problem with R being an eigenvalue. The straightforward solution $W = A_1 \cos(\pi z)$, $\Theta = A_2 \cos(\pi z)$, $\Phi = \dfrac{A_3}{\pi} \sin(\pi z)$, with A_1, A_2 and A_3 being constants, is taken into consideration. On applying the solvability condition, we obtain

$$R^{st} = \frac{\left(\pi^2 + a^2\right)^2 \left[Da^{-1} + \left(\pi^2 + a^2\right) \Lambda \right]}{a^2 \left[1 + G\left(\pi^2 + a^2\right) \right]} - \frac{N M_3 a^2}{\left(M_3 a^2 + \pi^2\right)} \tag{3.23}$$

where the superscript '*st*' stands for stationary convection. Equation (3.23) exactly coincides with that obtained by Soya Mathew and Maruthamanikandan [22] and Soya Mathew et al. [23] followed by the corresponding deductions.

3.2. Oscillatory Instability

The dimensionless equations concerning the overstable motion are

$$\left[\left(1+F_1\sigma\right)\frac{\sigma}{\Pr}+\left(1+F_2\sigma\right)\left(Da^{-1}+\Lambda\left(\pi^2+a^2\right)\right)\right]\left(\pi^2+a^2\right)A_1 -\left(1+F_1\sigma\right)\left(R+N\right)a^2 A_2 + \left(1+F_1\sigma\right)Na^2 A_3 = 0 \tag{3.24}$$

$$\left[1+2G\sigma+G\left(\pi^2+a^2\right)\right]A_1 - \left[\left(\pi^2+a^2\right)+\left(1+2G\sigma\right)\sigma\right]A_2 = 0 \tag{3.25}$$

$$\pi^2 A_2 - \left(\pi^2 + M_3 a^2\right)A_3 = 0 . \tag{3.26}$$

On applying the solvability condition, we obtain

$$R = \left\{ \frac{p\left[\Pr\left(Da^{-1}+p\Lambda\right)\left(1+f_2\sigma\right)+\sigma+f_1\sigma^2\right]\left(p+\sigma+2g\sigma^2\right)}{a^2 \Pr\left(1+f1\sigma\right)\left[1+g\left(p+2\sigma\right)\right]} \right\} - \frac{NM_3 a^2}{M_3 a^2 + \pi^2} \tag{3.27}$$

where $p = \pi^2 + a^2$. If we let $\sigma = i\omega$ with ω being the frequency of oscillations, we obtain R as $R = R_1 + i R_2$. Both R_1 and R_2 are computed by means of the MATHEMATICA software mathematical package.

4.   RESULTS AND DISCUSSION

The study is concerned with porous medium ferroconvection in a viscoelastic magnetic fluid with non-classical heat conduction. We have obtained the conditions for both stationary and oscillatory convection using linear theory, which is based on the normal mode technique. The thermal Rayleigh number R, characterising the stability of the system, is obtained as a function of the different parameters of the study. The eigenvalue expression and the associated critical numbers are determined by using MATHEMATICA software. As we can observe from the expression (3.23) stationary Rayleigh is independent of the viscoelastic parameters as obtained by Soya Mathew and Maruthamanikandan [22]. Also, if the Cattaneo number is taken below the threshold value, then only stationary convection occurs [23]. Hence, for stationary convection, viscoelastic fluid behaves same as Newtonian fluid. Rayleigh number for oscillatory mode is obtained as a function of Prandtl number, Cattaneo number, magnetic, viscoelastic and porous parameters.

In **Fig. 2** critical Rayleigh number R_c is expressed as a function of magnetic Rayleigh number N by keeping all other parameters as constant by fixing their values as $F_1 = 1.5$, $F_2 = 0.3$, $\Pr = 10$, $Da^{-1} = 5$, $\Lambda = 3$, $G = 0.06$ and $M_3 = 3$. As N increases, R_c decreases and hence the system is destabilized. We observe that oscillatory convection is preferred to stationary convection as R_c^{osc} is less than R_c^{st} and hence the principle of exchange of instabilities is not valid. In **Fig. 3** critical Rayleigh number R_c is expressed as a function of the magnetic Rayleigh number N by varying F_1 and keeping all other parameters as constant by fixing their values as $F_2 = 0.3$, $\Pr = 10$, $Da^{-1} = 5$, $\Lambda = 3$, $G = 0.06$ and $M_3 = 3$. We notice that, as F_1 increases, the R_c^{osc} value decreases which indicates that the stress relaxation parameter F_1 hastens the oscillatory ferroconvection. In **Fig. 4** critical Rayleigh number R_c is expressed as a function of the magnetic Rayleigh number N by varying F_2 and keeping all other parameters as constant by fixing their values as $F_1 = 1.5$, $\Pr = 10$, $Da^{-1} = 5$, $\Lambda = 3$, $G = 0.06$ and $M_3 = 3$. As there is an increase in the values of F_2, we notice that there is an increase in R_c^{osc} which indicates that the strain retardation parameter F_2 slows down the onset of oscillatory ferroconvection.
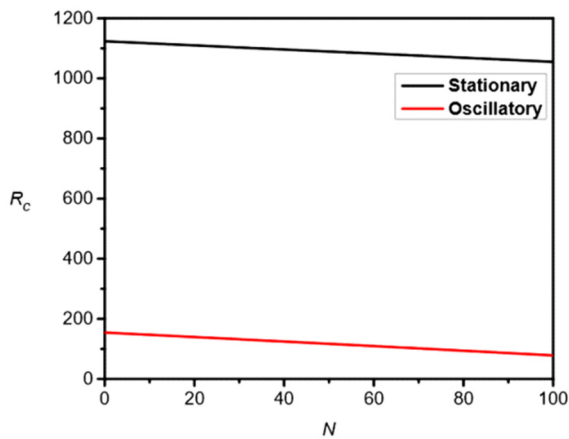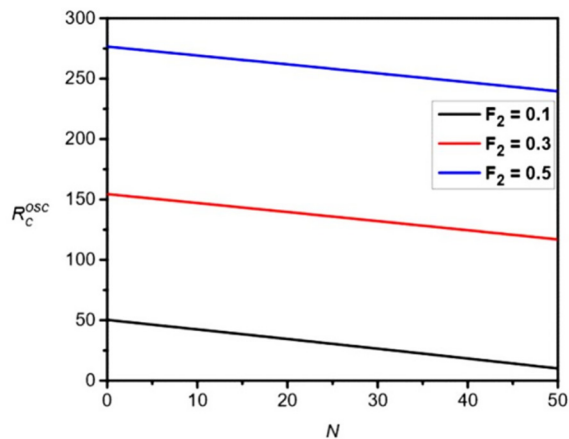
Figure 2. Plot of R_c versus N with $F_1 = 1.5$, $F_2 = 0.3$, Pr$=10$, $Da^{-1}=5$, $\Lambda=3$, $G=0.06$ and $M_3=3$.
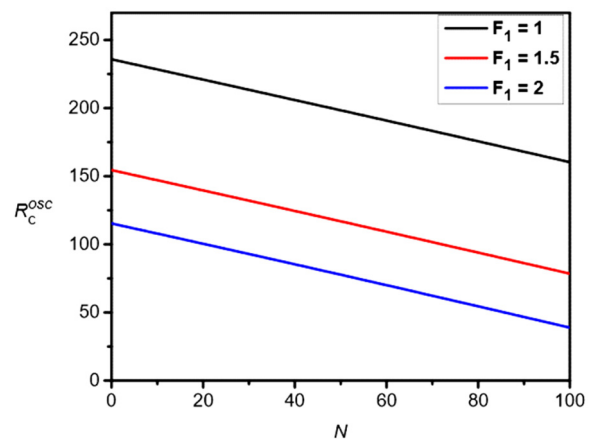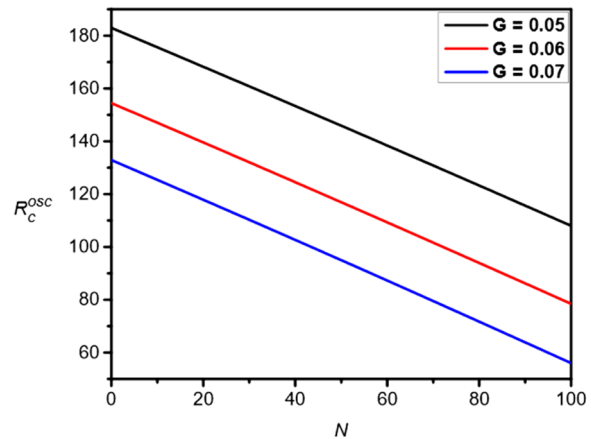

Figure 3. Plot of R_c^{osc} versus N with variation in F_1 with $F_2 = 0.3$, Pr$=10$, $Da^{-1}=5$, $\Lambda=3$, $G=0.06$ $M_3=3$ and $Ta=500$.

In **Fig. 5** critical Rayleigh number R_c is expressed as a function of N by varying G and keeping all other parameters as constant by fixing their values as $F_1 = 1.5$, $F_2 = 0.3$, Pr$=10$, $Da^{-1}=5$, $\Lambda=3$ and $M_3=3$. As G increases, there is a decrease in R_c^{osc}. As discussed by Straughan [24], the above threshold value of Cattaneo number G associated with oscillatory convection comes into picture. It destabilizes the system. In **Fig. 6** critical Rayleigh number R_c is expressed as a function of the magnetic Rayleigh number N by varying Pr and keeping all other parameters as constant by fixing their values as $F_1 = 1.5$, $F_2 = 0.3$, $Da^{-1} = 5$, $\Lambda=3$, $G= 0.06$ and $M_3 = 3$. As there is an increase in the values of Pr, we notice there is a decrease in R_c^{osc} due to the above threshold value of G and hence the system is destabilized. This is due to the hyperbolic nature instead of the parabolic one of the temperature equation.
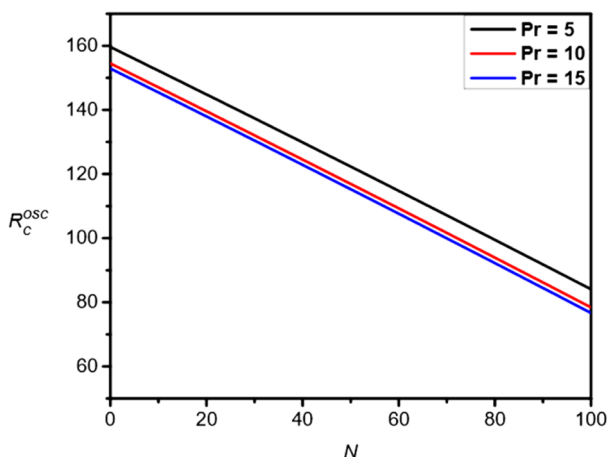

Figure 4. Plot of R_c^{osc} versus N with variation in F_2 with $F_1 = 1.5$, Pr$=10$, $Da^{-1}=5$, $\Lambda=3$, $G= 0.06$ and $M_3=3$.
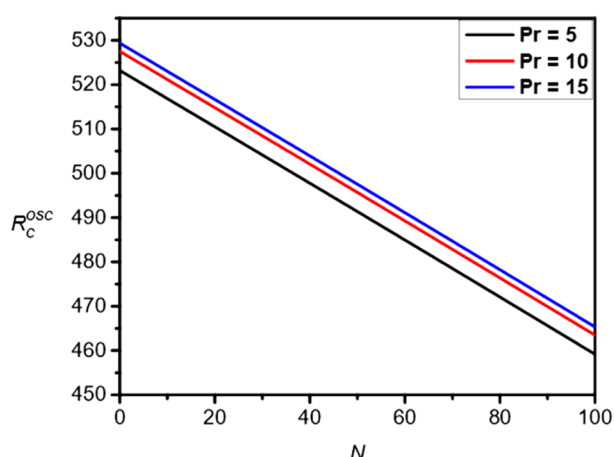

Figure 5. Plot of R_c^{osc} versus N with variation in G with $F_1 = 1.5$, $F_2 = 0.3$, Pr$=10$, $Da^{-1} = 5$, $\Lambda=3$ and $M_3 = 3$.

In **Fig. 7** critical Rayleigh number R_c^{osc} is expressed as a function of magnetic Rayleigh number N by varying Pr and keeping all other parameters as constant by fixing their values as $F_1 = 1.5$, $F_2 = 0.3$, $Da^{-1}=5$, $\Lambda=3$, $G= 0$ and $M_3=3$. We notice that R_c^{osc} increases as Pr increases and hence system is stabilized. This is due to the absence of Cattaneo number.

From Figures 6 and 7, we witness the dual nature of the Prandtl number Pr depending on the Cattaneo number G. If the Cattaneo number G is above the threshold value, then on increasing Pr there is a decrease in R_c^{osc} as noticed in the work of Nagouda and Pranesh [25] and if the Cattaneo number G is below the threshold value, then on increasing Pr there is an increase in R_c^{osc} as noticed in the work of Swamy et al. [18].

Figure 6. Plot of R_c^{osc} versus N with variation in Pr with $F_1 =1.5,\ F_2 =0.3, Da^{-1}=5, \Lambda=3, G=0.06\ and\ M_3=3.$

Figure 7. Plot of R_c^{osc} versus N with variation in Pr with $F_1 =1.5,\ F_2 =0.3,\ Da^{-1}=5,\ \Lambda=3,\ G=0\ and\ M_3=3.$

Stationary vs Oscillatory Instability

Table 1. Critical values of the Rayleigh number and wave number with $F_1 =1.5,\ F_2 =0.3,\ Pr=10,\ Da^{-1}=5,\ \Lambda=3,\ G=0.06$ and $M_3=3$.

N	Stationary		Oscillatory	
	R_c^{st}	α_c^{st}	R_c^{osc}	α_c^{osc}
0	1123.54	2.6486	154.486	3.05605
20	1109.91	2.65782	139.604	3.13009
40	1096.25	2.66701	124.546	3.20226
60	1082.56	2.67618	109.324	3.27246
80	1068.84	2.68533	93.9499	3.34063
100	1055.09	2.69446	78.4344	3.40676

Table 2. Critical values of the wave number varying with F_1 by fixing $F_2 = 0.3,\ Pr= 10,\ Da^{-1}= 5,\ \Lambda= 3,\ G= 0.06$ and $M_3= 3$.

N	$F_1 =1$	$F_1 =1.5$	$F_1 =2$
	α_c	α_c	α_c
0	3.06861	3.05605	3.04212
20	3.11749	3.13009	3.14058
40	3.16559	3.20226	3.23566
60	3.21286	3.27246	3.32715
80	3.25927	3.34063	3.41501
100	3.30481	3.40676	3.49928

Table 3. Critical values of the wave number varying with F_2 by fixing $F_1 = 1.5,\ Pr= 10,\ Da^{-1}= 5,\ \Lambda=3,\ G= 0.06$ and $M_3=3$.

| N	$F_2 =0.1$	$F_2 =0.3$	$F_2 =0.5$
	α_c	α_c	α_c
0	3.4042	3.05605	2.99105
10	3.52012	3.09329	3.01222
20	3.63083	3.13009	3.03327
30	3.73634	3.16642	3.05418
40	3.83684	3.20226	3.07495
50	3.93259	3.23761	3.09558

Table 4. Critical values of the wave number varying with G by fixing $F_1 = 1.5$, $F_2 = 0.3$, Pr$=10$, $Da^{-1} = 5$, $\Lambda = 3$ and $M_3 = 3$.

N	$G = 0.05$	$G = 0.06$	$G = 0.07$
	α_c	α_c	α_c
0	2.98828	3.05605	3.10812
20	3.05035	3.13009	3.19439
40	3.11118	3.20226	3.27804
60	3.17068	3.27246	3.35892
80	3.2288	3.34063	3.437
100	3.28551	3.40676	3.5123

Table 5. Critical values of the wave number varying with Pr by fixing $F_1 = 1.5$, $F_2 = 0.3$, $Da^{-1} = 5$, $\Lambda = 3$, $G = 0.06$ and $M_3 = 3$.

| N	Pr$=5$	Pr$=10$	Pr$=15$
	α_c	α_c	α_c
0	3.01748	3.05605	3.06942
20	3.08869	3.13009	3.14436
40	3.15822	3.20226	3.21737
60	3.22595	3.27246	3.28835
80	3.29182	3.34063	3.35723
100	3.35581	3.40676	3.42402

G = 0 (In the absence of Second Sound)

Table 6. Critical values of the wave number varying with Pr by fixing $F_1 = 1.5$, $F_2 = 0.3$, $Da^{-1} = 5$, $\Lambda = 3$, $G = 0$ and $M_3 = 3$.

N	Pr$=5$	Pr$=10$	Pr$=15$
	α_c	α_c	α_c
0	2.38141	2.38512	2.38669
20	2.39726	2.40086	2.40238
40	2.41302	2.41651	2.418
60	2.42869	2.43208	2.43352
80	2.44427	2.44756	2.44895
100	2.45975	2.46293	2.46428

In **Fig. 8** critical Rayleigh number R_c^{osc} is expressed as a function of N by varying Pr and keeping all other parameters as constant by fixing their values as $F_1 = 0$, $F_2 = 0$, $Da^{-1} = 5$, $\Lambda = 3$, $G = 0.06$ and $M_3 = 3$, i.e., in the absence of viscoelastic parameters. In this case also there is a decrease in R_c^{osc} as we increase Pr which again clearly suggests that the dual nature of Pr is only due to the presence of the Cattaneo number.
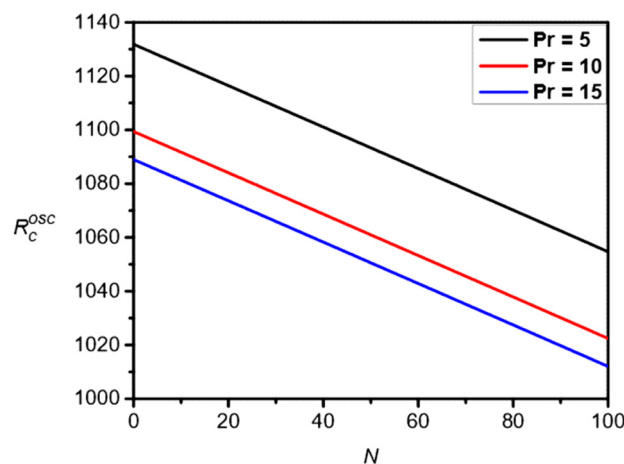
Figure 8. Plot of R_c^{osc} versus N with variation in Pr with $F_1 = 0$, $F_2 = 0$, $Da^{-1} = 5$, $\Lambda = 3$, $G = 0.06$ and $M_3 = 3$.

For Newtonian ferromagnetic fluid $\left(i.e.,\ F_1 = 0 \text{ and } F_2 = 0\right)$

Table 7. Critical values of the wave number α_c varying with Pr by fixing $F_1 = 0$, $F_2 = 0$, $Da^{-1} = 5$, $\Lambda = 3$, $G = 0.06$ and $M_3 = 3$.

N	$\mathrm{Pr} = 5$	$\mathrm{Pr} = 10$	$\mathrm{Pr} = 15$
	α_c	α_c	α_c
0	3.30324	3.28459	3.27851
20	3.31363	3.29529	3.28931
40	3.324	3.30595	3.30008
60	3.33432	3.31658	3.3108
80	3.3446	3.32716	3.32148
100	3.35485	3.3377	3.33212

Table 8. Critical values of the wave number varying with Da^{-1} by fixing $F_1 = 1.5$, $F_2 = 0.3$, $\mathrm{Pr} = 10$, $\Lambda = 3$, $G = 0.06$ and $M_3 = 3$.

N	$Da^{-1} = 0$	$Da^{-1} = 5$	$Da^{-1} = 10$
	α_c	α_c	α_c
0	2.94266	3.05605	3.15784
20	3.02243	3.13009	3.22714
40	3.10014	3.20226	3.29475
60	3.17561	3.27246	3.36059
80	3.24874	3.34063	3.42464
100	3.31951	3.40676	3.48689

In **Fig. 9** critical Rayleigh number R_c^{osc} is expressed as a function of magnetic Rayleigh number N by varying Da^{-1} and keeping all other parameters as constant by fixing their values as $F_1 = 1.5$, $F_2 = 0.3$, $\mathrm{Pr} = 10$, $\Lambda = 3$, $G = 0.06$ and $M_3 = 3$. Oscillatory ferroconvection is delayed because as Da^{-1} is increased, there is an increase in the values of R_c^{osc}. The reason for this is the increase in Da^{-1} will decrease the porous medium permeability and hence the convective instability is impeded.
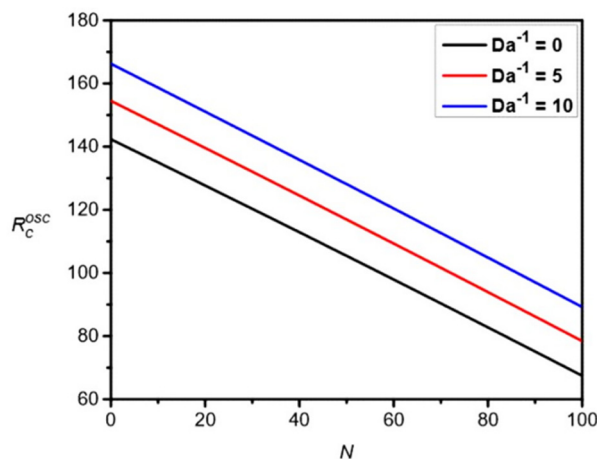
Figure 9. Plot of R_c^{osc} versus N with variation in Da^{-1} with $F_1 = 1.5$, $F_2 = 0.3$, $\mathrm{Pr} = 10$, $\Lambda = 3$, $G = 0.06$ and $M_3 = 3$.
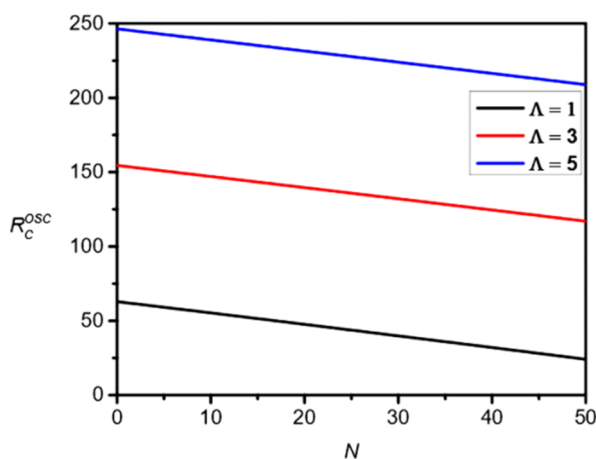
In **Fig. 10** critical Rayleigh number R_c^{osc} is expressed as a function of the magnetic Rayleigh number N by varying the Brinkman number Λ and keeping all other parameters as constant by fixing their values as $F_1 = 1.5$, $F_2 = 0.3$, $\mathrm{Pr} = 10$, $Da^{-1} = 3$, $G = 0.06$ and $M_3 = 3$. As the Brinkman number Λ increases, R_c^{osc} also increases and therefore oscillatory ferroconvection is delayed. As the Brinkman model accounts for an effective viscosity $\overline{\mu_f}$ which is different from fluid viscosity μ_f and the ratio is assigned as the Brinkman number Λ. Hence viscous effect increases on increasing Λ and hence ferroconvective instability is hampered due to the presence of porous media.

Table 9. Critical values of the wave number varying with Λ by fixing $F_1 =1.5$, $F_2 =0.3$, Pr=10, $Da^{-1}=5$, $G=0.06$ and $M_3=3$.

N	$\Lambda=1$	$\Lambda=3$	$\Lambda=5$
	α_c	α_c	α_c
0	3.16486	3.05605	3.02786
10	3.25535	3.09329	3.05126
20	3.3429	3.13009	3.07448
30	3.42738	3.16642	3.09754
40	3.50877	3.20226	3.12041
50	3.58714	3.23761	3.14309

Table 10. Critical values of the wave number varying with M_3 by fixing $F_1 =1.5$, $F_2 = 0.3$, Pr=10, $Da^{-1}=5$, $\Lambda=3$ and $G=0.06$.

N	$M_3=1$	$M_3=3$	$M_3=5$
	α_c	α_c	α_c
0	3.05605	3.05605	3.05605
20	3.15476	3.13009	3.11124
40	3.256	3.20226	3.16482
60	3.35878	3.27246	3.21682
80	3.46216	3.34063	3.26729
100	3.56526	3.40676	3.3163

Figure 10. Plot of R_c^{osc} versus N with variation in Λ with $F_1 =1.5$, $F_2 =0.3$, Pr=10, $Da^{-1}=5$, $G=0.06$ and $M_3=3$.
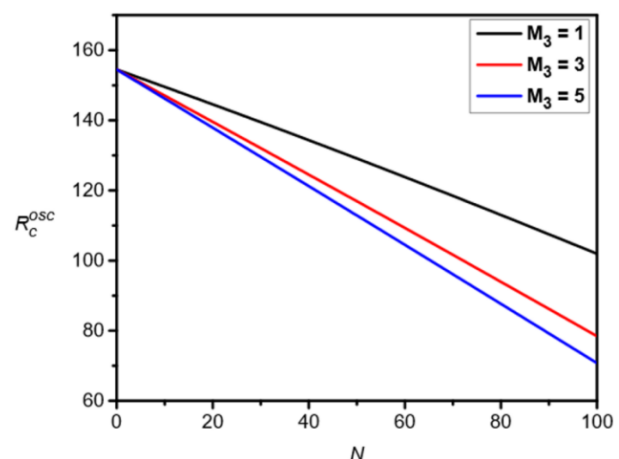
Figure 11. Plot of R_c^{osc} versus N with variation in M_3 with $F_1 =1.5$, $F_2 =0.3$, Pr=10, $Da^{-1}=5$, $\Lambda=3$ and $G=0.06$.

In **Fig. 11** critical Rayleigh number R_c^{osc} is expressed as a function of the magnetic Rayleigh number N by varying M_3 and keeping all other parameters as constant by fixing their values as $F_1 =1.5$, $F_2 =0.3$, Pr=10, $Da^{-1} = 5$, $\Lambda=3$ and $G=0.06$. The linearity departure of magnetic equation is addressed by the parameter M_3. We notice from Fig. 11 that as M_3 increases, the R_c^{osc} monotonically decreases which implies that magnetic equation of state grows more and more to nonlinear state due to which ferroconvection is hastened.

From Figs. 12 through 17, one can observe that when all the respective parameters increase, ω_c^2 also increases, whereas from Figs. 18 through 20, as all relevant parameters increase, ω_c^2 also decreases. Hence, we can conclude that from Figs. 12 through 20 that the frequency ω_c of oscillatory ferroconvective instability is sensitive to all the parameters of the study. On the other hand, wave number depicts the size and shape of the convection cell. From Tables 2 through 10, it follows that convection cell size is also sensitive to the all the parameters of the study at hand. Indeed, the convection cell size is enlarged with an increase in F_2, Λ and M_3 and the opposite is found to be true with respect to an increase in the rest of the parameters.
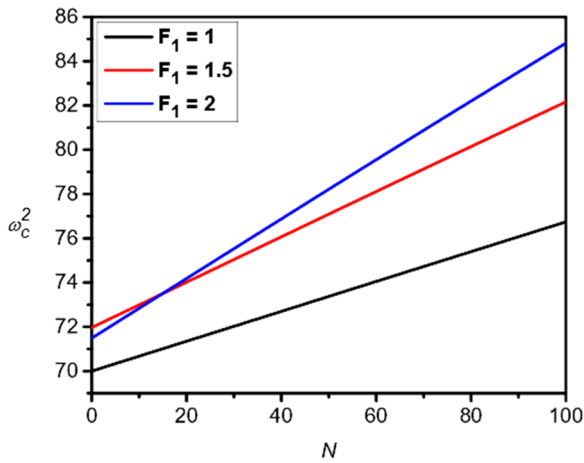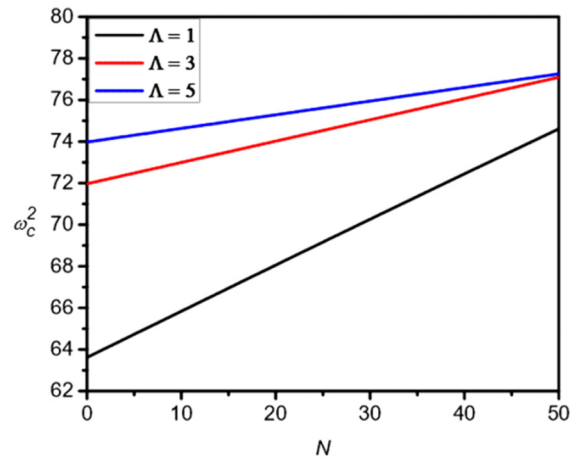
Figure 12. Plot of ω_c^2 versus N with variation in F_1 with $F_2 = 0.3$, $\text{Pr} = 10$, $Da^{-1} = 5$, $\Lambda = 3$, $G = 0.06$ *and* $M_3 = 3$.
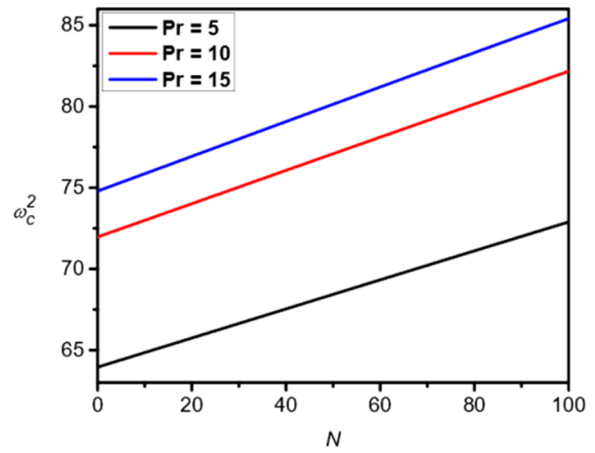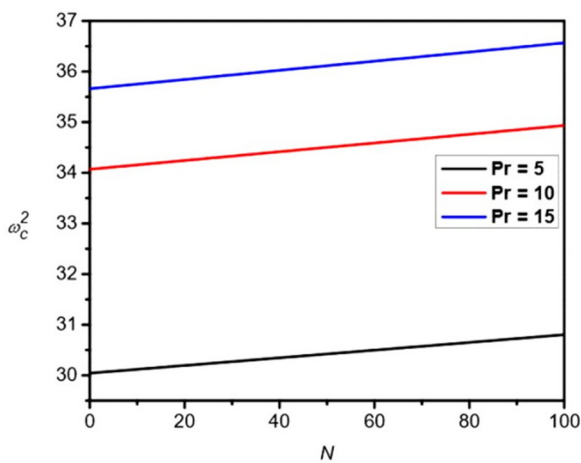

Figure 13. Plot of ω_c^2 versus N with variation in Pr with $F_1 = 1.5$, $F_2 = 0.3$, $Da^{-1} = 5$, $\Lambda = 3$, $G = 0.06$ *and* $M_3 = 3$.
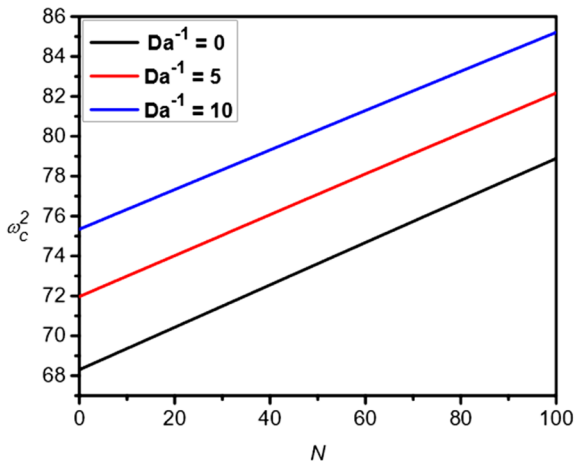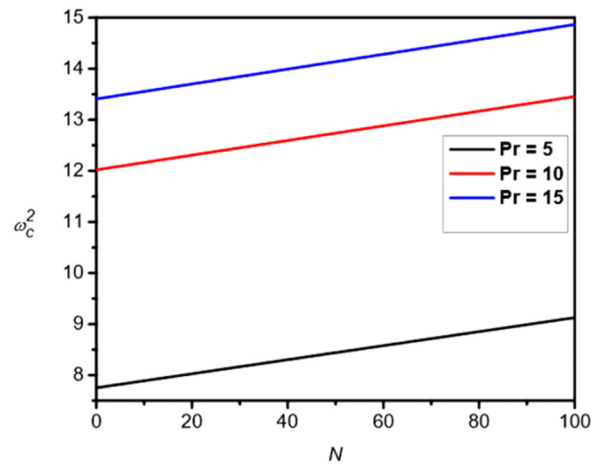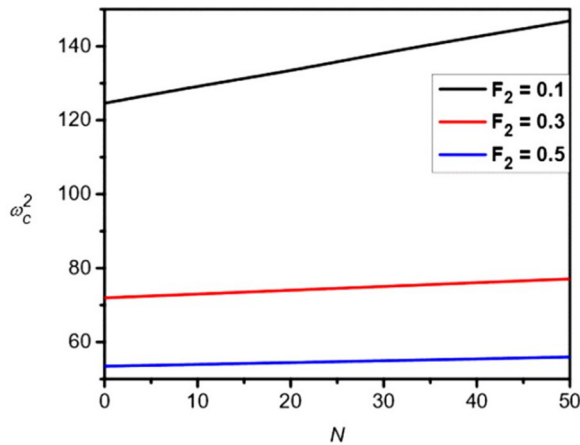

Figure 14. Plot of ω_c^2 versus N with variation in Da^{-1} with $F_1 = 1.5$, $F_2 = 0.3$, $\text{Pr} = 10$, $\Lambda = 3$, $G = 0.06$ and $M_3 = 3$.

Figure 15. Plot of ω_c^2 versus N with variation in Λ with $F_1 = 1.5$, $F_2 = 0.3$, $\text{Pr} = 10$, $Da^{-1} = 5$, $G = 0.06$ and $M_3 = 3$.
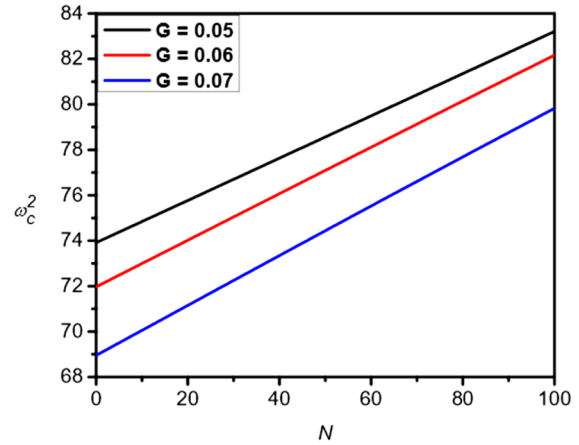

Figure 16. Plot of ω_c^2 versus N with variation in Pr with $F_1 = 1.5$, $F_2 = 0.3$, $Da^{-1} = 5$, $\Lambda = 3$, $G = 0$ and $M_3 = 3$.
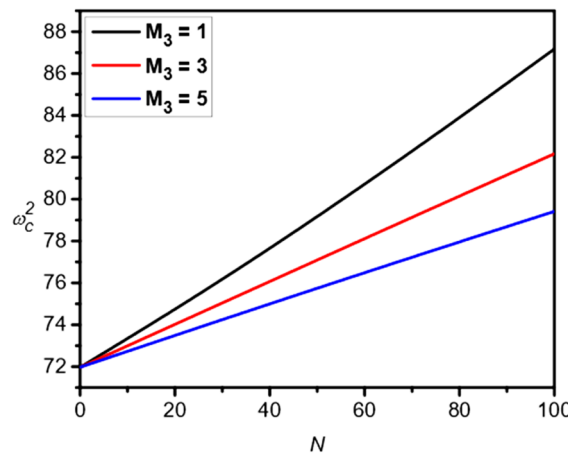

Figure 17. Plot of ω_c^2 versus N with variation in Pr with $F_1 = 0$, $F_2 = 0$, $Da^{-1} = 5$, $\Lambda = 3$, $G = 0.06$ and $M_3 = 3$.

Figure 18. Plot of ω_c^2 versus N with variation in F_2 with $F_1 = 1.5$, Pr=10, $Da^{-1}=5$, $\Lambda=3$, $G=0.06$ and $M_3=3$.

Figure 19. Plot of ω_c^2 versus N with variation in G with $F_1 = 1.5$, $F_2 = 0.3$, Pr=10, $Da^{-1}=5$, $\Lambda=3$ and $M_3=3$.

Figure 20. Plot of ω_c^2 versus N with variation in M_3 with $F_1 = 1.5$, $F_2 = 0.3$, Pr=10, $Da^{-1}=5$, $\Lambda=3$ and $G=0.06$.

It is worth mentioning that for Newtonian fluids only stationary convection is possible, but due to the presence of second sound, oscillatory instability is preferred to stationary stability as pointed out by Straughan [24].

CONCLUSIONS

1. The system is destabilized through the presence of magnetic forces caused by the magnetization of ferrofluids.
2. Nonlinearity in magnetization is shown to destabilize the system.
3. Viscoelastic relaxation and second sound are shown to destabilize the system.
4. Viscoelastic retardation, inverse Darcy number and Brinkman number are shown to stabilize the system.
5. Prandtl number destabilizes as well as stabilizes the system depending on the over and below threshold values of the Cattaneo number respectively.
6. Critical wavenumber and frequency of oscillatory motions are calculated as functions of all the parameters of the problem. They are shown to be sensitive to all the parameters of the problem.

ORCID ID

Naseer Ahmed, https://orcid.org/0000-0002-5327-9362; **S. Maruthamanikandan,** https://orcid.org/0000-0001-9811-0117
B.R. Nagasmitha, https://orcid.org/0009-0009-2930-3244

REFERENCES

[1] R. Kaiser, and G. Miskolczy, "Some applications of ferrofluid magnetic colloids," IEEE Transactions on Magnetics, **6**, 694-698 (1970). https://doi.org/10.1109/TMAG.1970.1066834
[2] K. Raj, and A.F. Chorney, "Ferrofluid technology-an overview," Indian J Eng Mater Sci. **5**(6), 372-389 (1998). http://nopr.niscpr.res.in/bitstream/123456789/29661/1/IJEMS%205%286%29%20372-389.pdf
[3] C. Scherer, and A.M.F. Neto, "Ferrofluids: properties and applications," Braz. J. Phys. **35**(3), 718-727 (2005). https://doi.org/10.1590/S0103-97332005000400018
[4] H.W. Muller, and L. Mario, Ferrofluid Dynamics, in: *Ferrofluids magnetically controllable fluids and their applications*, edited by S. Odenbach, (Springer, 2002), pp.112-123, https://link.springer.com/book/10.1007/3-540-45646-5

[5] R. Moskowitz, "Dynamic Sealing with Magnetic Fluids," Tribology Transactions, **18**, 135-143 (1975). https://doi.org/10.1080/05698197508982756

[6] Y. Morimoto, M. Akimoto, and Y. Yotsumoto, "Dispersion State of Protein-stabilized Magnetic Emulsions," Chemical and Pharmaceutical Bulletin, **30**, 3024-3027 (1982). https://doi.org/10.1248/CPB.30.3024

[7] R.E. Rosensweig, *Ferrohydrodynamics*, (Cambridge University Press, Cambridge, 1985).

[8] B.A. Finlayson, "Convective instability of ferromagnetic fluids," J. Fluid Mech. **40**, 753-767, (1970). https://doi.org/10.1017/S0022112070000423

[9] D.P. Lalas, and S. Carmi, "Thermoconvective stability of ferrofluids," Phys. Fluids, **14**(2), 436-437 (1971). https://doi.org/10.1063/1.1693446

[10] Nisha Mary Thomas, and S. Maruthamanikandan, "Gravity modulation effect on ferromagnetic convection in a Darcy-Brinkman layer of porous medium," J. Phys.: Conf. Series, **1139**, 012022 (2018). https://doi.org/10.1088/1742-6596/1139/1/012022

[11] Soya Mathew, and S. Maruthamanikandan, "Darcy-Brinkman ferroconvection with temperature dependent viscosity," J. Phys.: Conf. Series, **1139**, 012023, (2018). http://dx.doi.org/10.1088/1742-6596/1139/1/012023

[12] S. Maruthamanikandan, Nisha Mary Thomas, and Soya Mathew, "Thermorheological and magnetorheological effects on Marangoni-ferroconvection with internal heat generation," J. Phys.: Conf. Series, **1139**, 012024, (2018). https://doi.org/10.1088/1742-6596%2F1139%2F1%2F012024

[13] V. Vidya Shree, C. Rudresha, C. Balaji, and S. Maruthamanikandan, "Effect of MFD viscosity on ferroconvection in a fluid saturated porous medium with variable gravity," Journal of Mines, Metals and Fuels, **70**(3A), 98-103, (2022). http://dx.doi.org/10.26565/2312-4334-2022-4-10

[14] R.B. Bird, C. Armstrong, and O. Massager, *Dynamics of Polymeric Liquids*, vol. 1,2, 2nd edn. (Wiley, New York, 1987). https://doi.org/10.1002/bbpc.19870911221

[15] D.D. Joseph, Fluid Dynamics of Viscoelastic Liquids, (Springer, New York), (1990), https://doi.org/10.1007/978-1-4612-4462-2

[16] J.G. Oldroyd, "On the formulation of rheological equations of state," Proc. R. Soc. Lond. A, **200**, 523–541 (1950). https://doi.org/10.1098/rspa.1950.0035

[17] T. Green, "Oscillating convection in an elasticoviscous liquid," Phys. Fluids, **11**, 1410-1412 (1968). https://doi.org/10.1063/1.1692123

[18] M.S. Swamy, N.B. Naduvinamani, and W. Sidram, "Onset of Darcy–Brinkman convection in a binary viscoelastic fluid saturated porous layer," Transp. Porous Med. **94**(1), 339–357 (2012). https://doi.org/10.1007/s11242-012-0008-y

[19] D.S. Chandrasekharaiah, "Thermoelasticity with Second Sound: A Review," Applied Mechanics Reviews, **39**, 355-376 (1986). https://doi.org/10.1115/1.3143705

[20] M.E. Gurtin, and A.C. Pipkin, "A general theory of heat conduction with finite wave speeds," Arch. Ration. Mech. Anal. **31**(2), 113-126 (1968). https://doi.org/10.1007/BF00281373

[21] B. Straughan, and F. Franchi, "Bènard convection and the cattaneo law of heat conduction," Proc. R. Soc. Edinburgh Sect. A Math. **96**(1-2), 175-178 (1984). https://doi.org/10.1017/S0308210500020564

[22] Soya Mathew, and S. Maruthamanikandan, "Oscillatory porous medium ferroconvection with Maxwell-Cattaneo law of heat conduction," J. Phys. Conf. Ser. (1), 012024, (2021). https://doi.org/10.1088/1742-6596/1850/1/012024

[23] Soya Mathew, S. Maruthamanikandan, and S.S. Nagouda, "Gravitaional Instability in a Ferromagnetic Fluid Saturated Porous Medium with Non-Classical Heat Conduction," IOSR Journal of Mathematics, (IOSR-JM), **6**(1), 07-18 (2013). http://dx.doi.org/10.9790/5728-0610718

[24] B. Straughan, "Oscillatory convection and the Cattaneo law of heat conduction," Ricerche mat. **58**, 157-162 (2009). https://doi.org/10.1007/s11587-009-0055-z

[25] S.S. Nagouda, and S. Pranesh, "Rayleigh-Bènard convection in a second-order fluid with Maxwell-Cattaneo Law," The Bulletin of Society for Mathematical Services and Standards, **2**, 24-32 (2012). https://doi.org/10.18052/WWW.SCIPRESS.COM%2FBSMASS.2.24

КОЛИВАЛЬНА ФЕРОКОНВЕКЦІЯ У ПОРИСТОМУ СЕРЕДОВИЩІ У В'ЯЗКОПРУЖНІЙ МАГНІТНІЙ РІДИНІ З НЕКЛАСИЧНОЮ ТЕПЛОПРОВІДНІСТЮ

Насір Ахмед[a], С. Марутаманікандан[b], Б.Р. Нагасмітха[b]

[a]Факультет математики, Президентський коледж, Кемпапура, Хеббал, Бенгалуру 560024, Індія
[b]Факультет математики, Інженерна школа, Президентський університет, Бенгалуру 560064, Індія

Використано класичний аналіз стабільності для вивчення комбінованого впливу в'язкопружності та другого звуку на початок фероконвекції у пористому середовищі. Вважається, що рідина і тверда матриця знаходяться в локальній тепловій рівновазі. Враховуючи граничні умови, відповідні для аналітичного підходу, критичні значення, що стосуються як стаціонарної, так і коливальної нестабільності, отримані за допомогою аналізу нормального режиму. Помічено, що коливальний режим нестабільності є кращим перед стаціонарним режимом нестабільності. Показано, що фероконвекція коливального пористого середовища розвивається через магнітні сили, нелінійність намагніченості, релаксацію напружень за рахунок в'язкопружності та другий звук. З іншого боку, спостерігається, що наявність затримки деформації та пористого середовища затримує початок осцилюючої фероконвекції у пористому середовищі. Також окреслено подвійну природу числа Прандтля на число Релея по відношенню до числа Каттанео. Також обговорюється вплив різних параметрів на розмір конвекційної комірки та частоту коливань. Ця проблема може мати можливі наслідки для технологічних застосувань, у яких використовуються в'язкопружні магнітні рідини.

Ключові слова: *конвекція; рівняння Максвелла; рівняння Нав'є-Стокса для нестисливих в'язких рідин; пористі середовища; в'язкопружні рідини, фероконвекція*

ENHANCEMENT IN SOME PHYSICAL PROPERTIES OF (PVP:CMC) BLEND BY THE ADDITION OF MgO[†]

Widad H. Albanda[a]*, D.J. Fakralden[a], N.A. Hassan[b]

aScience Department - College of Basic Education, Mustansiriyah University, Iraq
bDepartment of Physics, College of Science, University of Diyala, Iraq
*Corresponding Author e-mail: albandawidada@gmail.com

This research study explores the effects of adding MgO nanoparticles to a polymeric blend composed of 50% PVP and 50% CMC. The blend was prepared using MgO nanoparticles (0.2%, 4%, and 6%) and varying processing conditions. The structural, optical, and electrical properties of the resulting blend were analyzed to determine the impact of the added nanoparticles on the blend's properties. Results showed that the addition of nanoparticles significantly improved the structural, optical, and electrical properties of the polymeric blend. Specifically, the energy gap is 4.224 eV for (PVA: CMC) film and increased to 3.432 eV for (PVA: CMC-6% MgO), the light transmission and reflection properties were enhanced. Additionally, the conductivity of the blend was increased, making it suitable for various applications, including optoelectronics, sensors, and biomedical devices. Overall, this study demonstrates the potential of adding nanoparticles to polymeric blends to improve their properties and highlights the importance of optimizing processing conditions to achieve the desired properties for specific applications.

Keywords: *PVA; CMC; MgO Nanoparticles; FTIR; SEM; Optical and electrical properties*
PACS: 71.20.Tx

INTRODUCTION

Polyvinylpyrrolidone is a water-soluble polymer made from the monomer vinylpyrrolidone. PVP has a variety of applications due to its unique properties, including its ability to form stable complexes with many different compounds [1], In the context of polymers used in personal care products, PVP is often used as a binder, film-former, and viscosity enhancer in hair styling products such as gels and mousses. It can also be found in skincare products such as moisturizers, which help to improve the texture and spreadability of the product. In addition to its use in personal care products [2,3]. carboxymethyl cellulose is a water-soluble polymer derived from cellulose. CMC is widely used in a variety of industries, including food, pharmaceuticals, and personal care products. In the food industry, CMC is used as a thickener, stabilizer, and emulsifier [4]. It is commonly found in ice cream, baked goods, and sauces. In the pharmaceutical industry, CMC is used as a binder in tablet formulations, and it is also used as an ingredient in eye drops and other topical medications [5,6]. Blending polyvinylpyrrolidone (PVP) and carboxymethyl cellulose (CMC) polymers can result in a material with enhanced properties, such as improved solubility, stability, and film-forming ability. The addition of (MgO) to the blend can further enhance these properties. MgO is an inorganic compound that is commonly used as a pH regulator and as a source of magnesium ions in various applications [7]. When added to a PVP: CMC blend, MgO can act as a crosslinking agent, which improves the mechanical strength and water resistance of the resulting material. The resulting PVP:CMC: MgO blend can have a variety of applications, including as a thickener, binder, and film-forming agent in various industries such as food, pharmaceuticals, and personal care products. For example, it can be used as a thickener in toothpaste or as a binder in tablet formulations [8]. Overall, the addition of MgO to a PVP: CMC polymer blend can result in a material with improved properties, making it more versatile and useful in a variety of applications [9,10]. In this study, we Preparation of the blend will depend on the 50% ratio of PVP, 50% CMC, and adding nanoparticles to the polymeric matrix, 0,2%,4%, and 6% from MgO, The addition of nanoparticles can improve the Structural, Optical, and electrical properties.

EXPERIMENTAL

The solution casting method is a relatively simple and efficient way to prepare PVP: CMC composite films and the addition of MgO can further enhance the properties of the resulting films, Pure and doped with MgO, the PVP: CMC composite films can be prepared by the solution casting method. This method involves dissolving the PVP, and CMC, in a suitable solvent (water) at (60°C), to form a homogenous solution, and adding MgO at different weight ratios of 2, 4, and 6 wt%, The solution is then cast onto a flat surface and allowed to dry, resulting in a thin film.

RESULTS AND DISCUSSIONS

The infrared spectra of (PVP: CMC) can provide information about the chemical composition and structural features of the polymer blend. Here are some of the characteristic peaks that may be observed in Fig. (1) FTIR spectra of (PVP: CMC):

A peak around 23500 cm^{-1}, corresponds to the -CH stretching vibration of the CMC backbone. A peak around 1650 cm^{-1}, corresponds to the -COO- stretching vibration of the carboxyl group in CMC. A peak around 1420 cm^{-1}, corresponds to the -CH bending vibration of the CMC backbone [11,12]. PVP peaks: A peak around 3400 cm^{-1}, which corresponds to the -NH stretching vibration of the amide group in PVP [13,14]. A peak around 2950 cm^{-1}, corresponds to the -CH stretching vibration of the PVP backbone. A peak around 1550 cm^{-1}, corresponds to the -C=O stretching vibration of the amide group in PVP [15]. In addition, the FTIR spectra of (PVP: CMC) may also show some overlapping peaks, such as the -OH stretching vibration of water molecules, which may be present as a result of the hygroscopic nature of CMC. It is important to note that the specific FTIR spectra of (PVP: CMC) may vary depending on the specific ratio and blending method used. MgO nanoparticles peaks: A peak around 3700-3500 cm^{-1} corresponds to the -OH stretching vibration of surface hydroxyl groups on the MgO nanoparticles [16]. A peak around 1600-1500 cm^{-1}, corresponds to the bending vibration of O-H on the surface of the MgO nanoparticles. A peak around 1400-1300 cm^{-1} [17,18], corresponds to the symmetric stretching vibration of Mg-O bonds in the MgO nanoparticles. In addition, the FTIR spectra of CMC: PVP doped with MgO nanoparticles may also show some overlapping peaks [19,20], such as the -OH stretching vibration of water molecules and the -CH stretching vibration of the CMC and PVP backbones [21]. It is important to note that the specific FTIR spectra of CMC: PVP doped with MgO nanoparticles may vary depending on the specific doping concentration and preparation method used [22].
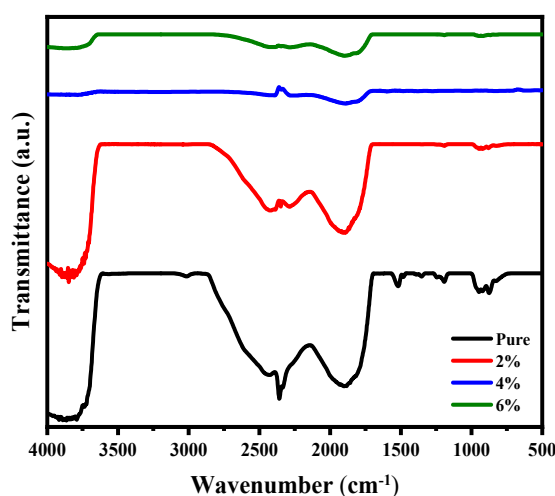
Figure 1. FTIR for PVP: CMC-MgO Nanocomposite

Figure (2) reviews the field-emitting scanning electron microscopy (FE-SEM) images of the prepared films (PVP: CMC) before (a) and after reinforcement with MgO nanopowder in the ratio (b). It shows that the (PVP: CMC) film has a rough surface. From a group of accumulated minutes stacked together

When MgO nanoparticles were added, the images showed that the reinforced polymeric films had irregular and rougher surfaces and high surface porosity compared to the films before cementation, and this is attributed to the hydrogen bonding resulting from the active carboxyl and hydroxyl Functional groups [23,24]. This irregular, rough, and high porosity of the surface enhances the adsorption Chemistry of the prepared overlapping films [25].
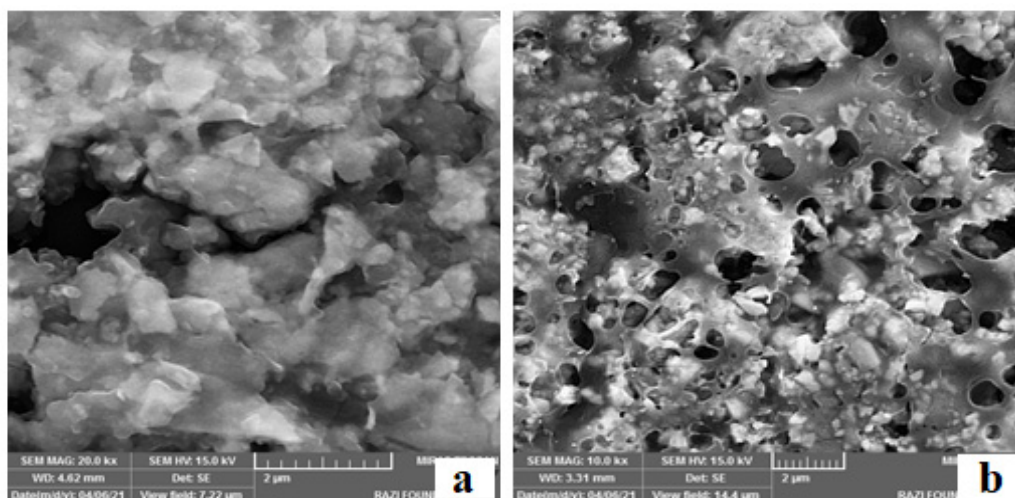
Figure 2. FE-SEM for PVP: CMC-MgO Nanocomposite

The addition of MgO nanoparticles to the (PVP: CMC) blend can have significant effects on both the transmittance and reflectance of the resulting material, The transmittance of (PVP: CMC) doped with MgO nanoparticles can be decreased in the visible and near-infrared regions,   The nanoparticles can scatter and absorb light more than the polymer blend, which can result in more light being reflected from the surface of the material [26,27], The effect of MgO nanoparticles on transmittance and reflectance can be dependent on the wavelength of light. Higher concentrations of nanoparticles can result in stronger scattering and absorption [28,29], which can result in more significant changes in transmittance (T%) and reflectance (R) as shown in Fig.(3).
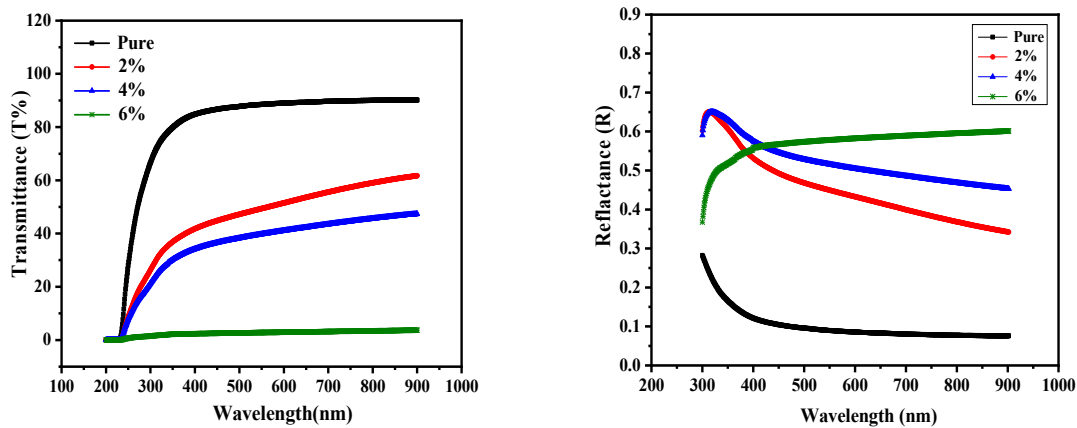

Figure 3. T% and R for PVP: CMC-MgO Nanocomposite

The energy gap of (PVP: CMC) doped with MgO nanoparticles can be decreased due to the additional electronic states introduced by the nanoparticles [30], The decrease in the energy gap can result in increased absorption in the UV-visible region, as shown in Fig. 4. The effect of MgO nanoparticles on the absorption coefficient and energy gap can also depend on the size of the nanoparticles. Smaller nanoparticles can introduce more additional electronic states and result in more significant changes in the energy gap [31], The surface properties of the MgO nanoparticles can also play a role in the effect on the absorption coefficient and energy gap, The presence of surface defects and impurities on the nanoparticles can introduce additional electronic states and result in changes in the optical properties of the resulting material [32]. As in the following equation [33]:
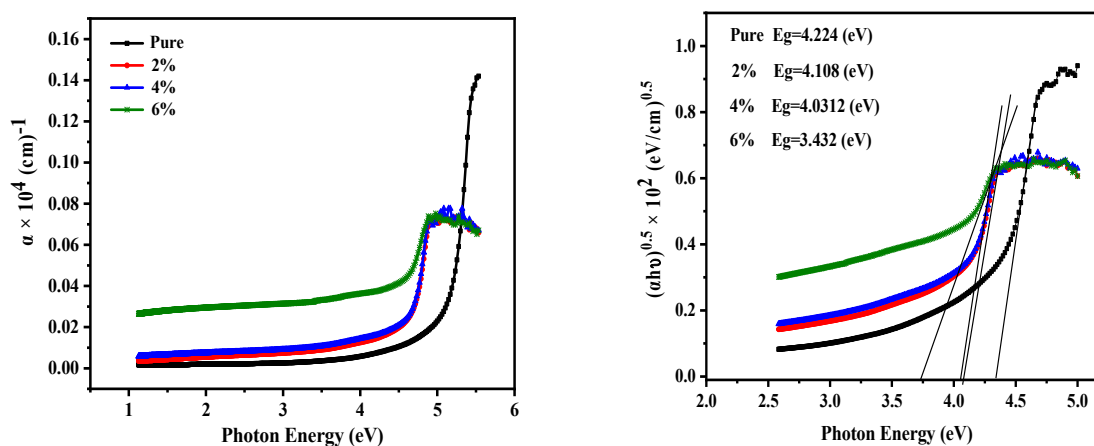
$$\alpha h\upsilon = A(h\upsilon - E_g)^n \tag{1}$$

Figure 4. α and Eg for PVP: CMC-MgO Nanocomposite

The extinction coefficient of PVP: CMC doped with MgO nanoparticles can be increased due to the additional absorption features introduced by the nanoparticles, MgO nanoparticles have a higher refractive index than PVP: CMC polymers, so the addition of the nanoparticles can increase the overall refractive index of the material, This can result in increased light bending and potential optical effects such as light confinement, as shown in Fig. (5). The refractive index (n_o) and the extinction coefficient (k_o) can be calculated using the two following equations below [34,35]:

$$n_o = \left[\frac{(1+R)^2}{(1-R)^2} - (k_o^2 - 1)\right]^{\frac{1}{2}} + \frac{(1+R)}{(1-R)} \tag{2}$$
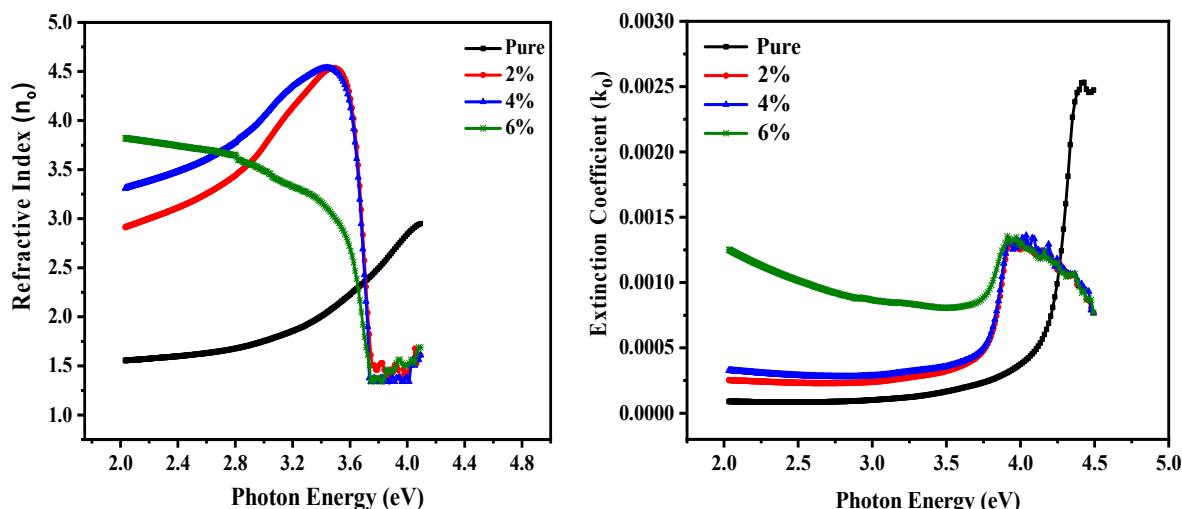
$$k_o = \frac{\alpha\lambda}{4\pi} \tag{3}$$

Figure 5. n_o and k_o for PVP: CMC-MgO Nanocomposite

Electrical Characterizations
Dielectric Constant (ε')

The addition of MgO nanoparticles to (PVP: CMC) polymers can increase the dielectric constant of the material due to the presence of additional polarizability from the nanoparticles, The effect of MgO nanoparticles on the dielectric constant of (PVP: CMC) polymers can also depend on the size of the nanoparticles. Smaller nanoparticles can have a greater surface area and more electronic states, which can result in more significant changes in the dielectric constant [36], The dielectric constant of (PVP: CMC) doped with MgO nanoparticles can also depend on the frequency of the applied electric field [37], The dielectric constant of (PVP: CMC) doped with MgO nanoparticles can also depend on the temperature of the material, At high temperatures, the polarizability of the material can change, resulting in a change in the dielectric constant [38], as shown in Fig.(6).
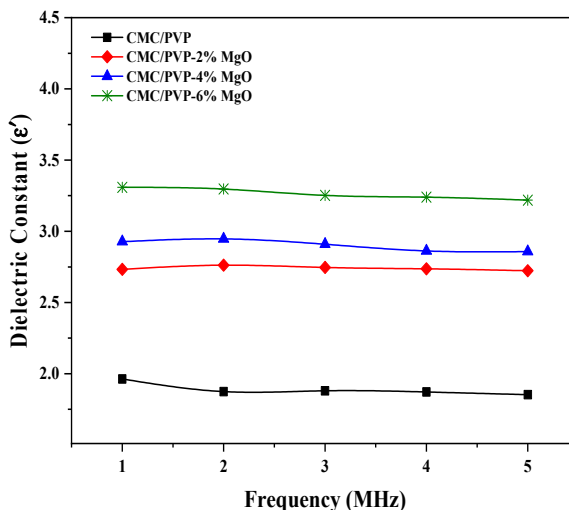

Figure 6. Dielectric Constant for PVP: CMC-MgO Nanocomposite

Dissipation Factor (tanδ)

The addition of MgO nanoparticles to PVP: CMC polymers can decrease the dissipation factor of the material due to the presence of additional polarizability from the nanoparticles, The dissipation factor can decrease with increasing concentration of the nanoparticles, as shown in Fig. 7. The effect of MgO nanoparticles on the dissipation factor of (PVP: CMC) polymers can also depend on the size of the nanoparticles. Smaller nanoparticles can have a greater surface area and more electronic states, which can result in more significant changes in the dissipation factor [39], The dissipation factor of (PVP: CMC) doped with MgO nanoparticles can also depend on the frequency of the applied electric field. The dissipation factor of (PVP: CMC) doped with MgO nanoparticles can also depend on the temperature of the material. At high temperatures, the polarizability of the material can change, resulting in a change in the dissipation factor, the effect of MgO nanoparticles on the dissipation factor of (PVP: CMC) polymers can depend on various factors such as nanoparticle size, concentration, temperature, and frequency. The resulting electrical properties can have potential applications in areas such as capacitors, sensors, and electronic devices [40].
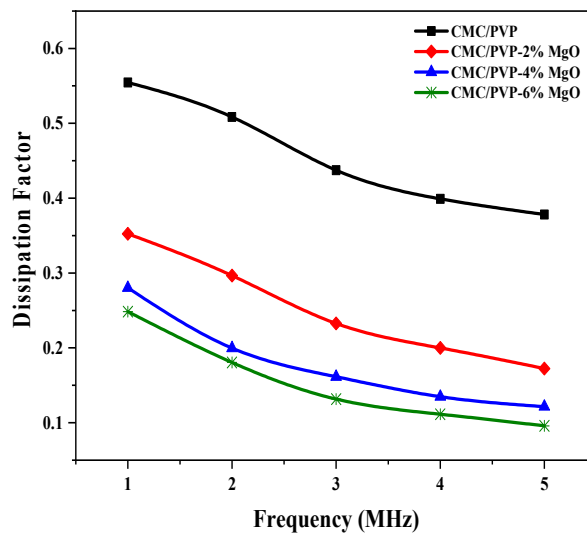
Figure 7. Dissipation Factor for PVP: CMC-MgO Nanocomposite.

A.C. Electrical Conductivity ($\sigma_{a.c}$)

The addition of MgO nanoparticles to (PVP: CMC) polymers can increase the electrical conductivity of the material due to the presence of additional free charge carriers, The effect of MgO nanoparticles on the electrical conductivity of (PVP: CMC) polymers can also depend on the size of the nanoparticles [41], The electrical conductivity of PVP: CMC doped with MgO nanoparticles can also depend on the frequency of the applied A.C. electric field. The conductivity can increase or decrease depending on the frequency range [42], as shown in Fig. (8).
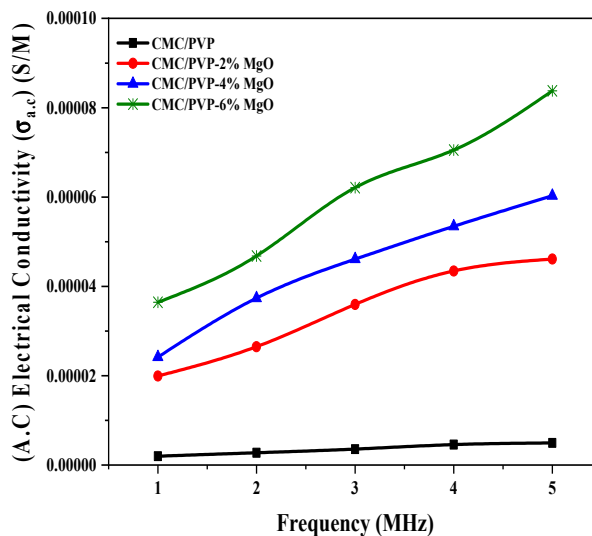

Figure 8. AC electrical conductivity for PVP: CMC-MgO Nanocomposite

CONCLUSIONS

The addition of MgO nanoparticles (0.2%, 4%, and 6%) to the 50% PVP, and 50% CMC can enhance the structural properties by improving the mechanical strength, thermal stability, and surface morphology by casting method. Additionally, the optical properties of the blend can be enhanced, leading to better light transmission and reflection properties. The energy gap is 4.224 eV for (PVA: CMC) film and when the MgO concentration at 6% is increased to 3.432 eV. the electrical properties can be improved by increasing the conductivity of the (PVA/CMC) blend. Therefore, the use of nanoparticles in the preparation of polymeric blends has significant potential for improving their properties, making them suitable for various applications such as optoelectronics, sensors, and biomedical devices. Further studies can be carried out to optimize the concentration and size of the nanoparticles, as well as the processing conditions, to achieve the desired properties for specific applications.

ORCID IDs

Widad H. Albanda, https://orcid.org/0000-0002-3214-395X; **D.J. Fakralden**, https://orcid.org/0000-0001-9712-7013
N.A. Hassan, https://orcid.org/0009-0008-5813-6265

REFERENCES

[1] M. Teodorescu, and M. Bercea, "Poly (vinylpyrrolidone)–a versatile polymer for biomedical and beyond medical applications," Polymer-Plastics Technology and Engineering, **54**(9), 923-943 (2015). https://doi.org/10.1080/03602559.2014.979506

[2] P. Franco, and I. De Marco, "The Use of Poly (N-vinyl pyrrolidone) in the Delivery of Drugs: A Review." Polymers, **12**(5), 1114 (2020). https://doi.org/10.3390/polym12051114

[3] S. Gono, Doctoral thesis, African University of Science and Technology, 2020. http://repository.aust.edu.ng/xmlui/handle/123456789/5007

[4] M.I.H. Mondal, M.S. Yeasmin, and M.S. Rahman, "Preparation of food grade carboxymethyl cellulose from corn husk agrowaste," International Journal of Biological Macromolecules, 79, 144-150 (2015). https://doi.org/10.1016/j.ijbiomac.2015.04.061

[5] S.S.H. Al-Mgrs, M.H. Al-Timimi, M.Z. Abdullah, and W.H. Al-Banda, "Structural and optical characterizations of synthesized CMC/PVP-SnO2 nano composites." AIP Conference Proceedings, **2475**(1), 090018 (2023). https://doi.org/10.1063/5.0102768

[6] A.B. Odunayo, F.I. Kayode, A.A. Benjamin, A.I. Adekola, and O.O. Ruth, "Evaluation of the binding property of some binders in metronidazole tablet formulation," Int. J. Pharmacy. Chem. **7**(2), 22-30 (2021). https://article.sciencepublishinggroup.com/pdf/10.11648.j.ijpc.20210702.11.pdf

[7] H.M. Hussein, and M.H. Al-Timimi, "Preparation and Study Some Physical Properties of (CMC/PAA: MgO) Nano Composites," Eurasian Journal of Physics, Chemistry and Mathematics, **8**, 47-55 (2022). https://www.geniusjournals.org/index.php/ejpcm/article/view/1944

[8] A. Paria, and V.K. Rai, "The fate of carboxymethyl cellulose as a polymer of pharmaceutical importance," Biological Sciences, **2**(2), 204-215 (2022). https://doi.org/10.55006/biolsciences.2022.2204

[9] S.S. Chiad, N.F. Habubi, S.F. Oboudi, and M.H. Abdul-Allah, "Effect of Thickness on The Optical Parameters of PVA: Ag," Diyala Journal for Pure Sciences, **7**, 153-161 (2011). https://www.iasj.net/iasj/pdf/4b03ea1b233568b1

[10] M.S. Rahman, M.S. Hasan, A.S. Nitai, S. Nam, A.K. Karmakar, M.S. Ahsan, et al., "Recent developments of carboxymethyl cellulose," Polymers, **13**(8), 1345 (2021). https://doi.org/10.3390/polym13081345

[11] A.H. Saputra, L. Qadhayna, and A.B. Pitaloka, "Synthesis and characterization of carboxymethyl cellulose (CMC) from water hyacinth using ethanol-isobutyl alcohol mixture as the solvents," International Journal of Chemical Engineering and Applications, **5**(1), 36 (2014). http://dx.doi.org/10.7763/IJCEA.2014.V5.347

[12] H.M. Hussein, M.H. Al-Timimi, and Y.M. Jawad, "The Properties, Preparation and Applications for Carboxymethyl Cellulose (CMC) Polymer: A Review," Diyala Journal for Pure Science, **18**(4), (2022). https://djfps.uodiyala.edu.iq/index.php/Home/article/view/37/36

[13] T. Franca, D. Goncalves, and C. Cena, "ATR-FTIR spectroscopy combined with machine learning for classification of PVA/PVP blends in low concentration," Vibrational Spectroscopy, **120**, 103378 (2022). https://doi.org/10.1016/j.vibspec.2022.103378

[14] S.S.H. Almgrs, and M.H. Al-Timimi, "(CMC-PVP) Films Filled with SnO2 Nanoparticles Synthesized by (Solution-Gel) Method," Journal of the college of basic education, **27**(113), (2021). https://www.iasj.net/iasj/pdf/d05159f9f9bc79f1

[15] A. Jalali, A. Shockravi, V. Vatanpour, and M. Hajibeygi, "Preparation and characterization of novel microporous ultrafiltration PES membranes using synthesized hydrophilic polysulfide-amide copolymer as an additive in the casting solution," Microporous and Mesoporous Materials, **228**, 1-13 (2016). https://doi.org/10.1016/j.micromeso.2016.03.024

[16] G. Balakrishnan, R. Velavan, K.M. Batoo, and E.H. Raslan, "Microstructure, optical and photocatalytic properties of MgO nanoparticles," Results in Physics, **16**, 103013 (2020). https://doi.org/10.1016/j.rinp.2020.103013

[17] F.R. Saeed, M.H.A.A. Al-Timimi, W.H.A. Al-Banda, M.Z. Abdullah, I. Stamatin, S. Voinea, et al., "Thermal Properties of Paraffin/Nano-Magnetitetrevorite Phase Change Materials," Journal of Ovonic Research, **14**(5). (2018). https://scholar.google.com/scholar?oi=bibs&cluster=14895011915883851214&btnI=1&hl=en

[18] A.A. Mohammed, A.R. Ahmed, and M.H. Al-Timimi, Structural, "Optical and Thermal Properties of (PEG/PAA: MnO2) Nano Composites," Technium BioChemMed, **3**(2), 107-119 (2022). https://doi.org/10.47577/biochemmed.v3i2.7116

[19] A. Khan, A. Naeem, T. Mahmood, B. Ahmad, Z. Ahmad, M. Farooq, and T. Saeed, "Mechanistic study on methyl orange and congo red adsorption onto polyvinyl pyrrolidone modified magnesium oxide," Int. J. Environ. Sci. Technol. 19, 2515–2528 (2022). https://doi.org/10.1007/s13762-021-03308-z

[20] M.Z. Abdullah, M.H. Al-Timimi, W.H. Albanda, M. Dumitru, A.E. Balan, C. Ceaus, et al., "Structural and Electrochemical Properties of P3-Na0. 67Mn0. 3Co0. 7O2 Nanostructures Prepared by Citric-Urea Self-Combustion Route as Cathode for Sodium Ion Battery," Digest Journal of Nanomaterials and Biostructures, **14**(4), 1179-1193 (2019). https://chalcogen.ro/1179_AbdullahMZ.pdf

[21] S.S. Sainudeen, L.B. Asok, A. Varghese, A.S. Nair, and G. Krishnan, "Surfactant-driven direct synthesis of a hierarchical hollow MgO nanofiber–nanoparticle composite by electrospinning," RSC advances, **7**(56), 35160-35168 (2017). https://doi.org/10.1039/C7RA05812H

[22] H.M. Ragab, "Optical, thermal and electrical characterization of PEO/CMC incorporated with ZnO/TiO$_2$ NPs for advanced flexible optoelectronic technologies," Ceramics International, **49**(8), 12563-12569 (2023). https://doi.org/10.1016/j.ceramint.2022.12.118

[23] A.J. Mawat, M.H. Al-Timimi, W.H. Albanda, and M.Z. Abdullah, "Morphological and optical properties of Mg1-xCdSx nanostructured thin films," AIP Conference Proceedings, **2475**(1), 090019 (2023). https://doi.org/10.1063/5.0103955

[24] Y.M. Jawad, M.F.H. Al-Kadhemy, and J.A.S. Salman, "Synthesis structural and optical properties of CMC/MgO nanocomposites," Materials Science Forum, **1039**, 104-114 (2021). https://doi.org/10.4028/www.scientific.net/MSF.1039.104

[25] M. Habeeb, and R.S.A. Hamza, "Synthesis of (Polymer blend-MgO) nanocomposites and studying electrical properties for piezoelectric application," Indonesian Journal of Electrical Engineering and Informatics, **6**(4), 428-435 (2018). http://dx.doi.org/10.52549/ijeei.v6i4.511

[26] S.A. Salman, M.H. Abdu-allah, and N.A. Bakr, "Optical characterization of red methyl doped poly (vinyl alcohol) films," International Journal of Engineering and Technical Research, **2**(4), 126-128 (2014).

[27] D.H. Wang, D.Y. Kim, K.W. Choi, J.H. Seo, S.H. Im, J.H. Park, et al., "Enhancement of donor–acceptor polymer bulk heterojunction solar cell power conversion efficiencies by addition of Au nanoparticles," Angewandte Chemie, **123**(24), 5633-5637 (2011). https://doi.org/10.1002/ange.201101021

[28] S. Biswas, S.S. Panja, and S. Bose, "Tailored distribution of nanoparticles in bi-phasic polymeric blends as emerging materials for suppressing electromagnetic radiation: challenges and prospects," Journal of Materials Chemistry C, **6**(13), 3120-3142 (2018). https://doi.org/10.1039/C8TC00002F

[29] J. Al-Zanganawee, M. Al-Timimi, A. Pantazi, O. Brincoveanu, C. Moise, R. Mesterca, et al., "Morphological and optical properties of functionalized SWCNTs: P3OT nanocomposite thin films, prepared by spincoating," Journal of Ovonic Research, **12**(4), 201-207 (2016). https://chalcogen.ro/201_AlzanganaweeJ.pdf

[30] A.M. El-Naggar, Z.K. Heiba, A.M. Kamal, K.E. Alzahrani, O.H. Abd-Elkader, and M.B. Mohamed, "Impact of natural melanin doping on the structural, optical and dielectric characteristics of the PVP/CMC blend," Journal of Taibah University for Science, **17**(1), 2190731 (2023). https://doi.org/10.1080/16583655.2023.2190731

[31] A.J. Kadham, D. Hassan, N. Mohammad, and A.H. Ah-Yasari, "Fabrication of (polymer blend-magnesium oxide) nanoparticle and studying their optical properties for optoelectronic applications," Bulletin of Electrical Engineering and Informatics, **7**(1), 28-34 (2018). https://doi.org/10.11591/eei.v7i1.839

[32] A. Hashim, and M.A. Habeeb, "Synthesis and characterization of polymer blend-CoFe 2 O 4 nanoparticles as a humidity sensors for different temperatures," Transactions on Electrical and Electronic Materials, **20**, 107-112 (2019). https://doi.org/10.1007/s42341-018-0081-1

[33] A.T. Abood, O.A.A. Hussein, M.H. Al-Timimi, M.Z. Abdullah, H.M.S. Al-Aani, and W.H. Albanda, "Structural and optical properties of nanocrystalline SnO2 thin films growth by electron beam evaporation," AIP Conference Proceedings, **2213**(1), 020036 (2020). https://doi.org/10.1063/5.0000454

[34] M.H. Saeed, M.H. Al-Timimi, and O.A.A. Hussein, "Structural, morphological and optical characterization of nanocrystalline WO3 thin films," Digest Journal of Nanomaterials and Biostructures, **16**(2), 563-569 (2021). https://chalcogen.ro/563_SaeedMH.pdf

[35] H.S. Al-Rikabi, M.H. Al-Timimi, A.H. Abed, and W. Albanda, "Surface Topography and Optical Properties for (MgOx-1ZnSx) Thin Films Prepared by Chemical Spray Pyrolysis," Diyala Journal for Pure Science, **18**(4), (2022). https://djfps.uodiyala.edu.iq/index.php/Home/article/view/36/35

[36] N.S. Alghunaim, "Effect of CuO nanofiller on the spectroscopic properties, dielectric permittivity and dielectric modulus of CMC/PVP nanocomposites," Journal of Materials Research and Technology, **8**(4), 3596-3602 (2019). https://doi.org/10.1016/j.jmrt.2019.05.022

[37] M.A. Morsi, R.A. Pashameah, K. Sharma, E. Alzahrani, M.O. Farea, and A.A. Al-Muntaser, "Hybrid MWCNTs/Ag nanofiller reinforced PVP/CMC blend-based polymer nanocomposites for multifunctional optoelectronic and nanodielectric applications," Journal of Polymers and the Environment, **31**(2), 664-676 (2023). https://doi.org/10.1007/s10924-022-02656-2

[38] A. Hashim, F.L. Rashid, Z. Al-Ramadan, and M.H. Abdul-Allah, "Characterization of (PVA-BaSO₄ 5H₂O) Composites," Diyala Journal for Pure Science, **8**, 296-302 (2012). https://www.iasj.net/iasj/pdf/a5577c17b8b8e701

[39] S.S. Chiad, N.F. Habubi, S.F. Oboudi, and M.H. Abdul-Allah, "Effect of Thickness on The Optical Parameters of PVA: Ag" . Diyala Journal for Pure Sciences, **7**, 153-161(2011). https://www.iasj.net/iasj/download/4b03ea1b233568b1

[40] A.A. Al-Muntaser, R.A. Pashameah, E. Alzahrani, S.A. Al-Subhi, S.T. Hameed, and M.A. Morsi, "Graphene Nanoplatelets/TiO₂ Hybrid Nanofiller Boosted PVA/CMC Blend Based High Performance Nanocomposites for Flexible Energy Storage Applications," J. Polym. Environ. **31**, 2534-2548 (2023). https://doi.org/10.1007/s10924-022-02748-z

[41] S. El-Gamal, and A.M. El-Sayed, "Physical properties of the organic polymeric blend (PVA/PAM) modified with MgO nanofillers," Journal of Composite Materials, **53**(20), 2831-2847 (2019). https://doi.org/10.1177/0021998319840802

[42] S.T. Hameed, T.F. Qahtan, A.M. Abdelghany, and A.H. Oraby, "Structural, optical, and dielectric characteristics of copper oxide nanoparticles loaded CMC/PEO matrix," Journal of Materials Science, **57**(15), 7556-7569 (2022). https://doi.org/10.1007/s10853-022-07134-7

ПОКРАЩЕННЯ ДЕЯКИХ ФІЗИЧНИХ ВЛАСТИВОСТЕЙ СУМІШІ (PVP:CMC) ШЛЯХОМ ДОДАВАННЯ MgO

Відад Х. Альбанда[a], Д.Дж. Факралден[a], Н.А. Хасан[b]
[a]Науковий відділ - Коледж базової освіти, Університет Мустансірія, Ірак
[b]Кафедра фізики, Науковий коледж, Університет Діяла, Ірак

Досліджено вплив додавання наночастинок MgO до полімерної суміші, що складається з 50% PVP і 50% CMC. Суміш готували з використанням наночастинок MgO (0,2%, 4% і 6%) і різних умов обробки., Для визначення впливу доданих наночастинок були проаналізовані структурні, оптичні та електричні властивості отриманої суміші. Результати показали, що додавання наночастинок значно покращило структурні, оптичні та електричні властивості полімерної суміші. Зокрема, енергетичний зазор становить 4,224 еВ для плівки (PVA:CMC) і збільшено до 3,432 еВ для (PVA:CMC-6% MgO). Також були покращені властивості пропускання світла та відбивання. Крім того, провідність суміші була збільшена, що зробило її придатною для різних застосувань, включаючи оптоелектроніку, датчики та біомедичні пристрої. Загалом це дослідження демонструє потенціал додавання наночастинок до полімерних сумішей для покращення їхніх властивостей і підкреслює важливість оптимізації умов обробки для досягнення бажаних властивостей для конкретних застосувань.
Ключові слова: *PVA; CMC; наночастинки MgO; FTIR; SEM; оптичні та електричні властивості*

THE MAGNETIC FORM FACTORS FOR SOME NUCLEI ^{51}V, ^{59}Co, ^{93}Nb, ^{115}In BY USING VALENCE WITH AND WITHOUT CORE POLARIZATION EFFECTS MODELS†

 Sajad A. Khasain*, Khalid S. Jassim

Department of Physics, College of Education for Pure Sciences, University of Babylon, 51002 Babylon, Iraq
E-mail: sajad.ali.pure304@student.uobabylon.edu.iq

The magnetic electron scattering form factor with glekpn, d3f7, ho models space for ^{51}V, ^{59}Co, ^{93}Nb, and ^{115}In nuclei are discussed with and without core polarization effects (CP). The calculations are done with the help of NuShellX@MUS code. The radial wave function for the single-particle matrix elements have been calculated with the SKyrme-Hartree Fock (SKX), Wood–Saxon(WS), and harmonic oscillator (HO) potentials. valence model (Vm) used in these calculation to calculate form factors with core-polarization effects. The results give a good agreement with available experimental data.

Keywords: *electron scattering; transverse form factor*

PACS: 25.30.Bf, 21.10.Ft, 25.30Dh

1. INTRODUCTION

A special method for examining the electromagnetic characteristics of nuclei and learning about their charge and current distributions is electron scattering. Several reasons for using electrons as probes. The electromagnetic force, the most well-known interaction and one that quantum electrodynamics (QED) fully describes, is what first causes the electron to interact with the nucleus. Additionally, the interaction's coupling constant is not strong enough to materially alter the nuclear structure under investigation. Additionally, one may operate in first order perturbation inside the one-photon exchange approximation due to the interaction's weakness. Second, unlike with actual photons, the energy transfer and momentum transfer may be changed separately, allowing for the mapping of the densities' Fourier transform. Past research on electron scattering in the elastic, inelastic, and quasi-elastic regimes has produced the most precise measurements of charge radii, transition probabilities, momentum distributions, and spectroscopic parameters [1].

The nuclear shell model has shown to be a highly useful tool for studying nuclear structure because it can accurately and systematically account for many observable by choosing the right residual effective interaction. The creation of a nuclear shell model has advanced the understanding of nuclear structure. The shell model, while fundamentally simple, describes a variety of nuclear phenomena, including spin, magnetic moment, and nuclear spectra [2].

One of these models, the shell model with a constrained model space (MS), when effective charges are utilized, is successful in characterizing the static characteristics of nuclei. The core orbits are deformed in a manner that is compatible with the quadrupling of the valance orbits [3].

The aim of this study is to investigate electron scattering form factors that constitute the inelastic transverse electron scattering of ^{51}V, ^{59}Co, ^{93}Nb and ^{115}In. In these calculations, the nucleation model in the fp-shell and g-shell regions. The coincidence model calculations will be performed using the interaction of w0, ho and glekpn (constraint) effective for the fp and gf model space. The shell model calculation will be performed using NushellX@MSU [4]. The Valence + core polarization (Vm+CP) and valence models (Vm) only uses the appropriate efficiencies for the neutron and proton inelastic form factors were calculated. Our theoretical results will be compared with previously collected experimental data. Electron scattering form factors of some nuclei have been studied by Jassim and et. al. [5]. Li, Xin and et.al. have been mode comparative studies on nuclear elastic magnetic form factors between the relativistic and non-relativistic mean-field approaches [6].

2. THEORY

The formalism of electron scattering from deformed nuclei that we follow in this work. All nuclear information is included in the longitudinal form factor $F_{L(q)}$, which represents scattering from the nuclear charge density, and the transverse form factor $F_T(q)$, which represents scattering from the nuclear current density

---

structural details [7]. The differential cross-section for electron scattering from a nucleus with mass (M) and charge (Ze) into angle (d) in PWBA (plane-wave Born approximation) is given by [8]:

$$\frac{d\sigma}{d\Omega} = \left(\frac{d\sigma}{d\Omega}\right)_{Mott} f_{rec} \sum_J |F_J(q,\theta)|^2, \tag{1}$$

where the cross-section of the Mott is represented by $\left(\frac{d\sigma}{d\Omega}\right)_{Mott}$. The scattering of a relativistic electron from a spin-free point charge at high energy is given by [9]:

$$\left(\frac{d\sigma}{d\Omega}\right)_{Mott} = \left(\frac{Ze^2 \cos\left(\frac{\theta}{2}\right)}{2E_i hc \sin^2\left(\frac{\theta}{2}\right)}\right)^2. \tag{2}$$

It is known as the nuclear recoil factor:

$$f_{rec} = \left(1 + \frac{2E_i}{M}\sin^2\left(\frac{\theta}{2}\right)\right)^{-1} \tag{3}$$

The total form factor $F_J(q,\theta)$ of a certain multi-polarity is described as having a transverse part $F_J^T(q)$ and a Longitudinal (Coulomb) part $F_J^L(q)$ and is defined as [10]:

$$F_J^2(q,\theta) = \left(\frac{q_u}{q}\right)^4 \left|F_J^L(q)\right|^2 + \left[\frac{q_u^2}{2q^2} + \tan^2\left(\frac{\theta}{2}\right)\right] \left|F_J^T(q)\right|^2, \tag{4}$$

where q_u stands for the four momentum transfer, q stands for momentum transfer and θ stands for the scattering angle. It is possible to express the effective momentum transfer by q_{eff} can be written as [11]:

$$q_{eff} = q\left[1 + \frac{3}{2}\frac{Ze^2}{E_i R_c}\right], \tag{5}$$

where $R_c = \sqrt{\frac{5}{3}} r_{rms}$.

Parity and time reversal invariance indicate that only the even and odd transverse magnetic multipoles contribute to elastic scattering. Then, in PWBA, only odd magnetic multipoles will remain after $\theta = 180$.

$$|F_T(q)|^2 = \sum_{\lambda=\text{odd}} \left|F^{M\lambda}\right|^2 \tag{6}$$

The definition of the magnetic multi pole operators is

$$\hat{T}_\mu^{M\lambda}(q) =_{i^\lambda} \int dr j_\lambda(qr) Y_{\lambda\lambda}^\mu(\Omega_r).\hat{J}(r), \tag{7}$$

where the operator for current density is $\hat{J}(r)$. The convection and magnetization components of the currents $\hat{J}$ in the transverse form factors result from the motion and intrinsic magnetic moments of the nucleons, respectively. We adjust for the center of mass (c.m.) and finite nucleon sizes when calculating the overall form factors. The common factor produced from the harmonic-oscillator approximation is used for the c.m. correction.

$$F_{c.m}(q) = \exp(q^2 b^2/4A), \tag{8}$$

where A is the mass number of the nucleus and b is the harmonic oscillator size parameter [1].

With isospin, the form factor adopts the form

$$F_J^2(q) = \frac{4\pi}{Z^2(2J_i+1)} \sum_{T=0,1} (-1)^{T_f-T_i} \begin{vmatrix} T_f & T & T_i \\ -T_Z & 0 & T_Z \end{vmatrix}, \tag{9}$$

$$|\langle J_f T_f \| \hat{L}_{JT}(q) \| J_i \rangle|^2 |F_{c.m}(q)|^2 |F_{f.s}(q)|^2.$$

Where $F_{f.s(q)}$ is the finite size correction given by

$$F_{f.s}(q) = \exp\left(-0.43q^2/4\right). \tag{10}$$

Where $T_Z = \frac{Z-N}{2}$ and T given by:

$$|T_i - T_f| \le T \le T_i - T_f, \tag{11}$$

see [12].

3. RESULT AND DISCUSSION

The nuclei under examination have 11 and 19 particles outside the core ^{40}Ca for ^{51}V and ^{59}CO, and 37,59 particles outside the core ^{56}Ni (with restriction usade) for ^{93}Nb and ^{115}In respectively. Calculations using Valence model with and without core-polarization effects. NuShellX@MUS was used for all calculations with the SKx, WS, HO potential.

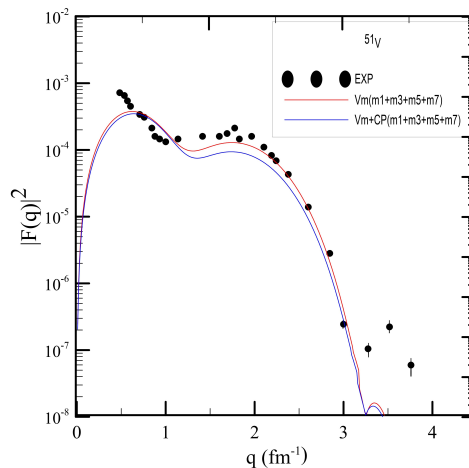### 3.1. Magnetic form factor for ^{51}V

The transverse form factor calculations have been performed in the d3f7 model space with the shell-model code NUSHELLX X@MUS since we are interested in the negative-parity states of ^{51}V for the valance particles states outside the core ^{40}Ca, The Vm(a) and the Vm with CP model (b) are compared in the (Figure 1) as the total magnetic form factor which symbolizes the sum.
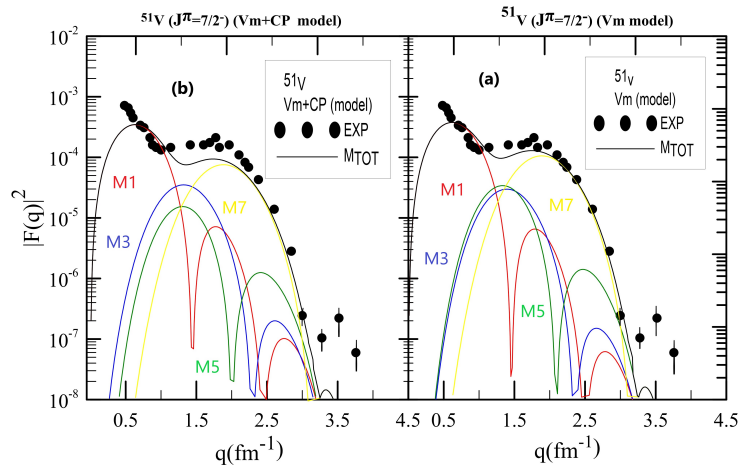
Figure 1. The transverse magnetic form factor for ^{51}V ($J^\pi = \frac{7}{2}^-$). The experiment's findings are based on Ref [12], [13], [14].

The contribution of M1, M3, M5, and M7 for ^{51}V ($J^\pi = \frac{7}{2}^-$) is shown in red, blue, green, and yellow, respectively. Effective interaction (W0). It was applied to the fp-shell model space wave function. In the first peak between $(0 \le q \le 1.5)fm^{-1}$, the dominant component is M1 where the maximum values are 10^{-3} and $(0.6)fm^{-1}$ for form factors and momentum transfer values respectively. At the second peak between $(1.5 \le q \le 3)fm^{-1}$, the dominant component is M7 where the maximum values are 10^{-4} and $(3)fm^{-1}$ for form factors and momentum transfer values respectively ,There is no rapprochement between the experiment's and the theoretical data for the final peak.
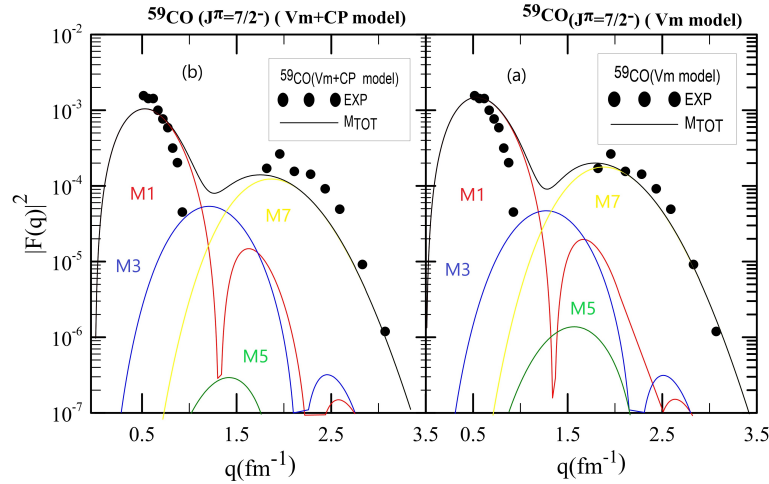
Figure (2) compares the total magnetic form factor between the Valence model(Vm)shown in red line and the Valence model with core polarization (Vm+Cp) shown in blue line It is clear from the peaks in the figure that the core effect is very small, because the form factor in our work is transverse.

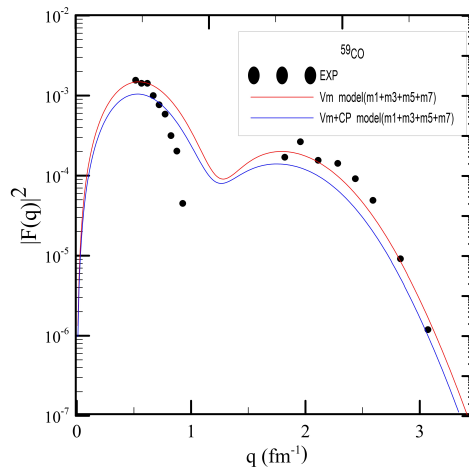**Figure 2.** Demonstrates compare between Vm and Vm+CP models for $^{51}V(J^\pi = \frac{7}{2}^-)$.

3.2. Magnetic form factor ^{59}Co

The transverse form factor calculations have been performed in the model space (ho) since we are interested in the negative-parity states of ^{59}Co for the valance particles states outside the core ^{40}Ca, The Vm(a) and the Vm with CP model (b) are compared as the total magnetic form factor, which symbolizes the sum. The contribution of M1, M3, M5, and M7 for ^{59}Co ($J^\pi = \frac{7}{2}^-$) is shown in red, blue, green, and yellow, respectively. Effective interaction (ho). It was applied to the fp-shell model space wave function. In the first peak between $(0 \le q \le 1.3)fm^{-1}$, the dominant component is M1 where the maximum values are 10^{-3} and $(0.7)fm^{-1}$ for form factors and momentum transfer values respectively. At the second peak between $(1.5 \le q \le 3.4)fm^{-1}$, the dominant component is M7 where the maximum values is 10^{-4} and $(2.3)fm^{-1}$ for form factors and momentum transfer values respectively.

Figure 3. The transverse magnetic form factor for ^{59}CO ($J^\pi = \frac{7}{2}^-$). The experiment's findings are based on Reference[12],[15][16].

Figure (4) compares the total magnetic form factor between the Valence model (Vm), shown in red line, and the Valence model with core polarization (Vm+Cp), shown in blue line. It is clear from the peaks in the figure that the core effect is very small, because the form factor in our work is transverse.


Figure 4. Demonstrates compare between Vm and Vm+CP models for $^{59}CO(J^\pi = \frac{7}{2}^-)$.

3.3. Magnetic form factor ^{93}Nb

The transverse form factor calculations (Figure 5) have been performed in the (glekpn with restriction) model space with the shell-model code NUSHELL X@MUS since we are interested in the positive-parity states of ^{93}Nb for the valance particles states (1g7/2) outside the core ^{56}Ni, The Vm (a) and the Vm with CP model (b) are compared as the total magnetic form factor, which symbolizes the sum. The contribution of M1, M3, M5, and M7 for ^{93}Nb ($J^\pi = \frac{9}{2}^+$) is shown in red, blue, green, and yellow, respectively. Effective interaction *glekpn*.
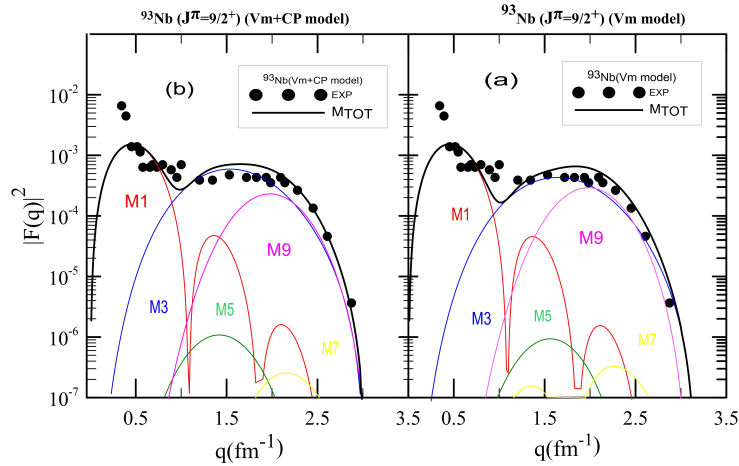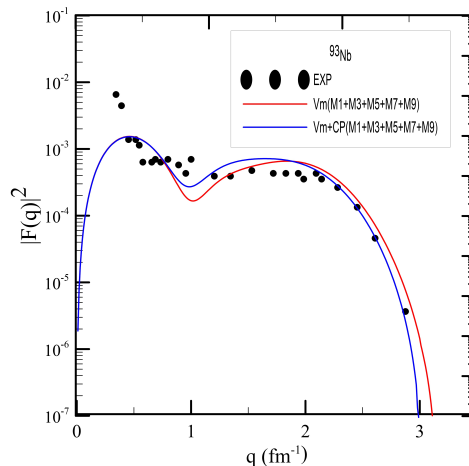
Figure 5. The transverse magnetic form factor for $^{93}Nb(J^\pi = \frac{9}{2}^+)$. The experiment's findings are based on Reference [12][17][15].

It was applied to the g-shell model space wave function. In the first peak between $(0 \leq q \leq 1.1)fm^{-1}$, the dominant component is M1 where the maximum values are 10^{-3} and $(0.6)fm^{-1}$ for form factors and momentum transfer values respectively. At the second peak between $(1.4 \leq q \leq 3)fm^{-1}$, the dominant component is M3 where the maximum values are 10^{-3} and $(1.7)fm^{-1}$ for form factors and momentum transfer values respectively.

Figure (6) compares the total magnetic form factor between the Valence model (Vm), shown in red line, and the Valence model with core polarization (Vm+Cp), shown in blue line. It is clear from the peaks in the figure that the core effect is very small, because the form factor in our work is transverse.

Figure 6. Demonstrates compare between Vm and Vm+CP models for $^{93}Nb(J^\pi = \frac{9}{2}^+)$.

3.5. Magnetic form factors of ^{115}In

The transverse form factor calculations Figure (7) have been performed in the (*glekpn* whit restriction) model space since we are interested in the positive-parity states of ^{115}In for the valance particles states (1g7/2) outside the core ^{56}Ni. The Vm (a) and the Vm with CP model (b) are compared as the total magnetic form factor, which symbolizes the sum. The contribution of M1, M3, M5, and M7 for ^{115}In ($J^\pi = \frac{9}{2}^+$) is shown in red, blue, green, and yellow, respectively. Effective interaction *glekpn*. It was applied to the g-shell model space wave function. In the first peak between $(0 \leq q \leq 1)fm^{-1}$, the dominant component is M1 where the maximum values are 10^{-3} and $0.5fm^{-1}$ for form factors and momentum transfer values respectively. At the second peak between $(1.6 \leq q \leq 2.8)fm^{-1}$, the dominant component is M9 where the maximum values is 10^{-4} and $(1.9)fm^{-1}$ for form factors and momentum transfer values respectively.

Figure (8) compares the total magnetic form factor between the Valence model (Vm), shown in red line, and the Valence model with core polarization (Vm+Cp), shown in blue line. It is clear from the peaks in the figure that the core effect is very small, because the form factor in our work is transverse.
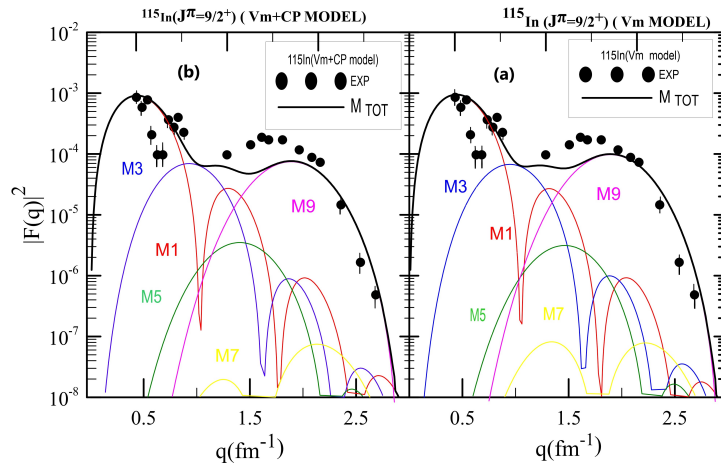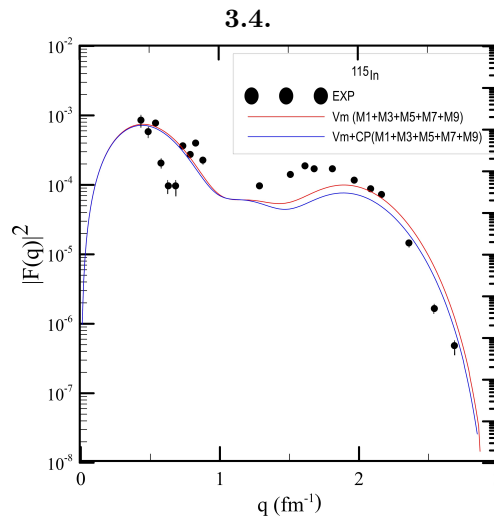
Figure 7. The transverse magnetic form factor for $^{115}In(J^\pi = \frac{9}{2}^+)$. The experiment's findings are based on Reference [12].

Figure 8. Demonstrates compare between Vm and Vm+CP models for $^{115}In(J^\pi = \frac{9}{2}^+)$.

4. CONCLUSIONS

We calculated The magnetic form factors for electron scattering from deformed nuclei (odd-A) in this work. The V_m and V_m with CP Models With W0,ho and glekpn as effect interaction and $Skx\&wsn\&ho$ as potential describe transversal form factors of ^{51}V, ^{59}Co and $^{93}Nb,^{115}$In well with experimental data.

ORCID

Sajad A. Khasain, https://orcid.org/0000-0003-0000-0000; **Khalid S. Jassim**, https://orcid.org/0000-0002-5990-3277

REFERENSES

[1] P. Sarriguren, D. Merino, O. Moreno, E. M. de Guerra, D. Kadrev, A. Antonov, and M. Gaidarov, Physical Review C 99, 034325 (2019). https://doi.org/10.1103/PhysRevC.99.034325

[2] R. R. Roy and B. P. Nigam, Nuclear physics: theory and experiment (Wiley, 1967).

[3] B. Brown, A. Arima, and J. McGrory, Nuclear Physics A 277, 77 (1977). https://doi.org/10.1016/0375-9474(77)90263-9

[4] B. Brown and W. Rae, Nuclear Data Sheets 120, 115 (2014). https://doi.org/10.1016/j.nds.2014.07.022

[5] K. S. Jassim, Physica Scripta 86, 035202 (2012). https://doi.org/10.1088/0031-8949/86/03/035202

[6] X. Pan, Y.-T. Zou, H.-M. Liu, B. He, X.-H. Li, X.-J. Wu, and Z. Zhang, Chinese Physics C 45, 124104 (2021). https://doi.org/10.1088/1674-1137/ac2421

[7] K. S. Jassim, A. A. Al-Sammarrae, F. I. Sharrad, and H. A. Kassim, Physical Review C 89, 014304 (2014). https://doi.org/10.1103/PhysRevC.89.014304

[8] T. de Forest Jr and J. D. Walecka, Advances in Physics 15, 1 (1966). https://doi.org/10.1080/00018736600101254

[9] N. F. Mott, Proceedings of the Royal Society of Lon- don. Series A, Containing Papers of a Mathematical and Physical Character 124, 425 (1929). https://doi.org/10.1098/rspa.1929.0127

[10] F. Sharrad, A. Hamoudi, R. Radhi, and H. Abdullah, Journal of the National Science Foundation of Sri Lanka 41 (2013). http://doi.org/10.4038/jnsfsr.v41i3.6053

[11] W. Richter, M. Van der Merwe, R. Julies, and B. Brown, Nuclear Physics A 577, 585 (1994). https://doi.org/10.1016/0375-9474(94)90934-2

[12] T. W. Donnelly and I. Sick, Reviews of modern physics 56, 461 (1984). https://doi.org/10.1103/RevModPhys.56.461

[13] K. Arita, A. Enomoto, S. Oguro, Y. Mizuno, T. Nakazato, S. Ohsawa, T. Saito, T. Terasawa, and Y. Torizuka, Physical Review C 23, 1482 (1981). https://doi.org/10.1103/PhysRevC.23.1482

[14] S. Platchkov, J. Cavedon, J. Clemens, B. Frois, D. Goutte, M. Huet, P. Leconte, X.-H. Phan, S. Williamson, I. Sick, et al., Physics Letters B 131, 301 (1983). https://doi.org/10.1016/0370-2693(83)90503-8

[15] S. Platchkov, J. Bellicard, J. Cavedon, B. Frois, D. Goutte, M. Huet, P. Leconte, P. Xuan-Ho, P. de Witt Huberts, L. Lapikas, et al., Physical Review C 25, 2318 (1982). https://doi.org/10.1103/PhysRevC.25.2318

[16] H. De Vries, G. Van Niftrik, and L. Lapikas, Physics Letters B 33, 403 (1970). https://doi.org/10.1016/0370-2693(70)90615-5

[17] R. York and G. Peterson, Physical Review C 19, 574 (1979). https://doi.org/10.1103/PhysRevC.19.574

МАГНІТНІ ФОРМ-ФАКТОРИ ДЛЯ ДЕЯКИХ ЯДЕР ^{51}V, ^{59}Co, ^{93}Nb, ^{115}In ЗА ВИКОРИСТАННЯМ ВАЛЕНТНОСТІ З МОДЕЛЯМИ ПОЛЯРИЗАЦІЙНИХ ЕФЕКТІВ ЯДРА ТА БЕЗ МОДЕЛЕЙ

Саджад А. Хасейн, Халід С. Джасім

Факультет фізики, Коледж навчання фундаментальним наукам, Університет Бабилона, 51002 Бабилон, Ірак

Форм-фактор магнітного розсіювання електронів із glekpn, d3f7, ho моделює простір для ядер ^{51}V, ^{59}Co, ^{93}Nb, ^{115}In обговорюється з ефектами поляризації ядра (CP) і без них. Розрахунки виконуються за допомогою коду NuShellX@MUS. Радіальну хвильову функцію для одночастинкових матричних елементів було розраховано за допомогою потенціалів Скірма-Хартрі Фока (SKX), Вуда-Саксона (WS) і гармонійного осцилятора (HO). Модель валентності (Vm), використана в цих розрахунках для розрахунку форм-факторів з ефектами поляризації ядра. Результати добре узгоджуються з наявними експериментальними даними.

Ключові слова: *розсіювання електронів; поперечний форм-фактор*

ISOSCALAR GIANT OCTUPOLE RESONANCE ISGOR OF ^{116}Cd
USING SELF-CONSISTENT SKYRME QRPA[†]

Maryam A. Akbar, **Ali H. Taqi***

Department of Physics, College of Science, Kirkuk University, Kirkuk, Iraq
Corresponding Author e-mail: alitaqi@uokirkuk.edu.iq
Received March 27, 2023; revised April 24, 2023; accepted April 25, 2023

Collective models based on the random phase approximation (RPA) are widely used to accurately depict collective modes of response. They can quickly calculate the strength function for the entire nuclear mass range. The quasi-particle random phase approximation (QRPA), which considers the pairing effect, is an enhanced RPA model. It is anticipated that this effect will be significant for open-shell nuclei. In this work, the self-consistent Skyrme Hartree-Fock-Bardeen, Cooper, and Schrieffer (HF-BCS) and QRPA models have been used to study the isoscalar giant octupole resonance (ISGOR) in the ^{116}Cd isotope. Ten Skyrme-type parameters are utilized in the computations since they may be identified by different values of the incompressibility modulus K_{MN} in nuclear matter. The calculated strength distributions and centroid energy are compared with available experimental data. We saw that the strength distributions varied depending on the type of Skyrme-interaction, and we also observed a definite impact of the K_{NM} values on the centroid energy.

Keywords: *Collective models; Isoscalar Giant Octupole Resonance (ISGOR); Skyrme force; Quasiparticle Random Phase Approximation (QRPA); Hartree-Fock (HF); Bardeen Cooper and Schrieffer (BCS)*
PACS: 21.00.00; 21.60.Ev; 21.60.−n; 21.10.Pc; 21.10.Ky.

1. INTRODUCTION

The Bardeen, Cooper, and Schrieffer (BCS) theory [1] provides both the quasi-particle energies and the occupation probabilities of the single particle levels to describe the ground state characteristics of even-even open shell nuclei. This method depends on a set of input single particle states. For each single particle state, the model gives partial occupation probabilities from using a pairing nucleon-nucleon interaction. The pairing effects on different ground state observables are determined using these probabilities. The description of the excited states must go farther because the HF+BCS cannot account for collective effects. The Random Phase Approximation (RPA) theory is frequently extended by the quasi-particle RPA (QRPA) [2,3], which was created to handle pairing and partial occupation probability of the single particle levels.

Giant resonances (GR) [4,5] serve as an example of the collective modes in atomic nuclei that occur at excitation energies between 10 and 30 MeV. These collective modes are related to the nucleons' collective motion inside the nucleus and are divided into different modes [6] based on their multipolarity L, spin S, and isospin T quantum numbers. According to theory, GR is influenced by the response's nucleon participation rate and transition amplitudes.

The E3 response is split into two branches, the 1ℏω component has been referred to as the low energy octupole resonance, which is firstly observe by Moss et al. in 1976 utilizing inelastic scattering of alpha particles, while the higher (3ℏω) component is referred to as the high energy octupole resonance [7].

The isotope ^{116}Cd is one of the most promising 2β nuclei thanks to the favorable theoretical estimations of the decay probability [8,9], large energy release $Q_{2\beta} = 2813.50(13)$ keV [10], relatively high isotopic abundance δ = 7.49% [11] and a possibility of isotopic enrichment in a large amount.

In this work, the isoscalar giant octupole resonance (ISGOR) of isotope ^{116}Cd was investigated within the framework of a self-consistent Hartree-Fock (HF)- Bardeen, Cooper, and Schrieffer (BCS) based on Quasi particle Random Phase Approximation (QPRPA) with 10 different sets of Skyrme effective nucleon-nucleon force: SkP [12], eMSL09 [13], MSL0 [14], T44 [15], BSK20 [16], Ska [17], SV [18], QMC2 [19], SII [20] and SGOI [17] of different incompressibility modulus [21] in nuclear matter K_{NM} = 200.97, 229.6, 230.00, 230.01, 241.39, 263.16., 305.70, 330.10, 341.40, and 361.59 MeV, respectively. Having a large number of Skyrme-force parameterisations requires a continuous search for the best for describing the experimental data. In order to establish the best sets of Skyrme-force parameterizations for defining the experimental data, the strength function and centroid energy of the isoscalar ISGOR (J; T = 3-; 0) were compared with the available experimental data. It was also studied how the computed centroid energy changes with values of K_{NM}.

2. DESCRIPTION OF CALCULATIONS

The occupation probabilities of the single particle levels and the quasi-particle energies are provided by the Bardeen, Cooper, and Schrieffer (BCS) theory to describe the ground state characteristics of even-even open shell nuclei. When the standard BCS equations, which under spherical symmetry provide particle number n and gap equation Δ_a, are coupled with the Hartree-Fock HF equations, the total HF-BCS energy can be determined.

It is necessary to go beyond the HF+BCS, which is unable to account for collective effects, in order to describe the excited states. As a result, the Random Phase Approximation (RPA) theory has been extended to include quasi-particle RPA (QRPA), which is effective in describing collective states of open-shell nuclei [22,23]. Here is

$$\begin{pmatrix} A_{ab,cd} & B_{ab,cd} \\ -B_{ab,cd}^* & -A_{ab,cd}^* \end{pmatrix} \begin{pmatrix} X_{cd}^\nu \\ Y_{cd}^\nu \end{pmatrix} = E_x^\nu \begin{pmatrix} X_{ab}^\nu \\ Y_{ab}^\nu \end{pmatrix} (1) \tag{1}$$

with,

$$A_{ab,cd} = \frac{1}{\sqrt{1+\delta_{ab}}\sqrt{1+\delta_{cd}}} \left[(E_a + E_b)\delta_{ac}\delta_{bd} + (u_a u_b u_c u_d + v_a v_b v_c v_d)G_{abcd} + (u_a v_b u_c v_d + v_a u_b v_c u_d)F_{abcd} - (-1)^{j_c+j_d-J'}(u_a v_b v_c u_d + v_a u_b u_c v_d)F_{abdc} \right] \tag{2}$$

$$B_{ab,cd} = \frac{1}{\sqrt{1+\delta_{ab}}\sqrt{1+\delta_{cd}}} \left[-(u_a u_b v_c v_d + v_a v_b u_c u_d)G_{abdc} - (-1)^{j_c+j_d-J'}(u_a v_b u_c v_d + v_a u_b v_c u_d)F_{abdc} + (-1)^{j_a+j_b+j_c+j_d-J-j}(u_a v_b v_c u_d + v_a u_b u_c v_d)F_{abcd} \right], \tag{3}$$

where,

$$G_{abcd} = \sum_{m_a m_b m_c m_d} \langle j_a m_a j_b m_b | JM \rangle \langle j_c m_c j_d m_d | J'M' \rangle V_{ab,cd}^{pp}, \tag{4}$$

$$F = \sum_{m_a m_b m_c m_d} \langle j_a m_a j_b m_b | JM \rangle \langle j_c m_c j_d m_d | J'M' \rangle V_{ab,cd}^{ph}. \tag{5}$$

here $V_{\alpha\beta\gamma\delta}^{pp}$ and $V_{\alpha\beta\gamma\delta}^{ph}$ are the particle-particle and hole-hole matrix elements, respectively.

The QRPA states $|n\rangle$ with matching energy E_n can be used to determine the strength or response function [24–26],

$$S(E) = \sum_n \left| \langle 0 | \hat{F} | n \rangle \right|^2 \delta(E - E_n| \tag{6}$$

The energy moments can be calculate using,

$$m_k = \int E^k S(E) dE \tag{7}$$

3. RESULTS AND DISCUSSION

In this work, the response in ^{116}Cd isotope has been studied in the framework of self-consistent QRPA+HFBCS method with Skyrme-type interactions. It is noteworthy to mention that 240 Skyrme interactions that were previously published in the literature underwent analysis by a separate team [27,28] to determine their ability to describe experimental data on nuclear matter, nuclei's properties and observational data of neutron stars, such as the binding energies, radii, effective mass, incompressibility coefficient, symmetry energy density, and fission barriers. The following 10 were chosen to be studied in this work: SkP [12], eMSL09 [13], MSL0 [14], T44 [15], BSK20 [16], Ska [17], SV [18], QMC2 [19], SII [20], and SGOI [17] of various incompressibility moduli in nuclear matter, with K_{MN} = 200.97, 229.6, 230.00, 230.01, 241.39, 263.16., 305.70, 330.10, 341.40, and 361.59 MeV, respectively.

The E3 resonance is divided into low and high energy octupole resonance, as was indicated in the introduction section. The low energy octupole resonance includes 25% of the energy-weighted sum rules for electric E3 and the high energy octupole resonance contains 75% of the energy-weighted sum rules, according to the Harmonic Oscillator Shell Model's explanation of the Giant Resonances. When these modes are connected with the octupole residual reaction, a low energy octupole resonance with around 35% of the energy-weighted sum rules and a high energy octupole resonance with 65% of the energy-weighted sum rules are generated [29].
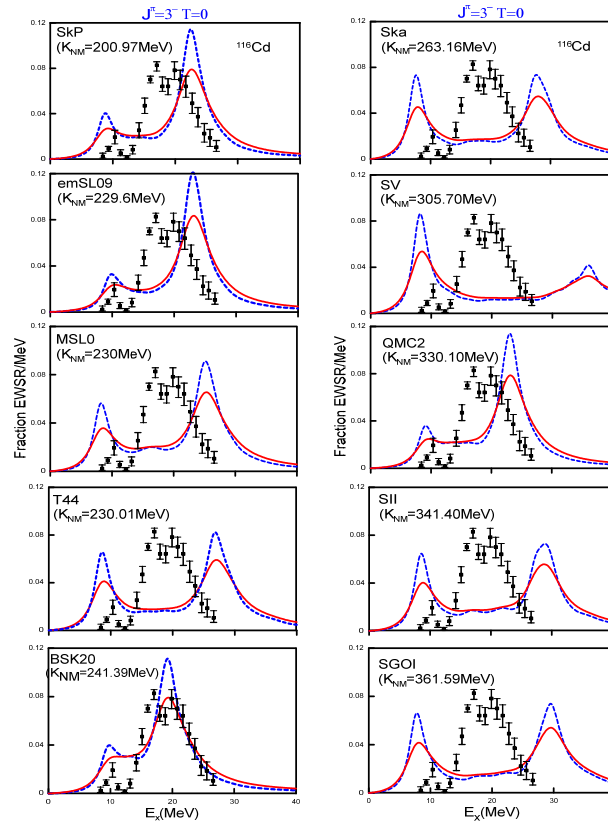
Our calculated fraction energy-weighted sum rules (EWSR/MeV) for ISGOR in ^{116}Cd are displayed in Fig. 1. The low energy octupole resonance strength is obtained in the energy range from 5 and 15 MeV, and the high energy octupole resonance strength is located between 15 and 35 MeV. Our results were compared with available experimental data using two Lorenzian smearing widths of 3 and 5 MeV. The calculations utilizing emSL09 and QMC2 Skyrme interactions with Γ = 5 MeV was the best in describing the practical results experimental data, as shown in Fig. 1.

Most of interactions work best and agree with data concerning centroid energy (m_1/m_0), widths and profiles of strength. The form of the calculated strength distribution for ^{116}Cd are in good agreement with the experimental, but the calculated strength distribution peaks were 1-4 MeV higher than the experimental. In ^{116}Cd, the form of the strength distribution is like Gaussian distribution in the low excitation region but with a large tailing on the high energy extending to 40 MeV.

It is not completely clear, from the experimental point of view, whether the constrained, centroid or scaling energies are more suitable to be compared with the experimental data. However, from what we have just concluded, it can be stated that the reasonable values of nuclear incompressibility that can be extracted from the present ^{116}Cd data are either the one of SkP or emSL09, namely 200.97 or 229.6 MeV.

The formula of the centroid energy $E_{cen} = m_1/m_0$ is measured in a particular energy band close to the resonance peak. Our theoretical calculations of m_1/m_0 (MeV) for ISGOR in ^{116}Cd and experimental values [30] are listed in Table 1.

The m_1/m_0 of the ISGOR as a function of the nuclear matter incompressibility coefficient K_{NM} is presented in Table 1 and depicted in Fig. 2. The calculated centroid energies of the most Skyrme interactions are near and below of the experimental value. We found that emSL09 interaction with K_{NM} = 229.6 MeV agree with data.

Figure 1. Our calculated fraction energy-weighted sum rules (EWSR/MeV) for ISGOR in ^{116}Cd with Lorentzian smearing widths of 3 MeV (blue-dashed lines) and 5 MeV (red lines) were calculated using ten sets of the Skyrme force: SkP, eMSL09, MSL0, T44, BSK20, Ska, SV, QMC2, SII, and SGOI in comparison with the experimental data [30] (Black symbol).

In ISGOR, a high K_{NM} causes the peak to shift to a lower energy while a low K_{NM} causes the peak to shift to a higher energy. For example, an SGOI interaction with a high K_{NM} of 361.59 MeV causes the centroid energy to be 14.964 MeV and a low K_{NM} of 200.97 MeV causes the centroid energy to be 16.800 MeV. The experimental value of $m_1/m_0 = 18.28^{-0.09}_{+0.25}$ MeV [30] for ^{116}Cd as shown in Table 2. Fig. 3, shows the significant change in the strength distribution with changing values of K_{MN}.

Whereas we can clearly confirm from the present results that the value of the nuclear matter incompressibility does play a key role in dictating the location of the ISGOR centroid energy, it is also true that the pairing interaction lowers the energy of the ISGOR to some extent, typically few hundreds keV. This qualitative conclusion is the same that was first found in Ref. [31]. Thus, the pairing interaction cannot be neglected if one aims to reproduce not only the ISGOR centroid energies in Cd isotopes, but also, more generally, in other open-shell nuclei.

For the low energy octupole resonance, the strength distributions are concentrated in a single peak around 10 MeV and for the high energy octupole resonance, the strength distributions are concentrated in a single peak around 25 MeV. However, the location of the peak found with each Skyrme interaction is slightly different. The SkP interaction predicts lowest peaks while the SGOI interaction gives peaks at the highest energies. As it is known from previous studies, the relative position of the peaks is governed by the nuclear matter incompressibility associated with each effective interaction.

Table 1. Our calculated ISGOR centroid energies, constrained energies, and scaling energies in ^{116}Cd based on ten Skyrme-type interaction are compared with the experimental data [30].

	K_{NM} MeV	$E_{cen} = m_1/m_0$ MeV	$E_{con} = \sqrt{m_1/m_{-1}}$ MeV	$E_s = \sqrt{m_3/m_1}$ MeV
Exp.		$\mathbf{18.28^{-0.09}_{+0.25}}$		
SkP	200.97	16.80	15.207	20.737
eMSL09	229.60	18.25	16.627	21.535
MSL0	230.00	15.63	13.590	21.816
T44	230.01	15.61	13.544	22.740
BSK20	241.39	15.99	15.165	18.165
Ska	263.16	13.93	11.735	22.741
SV	305.70	14.19	11.907	27.423
QMC2	330.10	17.45	15.917	21.191
SII	341.40	15.98	13.698	23.987
SGOI	361.59	14.96	12.503	24.395
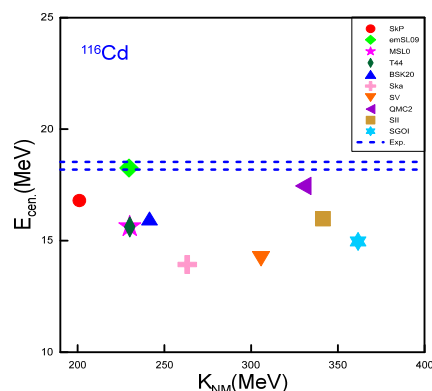
Figure 2. Our calculated ISGOR centroid energies (color symbols) as a function of K_{NM} in ^{116}Cd based on 10 Skyrme-type interaction in comparison with the experimental data [30] (shown as the regions between the dashed blue lines).
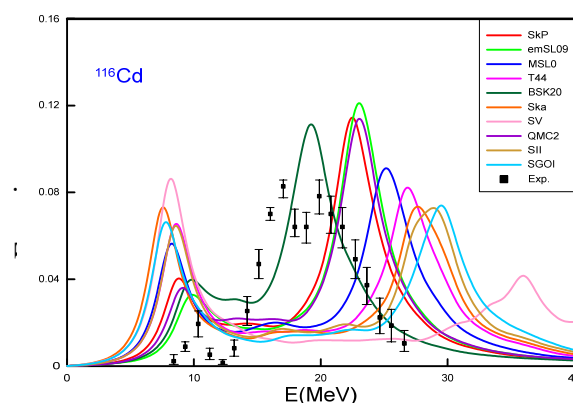
Figure 3. Using 10 Skyrme-type interaction and 3 MeV wide Lorenzian smearing, we estimated the fraction energy-weighted sum rules (EWSR/MeV) for ISGOR in ^{116}Cd and compared it to the experimental results [30].

4. CONCLUSIONS

The strength function of ISGOR has been subjected to self-consistent QRPA based on HF-BCS calculations. The low energy octupole resonance strength is identified between 5 and 15 MeV, and the high energy octupole resonance strength is focused between 15 and 40 MeV. The low energy octupole resonance strength is discovered between 5 and 15 MeV, while the high energy octupole resonance strength is concentrated between 15 and 40 MeV, putting the isoscalar E3 strength in the range of 5 to 40 MeV in ^{116}Cd. By using emSL09 with K_{NM} = 229.6 MeV. The centroid energy is pushed to a lower energy by high K_{NM}, whereas a higher energy is reached by low K_{NM}. For instance, the eMSL09 interaction with low K_{NM} = 229.60 MeV produces the energy equivalent to 18.25 MeV in ^{116}Cd while the SGOI interaction with high K_{NM} = 361.59 MeV does the same for ^{116}Cd.

ORCID IDs

Maryam A. Akbar, https://orcid.org/0009-0004-8290-0658; Ali H. Taqi, https://orcid.org/0000-0001-5007-4858

REFERENCES

[1] J. Dobaczewski, W. Nazarewicz, T.R. Werner, J.F. Berger, C.R. Chinn, and J. Dechargé, "Mean-field description of ground-state properties of drip-line nuclei: Pairing and continuum effects", Physical Review C, **53**, 2809 (1996). https://doi.org/10.1103/PhysRevC.53.2809

[2] M. Baranger, "Extension of the shell model for heavy spherical nuclei", Phys. Rev. **120**, 957 (1960). https://doi.org/10.1103/PhysRev.120.957

[3] V. Voronov, "Complex configurations and nuclear structure problems", J. Phys.: Conf. Ser. **1555**, 012002 (2020). https://doi.org/110.1088/1742-6596/1555/1/012002

[4] M. N. Harakeh, and A. van der Woude, *Giant Resonances, Oxford Studies on Nuclear Physics*, (Oxford Science Publications, 2001).

[5] S. Shlomo, G. Bonasera, and M.R. Anders, "Giant resonances in ^{40,48}Ca, ^{68}Ni, ^{90}Zr, ^{116}Sn, ^{144}Sm and ^{208}Pb and properties of nuclear matter," AIP Conference Proceedings, **2150**, 030011 (2019). https://doi.org/10.1063/1.5124600

[6] J. Button, Y.-W. Lui, D.H. Youngblood, X. Chen, G. Bonasera, and S. Shlomo, "Isoscalar E0, E1, E2, and E3 strength in ^{94}Mo", Phys. Rev. C, **94**, 034315 (2016). https://doi.org/10.1103/PhysRevC.94.034315

[7] Krishichayan, Y.-W. Lui, J. Button, D.H. Youngblood, G. Bonasera, and S. Shlomo, "Isoscalar Giant Resonances in $^{90, 92, 94}$Zr," Phys. Rev. C, **92**, 044323 (2015). https://doi.org/10.1103/PhysRevC.92.044323

[8] J. D. Vergados, H. Ejiri, and F. Simkovic, "Theory of neutrinoless double-beta decay", Rep. Prog. Phys. **75**, 106301 (2012). https://doi.org/10.1088/0034-4885/75/10/106301

[9] J. Barea, J. Kotila, F. Iachello, "Limits on Neutrino Masses from Neutrinoless Double-B Decay", Phys. Rev. Lett. **109**, 042501 (2012). https://doi.org/10.1103/PhysRevLett.109.042501

[10] S. Rahaman, V.-V. Elomaa, T. Eronen, J. Hakala, A. Jokinen, A. Kankainen, J. Rissanen, et al., "Double-beta decay Q values of ^{116}Cd and ^{130}Te", Phys. Lett. B, **703**, 412 (2011). https://doi.org/10.1016/j.physletb.2011.07.078

[11] M. Berglund, and M.E. Wieser, "Isotopic compositions of the elements 2009", Pure Appl. Chem. **83**, 397 (2011). https://doi.org/10.1351/PAC-REP-10-06-02

[12] B.A. Brown, "New Skyrme interaction for normal and exotic nuclei", Phys. Rev. C 58, 220 (1998).

[13] Z. Zhang, and L.W. Chen, "Extended Skyrme interactions for nuclear matter, finite nuclei and neutron stars", Phys. Rev. C, **94**, 064326 (2016). https://doi.org/10.1103/PhysRevC.94.064326

[14] L.W. Chen, C.M. Ko, B.A. Li, and J. Xu, "Density slope of the nuclear symmetry energy from the neutron skin thickness of heavy nuclei," Phys. Rev. C, **82**, 024321 (2010). https://doi.org/10.1103/PhysRevC.82.024321

[15] L.G. Cao, G. Colò, H. Sagawa, P.F. Bortignon, and L. Sciacchitano, "Effects of the Tensor Force on the Multipole Response in Finite Nuclei", Phys. Rev. C, **80**, 064304 (2009). https://doi.org/10.1103/PhysRevC.80.064304

[16] M. Samyn, S. Goriely, P.H. Heenen, and J.M. Pearson, "A Hartree-Fock-Bogoliubov mass formula", Nucl. Phys. A, **700**, 142 (2002). https://doi.org/10.1016/S0375-9474(01)01316-1

[17] Q. Shen, Y. Han, and H. Guo, "Isospin dependent nucleon-nucleus optical potential with Skyrme interactions", Phys. Rev. C, **80**, 024604 (2009). https://doi.org/10.1103/PhysRevC.80.024604

[18] M. Beiner, H. Flocard, N.V. Giai, and P. Quentin, "Nuclear ground-state properties and self-consistent calculations with the skyrme interaction: (I). Spherical description", Nucl. Phys. A, **238**, 29 (1975). https://doi.org/10.1016/0375-9474(75)90338-3

[19] P.A.M. Guichon, and A.W. Thomas, "Quark Structure and Nuclear Effective Forces", Phys. Rev. Lett. **93**, 13 (2004). https://doi.org/10.1103/PhysRevLett.93.132502

[20] D. Vautherin, and D. M. Brink, "Hartree-Fock Calculations with Skyrme's Interaction. I. Spherical Nuclei", Phys. Rev. C, **5**, 626 (1972). https://doi.org/10.1103/PhysRevC.5.626

[21] J.P. Blaizot, "Nuclear compressibilities", Phys. Rep. **64**(4), 171 (1980). https://doi.org/10.1016/0370-1573(80)90001-0

[22] S. Shlomo, V.M. Kolomietz, and G. Colò, "Deducing the nuclear-matter incompressibility coefficient from data on isoscalar compression modes", Eur. Phys. J. A, **30**, 23 (2006). https://doi.org/10.1140/epja/i2006-10100-3

[23] A. Bohr, and B.R. Mottelson, *Nuclear Structure*, Vol. 2, (W.A. Benjamin, New York, 1975).

[24] A.H. Taqi, and G.L. Alawi, "Isoscalar giant resonance in ^{100,116,132}Sn isotopes using Skyrme HF-RPA," Nucl, Phys. A, **983**, 103-117 (2019). https://doi.org/10.1016/j.nuclphysa.2019.01.001

[25] A. H. Taqi, and E.G. Khider, "Ground and transition properties of ^{40}Ca and ^{48}Ca nuclei," Nucl. Phys. At. Energy, **19**, 326 (2018). https://doi.org/10.15407/jnpae2018.04.326

[26] S.H. Amin, A.A. Al-Rubaiee, and A.H. Taqi, "Effect of Incompressibility and Symmetry Energy Density on Charge Distribution and Radii of Closed-Shell Nuclei", Kirkuk U. J. Sci. Stud. **17**(3), 17(2022).10.32894/kujss.2022.135889.1073

[27] M. Dutta, O. Lourenco, J.S.Sá. Martins, A. Delfino, J.R. stone, and P.D. Stevenson, "Skyrme interaction and nuclear matter constraints", Phys. Rev. C, **85**, 035201 (2012). https://doi.org/10.1103/PhysRevC.85.035201

[28] P.D. Stevenson, P.D. Goddard, J.R. Stone, and M. Dutta, "Do Skyrme forces that fit nuclear matter work well in finite nuclei," AIP Conference Proceedings, **1529**, 262 (2013). https://doi.org/10.1063/1.4807465

[29] J.M. Moss, D.H. Youngblood, C.M. Rozsa, D.R. Brown, and J.D. Bronson, "Observation of a Low-Energy Octupole Resonance in Medium-Mass Nuclei", Phys. Rev. Lett. **37**, 816 (1976). https://doi.org/10.1103/PhysRevLett.37.816

[30] Y.-W. Lui, D.H. Youngblood, Y. Tokimoto, H.L. Clark, and B. John, "Isoscalar multipole strength in ^{110}Cd and ^{116}Cd", Phys. Rev. C, **69**, 034611 (2004). https://doi.org/10.1103/PhysRevC.69.034611

[31] J. Li, G. Colò, and J. Meng, "Microscopic linear response calculations based on the Skyrme functional plus the pairing contribution", Phys. Rev. C, **78**, 064304 (2008). https://doi.org/10.1103/PhysRevC.78.064304

ІЗОСКАЛЯРНИЙ ГІГАНТСЬКИЙ ОКТУПОЛЬНИЙ РЕЗОНАНС ISGOR ^{116}Cd З ВИКОРИСТАННЯМ САМОУЗГОДЖЕНОГО SKYRME QRPA

Мар'ям А. Акбар, Алі Х. Такі

Кафедра фізики, Науковий коледж, Кіркукський університет, Кіркук, Ірак

Колективні моделі, засновані на апроксимації випадкової фази (RPA), широко використовуються для точного зображення колективних режимів реакції. Вони можуть швидко розрахувати функцію сили для всього діапазону ядерних мас. Квазічастинкове наближення випадкової фази (QRPA), яке враховує ефект спарювання, є розширеною моделлю RPA. Очікується, що цей ефект буде значним для ядер з відкритою оболонкою. У цій роботі використовуються самоузгоджені моделі Skyrme Hartree-Fock-Bardeen, Cooper, and Schrieffer (HF-BCS) і QRPA для дослідження ізоскалярного гігантського октупольного резонансу (ISGOR) в ізотопі ^{116}Cd. У розрахунках використовуються десять параметрів типу Скірма, оскільки вони можуть бути ідентифіковані різними значеннями модуля нестисливості KMN в ядерній речовині. Розраховані розподіли міцності та енергія центроїда порівнюються з наявними експериментальними даними. Ми побачили, що розподіл сили змінювався залежно від типу взаємодії Скірма, і ми також спостерігали певний вплив значень KNM на енергію центроїда.

Ключові слова: *колективні моделі; ізоскалярний гігантський октупольний резонанс (ISGOR); сила Skyrme; квазічастинкове наближення випадкової фази (QRPA); Хартрі-Фок (HF); Бардін Купер і Шріффер (BCS)*

HOLE-HOLE COLLECTIVE EXCITATIONS IN [106, 112, 130]Sn ISOTOPES[†]

●Fahima A. Saber, ●Ali H. Taqi*

Department of Physics, College of Science, Kirkuk University, Kirkuk, Iraq
Corresponding Author e-mail: alitaqi@uokirkuk.edu.iq
Received April 24, 2023; revised May 9, 2023; accepted May 10, 2023

In this paper, energy-level schemes of neutron rich and reduced electric transition strengths of Tin isotopes [106]Sn, [112]Sn and [130]Sn were studied using collective models, i.e., hole-hole Tamm-Dancoff Approximation (*hh* TDA) and hole-hole Random Phase Approximation (*hh* RPA). According to these models, the excited states of closed core A-2 systems with multipolarity J and isospin T can be described as a linear combination of hole-hole (*hh*) pairs. Therefore, in our approach, the low-lying states of the investigated isotopes [106]Sn, [112]Sn and [130]Sn are obtained by acting two-hole operators on a correlated core [108]Sn, [114]Sn and [132]Sn, respectively. The Hamiltonian is diagonalized within the model space include {$1g_{7/2}$, $2d_{5/2}$, $2d_{3/2}$, $3s_{1/2}$ and $1h_{11/2}$} orbits, using the matrix elements of neutron-neutron (N-N) interaction and modified surface delta interaction (MSDI). The *hh* TDA and *hh* RPA are checked by using the resultant eigenvalues and eigenvectors to calculate the excitation energies and reduced electric transition strengths. A comparison had been made between our theoretical predictions and the recent available experimental data. Reasonable agreements were obtained from these comparisons.
Keywords: *energy-level schemes; collective excitations; hh RPA; hh TDA*
PACS: 21.00.00; 21.60.Ev; 21.60.Cs; 21.60.−n; 21.10.Pc.

1. INTRODUCTION

The study of the Sn isotopes is intriguing from a theoretical perspective because they provide a special testing ground for calculations of nuclear structure. In the literature, several theories have been proposed to explain the shell model calculations, for neutron-deficient Sn isotopes by Engeland et al. [1], Covello et al. [2] and Schubert et al. [3] taking [100]Sn as core, for [106,107,108,109]Sn isotopes using CD-Bonn and Nijmegen1 interactions by E. Dikman [4], for exotic [134.136.138,140]Sn isotopes with a realistic effective interaction [5], for even [102-108]Sn and odd [103−107]Sn isotopes using different interactions by T. Trivedi, et.al. [6], for [104,106,108]Sn based on the CD-Bonn nucleon-nucleon interaction by Khalid S. Jassim [7], for even-even [100-108]Sn isotopes by with the effective interactions Snet, SN100PN Delta interaction by Khalid H.H. Al-Attiah et.al. [8].

Fouad A. Majeed and Sarah M. calculated the energy levels, binding energy, and reduced transition probabilities B(E2;$0^+ \rightarrow 2^+$) for even-even [134, 136]Sn, and [134, 136]Te around doubly magic core [132]Sn by using shell model code Nushellx@MSU for Windows and employing the effective interactions jj56pna, jj56pnb, kh5082, cw5082, jj56cdb, and khhe [9]. Fatema H. Obeed and Baneen S. Abed, used the surface delta and modified surface delta interactions by applying the nuclear shell model to calculate values of excitation energies for isotopes of equal mass number containing two nucleons outside the closed core [114]Sn, these nuclei are; the isotope (Tin) [116]Sn contains two neutrons within the model space ($3s_{1/2}$, $2d_{3/2}$, $1h_{11/2}$) and the other isotope is [116]Te (Tellurium) contains two protons within the model space ($1g_{7/2}$, $2d_{5/2}$, $3s_{1/2}$, $2d_{3/2}$, $1h_{11/2}$) [10]. A. K. Hasan et al., investigated on the energy levels and transition probabilities B ($E2$; ↓) and B ($M1$; ↓) for [21,23]Na isotopes by using the (USDA and USDB) interactions in the (sd-shell) model space [11]. S. Akkoyun, investigated the nuclear structure properties of A=49 isobars, the double-magic [40]Ca nucleus was considered an inert core, and fp model space was taken into account for the valance nucleons [12]. In 2022, Mustafa M. Jabbar and Fatema H. Obeed, used the surface delta and modified surface delta interactions by applying the nuclear shell model to calculate values of excitation energies for [92]Nb and [92]Mo [13].

One of the significant and practical models that became a widely accepted theoretical model in the nuclear physics structure is the nuclear shell model [14, 10]. According to the Pauli principle, we fill the shells in this model in order of increasing energy, resulting in an inert core of filled shells and a certain number of valence nucleons. The model then presupposes that the valence nucleons are primarily responsible for determining nuclear properties [16].

The excited states of A-2 nuclei can be characterized as a linear combination of hole-hole (*hh*) pairs, such an approximation named Tamm-Dancoff Approximation *hh* TDA [17, 18]. When the ground states and excited states are treated more symmetrically, i.e., both the ground state and the excited states may be characterized as linear combinations of hole-hole states, both the ground state and the excited states are treated equally in this scenario, such an approximation is referred as the hole-hole Random Phase Approximation *hh* RPA [19-21].

In this paper, hole-hole excitations of some [106, 112, 130]Sn (Z=50) isotopes were investigated using PPRPA code version 1, 2015 [22] in the presence of MSDI and N-N interactions. Our approach assumes that the low-lying states of [106]Sn, [112]Sn and [130]Sn by acting two-hole operators on a correlated core [108]Sn, [114]Sn and [132]Sn, respectively. A comparison had been made between our theoretical predictions and the recent available experimental data.

2. THEORY

A TDA generalization is the RPA. Bohm and Pines first presented this approach for investigating the plasma oscillations of the electron gas [20]. By using annihilation operators on the ground state $|A,0\rangle$ of the A-nucleon system, collective excited states of A-2 systems with multipolarity J and isospin T are produced [24],

---

$$|A - 2, \lambda, JT\rangle = \left(\sum_{i \leq j} X_{ij}^{\lambda,JT} a_i a_j - \sum_{m \leq n} Y_{mn}^{\lambda,JT} a_m a_n\right) |A,0\rangle \tag{1}$$

where a is annihilation operator, X and Y are amplitudes. indices ij and mn represent the quantum numbers of hole and particle stats, respectively. The compact matrix form of hh RPA equations has the following form [23, 24],

$$\begin{pmatrix} A_{iji'j'}^{\lambda,JT} & B_{ijmn}^{\lambda,JT} \\ B_{ijmn}^{\dagger,\lambda,JT} & C_{mnm'n'}^{\lambda,JT} \end{pmatrix} \begin{pmatrix} X_{ij}^{\lambda,JT} \\ Y_{mn}^{\lambda,JT} \end{pmatrix} = E_x \begin{pmatrix} 1 & 0 \\ 0 & -1 \end{pmatrix} \begin{pmatrix} X_{ij}^{\lambda,JT} \\ Y_{mn}^{\lambda,JT} \end{pmatrix} \tag{2}$$

with

$$A_{iji'j'}^{\lambda,JT} = -(\varepsilon_i + \varepsilon_j)\delta_{ii'}\delta_{jj'} + V_{iji'j'}$$

$$B_{ijmn}^{\lambda,JT} = -V_{ijmn}$$

$$C_{mnm'n'}^{\lambda,JT} = (\varepsilon_m + \varepsilon_n)\delta_{mm'}\delta_{nn'} + V_{mnm'n'} \tag{3}$$

where E_x is the excitation energy, ε_i is single particle energy and V_{ijmn} is antisymmetrized two-body matrix elements. A, B and C are submatrices of dimensions $n_h \times n_h, n_h \times n_p, n_p \times n_p$, respectively. If the sub-matrices C and B are vanished, the RPA equations will be reduced to TDA equation.

The antisymmetric matrix elements of the modified surface delta interaction (MSDI) used in this work has the form [25],

$$V_{ab,cd}^{JT} = \frac{1}{2}A_T(-1)^{n_a+n_b+n_c+n_d} \times \sqrt{\frac{(2j_a+1)(2j_b+1)(2j_c+1)(2j_d+1)}{(1+\delta_{ab})(1+\delta_{cd})}} \times \left\{(-1)^{j_a+j_b+j_c+j_d} \begin{pmatrix} j_a & j_b & J \\ \frac{1}{2} & \frac{-1}{2} & 0 \end{pmatrix} \times \begin{pmatrix} j_c & j_d & J \\ \frac{1}{2} & \frac{-1}{2} & 0 \end{pmatrix} [1 - \right.$$

$$\left. (-1)^{J+T+l_c+l_d} - \begin{pmatrix} j_a & j_b & J \\ \frac{1}{2} & \frac{1}{2} & 1 \end{pmatrix}\begin{pmatrix} j_c & j_d & J \\ \frac{1}{2} & \frac{1}{2} & -1 \end{pmatrix} [1 + (-1)^T] + \{[2T(T+1) - 3]B + C\}\delta_{ac}\delta_{bd} \right\} \tag{4}$$

where A_0, A_1, B and C are the strength parameters of the (MSDI) and $A_0 = 0$ or 1 for $T = 0$ (isoscalar) or $T = 1$ (isovector), respectively.

In terms of RPA amplitudes X and Y, the radial transition density of state $|\tau, JT\rangle$ is [20,21],

$$\rho_{\tau,JT} = \sqrt{\frac{2T+1}{8\pi(2J_i+1)}} e(T) \sum_{T=0,1} (-)^{T_f-T_z} \begin{pmatrix} T_f & T & T_i \\ -T_z & 0 & T_z \end{pmatrix} \times \sum_{ab} [X_{ab}^{\omega,JT} + Y_{ab}^{\omega,JT}]\langle a\|Y_J\|b\rangle R_{n_a\ell_a}(r)R_{n_b\ell_b}(r) \tag{5}$$

Where $e(T) = e\left(\frac{1}{2}\right) + (-1)^T e\left(-\frac{1}{2}\right)$, $T_z = \frac{A-N}{2}$. The reduced matrix elements of spherical harmonic can be written as [20],

$$\langle a\|Y_J\|b\rangle = (-1)^{j_a+\frac{1}{2}} \sqrt{\frac{(2j_a+1)(2j_b+1)(2J+1)}{4\pi}} \times \begin{pmatrix} j_a & J & j_b \\ \frac{1}{2} & 0 & -\frac{1}{2} \end{pmatrix} \frac{1}{2}[1 - (-1)^{\ell_a+J+\ell_b}] \tag{6}$$

and the radial wave function R of harmonic oscillator potential is given by [6],

$$R_{n\ell} = \frac{1}{(2\ell+1)!!} \sqrt{\frac{2^{\ell-n+3}(2n+2\ell-1)}{b^3\pi^{\frac{1}{2}}(n-1)!}} \left(\frac{r}{b}\right)^\ell e^{-\frac{r^2}{2b^2}} \times \sum_{k=0}^{n=1}(-1)^k \frac{(n-1)!2^k}{(n-k-1)!k!} \frac{(2\ell+1)!!}{(2\ell+2k+1)!!} \left(\frac{r}{b}\right)^{2k} \tag{7}$$

Thus, the reduced transition probability becomes [22],

$$B(EJ) = (2J+1)\left|\int r^{J+2} \rho_{\tau,JT} dr\right|^2 \tag{8}$$

3. RESULTS AND DISCUSSIONS

In the present study, the nuclear structures of Tin isotopes: ^{106}Sn, ^{112}Sn, ^{130}Sn are studied in the framework of hh TDA and hh RPA using PPRPA code version 1, 2015 [22]. The Hamiltonian is diagonalized within the model space include {$1g_{7/2}$, $2d_{5/2}$, $2d_{3/2}$, $3s_{1/2}$ and $1h_{11/2}$} orbits, using N-N interaction and modified surface delta interaction (MSDI), by choosing the coefficients values of the interaction strengths A_T by the values of {A_1 = 0.40 MeV, A_2=0.42 MeV, B = 0.5 MeV, C = 0 MeV} for ^{106}Sn, {A_1 = 0.20 MeV, A_2=0.35 MeV, B = 0.0 MeV, C = 0.0 MeV} for ^{112}Sn and {A_1 = 0.20 MeV, A_2=0.25 MeV, B = 0.0 MeV, C = 0.0 MeV} for ^{130}Sn , represented of the modified surface delta interaction. Our approach assumes that the low-lying states of ^{106}Sn are obtained by acting hh operator on a correlated ^{108}Sn core, of ^{112}Sn are obtained by acting hh operator on a correlated core of ^{114}Sn isotope, of ^{130}Sn are obtained by acting hh operator on a correlated core of ^{132}Sn isotope. The single particle energies are given in Table 1.

Table 1. Single particle energies used in different shell model approaches.

| Orbits (nlj)	S.P. Energy (MeV)
$1g_{7/2}$	5.6014
$2d_{5/2}$	5.2819
$2d_{3/2}$	3.7090
$3s_{1/2}$	3.7077
$1h_{11/2}$	3.9843

The calculated eigenvalues and experimentally known energy levels for ^{106}Sn and ^{112}Sn are tabulated in Tables 2 and 3, and are also plotted in Figs. 1 and 2. The *hh* RPA results are plotted in columns (second and third) for both interactions MSDI and N-N respectively, while the *hh* TDA results are plotted in columns (fourth and fifth) for both interactions MSDI and N-N respectively. The calculated results are compared with the experimental data (first column). Both the interactions predict very well the ordering of levels.

Table 2. Our calculated low-lying states (MeV) of ^{106}Sn using MSDI and N-N interactions for the *hh* RPA and *hh* TDA in comparison with the experimental data [26].

J^π	EXP.	J^π	RPA, MSDI	J^π	RPA, N-N	J^π	TDA, MSDI	J^π	TDA, N-N
0^+	0	0^+	0	0^+	0	0^+	0	0^+	0
2^+	1.208	1^+	1.201	1^+	0.638	1^+	0.842	1^+	0.635
4^+	2.019	7^+	1.532	7^+	0.968	7^+	1.027	7^+	0.821
6^+	2.325	2^+	1.74	2^+	1.173	2^+	1.28	2^+	1.035
		3^+	1.768	3^+	1.205	3^+	1.285	3^+	1.079
		5^+	1.807	5^+	1.244	5^+	1.304	5^+	1.098
		4^+	1.979	4^+	1.617	4^+	1.484	4^+	1.472
		6^+	2.086	6^+	1.796	6^+	1.582	6^+	1.648

Table 3. Our calculated low-lying states (MeV) of ^{112}Sn using MSDI and N-N interactions for the *hh* RPA and *hh* TDA in comparison with the experimental data [26].

J^π	EXP.	J^π	RPA, MSDI	J^π	RPA, N-N	J^π	TDA MSDI	J^π	TDA, N-N
0^+	0	0^+	0	0^+	0	0^+	0	0^+	0
2^+	1.256	1^+	1.408	1^+	0.772	1^+	1.064	1^+	0.637
2^+	2.15	2^+	2.113	2^+	1.522	2^+	1.729	2^+	1.327
4^+	2.247	2^+	2.568	2^+	1.932	2^+	2.161	2^+	1.733
2^+	2.476	4^+	2.692	0^+	2.024	4^+	2.279	4^+	1.852
6^+	2.549	6^+	2.706	4^+	2.056	6^+	2.293	0^+	1.855
0^+	2.617	3^+	2.735	6^+	2.263	0^+	2.618	6^+	2.061
3^+	2.756	4^+	2.83	2^+	2.377	3^+	2.703	2^+	2.192
4^+	2.783	2^+	2.895	3^+	2.478	2^+	2.736	3^+	2.276
		0^+	3.025	4^+	2.592	4^+	2.802	4^+	2.391
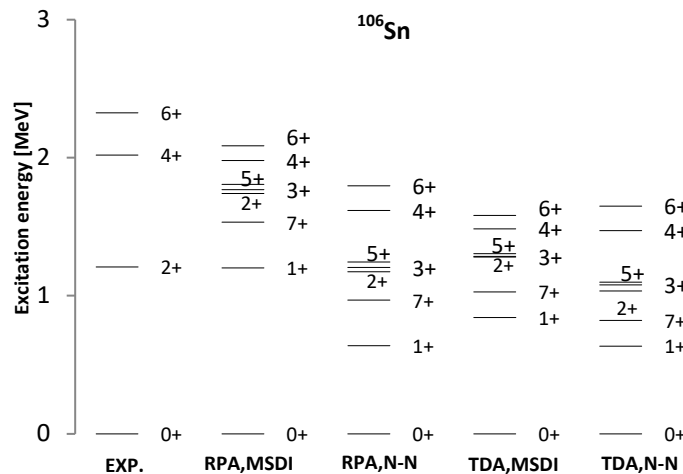
Figure 1. Energy level scheme of ^{106}Sn using MSDI and N-N interactions for the *hh* RPA and *hh* TDA in comparison with the experimental data [26].

For ^{106}Sn, Experimentally, only few excited states with $J^{\pi}= 2^{+}$, 4^{+} and 6^{+} are known, *hh* TDA and *hh* RPA calculations for MSDI and N-N predicted more states than those of experimental data. See Fig. 1.

For ^{112}Sn the obtained theoretical energy level for 1^{+} cannot be predicted by experiment. For example, the first experimental 2^{+} excited states occur at 1.256 MeV, while using *hh* RPA with the MSDI this state was found at 2.113 MeV, but with the N-N interaction the same state was found at 1.522 MeV, and using *hh* TDA with the MSDI this state was found at 1.729 MeV, but with the N-N interaction the same state was found at 1.327 MeV.
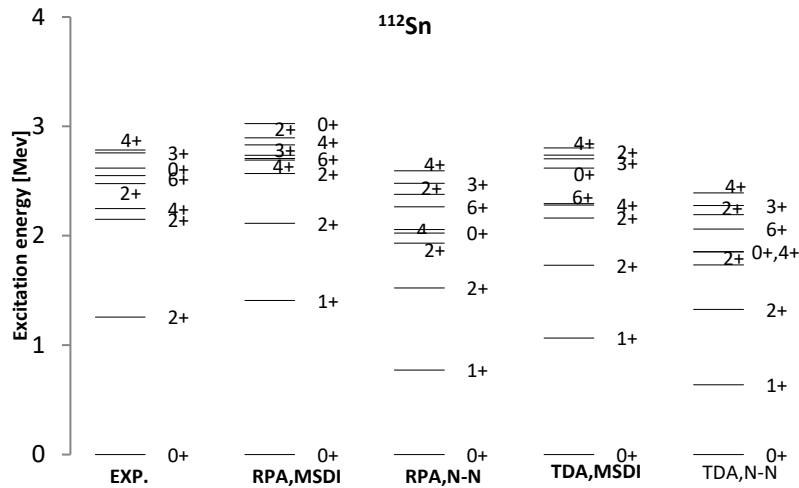
Figure 2. Energy level scheme of ^{112}Sn using MSDI and N-N interactions for the *hh* RPA and *hh* TDA in comparison with the experimental data [26].

In Table 4, we have tabulated all the calculated eigenvalues and experimentally known levels for ^{130}Sn and corresponding energy levels are also plotted in Fig. 3.

Table 4. Our calculated low-lying states (MeV) of ^{130}Sn using MSDI and N-N interactions for the *hh* TDA in comparison with the experimental data [26].

J^{π}	EXP.	J^{π}	TDA, MSDI	J^{π}	TDA, N-N
0^{+}	0	0^{+}	0	0^{+}	0
2^{+}	1.221	1^{+}	1.081	1^{+}	1.222
2^{+}	2.028	2^{+}	1.847	2^{+}	1.933
6^{+}	2.256	4^{+}	2.257	6^{+}	2.378
4^{+}	2.490	5^{+}	2.274	5^{+}	2.415
$4^{+},5^{+}$	2.492	2^{+}	2.298	2^{+}	2.438
3^{+}	3.167	6^{+}	2.367	4^{+}	2.442
4^{+}	3.425	4^{+}	2.544	4^{+}	2.684
2^{-}	4.119	3^{+}	2.986	3^{+}	3.126
9^{-}	4.206	4^{+}	3.145	4^{+}	3.242
3^{-}	4.224	9^{-}	3.811	2^{-}	3.633
4^{+}	4.405	2^{-}	4.184	9^{-}	3.951
4^{+}	4.463	3^{-}	4.222	3^{-}	4.226
4^{+}	5.262	4^{+}	4.459	4^{+}	4.275
		4^{+}	4.460	4^{+}	4.640
		4^{+}	5.688	4^{+}	5.768

The *hh* TDA results are plotted in columns (second and third) for both interactions MSDI and N-N respectively. The calculated results are compared with the experimental data [26] (first column).

For ^{130}Sn, one gets the ground state and low-lying excited states very nicely for both interactions (MSDI and N-N). But the obtained theoretical energy level for 1^{+} is not recorded by experiment.

Table 5 gives the calculated values of the reduced electric transition strengths B(E2) of transition $4^{+}\rightarrow2^{+}$ for the investigated isotopes without and with the effective charge's e_{p} = 1.5e and e_{n} = 0.5e. Good agreements were obtained.
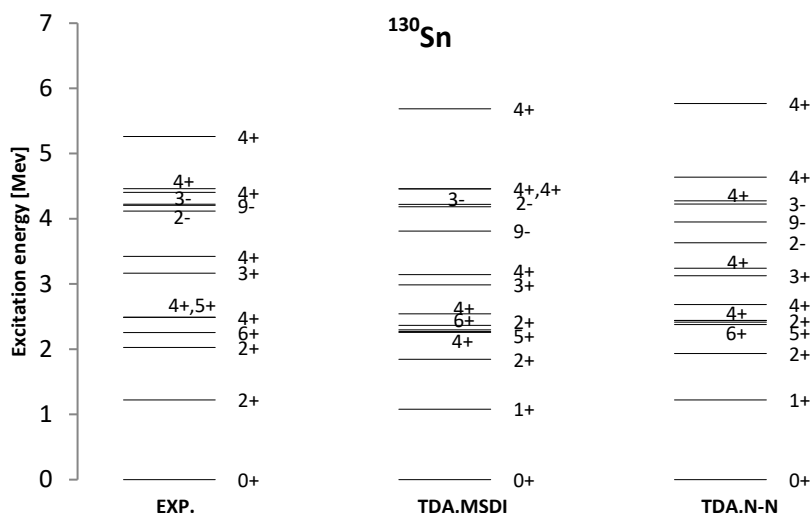
Figure 3. energy levels scheme of ^{130}Sn isotope using *hh* TDA with MSDI and N-N interactions in comparison with the experimental energies [26]

Table 5. reduced electric transition strengths B(E2) in units ($e^2.fm^4$) based on particle-particle calculations using different effective charge values.

Isotope	Exp.	TDA		RPA		Effective charges	
		MSDI	N-N	MSDI	N-N	e_p	e_n
^{106}Sn	811	470	470	450	480	1.0	0.0
		930	930	890	960	1.5	0.5
^{112}Sn	990	340	460	350	470	1.0	0.0
		670	910	690	950	1.5	0.5
	1264	450	480	440	510	1.0	0.0
		910	960	890	1000	1.5	0.5
^{130}Sn	774	500	600			1.0	0.0
		990	1200			1.5	0.5

4. CONCLUSIONS

When the Hamiltonian is diagonalized in the presence of N-N interactions and modifies surface delta interactions (MSDI), the calculated results of *hh* RPA and *hh* TDA are obtained in reasonable agreements to those of experimental data for the investigated Sn isotopes. Both the interactions predict very well the ordering of levels. But for ^{106}Sn, the N-N interaction have the same experimental 2^+ state. The ground states of ^{112}Sn and ^{130}Sn are very nicely predicted. The calculated electric transition strengths B(E2) for the investigated isotopes are well-obtained for the transition $4^+ \rightarrow 2^+$.

ORCID ID
Ali H. Taqi, https://orcid.org/0000-0001-5007-4858, **Fahima A. Saber**, https://orcid.org/0009-0001-6804-2915

REFERENCES
[1] T. Engeland, M. Hjorth-Jensen, A. Holt, and E. Osnes, "Large Shell Model Calculations with Realistic Effective Interaction," Physica Scripta, **1995**(T56), 58 (1995). https://doi.org/10.1088/0031-8949/1995/T56/009
[2] A. Covello, F. Andreozzi, L. Coraggio and A. Gargano, T.T.S. Kuo, and A. Porrino, "Nuclear Structure Calculations With Realistic Effective Interactions", Progress in Particle And Nuclear Physics, **38**, 165 (1997). https://doi.org/10.1016/S0146-6410(97)00023-9
[3] R. Schubart, H. Grawe, J. Heese, H. Kluge, K. H. Maier, and M. Schramm, "Shell Model Structure at ^{100}Sn - the Nuclides ^{98}Ag, ^{103}In, and $^{104, 105}$Sn", Zeitschrift Für Physik A Hadrons And Nuclei, **352**, 373-390 (1995). https://doi.org/10.1007/BF01299755
[4] E. Dikmen, "Shell Model Description of Neutron-Deficient Sn Isotopes," Communications in Theoretical Physics, **51**(5), 899 (2009). https://doi.org/10.1088/0253-6102/51/5/28
[5] A. Covello, L. Coraggio, A. Gargano, and N. Itaco, "Shell-model study of exotic Sn isotopes with a realistic effective interaction," Journal of Physics: Conference Series, **267**, 012019 (2011). https://doi.org/10.1088/1742-6596/267/1/012019
[6] T. Trivedi, P.C. Srivastava, D. Negi, and I. Mehrotra, "Shell Model Description of $^{102-108}$Sn Isotopes," International Journal of Modern Physics E, **21**(4), 1250049 (2012). https://doi.org/10.1142/S0218301312500498
[7] K.S. Jassim, "Nuclear Structure of ^{104,106,108}Sn Isotopes Using the Nushell Computer Code," Chinese Journal of Physics, **51**(3), 441 (2013). https://cdnx.uobabylon.edu.iq/research/repository1_publication889_30_1533.pdf
[8] K.H.H. Al-Attiah, F.A. Majeed, and T.J. Al-Kawwaz, "Calaculations of Even-Even $^{100-108}$Sn Isotopes Using Shell Model in the Vicinity of ^{100}Sn," Journal of Babylon University/Pure and Applied Sciences, **21**(8), 2831(2013). https://iasj.net/iasj/pdf/75f920c6c56d7091

[9]   F.A. Majeed, and S.M. Obaid, "Large-Scale Shell Model Calculations of ^{134,136}Sn, ^{134,136}Te around doubly-magic ^{132}Sn", International Journal of Scientific & Technology Research, **5**(4), 106(2016). https://www.ijstr.org/final-print/apr2016/Large-scale-Shell-Model-Calculations-Of-134136sn-134136te-Around-Doubly-magic-132sn.pdf

[10] F.H. Obeed, and B.S. Abed, "Study of energy spectrum of ^{116}Sn and ^{116}Te nuclei by using surface delta and modified surface delta interactions", Journal of Physics: Conference Series **1664**, 012145 (2020). https://doi.org/10.1088/1742-6596/1664/1/012145

[11] A.K. Hasan, F.H. Obeed, and A.N. Rahim, "Positive Parity Levels of ^{21,23}Na Isotopes by Using the Nuclear Shell", Ukrainian Journal of Physics, **65**(1), 3(2020). https://doi.org/10.15407/ujpe65.1.3

[12] S. Akkoyun, "Nuclear Shell Model Calculations for A=49 Isobars", Turkish Journal of Science and health, **1**(2), 3(2020). https://dergipark.org.tr/en/download/article-file/1178106

[13] M.M. Jabbar, and F.H. Obeed, "Description of the energy levels and electric quadrupole transitions of the ^{92}Nb and ^{92}Mo nuclei using nuclear shell model", Kuwait Journal of Science, **49**(2), 1 (2022). https://doi.org/10.48129/kjs.13631

[14] I. Kaplan, *Nuclear Physics*, (Addison – Wesley Pub.Com. Inc, 1963).

[15] N.D. Cook, *Models of the Atomic Nucleus*, (Springer -Verlag Berlin Heidelberg Netherlands, 2006).

[16] K.S. Krane, *Introductory Nuclear Physics*, (John Wiley &Sons, Inc, 1988).

[17] P. Ring, and P. Schuck, *The Nuclear Many-Body Problem*, (Springer-Verlag, New York, 1980).

[18] J. Suhonen, *From Nucleons to Nucleus*, (Springer-Verlag, Berlin Heidelberg, 2007).

[19] A.H. Taqi, A.A. Rasheed, and S.H. Amin, "Particle–particle and hole–hole random phase approximation calculations for ^{42}Ca and ^{38}Ca nuclei," Acta Physica Polonica B, **41**(6), 1327 (2010). https://www.actaphys.uj.edu.pl/R/41/6/1327/pdf

[20] A.H. Taqi, "Particle-Particle Tamm-Dancoff Approximation and Particle-Particle Randam Phase Approximation Calculations for ^{18}O and ^{18}F Nuclei," Pramana Journal of Physics, **80**(2), 355-360 (2013). https://doi.org/10.1007/s12043-012-0468-1

[21] A.H. Taqi, "The Electroexcitation of Low-Lying, Collective, Positive Parity, T=1 States in ^{18}O, Based on the Particle-Particle Random Phase Approximation", Chinese Journal of Physics, **45**(5), 530 (2007). https://www.airitilibrary.com/Publication/Index?DocID=05779073-200710-45-5-530-536-a&jsonString=

[22] A.H. Taqi, "A visual Fortran 90 program for the two-particle or two-hole excitations of nuclei: The PPRPA program," SoftwareX **5**, 51-61 (2016). https://doi.org/10.1016/j.softx.2016.04.003

[23] A.H. Taqi, and A.H. Ibrahim, "Collective Excitations of ^{14}N and ^{10}B Nuclei," Kirkuk University Journal-Scientific Studies, **11**(1), 202 (2016). https://doi.org/10.32894/kujss.2016.124396

[24] A.H. Taqi, and A.H. Ibrahim, "Electron scattering of ^{14}N based on two-hole excitations," Chinese Journal of Physics, **54**, 185-193 (2016). https://doi.org/10.1016/j.cjph.2016.04.003

[25] P.J. Brussaard, and P.W. Glaudemans, *Shell model applications in nuclear spectroscopy*, (Amsterdam: North-Holland, 1977).

[26] National Nuclear Data Center https://www.nndc.bnl.gov

ДІРКОВІ КОЛЕКТИВНІ ЗБУДЖЕННЯ В ІЗОТОПАХ ^{106,112,130}Sn

Фахіма А. Сабер, Алі Х. Такі
Факультет фізики, Науковий коледж, Кіркукський університет, Кіркук, Ірак

У цій статті було вивчено схеми енергетичних рівнів нейтронно-насичених і знижених електричних переходів ізотопів олова ^{106}Sn, ^{112}Sn і ^{130}Sn з використанням колективних моделей, тобто hole-hole наближення Тамма-Данкова (*hh* TDA) і hole-hole апроксимації випадкової фази (*hh* RPA). Згідно з цими моделями, збуджені стани замкнутих ядер А-2 систем з мультиполярністю J і ізоспіном T можна описати як лінійну комбінацію пар hole-hole (hh). Тому в нашому підході низьколежачі стани досліджуваних ізотопів ^{106}Sn, ^{112}Sn і ^{130}Sn отримані шляхом дії hole-hole операторів на корельоване ядро ^{108}Sn, ^{114}Sn і ^{132}Sn відповідно. Гамільтоніан був діагоналізований у просторі моделі, що включає {$1g_{7/2}$, $2d_{5/2}$, $2d_{3/2}$, $3s_{1/2}$ and $1h_{11/2}$} орбіти, з використанням матричних елементів нейтрон-нейтронної (N-N) взаємодії та модифікованої поверхні дельта взаємодії (MSDI). hh TDA і hh RPA перевіряються за допомогою результуючих власних значень і власних векторів для розрахунку енергій збудження та зменшених сил електричних переходів. Було проведено порівняння між нашими теоретичними прогнозами та останніми доступними експериментальними даними. У результаті цих порівнянь були отримані розумні згоди.

Ключові слова: *енергетичні схеми; колективні збудження; hh RPA; hh TDA*

MOLECULAR DOCKING STUDY OF THE INTERACTIONS BETWEEN CYANINE DYES AND DNA[†]

Olga Zhytniakivska[a,*], Uliana Tarabara[a], Pylyp Kuznietsov[b], Kateryna Vus[a],
Valeriya Trusova[a], Galyna Gorbenko[a]

[a]*Department of Medical Physics and Biomedical Nanotechnologies, V.N. Karazin Kharkiv National University*
4 Svobody Sq., Kharkiv, 61022, Ukraine
[b]*O. I. Akhiezer Department for Nuclear and High Energy Physics, V.N. Karazin Kharkiv National University*
4 Svobody Sq., Kharkiv, 61022, Ukraine
Corresponding Author e-mail: olga.zhytniakivska@karazin.ua

Among the various fluorescent probes currently used for biomedical and biochemical studies, significant attention is paid to cyanine dyes possessing advantageous properties upon their complexation with biomolecules, particularly nucleic acids. Given the wide range of cyanine applications in DNA studies, a better understanding of their binding mode and intermolecular interactions governing the dye-DNA complexation would facilitate the synthesis of new molecular probes of the cyanine family with optimized properties and would lead to the development of new cyanine-based strategies for nucleic acid detection and characterization. In the present study, the molecular docking technique has been employed to evaluate the mode of interaction between one representative of monomethines (AK12-17), three trimethines (AK3-1, AK3-3, AK3-5), three pentamethines (AK5-1, AK5-3, AK5-9) and one heptamethine (AK7-6) cyanine dyes and B–DNA dodecamer d(CGCGAATTCGCG)2 (PDB ID: 1BNA). The molecular docking studies indicate that: i) all cyanines under study (except AK5-9 and AK7-6) form the most stable complexes with the minor groove of double-stranded DNA; ii) the cyanines AK5-9 and AK7-6 interact with the major groove of DNA due to their more extended structure and less hydrophilicity in comparison with the other examined dyes; iii) cyanine dye binding is governed by the hydrophobic and van der Waals interactions presumably with the nucleotide residues C9A, G10A (except AK3-1, AK3-5), A17B (except AK3-5, AK5-3) and A18B in the minor groove and the major groove residues C16B, A17B, A18B, C3A, G4A, A5A, A6A (AK5-9 and AK7-6); iv) all dyes under study (except AK3-1, AK3-5 and AK5-39) possess an affinity for adenine and cytosine residues, whereas AK3-1, AK3-5 and AK5-3 also interact with thymine residues of the double-stranded DNA.

Keywords: *Cyanine dyes; DNA; dye-DNA interactions; molecular docking*
**PACS:** 87.14.C++c, 87.16.Dg

During the last decades cyanine dyes have become increasingly utilized across a wide range of research areas, such as laser technologies, optoelectronics, photoelectrochemistry, bioanalysis, pharmacology, medicine, etc. [1-5]. Likewise, these probes appeared to be particularly useful as molecular probes for biomedical studies [6-30]. More specifically, cyanine dyes were effectively used i) in cell labeling, including life-cell imaging [6,7], labeling neural circuits for the visualization of the structure and function of the brain [8,19], and stem cell tracking in neurodegenerative medicine [10, 11]; ii) detection of oxidative stress and reactive oxygen species [12-14], iii) for synthesis of the fluorescently labeled antibodies [15]; iv) in cancer research for tumor imaging in the fluorescence-guided surgery [16, 17] and in photodynamic therapy [18, 19]; v) for pathogen detection [20]; vi) in gene expression studies to measure the levels of specific mRNAs or miRNAs [20,21]; vii) in high-throughput screening assays to evaluate the effectiveness and toxicity of potential drug candidates [21], viii) for the detection of biomolecules and their interactions [22-25], to name only a few. However, one of the greatest potentials of cyanine dyes lies in their application in DNA research [26-32]. The advantageous photophysical properties of cyanines, such as long-lasting photostability, high brightness, low cytotoxicity, and the sharp increase in emission upon their association with nucleic acids, gave impetus for their use in DNA bioanalytical assays [27,28], sizing, and purification of DNA fragments [29], DNA damage detection [30]; DNA sequencing [31], etc. Given the wide range of cyanine applications in DNA studies, a better understanding of their binding mode and intermolecular interactions governing the dye-DNA complexation would facilitate the synthesis of new molecular probes of the cyanine family with optimized properties and would lead to the development of new cyanine-based strategies for nucleic acid detection and characterization.

In recent decades computational methods have been recommended as particularly useful for providing insights into interactions between potential ligands and their macromolecular targets, thereby significantly decreasing traditional resource requirements encountered in experimental testing [32]. Molecular docking and molecular dynamics simulation have been successfully applied to investigate the potential mode of binding of fluorescent dyes to DNA [33,34]. Despite significant progress in understanding the main structural requirements for the ideal fluorescent marker in DNA research, the mechanisms of the dye interactions with the targeted biomolecules need to be clarified. To fill this gap, the aim of the present study was to investigate the interactions between cyanine dyes and DNA using the molecular docking technique. More specifically, the potential binding sites of one representative of monomethines (AK12-17), three trimethines

(AK3-1, AK3-3, AK3-5), three pentamethines (AK5-1, AK5-3, AK5-9) and one heptamethine dye (AK7-6) were characterized with the main purpose to determine the interactions governing the dye-DNA complexation and the structural requirements of cyanines responsible for their association. The structures of the dyes used in the study are presented in Figure 1.
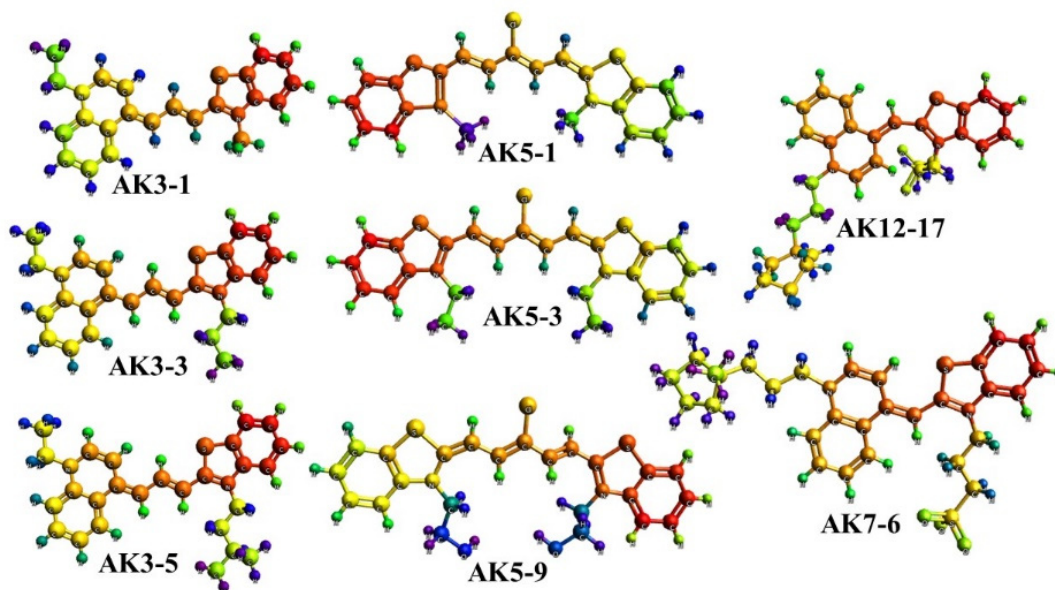
Figure 1. Structural formulas of the dyes under study (monomethines AK12-17, trimethines AK3-1, AK3-3, AK3-5, pentamethines AK5-1, AK5-3, AK5-9 and heptamethine AK7-6)

## MATERIALS AND METHODS
Molecular docking studies

To define the most energetically favorable binding sites for the examined dyes on the DNA, the molecular docking studies were performed using the AutoDock (version 4.2) incorporated in the PyRx software (version 0.8) [35]. For the prediction of the docking poses the AutoDock tool utilizes an empirical scoring function based on the binding free energy of the complex [35]. This approach enables the automated docking of flexible ligands to a rigid macromolecular receptor. The crystal structure of the B–DNA dodecamer d(CGCGAATTCGCG)2 (PDB ID: 1BNA) was downloaded from the protein data bank (http://www.rcsb.org./pdb) and was used for the docking studies. The dye structures were built in MarvinSketch (version 18.10.0) and optimized in Avogadro (version 1.1.0) [36,37]. The docking studies were performed in two steps. Initially, the "blind docking" modeling was used to determine the most energetically favorable binding sites for the cyanine dyes on the DNA molecule. The grid size was set as 60 Å, 72 Å, and 119 Å along X, Y, and Z axes, respectively. The grid spacing was 0.375 Å. Next, the lowest binding energy conformer was selected from 10 different conformations for each docking simulation, and was applied for further analysis using the "targeted docking". The grid size was set as 37 Å, 48 Å, and 50 Å along X, Y, and Z axes, respectively.

RESULTS AND DISCUSSION

The investigation of molecular bases of various diseases requires a deep understanding of the underlying biochemical and biophysical processes. To this end, it is crucial to characterize and visualize biological processes and biomolecular functions at the tissular, cellular, and macromolecular levels. In this regard, a number of bioassays and diagnostic methods (including PCR analysis, flow cytometry, fluorescence spectroscopy, microscopy, etc.) utilize organic dyes as molecular probes. Understanding the interactions between small organic chromophores and macromolecules has become essential for designing the advanced molecular probes capable of operating within living cells and in vivo. Consequently, there is a constantly growing interest in the acquisition and successful application of novel selective biomolecular sensors. Among a variety of fluorescent probes currently used for biomedical and biochemical studies, significant attention is devoted to cyanine dyes possessing advantageous properties upon their complexation with biomolecules, particularly nucleic acids, since DNA serves as the main target for drugs in the treatment of many pathologies. The representatives of the monomethine [38], trimethine [39], pentamethine [40], and heptamethine [41] families were experimentally tested and recommended as effective molecular probes for DNA detection and characterization. However, the mechanism of their interaction with DNA needs to be clarified. Therefore, we selected the most effective DNA probes with different lengths of polymethine bridges in their structure to uncover the main determinants governing the strong complexation of these dyes with DNA. More specifically, the molecular docking technique was used to investigate the interactions and the structural factors responsible for the DNA complexation of one representative of monomethines (AK12-17), three trimethines (AK3-1, AK3-3, AK3-5), three pentamethines (AK5-1, AK5-3, AK5-9) and one heptamethine dye (AK7-6).

Initially, the "blind docking" calculation was performed using the maximally accessible dimensional grid in the Autodock software, allowing it to cover the full length of DNA and explore all possible binding sites. Schematic representations of the energetically most favorable dye complexes with double-stranded DNA are given in Figure 2.

AK12-17   **AK3-1**   **AK3-3**   **AK3-5**

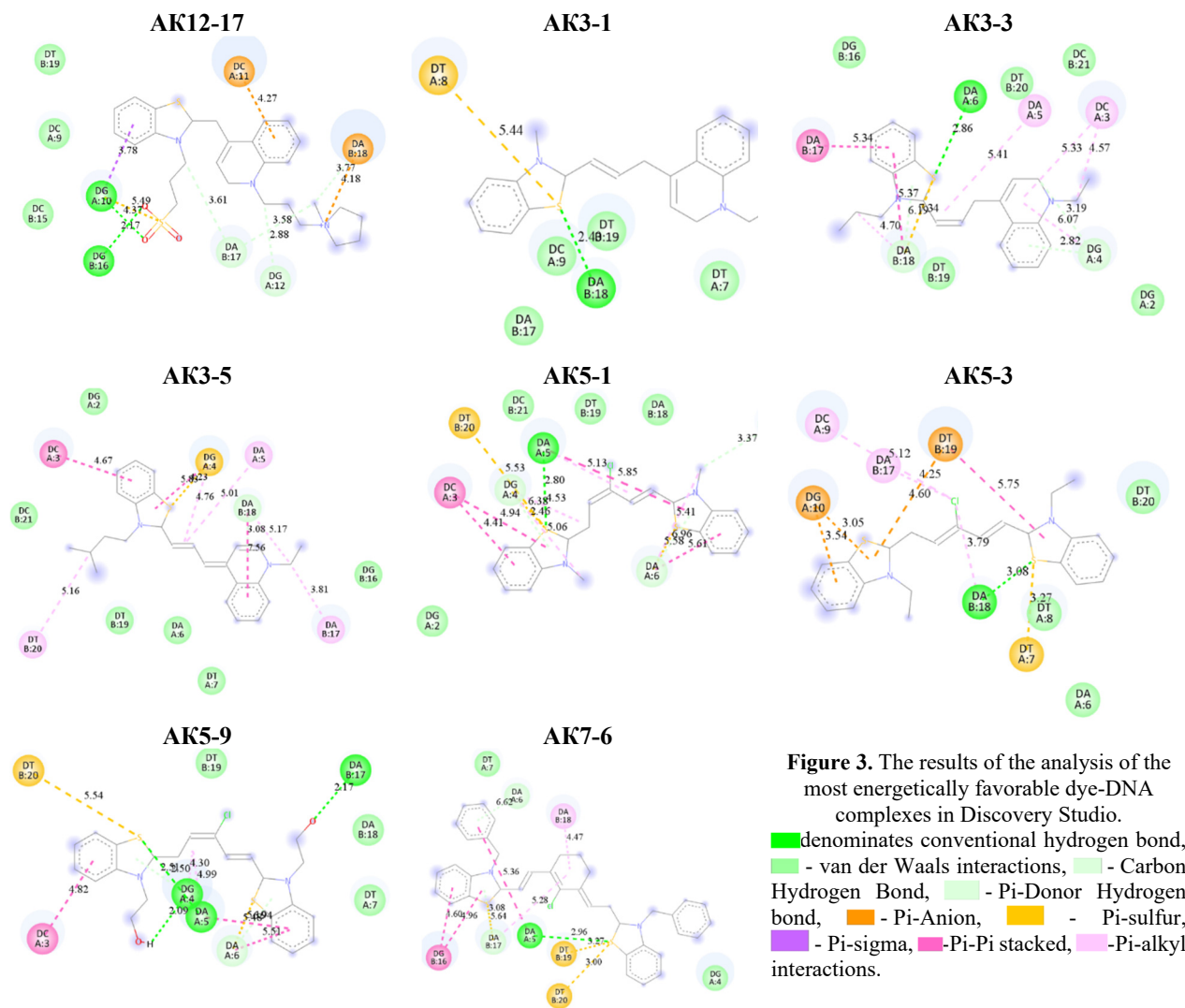**AK5-1**   **AK5-3**   **AK5-9**   **AK7-6**
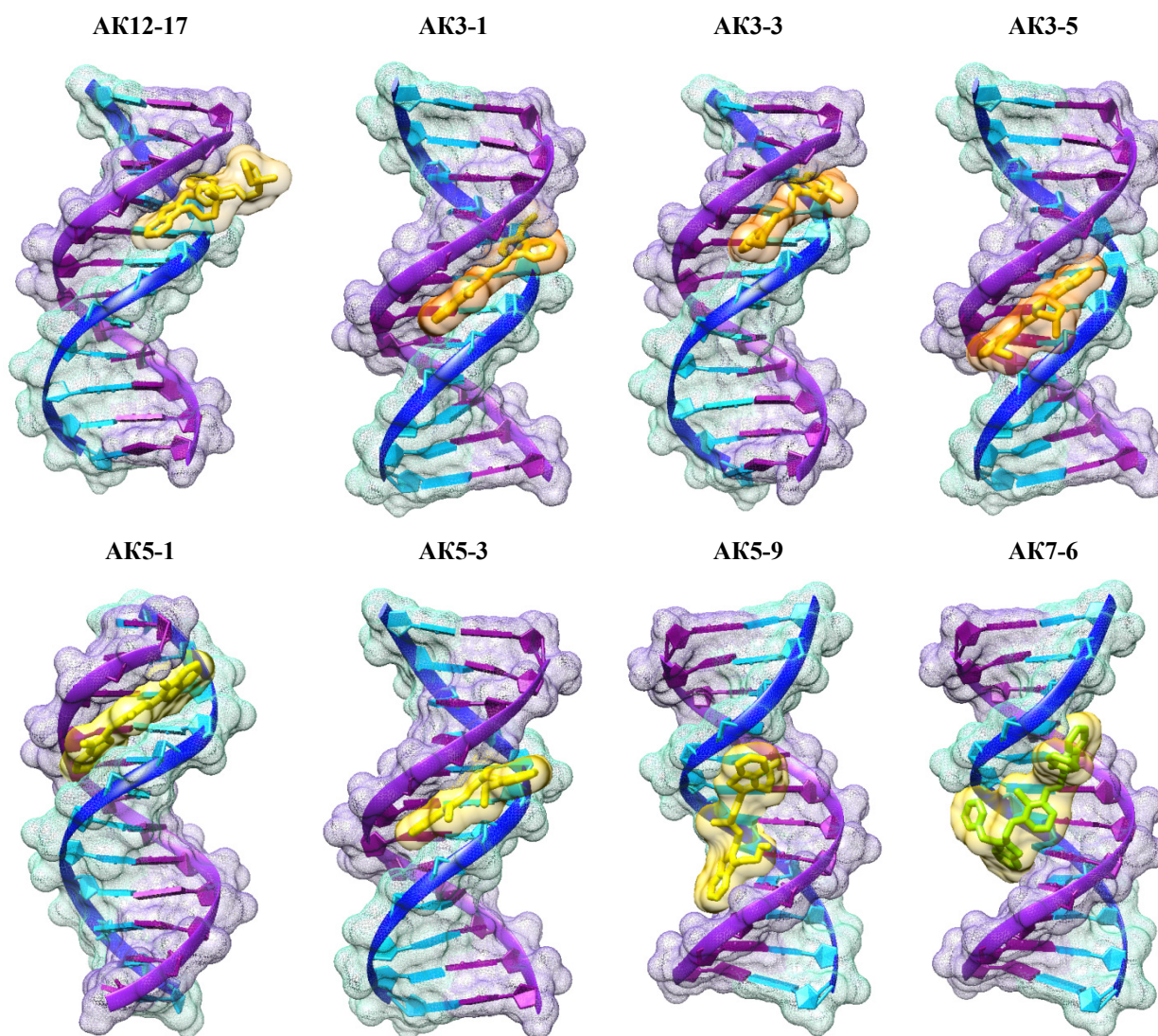
Figure 2. Schematic representation of the most energetically favorable dye-DNA complexes

Accumulating evidence suggests that cyanine dyes could interact with DNA through three primary binding modes: i) intercalation between adjacent base pairs, ii) groove binding, and electrostatic interaction of positively charged dye molecules with the phosphate backbone. The specific molecular mechanism by which cyanine dyes form complexes with nucleic acids relies heavily on the structural and physicochemical properties of the fluorophore (its planarity, conformational flexibility, etc.) as well as on the nucleic acid sequence and the dye-to-phosphate ratio. The molecular docking results indicate that both the minor and major DNA grooves may represent the sites for the dye binding. However, the minor groove is a more energetically favorable location for all cyanines under study except AK5-9 and AK7-6, for which the major grove binding was identified. It seems that significantly extended structure and less hydrophilicity of AK5-9 and AK7-6 make unfavorable their binding to the minor groove of the DNA [42]. The free energy binding score for the most energetically favorable docking poses of the selected compounds was found to rise in the order AK3-1 (-9,73 kcal/mol) → AK5-1 (-9,69 kcal/mol) → AK3-5 (-9,53 kcal/mol) → AK5-3 (-8,79 kcal/mol) → AK12-17 (-7,0 kcal/mol) → AK7-6 (-5,91 kcal/mol) → AK3-3 (-5,03 kcal/mol) → AK5-9 (-4,4 kcal/mol).

At the next step, the lowest binding energy conformers from the "blind docking" for each dye were selected and further used for the targeted docking with the grid spacing 0.375 A and the grid size 37 Å, 48 Å, and 50 Å along X, Y, and Z axes, respectively. Presented in Figure 3 and Table 1 are the results of the analysis of the most energetically favorable dye-DNA complexes obtained after the "targeted docking" in AutoDock after their characterization in the Discovery Studio. These data indicate that the dye association with DNA is predominantly driven by the hydrophobic interactions (Pi-Pi T-Shaped, Pi-alkyl) and van der Waals interactions for all dyes under study. More specifically, the dye binding to the minor groove was governed by the hydrophobic contacts and the van der Waals interactions preferably with the nucleotide residues C9A, G10A (except

AK3-1, AK3-5), A17B (except AK3-5, AK5-3) and A18B. The main nucleotide residues involved in the association of cyanine dyes AK5-9 and AK7-6 with DNA major groove were C16B, A17B, A18B, C3A, G4A, A5A and A6A. Likewise, the impact of the hydrophobic and van der Waals contacts was found to differ significantly between various dyes. Particularly, the docking results indicate that trimethine cyanine dyes form more van der Waals interactions in comparison with the monomethines and pentamethines. The lowest affinity of AK5-9 for the DNA major groove can be explained by the lower contribution (compared to those that observed for the cyanines associating with the minor groove) of van der Waals interactions. Indeed, the comparison of the intermolecular contacts formed between AK5-9 or AK3-1 and double-stranded DNA (the probe that has the highest affinity for DNA) indicates the higher value of van der Waals interactions with DNA for the latter one.

Figure 3. The results of the analysis of the most energetically favorable dye-DNA complexes in Discovery Studio.
■ denominates conventional hydrogen bond, ■ - van der Waals interactions, □ - Carbon Hydrogen Bond, ■ - Pi-Donor Hydrogen bond, ■ - Pi-Anion, ■ - Pi-sulfur, ■ - Pi-sigma, ■ -Pi-Pi stacked, ■ -Pi-alkyl interactions.

The obtained docking results indicate that the dye-DNA complexes are additionally stabilized by the hydrogen bonds (light green color in Figure 3). More specifically, the hydrogen bonds were formed predominantly with adenine (all dyes under study except AK3-5) and guanine (AK12-17) residues. Notably, all examined dyes (except AK3-1, AK3-5 and AK5-3) possess affinity to adenine and cytosine residues, whereas AK3-1, AK3-5 and AK5-3 also interact with thymine residues of the double-stranded DNA.

Table 1. The parameters of the dye-DNA complexation obtained by the "targeted docking" in AutoDock

Dye	Interactions and DNA residues.
AK12-17	Carbon hydrogen bond (DA, B:18, DA, B:17, DG, A:12), Pi-Alkyl (DC, A:11, DA, B:18), conventional hydrogen bond (DG, A:10, DG, B:16), van der Waals (DT, B:19; DC, A9; DC, B15)
AK3-1	Conventional hydrogen bond (DA, B:18), Pi-Sulfur *(DT, A:8),* van der Waals (DT, B19; DT, A7; DC, A9; DA, B17*)*
AK3-3	Pi-Alkyl (DA, B:18, DG, A:4, DC, A:3, DC, A:5, DC, A:6), Pi-Pi T-shaped (DA, B:18, DA, B:17), Pi-Donor Hydrogen Bond (DA, B:18, DG, A:4), conventional hydrogen bond (DA, A:6), van der Waals (DG, B16; DT, B20; DC, B21; DT, B19; DG, A2).

Dye	Interactions and DNA residues.
AK3-5	Pi-Alkyl (DA, B:18, DT, B:20, DA, B:17, DA, A:5, DG, A:4), Pi-Pi T-shaped (DG, A:4,), Pi-Sulfur (DG, A:4), van der Waals (DG, A2; DC, B21; DA, B18; DT, B19; DA, A6; DT, A7; DG, B16).
AK5-1	Pi-Donor Hydrogen Bond (DG, A:4, DA, A:6, DT, A:7), Pi-Alkyl (DG, A:4, DG, A:6), Pi-Pi T-shaped (DA, A:4, DA, A:6, DC, A:3), van der Waals (DC, B21; DT, B19; DA, B18; DG, A2)
AK5-3	Pi-Anion (DG, A:10, DT, B:19), Pi-Pi Stacked (DT, B:19), Pi- Alkyl (DC, A:9, DA, B:17, DA, B:18), Pi- Sulfur (DT, A:7), van der Waals (DT, B20; DT, A8; DA, A6), Conventional hydrogen bond (DA, B:18)
AK5-9	Conventional hydrogen bond (DA, B:17, DG, A:4), Pi- Donor Hydrogen bond (DG, A:4, DA, A:6), Pi- Alkyl (DG, A:4, DA, A:5), Pi-Pi T-shaped (DA, A:5, DA, A:6, DC, A:3), Pi-sulfur (DT, B:20), van der Waals (DT, B:19; DA, B18; DT, A7)
AK7-6	Pi- Alkyl (DA, B:17, DA, B:18), Pi-Pi T-shaped (DG, B:16), Pi-Sulfur (DA, B:17, DT, B:19, DT, B: 20), van der Waals (DT, A7; DG, A4)

CONCLUSIONS

To summarize, in the present study molecular docking technique was used to investigate the interactions between one representative of monomethines (AK12-17), three trimethines (AK3-1, AK3-3, AK3-5), three pentamethines (AK5-1, AK5-3, AK5-9) and one heptamethine (AK7-6) cyanine dyes and double-stranded DNA. It was found that all cyanines under study interact with DNA preferably via non-covalent groove binding mode with the lowest binding free energy ranging from −9.73 kcal/mol to -4,4 kcal/mol, depending on the dye structure. The obtained results indicate that the association of the dyes with double-stranded DNA is predominantly driven by the hydrophobic and van der Waals interactions. These findings are expected to be useful for further application of cyanine dyes in DNA studies and designing the advanced molecular probes.

ORCID IDs

Olga Zhytniakivska, https://orcid.org/0000-0002-2068-5823; Uliana Tarabara, https://orcid.org/0000-0002-7677-0779
Pylyp Kuznietsov, https://orcid.org/0000-0001-8477-1395; Kateryna Vus, https://orcid.org/0000-0003-4738-4016
Valeriya Trusova, https://orcid.org/0000-0002-7087-071X; Galyna Gorbenko, https://orcid.org/0000-0002-0954-5053

REFERENCES

[1] C. Shi, J.B. Wu, and D. Pan. J. Biomed. Opt. 21(5), 05901 (2022). https://doi.org/10.1117/1.JBO.21.5.050901
[2] O. Cavuslar, and H. Unal, RSC Advances, 5, 22380 (2015). https://doi.org/10.1039/C5RA00236B
[3] M. Bokan, G. Gellerman, and L. Patsenker. Dyes Pigm. 171, 107703 (2019). https://doi.org/10.1016/j.dyepig.2019.107703.
[4] M. Guo, P. Diao, Y.-J. Ren, F. Meng, H. Tian, and S.-M. Cai, Sol. Energy Mater. Sol. Cells, 88, 33 (2005). https://doi.org/10.1016/j.solmat.2004.10.003.
[5] C. Mu, F. Wu, R. Wang, Z. Huang, et al., Sens Actuators B. Chemical. 338, 29842, (2021). https://doi.org/10.1016/j.snb.2021.129842
[6] C. Schwechheimer, F. Rönicke, U. Schepers, H.-A. Wagenknecht, Chem Sci. 9, 6557 (2018). https://doi.org/10.1039/C8SC01574K
[7] C. Sun, W. Du, B. Wang, B. Dong, and B. Wang, BMC Chemistry, 14, 21 (2020). https://doi.org/10.1186/s13065-020-00677-3
[8] M.G. Honig, and R.I. Hume, Trends Neurosci. 12, 333 (1989). https://doi.org/10.1016/0166-2236(89)90040-4
[9] K.A. Mesce, K.A. Klukas, T.C. Brelje, Cell Tissue Res., 271, 381 (1993). https://doi.org/10.1007/BF02913721
[10] Z. Wang, X. Yue, Y. Wang, C. Qian, et al., Adv. Healthc. Mater. 3, 1326 (2014). https://doi.org/10.1002/adhm.201400088
[11] C. Zhang, X. Tan, T. Liu, D. Liu, L. Zhang, et al., Cell Transplantation, 20, 741 (2011). https://doi.org/10.3727/096368910X536536
[12] D. Oushiki, H. Kojima, T. Terai, M. Arita, et al., J. Am. Chem. Soc. 132 (8), 2795 (2010). https://doi.org/10.1021/ja910090v
[13] K. Yin, F. Yu, W. Zhang, L. Chen, Biosens. Bioelectron. 74, 156 (2015). https://doi.org/10.1016/j.bios.2015.06.039
[14] X. Lin, Y. Hu, D. Yang, B. Chen, Dyes Pigm., 174, 107956 (2020). https://doi.org/10.1016/j.dyepig.2019.107956
[15] P. Zou, S. Xu, S. P. Povoski, A. Wang, et al., Mol. Pharmaceutics, 6 (2), 428 (2009). https://doi.org/10.1021/mp9000052
[16] A. Haque, M.S.H. Faizi, J.A. Rather, and M.S. Khan, Bioorg. Med. Chem. 25(7), 2017 (2017). https://doi.org/10.1016/j.bmc.2917.02.061
[17] Y. Wu, and F. Zhang, View, 1(4), 20200068 (2020). https://doi.org/10.1002/VIW.20200068
[18] J. Atchison, S. Kamila, H. Nesbitt, K.A. Logan, D.N. Nicholas, et al., Chem. Commun. 53, 2009 (2017). https://doi.org/10.1039/C6CC09624G
[19] X. Yang, J. Bai, and Y. Qian, Spectrochim Acta A, 228, 117702 (2020). https://doi.org/10.1016/j.saa.2019.117702
[20] J. Duy, R.L. Smith, S.D. Collins, and L.B. Connell. AJPR, 92, 398 (2015). https://doi.org/10.1007/s12230-015-9450-z
[21] N. Kimura, T. Tamura, and M. Murakami, Biotechniques, 38, 797 (2005). https://doi.org/10.2144/05385MT02
[22] O. Zhytniakivska, A. Kurutos, U. Tarabara, K. Vus, V. Trusova, G. Gorbenko, N. Gadjev, and T. Deligeorgiev, J. Mol. Liq. 11, 113287 (2020), https://doi.org/10.1016/j.molliq.2020.113287

[23] K. Vus, M. Girych, V. Trusova, et al. J. Mol. Liq. **276**, 541 (2019). https://doi.org/10.1016/j.molliq.2018.11.149
[24] M. Levitus, and S. Ranjit, Quarterly Reviews of Biophysics, **44**(1), 123-151. (2011). https://doi.org/10.1017/S0033583510000247
[25] K. Vus, U, Tarabara, Z. Balklava, D. Nerukh, et al., J. Mol. Liq. **302**, 112569 (2020), https://doi.org/10.1016/j.molliq.2020.112569
[26] O. Zhytniakivska, M. Girych, V. Trusova, et al., Dyes Pigm., **180**, 108446 (2020). https://doi.org/10.1016/j.dyepig.2020.108446
[27] M. Bengtsson, H.J. Karlsson G. Westman, and M. Kubita, Nucleic Acids Res, **31**, e45 (2003). https://doi.org/10.1093/nar/gng045
[28] A. Kurutos, O. Ryzhova, V. Trusova, U. Tarabara, et al. Dyes Pigm. **130**, 122 (2016). https://doi.org/10.1016/j.dyepig.2016.03.021
[29] X. Yan, W. Grace, T. Yoshida, R. Habbersett, N. Velappan, et al., Anal. Chem. **71**(24), 5470 (1999). https://doi.org/10.1021/ac990780y
[30] B. Armitage, Top. Curr. Chem. **253**, 55 (2005). https://link.springer.com/chapter/10.1007/b100442
[31] T. Biver, A. Boggioni, F. Secco, E. Turriani, S. Venturini, and S. Yarmoluk, Arch Biochem Biophys., **465**, 90 (2007). https://doi.org/10.1016/j.abb.2007.04.034
[32] T. Maximova, R. Moffatt, B. Ma, R. Nussinov, and A. Shenu, PLOS Comp. Biol. **12**(4), e1004619 (2016). https://doi.org/10.1371/journal.pcbi.1004619
[33] Y. Guo, Q. Yue, and B. Gao, Int. J. Biol. Macromol. **49**, 55 (2011). https://doi.org/10.1016/j.ijbiomac.2011.03.009
[34] A. Mukherjee, B. Singh, J. Lumin. **190**, 319 (2017). https://doi.org/10.1016/j.jlumin.2017.05.068
[35] S. Dallakyan, A.J. Olson, Methods Mol. Biol. **1263**, 243-250 (2015). https://doi.org/10.1007/978-1-4939-2269-7_19
[36] P. Csizmadia, in: *Proceedings of ECSOC-3, the third international electronic conference on synthetic organic chemistry*, (1999), pp. 367-369. https://doi.org/10.3390/ECSOC-3-01775
[37] M.D. Hanwell, D.E. Curtis, D.C. Lonie, T. Vandermeersch, E. Zurek, and G.R. Hutchison, J. Cheminform. **4**, 17 (2012). https://doi.org/10.1186/1758-2946-4-17
[38] A. Kurutos, O. Ryzhova, V. Trusova, U. Tarabara, et al., Dyes Pigments. **130**, 122 (2016). https://doi.org/10.1016/j.dyepig.2016.03.021
[39] A. Kurutos, I. Crnolatac, I. Orehovec, I. Gadjev, I. Piantanida, and T. Deligeorgiev, J. Lumin. **174**, 70 (2016). https://doi.org/10.1016/j.jlumin.2016.01.035
[40] A. Kurutos, O. Ryzhova, V. Trusova, G. Gorbenko, et al., J. Fluoresc. **26**, 177 (2016). https://doi.org/10.1007/s10895-015-1700-4
[41] A. Kurutos, O. Ryzhova, U. Tarabara, V. Trusova, G. Gorbenko, et al., J. Photochem. Photobiol. A, **328**, 87 (2016). https://doi.org/10.1016/j.jphotochem.2016.05.019
[42] K. Vus, M. Girych, V. Trusova, et al. J. Mol. Liq. **276**, 541 (2019). https://doi.org/10.1016/j.molliq.2018.11.149

ДОСЛІДЖЕННЯ ВЗАЄМОДІЇ МІЖ ЦІАНІНОВИМИ БАРВНИКАМИ ТА ДНК МЕТОДОМ МОЛЕКУЛЯРНОГО ДОКІНГУ

О. Житняківська[a], У. Тарабара[a], П. Кузнєцов[b], К. Вус[a], В. Трусова[a], Г. Горбенко[a]

[a]*Кафедра медичної фізики та біомедичних нанотехнологій, Харківський національний університет імені В.Н. Каразіна, м. Свободи 4, Харків, 61022, Україна*
[b]*Кафедра фізики ядра та високих енергій імені О.І. Ахієзера, Харківський національний університет імені В.Н. Каразіна, м. Свободи 4, Харків, 61022, Україна*

Серед різноманітних флуоресцентних зондів, які в даний час використовуються для біомедичних і біохімічних досліджень, значну увагу привертають ціанінові барвники, що характеризуються суттєвими перевагами при комплексоутворенні з біомолекулами, зокрема нуклеїновими кислотами. Враховуючи широкий спектр застосувань ціанінів при дослідженні ДНК, краще розуміння способів їх зв'язування та міжмолекулярних взаємодій, що регулюють утворення комплексу барвник-ДНК, сприяло б синтезу нових молекулярних зондів сімейства ціанінів з оптимізованими властивостями та призвело б до розробки нових стратегій на основі ціанінів для виявлення та характеризації нуклеїнових кислот. У даній роботі за допомогою молекулярного докінгу були досліджені механізми взаємодії одного представника монометинів (АК12-17), трьох триметинів (АК3-1, АК3-3, АК3-5), трьох пентаметинів (АК5-1, АК5-3, АК5-9) та одного гептаметинового (АК7-6) ціанінових барвників з додекамером B–DNA d(CGCGAATTCGCG)2 (PDB ID: 1BNA). Результати молекулярного докінгу вказують на те, що: i) усі досліджувані ціаніни (за винятком АК5-9 і АК7-6) утворюють найбільш стабільні комплекси із малою борозенкою дволанцюгової ДНК; ii) ціаніни АК5-9 і АК7-6 взаємодіють з великою борозенкою ДНК внаслідок їх більш розширеної структури і меншої гідрофільності у порівнянні з іншими барвниками; iii) зв'язування ціанінів регулюється гідрофобними та ван-дер-Ваальсовими взаємодіями із нуклеотидними залишками C9A, G10A (за винятком АК3-1, АК3-5), A17B (за винятком АК3-5, АК5-3) та A18B у малій борозенці ДНК та залишками великої борозенки C16B, A17B, A18B, C3A, G4A, A5A, A6A (АК5-9 та АК7-6); iv) усі досліджувані барвники (за винятком АК3-1, АК3-5 та АК5-39 мають спорідненість до залишків аденіну та цитозину, тоді як АК3-1, АК3-5 та АК5-3 також взаємодіють із залишками тиміну дволанцюгової ДНК.

Ключові слова: *ціанінові барвники; ДНК; взаємодії барвник-ДНК; молекулярний докінг*

IMPROVEMENT STRUCTURAL AND DIELECTRIC PROPERTIES OF PS/SiC/Sb₂O₃ NANOSTRUCTURES FOR NANOELECTRONICS DEVICES†

Nawras Karim Al-Sharifi§, ⓘMajeed Ali Habeeb*

University of Babylon, College of Education for Pure Sciences, Department of Physics, Iraq
§e-mail: Nkareem769@gmail.com
*Corresponding Author e-amil: pure.majeed.ali@uobabylon.edu.iq
Received March 29, 20223; revised May 14, 2023; accepted May 15, 2023

In the current study, the PS/SiC/Sb₂O₃ nanocomposites have been prepared by using solution casting method with different concentrations of SiC/Sb₂O₃ nanoparticles (0,2,4,6,8) % wt. The structural and dielectric properties of (PS/SiC/Sb₂O₃) nanocomposites have been investigated. Full emission scanning electron microscope (FE-SEM) used to study the surface of nanocomposite. FE-SEM confirmed that good distribution of SiC and Sb₂O₃ NPs into the polymer matrix. Optical microscope (OM) was tested the morphological of nanocomposite that proven that the polystyrene is exceptionally miscible, as seen by its finer form and smooth, homogeneous surface, while the additive concentration SiC and Sb₂O₃ NPs are well distributed on the surface of the polymer nanocomposite films. Fourier transformation spectroscopy (FTIR) was examining the structural of nanocomposite and give the information of the vibration of molecules. From FTIR, the additive SiC and Sb₂O₃ NPs caused interaction with polymer matrix. FTIR proven that there is physical interactions between polystyrene and SiC and Sb₂O₃ NPs. According to AC electrical properties, dielectric constant and dielectric loss of the NCs reduce with increasing the frequency of the applied electric field and increased with increasing concentration of SiC/Sb₂O₃ nanoparticles, while AC electrical conductivity increased with increasing frequency and concentration of SiC/Sb₂O₃ NPs. The results of structural and electrical characteristics show that the PS/SiC/Sb₂O₃ nanocomposites may be used for various electronics devices.

Keywords: *Nanocomposites; Polystyrene; SiC and Sb₂O₃ Nanoparticles; AC electrical properties*
PACS: 77.22.-d, 77.84.Lf, 77.22Ch

1. INTRODUCTION

The nanocomposite material, which is made from non-metallic, metallic, and polymeric materials using a particular procedure, has the unique advantage of keeping key qualities that can be employed to resolve flaws and exhibit some novel properties. This variety of substance is a multistage cross of matrices and reinforcing substance. In contrast to the polymeric matrix, which is a phase separation made up of metallic, inorganic non-metallic, and polymer matrix materials, the reinforcement is a continuous phase that typically comprises of fibrous materials like glass fiber, organic fiber, and so on [1,2]. In comparison to the different phases, nanocomposite exhibits improved thermal, mechanical, electrical, and optical properties. It is a multiphase material that consists of the matrix phase and the contributing to better [2]. Nanocomposites have a wide range of possible uses because of how adaptable they are. The immediate result of the nanometer-sized particles put into nanocomposites as contrasted to typical scaled composites is their smaller size. Additionally, the connection of the nanoparticle with the polymer network sections as well as the role of the interfacial region between the nanoparticles and the polymer matrices are significant. The volume percentage of this contact area is high due to the high surface - to - volume of the nanoparticles [3,4]. Due to its expected remarkable thermal, optical, electrical, and antibacterial capabilities, polymer-based nanocomposites have received a lot of attention. Inorganic materials are favored because of their great thermal stability, good electrical characteristics, and high refractive index. However, research has indicated that inorganic nanoparticles cannot effectively serve a variety of industrial device applications due to a number of limitations [5, 6]. One of the extensively utilized plastics is polystyrene, which is produced at a rate of several million tons annually. Although polystyrene could be clear by nature, it can also be colored with colorants. Among the many uses for polystyrene are the following: It is employed in the manufacture of toys, refrigerator, and furniture, among other things. Additionally, polystyrene is used in the manufacture of radio knobs, clear plastic drinking cups, and a majority of the molded components found inside automobiles. Toys, hair dryers, televisions, and kitchen equipment all use polystyrene. It serves as a cushioning agent and is used in packing. About 70% of polystyrene is used in building and construction, 25% is used in packaging and 5% is utilized for other purposes [7,8]. High stability and colorless or white crystals are how polystyrene is described. It has a solubility of 730 g/L in water, making it easily soluble. PS dissolves in acidic water. Its symmetric structure, O-O bond distance of 1.497, and bond energy of 140 kJ/mol are all positive [9,10]. A non-oxide substance is silicon carbide (SiC). Semiconductor ceramic material has a variety of exceptional qualities, including great oxidation resistance, high thermal conductivity, reaction passivity for acids and melts, and thermal stability Microwave dielectrics and power energy storage materials extensively utilize this material due to its stress resilience and extraordinarily high toughness. Sic nanoparticles, however, are incredibly easy to make. impact the physicochemical characteristics of the composites as they aggregate. As a result, excellent results are achievable. Sic nanoparticles that have been surface modified increase composite performance [11,12]. A semiconducting substance with outstanding chemical stability in flame retardance and strong photocatalytic performance is antimony trioxide (Sb₂O₃). The creation of Sb₂O₃ films and the study of their new properties have received most of the attention thus far.

Contrarily, it is anticipated that low-dimensional Sb_2O_3 nanoparticles, nanowires, nanotubes, and nanoribbons will each have distinctive features. Because many of the features of material at the nanoscale are known to be dependent on their form, carefully orchestrating the synthesis of desirable nanomaterial morphologies is essential. Despite significant research, it is still challenging for researchers to effectively and controllably synthesis a predefined material shape [13,14].

2. EXPERIMENTAL PART

$(PS/SiC/Sb_2O_3)$ nanocomposites were created by dissolving 1gm of polystyrene (PS) in 30 ml of chloroform and mixing the polymers for 30 minutes by using magnetic stirrer at room temperature to achieve a more homogeneous solution, silicon carbide (SiC) and tertiary antimony oxide (Sb_2O_3) nanoparticales were added to the polystyrene in various concentrations (0, 2, 4, 6 and 8) wt. %. The structural characteristics of $(PS/SiC/Sb_2O_3)$ nanocomposites examined by (FE-SEM) analyses were performed using a Hitachi SU6600 variable pressure, optical microscope (OM) provided by Olympus (Top View, type Nikon-73346) and Fourier Transformation Infrared Spectroscopy (FTIR) (Bruker company type vertex-70, German origin) with range wavenumber (500-4000) cm^{-1}. The dielectric characteristics were studied at range (f=100 Hz to 5×10^6 Hz) by LCR meter (HIOKI 3532-50 LCR HI TESTER).

The dielectric constant (έ) is given by [15]:

$$\acute{\varepsilon} = \frac{c_p}{c_o}, \tag{1}$$

Where, Cp is capacitance and C_o is a vacuum capacitance

Dielectric loss (ε'') is calculated by [16]

$$\varepsilon'' = \acute{\varepsilon}D, \tag{2}$$

Where, D is displacement
The A.C electrical conductivity is determind by [17]

$$\sigma_{AC} = \omega\acute{\varepsilon}\,\varepsilon_o \tag{3}$$

Where, w is the angular frequency.

3. RESULTS AND DISCUSSION

Full emission scanning electron microscope (FE-SEM) is used to study the morphological of $(PS/SiC/Sb_2O_3)$ nanocomposites. Fig. (1) illustration of (FE-SEM) images of pure polystyrene and $(PS/SiC/Sb_2O_3)$ nanocomposites with various concentration 2, 4, 6 and 8 wt.% of SiC and Sb_2O_3 NPs with a magnification 50 KX and scale 200 nm. In the image (A), the surface of polymer is homogenous this indicates a good method for prepared film. In image (B, C, and D) which explain the increasing concentration of SiC and Sb_2O_3 NPs, the distribution uniform and homogenous inside the polymer matrix while in image E, the grain aggregates as nonuniform clusters, which may be attributed to the nature of the SiC and Sb_2O_3 NPs [18,19]. In nanocomposites, the number of groups or fragments that are spread out on the upper surface rises as the concentration of SiC/Sb_2O_3 nanoparticles.
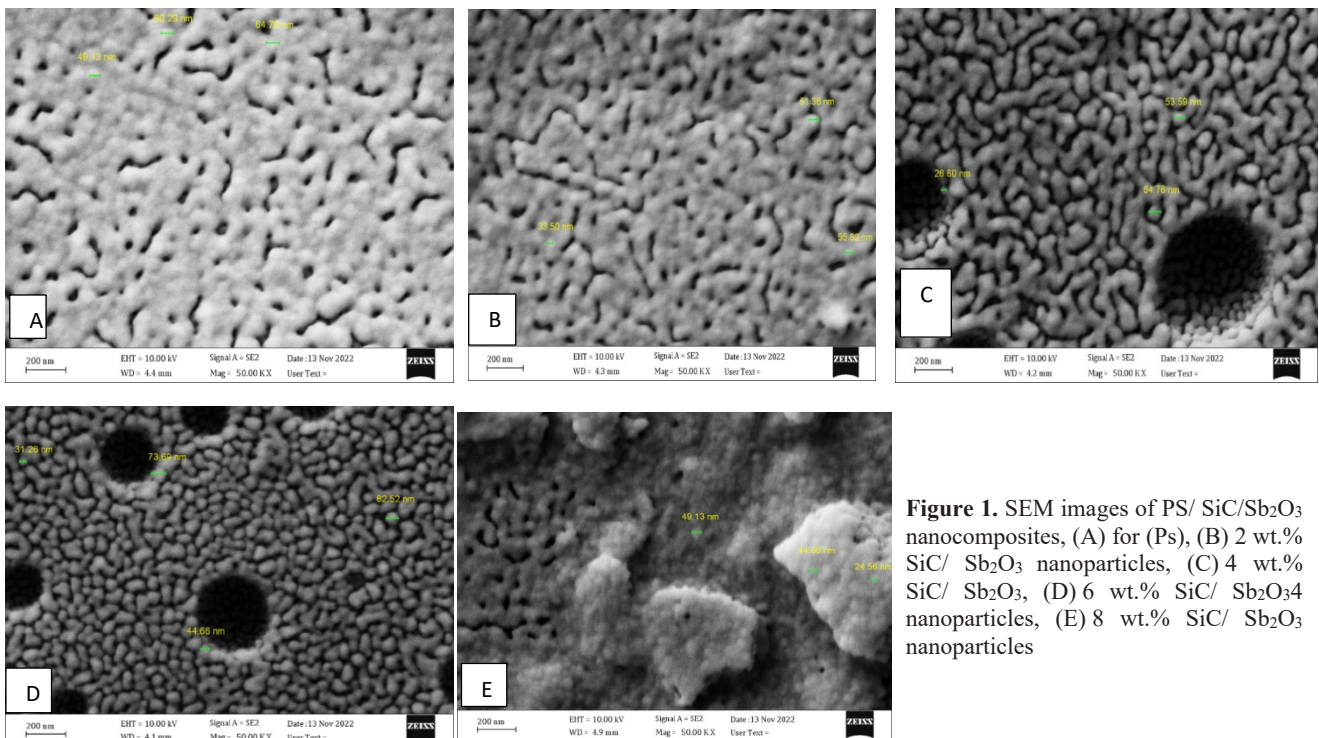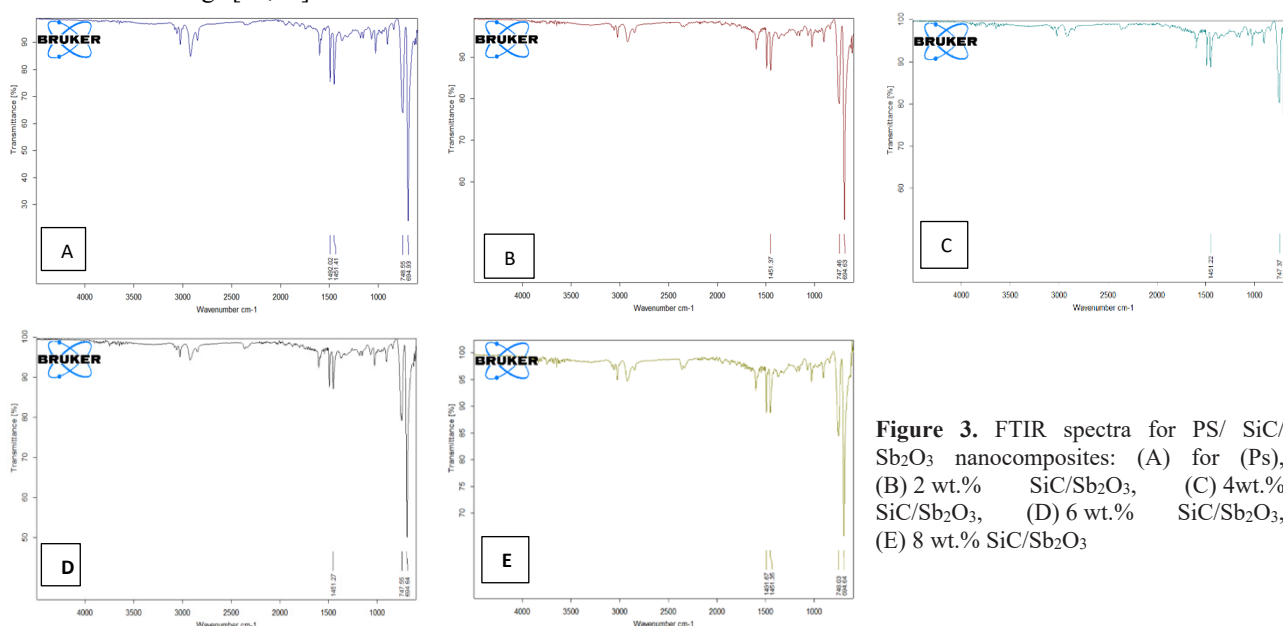

Figure 1. SEM images of PS/ SiC/Sb_2O_3 nanocomposites, (A) for (Ps), (B) 2 wt.% SiC/ Sb_2O_3 nanoparticles, (C) 4 wt.% SiC/ Sb_2O_3, (D) 6 wt.% SiC/ Sb_2O_3 4 nanoparticles, (E) 8 wt.% SiC/ Sb_2O_3 nanoparticles

Fig. (2) shows optical microscope images of PS/SiC/Sb$_2$O$_3$ nanocomposites with and without different concentrations of SiC and Sb$_2$O$_3$ NPs at magnification power (10X). In portrait A, polystyrene (Ps) is exceptionally miscible, as seen by its finer form and smooth, homogeneous surface, while in portraits B, C, D and E, it can be seen, that SiC and Sb$_2$O$_3$ NPs are well distributed on the surface of the polymer. From these images, the SiC and Sb$_2$O$_3$ NPs formed a clusters in the form of chains that extended along the surface of the films, attributed to the novel property in SiC and Sb$_2$O$_3$ NPs [20,21], other than charge transport within polymer matrices, which also was enhanced by raising the percentages of SiC and Sb$_2$O$_3$ NPs.
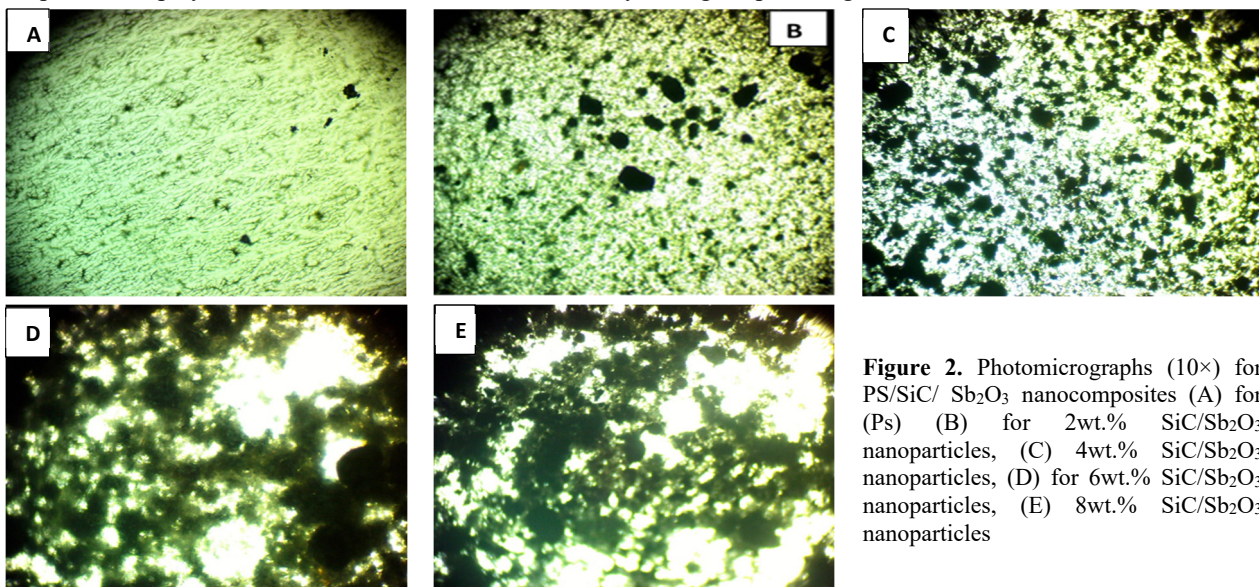
Figure 2. Photomicrographs (10×) for PS/SiC/ Sb$_2$O$_3$ nanocomposites (A) for (Ps) (B) for 2wt.% SiC/Sb$_2$O$_3$ nanoparticles, (C) 4wt.% SiC/Sb$_2$O$_3$ nanoparticles, (D) for 6wt.% SiC/Sb$_2$O$_3$ nanoparticles, (E) 8wt.% SiC/Sb$_2$O$_3$ nanoparticles

FTIR spectra of (Ps/SiC/Sb$_2$O$_3$) nanocomposites in the range (500-4000) cm^{-1} are shown in Figure (3). The absorption band of pure Ps in image (A) at 2980 cm^{-1} corresponding to the C-H stretching vibrations in the main chain and in aromatic rings [22,23].


Figure 3. FTIR spectra for PS/ SiC/ Sb$_2$O$_3$ nanocomposites: (A) for (Ps), (B) 2 wt.% SiC/Sb$_2$O$_3$, (C) 4wt.% SiC/Sb$_2$O$_3$, (D) 6 wt.% SiC/Sb$_2$O$_3$, (E) 8 wt.% SiC/Sb$_2$O$_3$

The bands (1492.02 cm^{-1} and 1451.41 cm^{-1}) attributed to the C-H stretching vibrations [24,25] while the bands (748.55 cm^{-1} 694.93 cm^{-1} corresponding to the C-H out phase bend [26]. The spectral of polystyrene with additive different concentration of SiC and Sb$_2$O$_3$ NPs in images B, C, D and E respectively. In image B where the additive 2 wt.% from SiC and Sb$_2$O$_3$ NPs caused shift to low wavenumber in some bands and intensities at (1451.37, 747.45, 694.43) cm^{-1} but bands 1492.02 cm^{-1} and 2980 cm^{-1} there is not affected on this band. The image C which additive concentration of 4 wt.% from SiC and Sb$_2$O$_3$ NPs, the bands (1451.22, 747.37 cm^{-1}, 694.68) cm^{-1} was shifted to low wavenumber and the band 1492.02 cm^{-1} and 2980 cm^1 there is not influenced. The bands (1451.27, 747.55 cm^{-1}, 694.64) cm^{-1} in image D where additive 6wt.% from NPs, caused shift to low wavenumber while in the other hand, the band 1492.02 cm^{-1} and 2980 cm^{-1} there is not change. From the additive concentration 8wt.% from NPs in image E, the band (1491.67, 694.64) cm^{-1} caused change to low wave number, while the band 748.03 cm^{-1} caused change to high wave number but the band 1451.37 cm^{-1} and 2980 cm^{-1} there is not affected. The FTIR proven that there are no chemical interactions between polystyrene and SiC and Sb$_2$O$_3$ NPs.

Equation (1) was used to calculate the dielectric constant (έ) of PS/SiC/Sb$_2$O$_3$ nanocomposites. The variation of the dielectric constant with frequency is shown in Fig. 4. As can be observed, the dielectric constant values drop with increasing applied frequency, which leads to a reduction in the space charge to total polarization ratio. At low frequencies, space charge polarization is the most significant type of polarization, and as frequency rises, its significance decreases. As the electric field frequency rises, different kinds of polarizations take place, and the dielectric constant values for all samples of Ps/SiC/Sb$_2$O$_3$ drop. Ionic polarization responds to variations in field frequency in a slightly different manner than electronic polarization because an ion has a larger mass than an electron [27-29].

The dielectric constant for (PS/SiC/Sb$_2$O$_3$) NCs at 100Hz variation with concentrations as shown in Fig. 5. As the percentage of SiC and Sb$_2$O$_3$ NPs rise, the dielectric constant of nanocomposites also rises. Interfacial polarization, a process that occurs when two surfaces within NCs are separated by an alternating electric field and causes a rise in charge carriers, could be used to explain this activity [30-33].
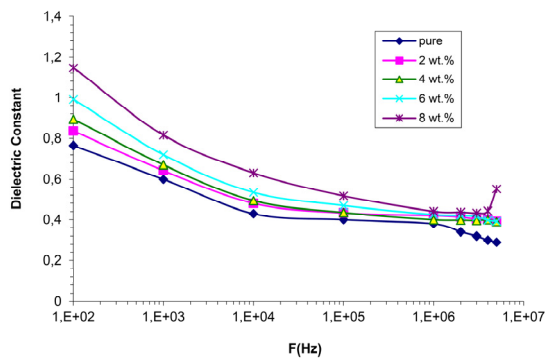

Figure 4. Dielectric constant of PS/SiC/Sb$_2$O$_3$ nanocomposites varies with frequency
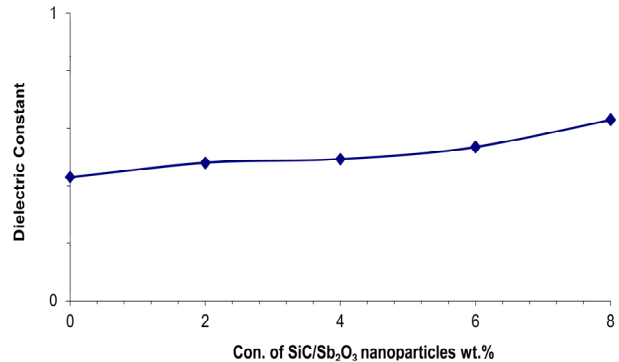
Figure 5. Difference of dielectric constant with concentration of (PS/SiC/Sb$_2$O$_3$)

Equation (2) was used to calculate the dielectric loss (ε″) of nanocomposites. Fig. 6 shows the dielectric loss of PS/SiC/Sb$_2$O$_3$ nanocomposites with frequency. From this figure it can be seen the dielectric loss is high at lower applied frequencies, but decreases with increasing applied frequencies. This can be attributed to the actuality that as the frequency rises, the space charge polarization contribution decreases [34-37].

The relationship between SiC and Sb$_2$O$_3$ NPs concentration and dielectric loss (ε″) is shown in Fig. 7. As the concentration of NPs rises, the dielectric loss of PS/SiC/Sb$_2$O$_3$ NCs also rises, which is related to an increase in charge carriers [38,39].
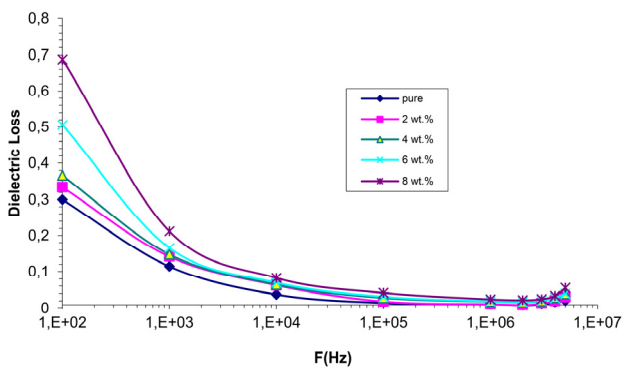
Figure 6. Dielectric loss variation with frequency for (PS/SiC/Sb$_2$O$_3$) nanocomposites
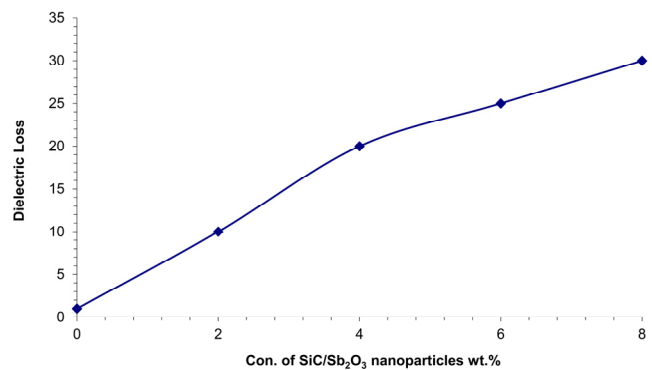
Fig. (7) Difference of dielectric loss for PS/ Sic/Sb$_2$O$_3$ NCs with different concentrations of Sic/Sb$_2$O$_3$ NPs

The A.C electrical conductivity was calculated from equation (3). Fig. (8) Shows the variation in electrical conductivity of PS/SiC/Sb$_2$O$_3$ NCs with frequency. This figure demonstrates that electrical conductivity significantly rises with frequency, which is caused by space charge polarization, which happens at low frequencies, and the hopping process, which causes charge carriers to move. The increase in electrical conductivity is only moderate at high frequencies due to electronic polarization and charge carriers that move through hopping [40, 41].

Table 1. Values of the dielectric constant, dielectric loss and AC electrical conductivity at 100Hz of (PS/SiC/Sb$_2$O$_3$) nanocomposites

Con.(wt.)%	Dielectric constant	Dielectric loss	AC electrical conductivity(S/cm)
0	0.43	1	2.08E-10
2	0.479	10	3.47E-10
4	0.492	20	3.56E-10
6	0.534	25	3.86E-10
8	0.63	30	4.56E-10

Fig. 9. shows influence of SiC and Sb$_2$O$_3$ NPs on the A.C electrical conductivity of PS/SiC/Sb$_2$O$_3$ NCs at 100 Hz. The A.C. electrical conductivity of NCs rises as SiC and Sb$_2$O$_3$ NPs concentration rises. Due to the composition of the dopant nanoparticles, there are more charge carriers, which reduces the NCs resistance and boosts electr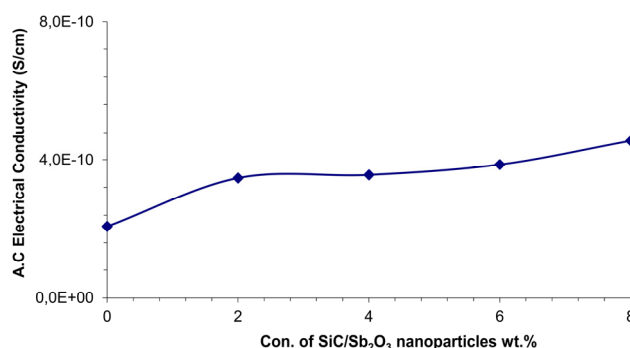ical conductivity [42,43]. Table (1) shows the values of dielectric constant, dielectric loss and A.C electrical conductivity at 100 Hz.
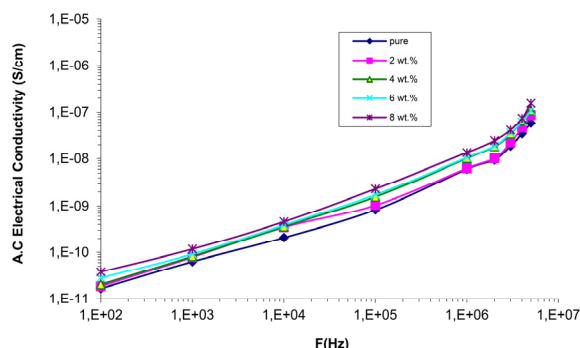
Figure 8. Difference of A.C electrical conductivity with frequency for PS/SiC/Sb$_2$O$_3$ NCs

Figure 9. Difference of A.C electrical conductivity with (Sic/Sb$_2$O$_3$) NPs for (PS/SiC/Sb$_2$O$_3$) NCs

4. CONCLUSSION

In this work, the solution casting technique was used to prepare (PS/SiC/Sb$_2$O$_3$) NCs films. The surface morphology of the (PS/SiC/Sb$_2$O$_3$) nanocomposites films is shown by scanning electron microscopy (FE-SEM) confirmed that the good distribution of the SiC and Sb$_2$O$_3$ NPs into the polymer polystyrene matrix. The optical microscope (OM) proven the morphological of nanocomposite that confirmed that the polystyrene is exceptionally miscible, as seen by its finer form and smooth, homogeneous surface, while the additive concentration SiC and Sb$_2$O$_3$ NPs are well distributed on the surface of the polymer blend films. The Fourier transformation spectroscopy (FTIR) confirmed the additive SiC and Sb$_2$O$_3$ NPs caused physical interaction with polymer matrix. The dielectric constant and dielectric loss of PS/SiC/Sb$_2$O$_3$ decreased with increasing of frequency and increased with increasing concentration of SiC/Sb$_2$O$_3$ nanoparticles. The A.C. electrical conductivity of Ps/SiC/Sb$_2$O$_3$ NCs increase with increasing of frequency and concentration of SiC/Sb$_2$O$_3$ nanoparticles. These characteristics can be applied to films in a variety of electrical applications.

ORCID IDs

Majeed Ali Habeeb, https://orcid.org/0000-0001-5064-2835

REFERENCES

[1] E. Omanović-Mikličanin, A. Badnjević, A. Kazlagić, and M. Hajlovac, "Nanocomposites: a brief review," Health Technol. (Berl)., **10**(1), 51-59 (2020). https://doi.org/10.1007/s12553-019-00380-x

[2] M.A. Habeeb, "Effect of rate of deposition on the optical parameters of GaAs films," European Journal of Scientific Research, **57** (3), 478-484 (2011)

[3] G. Sahu, M. Das, M. Yadav, B.P. Sahoo, and J. Tripathy, "Dielectric relaxation behavior of silver nanoparticles and graphene oxide embedded poly(vinyl alcohol) nanocomposite film: An effect of ionic liquid and temperature," Polymers (Basel), **12**(2), 1-16 (2020). https://doi.org/10.3390/polym12020374

[4] M.A. Habeeb, and W.K. Kadhim, "Study the optical properties of (PVA-PVAC-Ti) nanocomposites," Journal of Engineering and Applied Sciences, **9** (4), 109-113(2014). https://doi.org/10.36478/jeasci.2014.109.113

[5] A.H. Hadi, M.A. Habeeb, "Effect of CdS nanoparticles on the optical properties of (PVA-PVP) blends," Journal of Mechanical Engineering Research an Developments, **44** (3), 265-274 (2021). https//jmerd.net/03-2021-265-274/

[6] P.H.C. Camargo, K.G. Satyanarayana, and F. Wypych, "Nanocomposites: Synthesis, structure, properties and new application opportunities," Mater. Res. **12**(1), 1-39 (2009). https://doi.org/10.1590/S1516-14392009000100002

[7] S.M. Mahdi, M.A. Habeeb, "Synthesis and augmented optical characteristics of PEO–PVA–SrTiO3–NiO hybrid nanocomposites for optoelectronics and antibacterial applications," Optical and Quantum Electronics, **54** (12) , 854 (2022). https://doi.org/10.1007/s11082-022-04267-6

[8] A.A. Bani-Salameh, A.A. Ahmad, A.M. Alsaad, I.A. Qattan, and I.A. Aljarrah, "Synthesis, optical, chemical and thermal characterizations of PMMA-PS/CeO2 nanoparticles thin film," Polymers (Basel). **13**(7), (2021). https://doi.org/10.3390/polym13071158

[9] S.M. Mahdi, M.A. Habeeb, "Low-cost piezoelectric sensors and gamma ray attenuation fabricated from novel polymeric nanocomposites," AIMS Materials Science, **10** (2), 288–300 (2023). https://doi.org/10.3934/matersci.2023015

[10] M.A. Habeeb, and W.H. Rahdi, "Titanium carbide nanoparticles filled PVA‑PAAm nanocomposites, structural and electrical characteristicsfor application in energy storage," Optical and Quantum Electronics, **55** (4) , 334 (2023). https://doi.org/10.1007/s11082-023-04639-6

[11] S.K. Kumar, and R. Krishnamoorti, "Nanocomposites: Structure, phase behavior, and properties," Annu. Rev. Chem. Biomol. Eng. **1**, 37-58 (2010). https://doi.org/10.1146/annurev-chembioeng-073009-100856

[12] M.A. Habeeb, Z.S. Jaber, "Enhancement of Structural and Optical Properties of CMC/PAA Blend by Addition of Zirconium Carbide Nanoparticles for Optics and Photonics Applications," East Eur. J. Physics, **4**, 176-182 (2022). https://doi.org/10.26565/2312-4334-2022-4-18

[13] A.H. Hadi, M.A. Habeeb, "The dielectric properties of (PVA-PVP-CdS) nanocomposites for gamma shielding applications," Journal of Physics: Conference Series,1973(1),012063 (2021). https://doi.org/10.1088/1742-6596/1973/1/012063

[14] M.S. Aziz, and H.M. El-Mallah, "AC Conductivity and Dielectric Properties of Polycarbonate Sheet," International Journal of Polymeric Materials, **54**(12), 1157-1168 (2005).

[15] S.M. Mahdi, M.A. Habeeb, "Fabrication and Tailored Structural and Dielectric characteristics of (SrTiO3/NiO) Nanostructure Doped (PEO/PVA) polymeric Blend for Electronics Fields," Physics and Chemistry of Solid State, **23** (4), 785-792 (2022). https://doi.org/0.15330/pcss.23.4.785-792

[16] J. Wang, and S. Wang, "Activation of persulfate (PS) and peroxymonosulfate (PMS) and application for the degradation of emerging contaminants," Chem. Eng. J. **334**, 1502-1517 (2018), https://doi.org/10.1016/j.cej.2017.11.059

[17] M.H. Dwech, M.A. Habeeb, and A.H. Mohammed, "Fabrication and Evaluation of Optical Characterstic of (PVA-MnO2–ZrO2) Nanocomposites for Nanodevices in Optics and Photonics," Ukr. J. Phys. **67** (10), 757-762 (2022). https://doi.org/10.15407/ujpe67.10.757

[18] S.M. Mahdi, and M.A. Habeeb, "Tailoring the structural and optical features of (PEO–PVA)/(SrTiO3–CoO) polymeric nanocomposites for optical and biological applications," Polymer Bulletin, (2023). https://doi.org/10.1007/s00289-023-04676-x

[19] J.P. Cao, J. Zhao, X. Zhao, G.H. Hu, and Z.M. Dang, "Preparation and characterization of surface modified silicon carbide/polystyrene nanocomposites," J. Appl. Polym. Sci, 130(1), 638-644 (2013). https://doi.org/10.1002/app.39186

[20] A.A. Mohammed, and M.A. Habeeb, "Modification and Development of the Structural, Optical and Antibacterial Characteristics of PMMA/Si3N4/TaC Nanostructures," Silicon, (2023). https://doi.org/10.1007/s12633-023-02426-2

[21] S.M. Mahdi, M.A. Habeeb, "Evaluation of the influence of SrTiO3 and CoO nanofillers on the structural and electrical polymer blend characteristics for electronic devices," Digest Journal of Nanomaterials and Biostructures, **17**(3), 941-948 (2022). https://doi.org/10.15251/DJNB.2022.173.941

[22] C. Ye, G. Wang, M. Kong, and L. Zhang, "Controlled synthesis of Sb_2O_3 nanoparticles, nanowires, and nanoribbons," J. Nanomater. **2006**, 1-5 (2006). https://doi.org/10.1155/JNM/2006/95670

[23] N.K. Al‑Sharifi, and M.A. Habeeb, "Synthesis and Exploring Structural and Optical Properties of Ternary PS/SiC/Sb2O3 Nanocomposites for Optoelectronic and Antimicrobial Applications," Silicon, (2023). https://doi.org/10.1007/s12633-023-02418-2

[24] M.A. Habeeb, "Dielectric and optical properties of (PVAc-PEG-Ber) biocomposites," Journal of Engineering and Applied Sciences, **9** (4), 102-108 (2014). https://doi.org/10.36478/jeasci.2014.102.108

[25] M.A. Habeeb, A. Hashim, and N. Hayder, "Structural and optical properties of novel (PS-Cr2O3/ZnCoFe2O4) nanocomposites for UV and microwave shielding," Egyptian Journal of Chemistry, **63**, 697-708 (2020). https://dx.doi.org/10.21608/ejchem.2019.12439.1774

[26] A. De Girolamo Del Mauro, S. Galvagno, G. Nenna, R. Miscioscia, C. Minarini, and S. Portofino, "End-of-Waste SiC-Based Flexible Substrates with Tunable Electrical Properties for Electronic Applications," Langmuir, **32**(41), 10497-10504 (2016). https://doi.org/10.1021/acs.langmuir.6b02716

[27] M.A. Habeeb, and R.S. Abdul Hamza, "Novel of (biopolymer blend-MgO) nanocomposites: Fabrication and characterization for humidity sensors," Journal of Bionanoscience, **12** (3), 328-335 (2018). https://doi.org/10.1166/jbns.2018.1535

[28] M.A. Habeeb, and R.S.A. Hamza, "Synthesis of (polymer blend –MgO) nanocomposites and studying electrical properties for piezoelectric application," Indonesian Journal of Electrical Engineering and Informatics, **6** (4), 428-435 (2018). https://doi.org/10.11591/ijeei.v6i1.511

[29] D.K. Pradhan, R.N.P. Choudhary, and B.K. Samantaray, "Studies of dielectric relaxation and AC conductivity behavior of plasticized polymer nanocomposite electrolytes," Int. J. Electrochem. Sci. **3**(5), 597-608 (2008).

[30] M.A. Habeeb, and W.S. Mahdi, "Characterization of (CMC-PVP-Fe2O3) nanocomposites for gamma shielding application," International Journal of Emerging Trends in Engineering Research, **7** (9), 247-255 (2019). https://doi.org/10.30534/ijeter/2019/06792019

[31] M.F.H. Al-Kadhemy, Z.S. Rasheed, and S.R. Salim, "Fourier transform infrared spectroscopy for irradiation coumarin doped polystyrene polymer films by alpha ray," Journal of Radiation Research and Applied Sciences, **9**(3), 321-331 (2016).

[32] Q.M. Jebur, A. Hashim, and M.A. Habeeb, "Fabrication, structural and optical properties for (Polyvinyl alcohol-polyethylene oxide iron oxide) nanocomposites," Egyptian Jour of Chemistry, **63** (2), 611-623 (2020). https://dx.doi.org/10.21608/ejchem.2019.10197.1669

[33] R.N. Bhagat, and V.S. Sangawar, "Synthesis and Structural Properties of Polystyrene Complexed with Cadmium Sulfide," Int. J. Sci. Res. (IJSR), **6**, 361-365 (2017).

[34] A. Hashim, M.A. Habeeb, and Q.M. Jebur, "Structural, dielectric and optical properties for (Polyvinyl alcohol-polyethylene oxide manganese oxide) nanocomposites," Egyptian Journal of Chemistry, **63**, 735-749 (2020). https://dx.doi.org/10.21608/ejchem.2019.14849.1901

[35] L. Kungumadevi, R. Sathyamoorthy, and A. Subbarayan, "AC conductivity and dielectric properties of thermally evaporated PbTe thin films," Solid. State. Electron. **54**(1), 58-62 (2010). https://doi.org/10.1016/j.sse.2009.09.023

[36] M.A. Habeeb, A. Hashim, and N. Hayder, "Fabrication of (PS-Cr2O3/ZnCoFe2O4) nanocomposites and studying their dielectric and fluorescence properties for IR sensors," Egyptian Journal of Chemistry, **63**, 709-717 (2020). https://dx.doi.org/10.21608/ejchem.2019.13333.1832

[37] Q.M. Jebur, A. Hashim, and M.A. Habeeb, "Structural, A.C electrical and optical properties of (polyvinyl alcohol-polyethylene oxide-aluminum oxide) nanocomposites for piezoelectric devices," Egyptian Journal of Chemistry, **63**, 719-734 (2020). https://dx.doi.org/10.21608/ejchem.2019.14847.1900

[38] R. Dalven, and R. Gill, "Electrical properties of β-Ag2Te and β-Ag2Se from 4.2°to 300°K," J. Appl. Phys. **38**(2), 753-756 (1967). https://doi.org/10.1063/1.1709406

[39] N. Hayder, M.A. Habeeb, and A. Hashim, Structural, optical and dielectric properties of (PS-In$_2$O$_3$/ZnCoFe$_2$O$_4$) nanocomposites," Egyptian Journal of Chemistry, **63**, 577-592 (2020). https://doi.org/10.21608/ejchem.2019.14646.1887

[40] Y. Li, H. Porwal, Z. Huang, H. Zhang, E. Bilotti, and T. Peijs, "Enhanced Thermal and Electrical Properties of Polystyrene-Graphene Nanofibers via Electrospinning," J. Nanomater. **2016**, (2016). https://doi.org/10.1155/2016/4624976

[41] S. Ju1, M. Chen, H. Zhang, and Z. Zhang, "Dielectric properties of nanosilica/low-density polyethylene composites: The surface chemistry of nanoparticles and deep traps induced nanoparticles," Journal of express Polymer Letters, **8**(9), 682-691 (2014).

[42] C. M. Mathew, K. Kesavan, and S. Rajendran, "Structural and Electrochemical Analysis of PMMA Based Gel Electrolyte Membranes," Int. J. Electrochem. **2015**, 1-7 (2015). https://doi.org/10.1155/2015/494308

[43] O. Abdullah, G.M. Jamal, D.A. Tahir, and S.R. Saeed, "Electrical Characterization of Polyester Reinforced by Carbon Black Particles," International Journal of Applied Physics and Mathematics, **1**(2), 101-105 (2011).

ПОКРАЩЕННЯ СТРУКТУРНИХ І ДІЕЛЕКТРИЧНИХ ВЛАСТИВОСТЕЙ НАНОСТРУКТУР PS/SiC/Sb₂O₃ ДЛЯ ПРИСТРОЇВ НАНОЕЛЕКТРОНІКИ

Наврас Карім Аль-Шаріфі, Маджід Алі Хабіб

Вавилонський університет, освітній коледж чистих наук, фізичний факультет, Ірак

У поточному дослідженні нанокомпозити PS/SiC/Sb$_2$O$_3$ були виготовлені методом лиття з розчину з різними концентраціями наночастинок Sb$_2$O$_3$ (0,2,4,6,8) % мас. Досліджено структурні та діелектричні властивості нанокомпозитів (PS/SiC/ Sb$_2$O$_3$). Повний емісійний скануючий електронний мікроскоп (FE-SEM), який використовується для дослідження поверхні нанокомпозиту. FE-SEM підтвердив хороший розподіл НЧ SiC і Sb$_2$O$_3$ в полімерній матриці. Під оптичним мікроскопом (OM) було перевірено морфологію нанокомпозиту, що довело, що полістирол є винятково змішуваним, як видно з його більш тонкої форми та гладкої однорідної поверхні, тоді як концентрація добавок SiC та Sb$_2$O$_3$ NPs добре розподілена на поверхні полімерного плівки нанокомпозиту. Інфрачервоною Фур'є спектроскопія (FTIR) досліджено структуру нанокомпозиту та отримана інформація про коливальні властивості молекул. З FTIR додавання SiC і Sb$_2$O$_3$ NP викликало взаємодію з полімерною матрицею. За допомогою FTIR доведено, що існує фізична взаємодія між полістиролом і наночастинками SiC і Sb$_2$O$_3$. Відповідно до електричних властивостей змінного струму діелектрична проникність і діелектричні втрати НК зменшуються зі збільшенням частоти прикладеного електричного поля та збільшуються зі збільшенням концентрації наночастинок SiC/Sb$_2$O$_3$, тоді як електропровідність змінного струму зростає зі збільшенням частоти та концентрації НЧ SiC/Sb$_2$O$_3$. Результати структурних та електричних характеристик показують, що нанокомпозити PS/SiC/Sb$_2$O$_3$ можуть бути використані для різних електронних пристроїв.

Ключові слова: *нанокомпозити; полістирол; наночастинки SiC і Sb$_2$O$_3$; електричні властивості для змінного струму*

BOTTOMONIA UNDER EFFECT THREE INSPIRED QCD POTENTIALS IN THE FRAMEWORK OF NON-RELATIVISTIC QUARK MODEL[†]

 Moustafa Ismail Hapareer[a,*], **M. Allosh**[b], **G.S. Hassan**[a], **A.M. Yasser**[b]

[a] Physics Department, Faculty of Science, Assiut, Assiut University, 71515 Assiut, Egypt
[b] Physics Department, Faculty of Science, Qena, South Valley University, 83523 Qena, Egypt
[*] E-mail: mostafa.ismail.hapareer@science.aun.edu.eg

In this paper, we have studied the spectrum of bottomonium mesons behavior under the effect of three types of potentials inspired by Quantum Chromodynamics. In addition, other properties like Hyperfine splitting behavior, and Fine splitting behavior have been studied. We used these potential models within the non-relativistic quark model to present this study. We found that our expectations are consistent with experimental data and other theoretical works as well we presented new conclusions regarding the spectrum of unseen bottomonium states for S, P, and D-wave bottomonia. And we have expected other their characteristics.

Keywords: *Hyper splitting behavior, Fine splitting behavior, bottomonia*

PACS: 12.40.Yx, 14.40.Pq, 02.60.Cb, 12.39.Jh, 14.65.Dw, 14.40.Lb, 14.80.Bn

1. INTRODUCTION

Investigation of heavy quarkonia systems like charmonium, bottomonium, and toponium, offers a clear understanding of particle physics, the standard model, and the quantification characterization of the QCD quantum chromodynamics theory [1, 2, 3, 4]. But because of the tiny lifetime for the top quark approximately equals $0.5 \times 10^{-24}s$, it is very hard to appear in nature [5]. So we can say the bottomonia are the heaviest mesons that the experiments discovered them over a long time. From that, the bottomonium family holds a substantial place in the hadronic particles and participates effectively in the inspecting of strong interactions.

The full observed bottomonium spectra are still very far from the establishing, in comparison with the theoretical calculations of spectra. Ref.[5] provides a good review of the practical history of the bottomonium states, but here we offer a brief summary. At Fermilab by the E288 Collaboration in 1977, the first bottomonia $\Upsilon(1S)$ and $\Upsilon(2S)$ plus $\Upsilon(3S)$ have been detected [6, 7]. Then $\Upsilon(4S)$ state was observed in 1984 [8]. BaBar Collaboration has observed $\eta_b(1S)$, the spin-singlet partner of the spin-triplet state $\Upsilon(1S)$, in 2008 [9]. After four years, Belle collaboration has announced the initial evidence for spin-singlet partner $\eta_b(2S)$ of the $\Upsilon(2S)$ in 2012 utilizing the transition process, $h_b(2P) \longrightarrow \gamma$ [10]. In 1982 [11, 12] and 1983 [13, 14], the radiative transitions of the $\Upsilon(2S)$ and $\Upsilon(3S)$ have led to the observation of the two triplet-spin P-wave mesons $\chi_{bJ}(1P)$ and $\chi_{bJ}(2P)$ with $J = 2, 1, 0$. $h_b(1P)$ has firstly manifested in BABAR in 2011 via cascade transitions; $\Upsilon(3S) \rightarrow \pi^o h_b(1P) \rightarrow \pi^o \gamma \eta_b(2S)$ [15], with a mass of 9902 $\pm 4 \pm 2$. Belle has not long waited to announce significant observation of the singlet spin states $h_b(2P)$ [16]. In the cascade transitions, $\Upsilon(3S) \longrightarrow \chi_b(2P)\gamma \longrightarrow \Upsilon(1^3D_2)\gamma\gamma \longrightarrow \chi_b(1P)\gamma\gamma\gamma \longrightarrow \Upsilon(1S)\gamma\gamma\gamma\gamma$, the candidate for the mesonic state;1^3D_2 has appeared in the CLEO Collaboration in 2004 [17].

So clear, it is hard to assign the whole spectrum of bottomonia. As a part of fact, we are still at the beginning of this road. Until now many lower bottomonium states that are under the threshold of creation of the $B\bar{B}$ pair have not appeared. But the running of the Belle II [18] and upcoming colliders will open the hope door towards this challenge, and we foresee the appearance of new bottomonium states. To achieve that, we need to probe the bottomonia with many theoretical techniques that provide us with accurate expectations and inspired QCD. There are many techniques have utilized for example; the QCD sum rule [19, 20], Bethe-Salpeter [21], the Regge phenomenology [22, 23, 24, 25], the method of perturbative QCD [26], the lattice QCD [27, 28, 29], and the coupled-channel model [30, 31, 32, 33] in addition to utilizing the versions of relativistic [34, 35], relativized [36, 37, 38], semi-relativistic [39, 40], and finally the non-relativistic [41].

Our purpose in this paper is to obtain the accurate mass spectrum of bottomonia in addition to the characteristics of hyperfine splitting behavior and fine splitting behavior. We suggest applying three QCD-inspired potentials, the first one is the simplest. For more accurate results, we use the second one, which takes into account the spin-spin interactions between quarks. Here appears the hyperfine splitting behavior. To obtain the best potential, which is more sophisticated and more accurate, we apply the third one, which

includes spin-orbit interactions and tensor interactions, and here the fine-splitting behavior appears, and the results become more accurate. The theoretical frame for this work is in the next section, while we offer our findings and discussion in section 3. Our conclusions appear in the last section.

2. THE THEORETICAL FRAME

We adopt the non-relativistic approximation, which includes the Hamiltonian that rules the dynamics of mesons, consisting of the kinetic energy part $\mathcal{T}$ and the potential energy part $\mathcal{V}$ which considers the phenomenological interactions of the constituent quarks. We can write the Hamiltonian operator $\hat{\mathcal{H}}$ as:

$$\hat{\mathcal{H}}_{nr} = \hat{\mathcal{T}}_{nr} + \hat{\mathcal{V}}. \tag{1}$$

We can express the wave functions of mesons as the eigenfunctions in the Schrödinger equation as follows:

$$\hat{\mathcal{H}}_{nr}\psi = \mathcal{E}\psi. \tag{2}$$

2.1. The Kinetic Energy of Bottomonia

We can treat the bottomonium mass center of motion as the non-relativistic kinetic energy. The expression of the non-relativistic kinetic energy operator is as the next [42]:

$$\hat{\mathcal{T}}_{nr} = m_b + m_{\bar{b}} + \frac{\hat{\mathcal{P}}^2}{\mu}. \tag{3}$$

The m_b and $m_{\bar{b}}$ are the masses of the bottom quark and the bottom antiquark. The μ and $\hat{\mathcal{P}}$ are the reduced mass and the relative momentum of bottomonium meson, respectively. The constituent quark mass is used to provide us with suitable calculations of bottomonium properties that could be performed. We can compare the findings to the experimental data [43] to appear how our models work.

2.2. The Potential Models

From a time the first detection of the charmonium states in 1974, the first system of quark and antiquark, it became prototypical of the exotic positronium atom e^+e^- for meson spectroscopy [44, 45, 46]. There is a similarity between them roughly [1]. So the initial attempt started to improve positronium-like potential, to obtain a fine static potential of quarkonium, which is known as a vector color coulomb-like potential. The improved color coulomb-like potential depends on QCD spirit. In this potential, the effectiveness of quark interaction is in the short distances [47, 48]. According to the rules of quantum chromodynamics (QCD) theory, the behavior of short distance has dominated via one-gluon exchange (OGE) interaction[49, 1]. Hence the color coulomb-like potential takes the following formula:

$$\mathcal{V}_{coulomb-like}(r) = \frac{-4}{3}\frac{\alpha_s}{r} \tag{4}$$

where α_s and $\frac{-4}{3}$ are the running strong coupling constant and the color factor, respectively. From the phenomenological side, we must consider the quark confinement at the long ranges[36, 42], where one of the significant properties of strong interactions is confinement, which is generally acknowledged. From QCD rules, the confining potential increases with increasing the inter-quark distance[50, 1]. So we can write the confinement potential as:

$$\mathcal{V}_{conf}(r) = br. \tag{5}$$

From the previous, we can obtain the conventional potential, which collects the vector color Coulomb-like potential as in Eq.4 and the scalar linear potential as in Eq.5. This is the first suggested potential that we can write as:

$$\mathcal{V}_I(r) = \frac{-4}{3}\frac{\alpha_s}{r} + br. \tag{6}$$

We will investigate $b\bar{b}$ system spectra under the effect of this potential as a minimal potential model, as shown in Table 2; column 4.

Here, we go ahead a step toward the front to consider the spin-spin interactions between $b\bar{b}$ systems, which takes the following relation:

$$\mathcal{V}_{SS}(r) = \frac{32\pi\alpha_s}{9m_b m_{\bar{b}}}\delta_\sigma(r)\mathbf{S}_b.\mathbf{S}_{\bar{b}} \tag{7}$$

where

$$\delta_\sigma(r) = (\sigma/\sqrt{\pi})^3 e^{-\sigma^2 r^2}. \tag{8}$$

When we add Eq.7 to Eq.6, we acquire the second potential that takes the following form:

$$\mathcal{V}_{II}(r) = \frac{-4}{3}\frac{\alpha_s}{r} + br + \frac{32\pi\alpha_s}{9m_b m_{\bar{b}}}\delta_\sigma(r)\mathbf{S}_b.\mathbf{S}_{\bar{b}}, \tag{9}$$

where

$$\langle SM_s|\mathbf{S}_b\mathbf{S}_{\bar{b}}|SM_s\rangle = \frac{S(S-1)}{2} - \frac{3}{4} \tag{10}$$

as S is the total spin of the meson [51]. The second potential considers the hyperfine behavior that arises due to spin-spin interaction between quarks, so it differentiates between the triplet spin states and singlet spin states. Now we take into account two significant parts spin-orbit interactions and tensor interactions. They have the next formulas[52]:

$$\mathcal{V}_{SL}(r) = \frac{1}{2m_b^2 r}(3\mathcal{V}_V'(r) - \mathcal{V}_S'(r))\mathbf{L}.\mathbf{S}, \tag{11}$$

and

$$\mathcal{V}_T(r) = \frac{1}{12m_b^2}(\frac{1}{r}\mathcal{V}_V'(r) - \mathcal{V}_V''(r))\mathrm{T} \tag{12}$$

where the spin-orbit matrix elements of the **L.S** operator is determined by

$$\langle\mathbf{L}.\mathbf{S}\rangle = \frac{J(J+1)}{2} - \frac{L(L+1)}{2} - \frac{S(S+1)}{2}, \tag{13}$$

where L and J are orbital angular momentum and total angular momentum quantum numbers. This operator has a diagonal base $|J,L,S\rangle$, and T represents the tensor operator [53]:

$$\mathrm{T} = \mathbf{S}_q.\hat{r}\mathbf{S}_{\bar{q}}.\hat{r} - \frac{1}{3}\mathbf{S}_q.\mathbf{S}_{\bar{q}} \tag{14}$$

From the equations (9,11,12), we can write the third potential as follows:

$$\mathcal{V}_{III}(r) = \frac{-4}{3}\frac{\alpha_s}{r} + br + \frac{32\pi\alpha_s}{9m_b m_{\bar{b}}}\delta_\sigma(r)\mathbf{S}_b.\mathbf{S}_{\bar{b}} + \mathcal{V}_{SL}(r) + \mathcal{V}_T(r). \tag{15}$$

This potential considers fine splitting behavior due to taking into account the spin-orbit and the tensor interactions in addition to the hyperfine splitting behavior due to spin-spin interaction.

We have determined the utilized parameters in these potentials by fitting the corresponding spectrum of bottomonium states for each different potential, as in Table 1. We can have high expectations concerning the bottomonia spectrum ($b\bar{b}$), as shown in Table 2 due to, these modified parameters tabulated in Table 1.

Table 1. The modified parameters were utilized in three potentials to obtain the masses of $b\bar{b}$-bottomonium states

Model		The potentials in the (NRQM)	
Parameters	$\mathcal{V}_I$	$\mathcal{V}_{II}$	$\mathcal{V}_{III}$
$m_b = m_{\bar{b}}$ GeV	4.7836	4.7916	4.8087
α_s	0.3811	0.3981	0.4040
b $(GeV)^2$	0.1625	0.1671	0.1620
σ GeV	—	2.8241	2.2927

3. RESULTS AND DISCUSSION

In this paper, we remedied Schrodinger's equation using the matrix method to obtain its numerical solution. Using the previous three potentials, the bottomonium mesons' characteristics are probed in the frame of the non-relativistic kinetic energy. We have obtained Hamiltonian values for the $nS(n \le 4)$, $nP(n \le 3)$, and $nD(n \le 3)$ bottomonium states with the spectroscopic notation $n^{2S+1}L_J$. The mass and other characteristics are introduced in Tables (2 : 4).

3.1. The Mass Spectrum of Bottomonium Mesons

We investigated the spectrum of S, P, and D-Wave bottomonium mesons under the influence of three potentials. This study includes thirty-six seen and unseen meson states. Fitting with seventeen mesonic states in the last update of data, due to it yields new parameters in each potential to get the best new theoretical bottomonium spectra in three QCD-inspired potentials types, as shown in Table 1. These newly yielded theoretical spectra were compared with the current experimental data [43] and compared to other works for calculated spectra [54, 55, 56].

The χ^2 values for the expectations of the three potential types are (0.0010), (0.0005), and (0.0002), respectively. So, one observes that the first potential type provides us an agreement with the experiment, although it is a blind model concerning the multiplets of bottomonium states that own the same orbital angular momentum L quantum number with different spin quantum number S and different total angular momentum J as in column 4 of Table 2. When we go ahead a step toward more accuracy, we find the second potential type that supplies us with more accuracy than the first one, but one notices it is a blind relative to the multiplets that own the same orbital angular momentum L quantum number, with a different total angular momentum quantum number J, as seen in column 5 of Table 2. Now we continue ahead another step toward more accuracy, and we have found that the third type of potential has achieved the most accuracy concerning these potentials, in addition, this potential provides us with the ability to distinguish between the multiplets of bottomonia that own the same quantum number L and with different quantum numbers S and J, as shown in Table 2 column 6.

The masses of bottomonia are plotted in Fig.1 and Fig.2 with the principle quantum number (n). Where the masses are extracted within the third potential type; based on its parameters which are in Table 1. The figures illustrate the masses of S, P, and D-wave states with triplet spin (in Fig.1) and singlet spin (in Fig.2) with various values of J. The graphs demonstrate that the mass spectra increase along with increasing the principle quantum number (n). Here, we find (n) has a strong influence on the S, P, and D-wave bottomonia masses when particles have the same S and J quantum numbers.

Figures 6 and 7 illustrate the theoretical masses of S, P-wave bottomonium states ($\Upsilon(nS)$ and $\eta(nS)$) and (χ (nS)and $h(nS)$), respectively. They provide us with a comparison between the practical data and the theoretical expectations using the third potential, tabulated in Table 2. we find a good consistency between them and observe a tiny distinction between them.
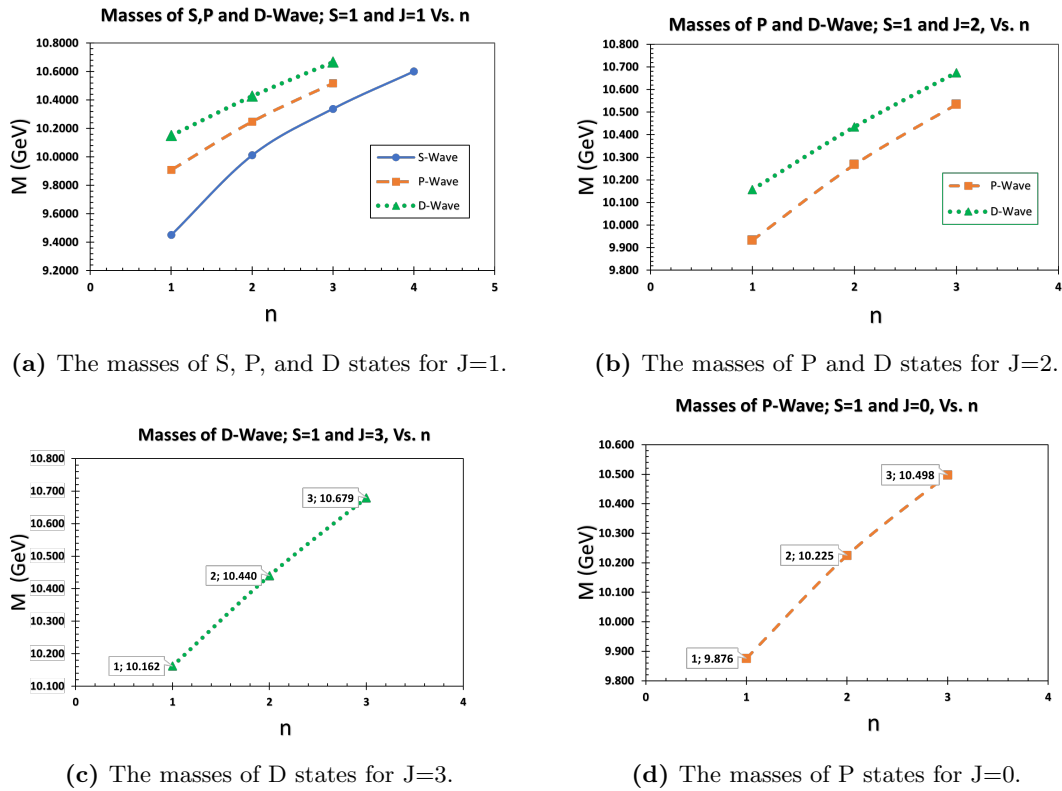
The other studies for the bottomonium spectra employed a variety of models, including the variational method with a single Gaussian trial wavefunction in a Cornell potential model in the relativistic Quark Model framework used by (Virendrasinh Kher et al.) [54]. While (B. Chen et al.) utilized the RFT model[55], meanwhile the Non-Relativistic with Screened Potential Model is applied by (W.J. Deng et al.) [56]. And (M. Wurtz et al.) use the LATTICE Field Theory estimations [29]. We find from Table. 2 that the three potentials to which we applied them agree in general in the most estimations with these models, but the third one owns the most agreement with the most states.

### 3.2. Hyperfine Splitting Behavior $\Delta M_{Hyp.Sp.}$

The hyperfine splitting force plays an influential role in the calculations of the mass of bottomonia. So, we have to take it into account. This force started with the appearance through the second potential, so the second potential provides us with more accurate calculations for masses than the first potential, as evident in column 5 of Table 2. However, its accuracy is further improved in the third potential to supply us with more accurate calculations, as extremely evident in column 6 of Table 2. We notice that the difference between the multiplets decreases by increasing (n) for S-wave bottomonia; the same thing concerning P-wave, but in the S-wave bottomonia the triplet spin particles have greater mass than the singlet spin particles. While the opposite happens for the P-wave bottomonia, the spectrum mass of singlet spin particles is heaviest than triplet spin particles. While in the D-wave bottomonia, the mass difference is constant between triplet, and singlet spin particles, and compared to the singlet spin particles, the triplet spin particles are heavier. Fig. 3 shows the relation between the hyperfine splitting mass and the quantum number (n) in comparison with experimental data for the S-wave in a graph (a) and also for the P-wave in graph (b) according to the third potential.

3.3. Fine Splitting Behavior $\Delta M_{F.S.}$

The role of fine splitting force, which appears in the third potential is very significant for estimations of the masses of bottomonium mesons. That matter makes us enter this force in our calculations of mass spectra, not only in the bottomonium spectrum but in all hadronic spectra. Consequently, we find the mass estimations are the most accurate. Also, it can distinguish between the multiplets that have the same L and S, but they have various J because of spin-orbit force and tensor force, as is very clear in Table 2; column 6. Now we find the 1^3P_1-1^3P_0 is the dominant partial splitting where it is of ($\cong 59\%$) relative to total splitting concerning the 1P-level. Also, the 2^3P_1-2^3P_0 takes ($\cong 55\%$) to be the dominant partial splitting relative to the 2P-level.

(a) The masses of S, P, and D states for J=1.

(b) The masses of P and D states for J=2.

(c) The masses of D states for J=3.

(d) The masses of P states for J=0.

Figure 1. The Masses of S, P, and D states for QCD-inspired $\mathcal{V}_{III}$, which have spin one and various total angular momentum J versus **n** quantum number

(a) The masses of S states for J=0.

(b) The masses of P states for J=1.

(c) The masses of D states for J=2.
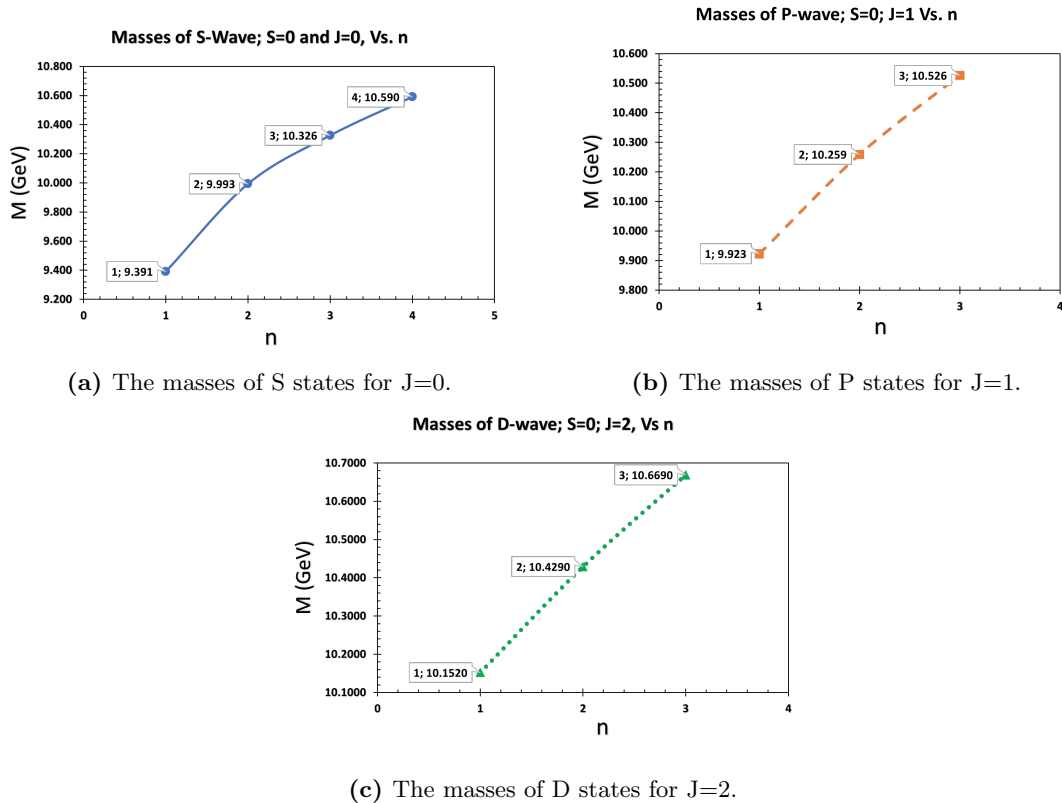
Figure 2. The Masses of S, P, and D states for QCD-inspired $\mathcal{V}_{III}$, which have spin zero and various total angular momentum states J versus **n** quantum number

Table 2. Theoretical spectra of $b\bar{b}$ states in GeV under the influence of three QCD-inspired potentials compared with experimental data [43] and with theoretical results of Refs.[[54], [55], [56], [29]].

state	name	EXP.Mass [43]	Theoretical masses			[54]	[55]	[56]	[29]
			$\mathcal{V}_I$	$\mathcal{V}_{II}$	$\mathcal{V}_{III}$				
$1\,^3S_1$	$\Upsilon(1S)$	9.4603 ± 0.26	9.4353	9.4383	9.4510	9.4630	–	9.4600	9.4600
$1\,^1S_0$	$\eta_b(1S)$	9.3987 ± 2.0	9.4353	9.3633	9.3910	9.4230	–	9.3900	9.4020
$2\,^3S_1$	$\Upsilon(2S)$	10.0233 ± 0.31	9.9804	9.9974	10.0110	10.0010	10.0230	10.0150	10.0200
$2\,^1S_0$	$\eta_b(2S)$	9.9990 ± 4.0	9.9804	9.9722	9.9930	9.9830	9.9990	9.9900	9.9980
$3\,^3S_1$	$\Upsilon(3S)$	10.3552 ± 0.5	10.3042	10.3285	10.3380	10.3540	10.3570	10.3430	10.3340
$3\,^1S_0$	$\eta_b(3S)$		10.3042	10.3112	10.3260	10.3420	10.3370	10.3260	10.3140
$4\,^3S_1$	$\Upsilon(4S)$	10.5794 ± 1.2	10.5649	10.5949	10.6000	10.6500	10.6370	10.5970	–
$4\,^1S_0$	$\eta_b(4S)$		10.5649	10.5809	10.5900	10.6380	10.6270	10.5840	–
$1\,^3P_2$	$\chi_{b2}(1P)$	$9.9122 \pm 0.26 \pm 0.31$	9.8901	9.9012	9.9320	9.9070	9.9110	9.9210	9.9130
$1\,^3P_1$	$\chi_{b1}(1P)$	$9.8928 \pm 0.26 \pm 0.31$	9.8901	9.9012	9.9090	9.8940	9.8930	9.9030	9.8930
$1\,^3P_0$	$\chi_{b0}(1P)$	$9.8594 \pm 0.42 \pm 0.31$	9.8901	9.9012	9.8760	9.8740	9.8540	9.8640	9.8650
$1\,^1P_1$	$h_b(1P)$	9.8993 ± 0.8	9.8901	9.8990	9.9230	9.8990	9.8990	9.9090	9.9000
$2\,^3P_2$	$\chi_{b2}(2P)$	$10.2686 \pm 0.22 \pm 0.50$	10.2230	10.2433	10.2670	10.2740	10.2680	10.2640	10.2270
$2\,^3P_1$	$\chi_{b1}(2P)$	$10.2555 \pm 0.22 \pm 0.50$	10.2230	10.2433	10.2480	10.2650	10.2590	10.2490	10.2120
$2\,^3P_0$	$\chi_{b0}(2P)$	$10.2325 \pm 0.40 \pm 0.50$	10.2230	10.2433	10.2250	10.2480	10.2390	10.2200	10.1940
$2\,^1P_1$	$h_b(2P)$	10.2598 ± 1.20	10.2230	10.2409	10.2590	10.2680	10.2620	10.2540	10.2190
$3\,^3P_2$	$\chi_{b2}(3P)$	10524.0 ± 0.8	10.4896	10.5162	10.5340	10.5760	10.5560	10.5280	–
$3\,^3P_1$	$\chi_{b1}(3P)$	10513.4 ± 0.7	10.4896	10.5162	10.5170	10.5670	10.5570	10.5150	–
$3\,^3P_0$	$\chi_{b0}(3P)$		10.4896	10.5162	10.4980	10.5510	10.5510	10.4900	–
$3\,^1P_1$	$h_b(3P)$		10.4896	10.5138	10.5260	10.5700	10.5560	10.5190	–
$4\,^3P_2$	$\chi_{b2}(4P)$		10.7220	10.7537	10.7667	–	10814	–	–
$4\,^3P_1$	$\chi_{b1}(4P)$		10.7220	10.7537	10.7500	–	10817	–	–
$4\,^3P_0$	$\chi_{b0}(4P)$		10.7220	10.7537	10.7342	–	10815	–	–
$4\,^1P_1$	$h_b(4P)$		10.7220	10.7512	10.7594	–	10815	–	–
$1\,^3D_3$	$\Upsilon_3(1D)$		10.1238	10.1423	10.1620	10.1500	10.1830	10.1570	10.1720
$1\,^3D_2$	$\Upsilon_2(1D)$	10.1637 ± 1.40	10.1238	10.1423	10.1570	10.1490	10.1640	10.1530	10.1610
$1\,^3D_1$	$\Upsilon_1(1D)$		10.1238	10.1423	10.1500	10.1450	10.1360	10.1460	10.1500
$1\,^1D_2$	$\eta_{b2}(1D)$		10.1238	10.1422	10.1520	10.1490	10.1670	10.1530	10.1630
$2\,^3D_3$	$\Upsilon_3(2D)$		10.3996	10.4245	10.4400	10.4660	10.4780	10.4360	10.4590
$2\,^3D_2$	$\Upsilon_2(2D)$		10.3996	10.4245	10.4340	10.4650	10.4760	10.4320	10.4010
$2\,^3D_1$	$\Upsilon_1(2D)$		10.3996	10.4245	10.4270	10.4620	10.4670	10.4250	10.4580
$2\,^1D_2$	$\eta_{b2}(2D)$		10.3996	10.4244	10.4290	10.4650	10.4750	10.4320	10.4470
$3\,^3D_3$	$\Upsilon_3(3D)$		10.6383	10.6684	10.6790	10.7410	10.7400	–	–
$3\,^3D_2$	$\Upsilon_2(3D)$		10.6383	10.6684	10.6740	10.7400	10.7440	–	–
$3\,^3D_1$	$\Upsilon_1(3D)$		10.6383	10.6684	10.6660	10.7360	10.7420	–	–
$3\,^1D_2$	$\eta_{b2}(3D)$		10.6383	10.6683	10.6690	10.7400	10.7420	–	–
		χ^2	0.0010	0.0005	0.0002				
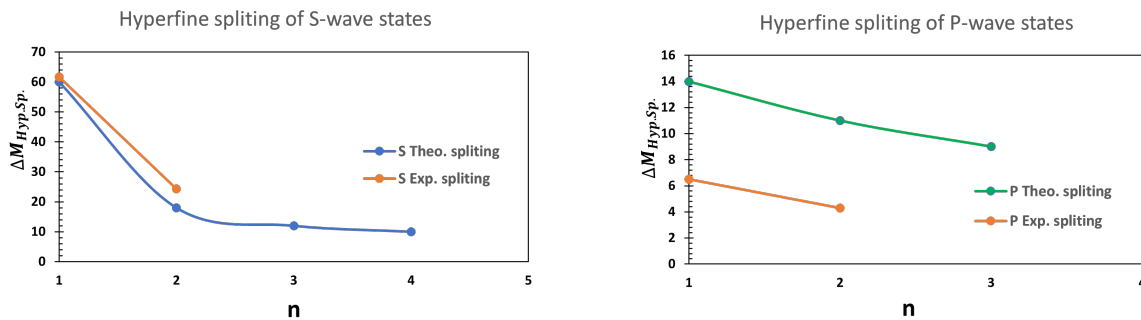
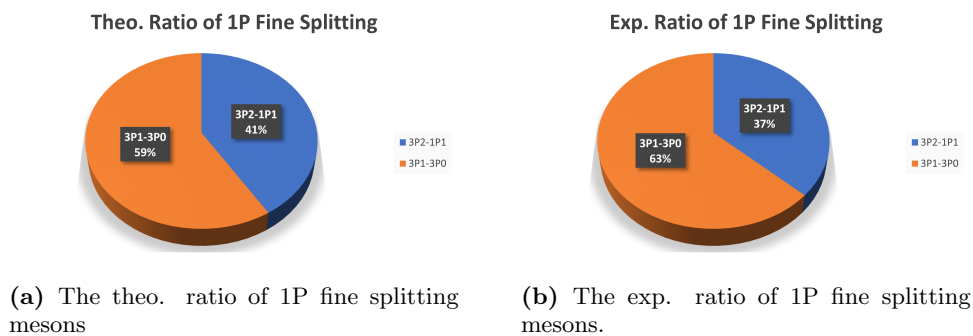**(a)** The hyperfine splitting of S states.

(b) The hyperfine splitting of P states.

Figure 3. The theoretical and experimental mass hyperfine splitting behavior of S and P states versus **n**

Also, in the experimental data, $n^3P_1 - n^3P_0; n = 1, 2$ is the dominant partial splitting. So, these expectations are consistent with practical results, as appear in Figs. 4 and 5. And we have presented our predictions for these states and the rest of the states, as in Table 4.

Table 3. Theoretical hyperfine splitting (Theo. $\Delta M_{Hyp.Sp.}$) and Experimental hyperfine splitting (Exp. $\Delta M_{Hyp.Sp.}$) of $[b\bar{b}]$ states in MeV for S, P, D-Wave studied states.

(n)	**Wave Level** (L)	Total Spin of states (S)	**Hyperfine Splitting**	Theoretical $|\Delta M_{Hyp.Sp}|$	Experimental $|\Delta M_{Hyp.Sp}|$ [43]
1	S	1-0	$^3S_1$-$^1S_0$	60	61.60
2	S	1-0	$^3S_1$-$^1S_0$	18	24.30
3	S	1-0	$^3S_1$-$^1S_0$	12	–
4	S	1-0	$^3S_1$-$^1S_0$	10	–
1	P	1-0	$^3P_1$-$^1P_1$	14	6.50
2	P	1-0	$^3P_1$-$^1P_1$	11	4.30
3	P	1-0	$^3P_1$-$^1P_1$	9	–
4	P	1-0	$^3P_1$-$^1P_1$	9	–
1	D	1-0	$^3D_2$-$^1D_2$	5	–
2	D	1-0	$^3D_2$-$^1D_2$	5	–
3	D	1-0	$^3D_2$-$^1D_2$	5	–

(a) The theo. ratio of 1P fine splitting mesons

(b) The exp. ratio of 1P fine splitting mesons.

Figure 4. The theoretical and experimental fine splitting behavior of one spin 1P bottomonium states

4. CONCLUSION

In this work, we propose applying the three potentials in the framework of the non-relativistic quark model to probe the bottomonia spectra and obtain accurate yields. Our perspective depends on the non-relativistic framework that is suitable generally for the heavy mesons sector and particularly for bottomonium mesons because they are the heaviest mesons. The expectations of all these potentials present overall agree with practical data and with the theoretical expectations of other groups. The first one involves the one-gluon exchange interaction (like color coulomb potential) in addition to the scalar linear confinement potential, which provides us sensible findings where its uncertainty almost equals 0.0010, but it blinds concerning splitting between the multiples of bottomonium states which have the different S, and the J, but the same L quantum numbers. When we add the spin-spin interactions of quarks, we obtain the second potential, which is more accurate than the first one. Its χ value almost equals 0.005 and also exhibits hyperfine splitting behavior.

The third potential achieves our computational strategy that aims towards more accurate outputs using sophisticated treatments concerning the bottomonia spectrum, and we can extend and apply it to other heavy mesons. This potential is the most complex, but it is the most accurate one, with a χ value is almost 0.002. Additionally, it indicates the fine splitting behavior for bottomonium spectra. Our expected masses of unseen

(a) The theo. ratio of 2P fine splitting mesons

(b) The exp. ratio of 2P fine splitting mesons.
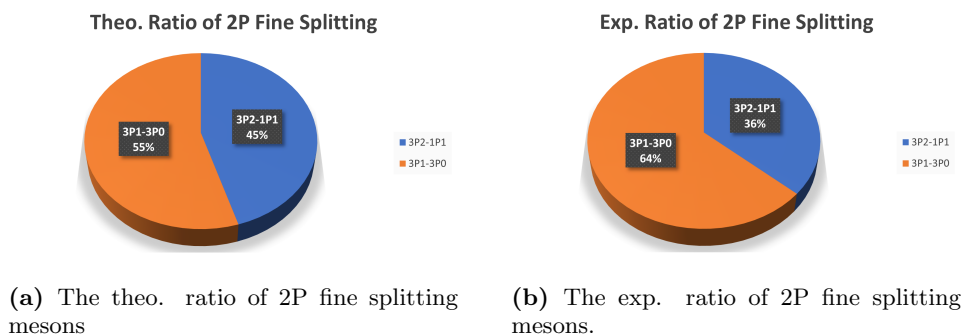
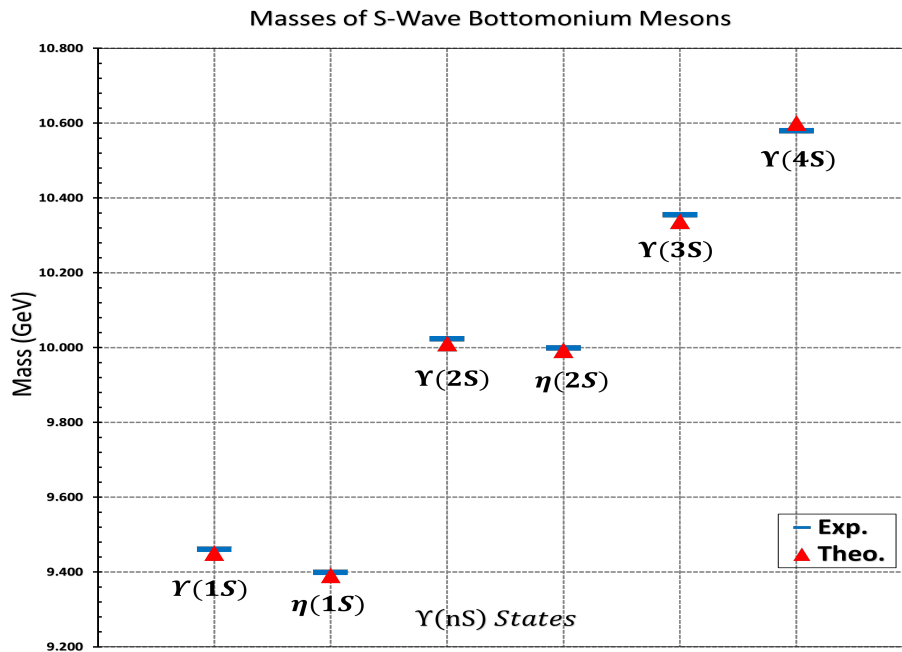**Figure 5.** The theoretical and experimental fine splitting behavior of one spin 2P bottomonium states

Figure 6. Comparing of the masses of S-wave bottomonia in GeV with the last update experimental data
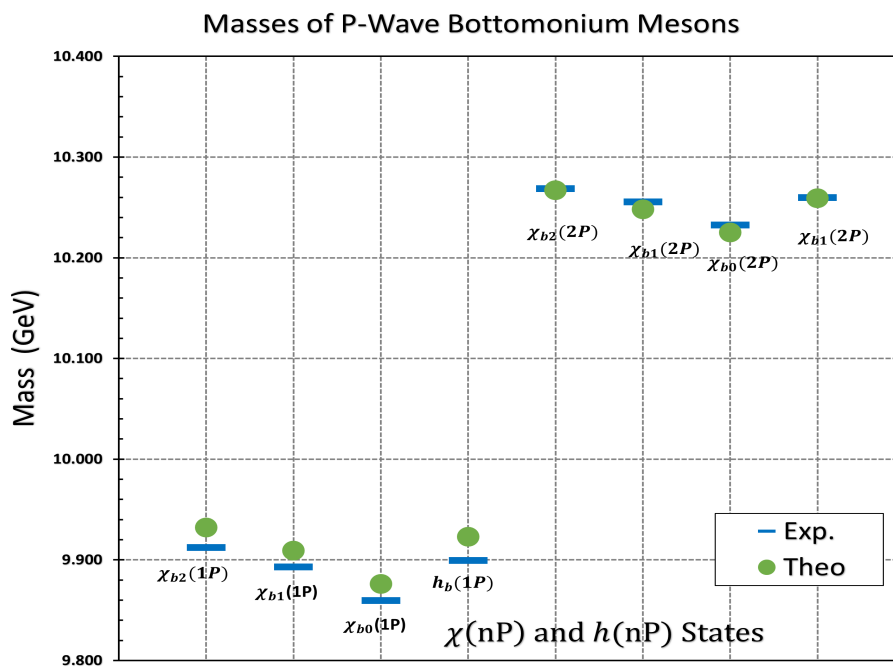

Figure 7. Comparing of the masses of P-wave bottomonia in GeV with the last update experimental data

Table 4. Theoretical fine splitting (Theo. $\Delta M_{F.Sp.}$) and Experimental fine splitting (Exp. $\Delta M_{F.Sp.}$) of $[b\bar{b}]$ states in MeV for P, D-Wave studied states.

n	Wave Level L	Total angular momentum of states (J)	Fine Splitting	Theo. $\Delta M_{F.Sp.}$	Exp. $\Delta M_{F.Sp.}$[43]
1	P	2-1	$^3P_2$-$^3P_1$	23	19.4
	P	1-0	$^3P_1$-$^3P_0$	33	33.4
2	P	2-1	$^3P_2$-$^3P_1$	19	13.2
	P	1-0	$^3P_1$-$^3P_0$	23	23.0
3	P	2-1	$^3P_2$-$^3P_1$	17	–
	P	1-0	$^3P_1$-$^3P_0$	19	–
4	P	2-1	$^3P_2$-$^3P_1$	17	–
	P	1-0	$^3P_1$-$^3P_0$	16	–
1	D	3-2	$^3D_3$-$^3D_2$	5	–
	D	2-1	$^3D_2$-$^3D_1$	7	–
2	D	3-2	$^3D_3$-$^3D_2$	6	–
	D	2-1	$^3D_2$-$^3D_1$	7	–
3	D	3-2	$^3D_3$-$^3D_2$	5	–
	D	2-1	$^3D_2$-$^3D_1$	8	–

bottomonia states, via the third model, can provide good benefits to discovering these states in the incoming experiments.

So we use the yieldings from the third potential to study the hyperfine splitting behavior and the fine splitting behavior of the S, P, and D-wave bottomonia spectrum. This study of the bottomonia multiples behaviors agrees with the experimental data and presents significant predictions; we can use them to observe unseen bottomonium states in the future.

ORCID

Moustafa Ismail Hapareer, https://orcid.org/0000-0002-7654-6099; **M. Allosh**, https://orcid.org/0000-0001-8389-7076; **G.S. Hassan**, https://orcid.org/0000-0002-4830-0809; **A.M. Yasser**, https://orcid.org/0000-0002-5891-1953

REFERENCES

[1] D. Griffiths, *Introduction to Elementary Particles*, (John Wiley, and Sons, Weinheim, 2020).

[2] A. Bettini, *Introduction to Elementary Particle Physics*, Cambridge University Press, 2014.

[3] F. Hanzel and A. D. Martin, *Quarks and leptons: An introductory course in modern particle physics*, (John Wiley, and Sons, New York, 1984).

[4] D.H. Perkins, and D.H. Perkins, *Introduction to high energy physics.* (Cambridge university press, 2000). https://doi.org/10.1017/CBO9780511809040

[5] I. Bigi, Y. Dokshitzer, V. Khoze, J. Kühn, and P. Zerwas, Physics Letters B, **181**(1-2), 157-163 (1986). https://doi.org/10.1016/0370-2693(86)91275-X

[6] S. Herb, D. Hom, L. Lederman, J. Sens, H. Snyder, J. Yoh, J. Appel, B. Brown, C. Brown, W. Innes, *et al.*, "Physical Review Letters, **39**(5), 252 (1977). https://doi.org/10.1103/PhysRevLett.39.252

[7] W. R. Innes, J. Appel, B. Brown, C. Brown, K. Ueno, T. Yamanouchi, S. Herb, D. Hom, L. Lederman, J. Sens, *et al.* Physical Review Letters, **39**(20), 1240 (1977). https://doi.org/10.1103/PhysRevLett.39.1240

[8] D. Besson, J. Green, R. Namjoshi, F. Sannes, P. Skubic, A. Snyder, R. Stone, A. Chen, M. Goldberg, N. Horwitz, *et al.* Physical Review Letters, **54**(5), 381 (1985). https://doi.org/10.1103/PhysRevLett.54.381

[9] B. Aubert, M. Bona, Y. Karyotakis, J. Lees, V. Poireau, E. Prencipe, X. Prudent, V. Tisserand, J. G. Tico, E. Grauges, *et al.* Physical Review Letters, **101**(7), 071801 (2008). https://doi.org/10.1103/PhysRevLett.101.071801

[10] R. Mizuk, D. Asner, A. Bondar, T. Pedlar, I. Adachi, H. Aihara, K. Arinstein, V. Aulchenko, T. Aushev, T. Aziz, *et al.* Physical Review Letters, **109**(23), 232002 (2012). https://doi.org/10.1103/PhysRevLett.109.232002

[11] K. Han, T. Böhringer, P. Franzini, G. Mageras, D. Peterson, E. Rice, J. Yoh, J. Horstkotte, C. Klopfenstein, J. Lee-Franzini, *et al.* Physical Review Letters, **49**(22), 1612 (1982). https://doi.org/10.1103/PhysRevLett.49.1612

[12] G. Eigen, G. Blanar, and H. Dietl "Evidence for χb' Physical Review Letters, **49**(22), 1616 (1982). https://doi.org/10.1103/PhysRevLett.49.1616

[13] C. Klopfenstein, J. Horstkotte, J. Lee-Franzini, R. Schamberger, M. Sivertz, L. Spencer, P. Tuts, P. Franzini, K. Han, E. Rice, *et al.* Physical Review Letters, **51**(3), 160 (1983). https://doi.org/10.1103/PhysRevLett.51.160

[14] F. Pauss, H. Dietl, G. Eigen, E. Lorenz, G. Mageras, H. Vogel, P. Franzini, K. Han, D. Peterson, E. Rice, *et al.* Physics Letters B, **130**(6), 439 (1983). https://doi.org/10.1016/0370-2693(83)91539-3

[15] J. Lees, V. Poireau, E. Prencipe, V. Tisserand, J. G. Tico, E. Grauges, M. Martinelli, D. Milanes, A. Palano, M. Pappagallo, *et al.* Physical Review D, **84**(9), 091101 (2011). https://doi.org/10.1103/PhysRevD.84.091101

[16] I. Adachi, H. Aihara, K. Arinstein, D. M. Asner, T. Aushev, T. Aziz, A. Bakich, E. Barberio, K. Belous, V. Bhardwaj, *et al.* Physical Review Letters, **108**(3), 032001 (2012). https://doi.org/10.1103/PhysRevLett.108.032001

[17] P. del Amo Sanchez, J. Lees, V. Poireau, E. Prencipe, V. Tisserand, J. G. Tico, E. Grauges, M. Martinelli, A. Palano, M. Pappagallo, *et al.* Physical Review D, **82**(11), 111102 (2010). https://doi.org/10.1103/PhysRevD.82.111102

[18] T. Kuhr, C. Pulvermacher, M. Ritter, T. Hauth, and N. Braun, Computing and Software for Big Science, **3**, 1 (2019). https://doi.org/10.1007/s41781-018-0017-9

[19] Z.-G. Wang, The European Physical Journal C, **73**, 1 (2013). https://doi.org/10.1140/epjc/s10052-013-2559-7

[20] K. Azizi and J. Süngü, Journal of Physics G: Nuclear and Particle Physics, **46**(3), 035001 (2019). https://doi.org/10.1088/1361-6471/aaee21

[21] C.S. Fischer, S. Kubrak, and R. Williams, The European Physical Journal A, **51**(1), 10 (2015). https://doi.org/10.1140/epja/i2015-15010-7

[22] D.-M. Li, B. Ma, Y.-X. Li, Q.-K. Yao, and H. Yu, The European Physical Journal C-Particles and Fields, **37**, 323 (2004). https://doi.org/10.1140/epjc/s2004-02002-5

[23] S. Gershtein, A. Likhoded, and A. Luchinsky, Physical Review D, **74**(1), 016002 (2006). https://doi.org/10.1103/PhysRevD.74.016002

[24] K.-W. Wei, X.-H. Guo, *et al.* Physical Review D, **81**(7), 076005, (2010). https://doi.org/10.1103/PhysRevD.81.076005

[25] A. Badalian and B. Bakker, Physical Review D, **100**(5), 054036 (2019). https://doi.org/10.1103/PhysRevD.100.054036

[26] Y. Kiyo, and Y. Sumino, Physics Letters B, **730**, 76 (2014). https://doi.org/10.1016/j.physletb.2014.01.030

[27] J. Daldrop, C. Davies, R. Dowdall, H. Collaboration, *et al.* Physical Review Letters, **108**(10), 102003 (2012). https://doi.org/10.1103/PhysRevLett.108.102003

[28] R. Lewis and R. Woloshyn, Physical Review D, **85**(11), 114509 (2012). https://doi.org/10.1103/PhysRevD.85.114509

[29] M. Wurtz, R. Lewis, and R. Woloshyn, Physical Review D, **92**(5), 054504 (2015). https://doi.org/10.1103/PhysRevD.92.054504

[30] E. Van Beveren, G. Rupp, T. Rijken, and C. Dullemond, Physical Review D, **27**(7), 1527 (1983). https://doi.org/10.1103/PhysRevD.27.1527

[31] N. Törnqvist Physical Review Letters, **53**(9), 878 (1984). https://doi.org/10.1103/PhysRevLett.53.878

[32] J.-F. Liu and G.-J. Ding, The European Physical Journal C, **7253**(1), 18 (2012). https://doi.org/10.1140/epjc/s10052-011-1853-5

[33] Y. Lu, M. N. Anwar, and B.-S. Zou, Physical Review D, **94**(3), 034021 (2016). https://doi.org/10.1103/PhysRevD.94.034021

[34] D. Ebert, R. N. Faustov, and V. O. Galkin The European Physical Journal C, **71**, 1825 (2011). https://doi.org/10.1140/epjc/s10052-011-1825-9

[35] M. Bhat, A. P. Monteiro, and K. Kumar, https://doi.org/10.48550/arXiv.1702.06774

[36] S. Godfrey and N. Isgur Physical Review D, **32**(1), 189 (1985). https://doi.org/10.1103/PhysRevD.32.189

[37] S. Godfrey and K. Moats Physical Review D, **92**(5), 054034 (2015). https://doi.org/10.1103/PhysRevD.92.054034

[38] J.-Z. Wang, Z.-F. Sun, X. Liu, and T. Matsuki The European Physical Journal C, **78**, 915 (2018). https://doi.org/10.1140/epjc/s10052-018-6372-1

[39] S. N. Gupta, S. F. Radford, and W. W. Repko Physical Review D, **34**(1), 201 (1986). https://doi.org/10.1103/PhysRevD.34.201

[40] A. Badalian, A. Veselov, and B. Bakker, Physical Review D, **70**(1), 016007 (2004). https://doi.org/10.1103/PhysRevD.70.016007

[41] M. Shah, A. Parmar, and P. Vinodkumar Physical Review D, **86**(3), 034015 (2012). https://doi.org/10.1103/PhysRevD.86.034015

[42] C. Semay and B. Silvestre-Brac Nuclear Physics A, **618**(4), 455 (1997). https://doi.org/10.1016/S0375-9474(97)00060-2

[43] R.L. Workman, et al., "Review of Particle Physics," PTEP, **2022**, 083C01 (2022). https://doi.org/10.1093/ptep/ptac097

[44] J.-E. Augustin, A. Boyarski, M. Breidenbach, F. Bulos, J. Dakin, G. Feldman, G. Fischer, et al., Physical Review Letters, **34**(4), 233 (1975). https://doi.org/10.1103/PhysRevLett.34.233

[45] T. Appelquist, A. De Rujula, S.L. Glashow, and H. Plitzer, tech. rep., SIS-75-0111, 1974

[46] A. De Rujula, and S.L. Glashow, Physical Review Letters, **34**(1), 46 (1975). https://doi.org/10.1103/PhysRevLett.34.46

[47] A.A. Bykov, I.M. Dremin, and A.V. Leonidov, Soviet Physics Uspekhi, **27**(5), 321 (1984)

[48] T. Barnes, S. Godfrey, and E. Swanson, Physical Review D, **72**(5), 054026 (2005). https://doi.org/10.1103/PhysRevD.72.054026

[49] B.L. Ioffe, V.S. Fadin, and L.N. Lipatov, *Quantum chromodynamics: Perturbative and nonperturbative aspects.* No. 30, (Cambridge University Press, 2010).

[50] O. Lakhina, PhD thesis, University of Pittsburgh, 2007

[51] A. Yasser, T. Nahool, and G. Hassan, (2014). https://doi.org/10.48550/arXiv.1410.5005v

[52] L. Bai-Qing and C. Kuang-Ta, Communications in Theoretical Physics, **52**(4), 653 (2009). https://doi.org/10.1088/0253-6102/52/4/20

[53] I. Asghar, F. Akram, B. Masud, and M.A. Sultan, Physical Review D, **100**(9), 096002 (2019). https://doi.org/10.1103/PhysRevD.100.096002

[54] V. Kher, R. Chaturvedi, N. Devlani, and A. Rai, The European Physical Journal Plus, **137**(3), 357 (2022). https://doi.org/10.1140/epjp/s13360-022-02538-5

[55] B. Chen, A. Zhang, and J. He, Physical Review D, **101**(1), 014020 (2020). https://doi.org/10.1103/PhysRevD.101.014020

[56] W.-J. Deng, H. Liu, L.-C. Gui, and X.-H. Zhong, Physical Review D, **95**(7), 074002 (2017). https://doi.org/10.1103/PhysRevD.95.074002

БОТОМОНІЯ ПІД ВПЛИВОМ ТРЬОХ ІНСПІРОВАНИХ ПОТЕНЦІАЛІВ КХД У РАМКАХ НЕРЕЛЯТИВІСТСЬКОЇ КВАРКОВОЇ МОДЕЛІ

Мустафа Ісмаїл Хапарір,[a]**, М. Аллош**[b]**, Г.С. Хассан**[a]**, А.М. Ясер**[b]

[a] *Кафедра фізики, Факультет природничих наук, Асьют, Університет Асьют, 71515 Асьют, Єгипет*

[b] *Фізичний факультет, природничий факультет, Кена, Університет Південної долини, 83523 Кена, Єгипет*

У цій статті ми досліджували спектр поведінки боттонієвих мезонів під впливом трьох типів потенціалів, навіяних квантовою хромодинамікою. Крім того, були вивчені інші властивості, такі як поведінка гіпертонкого розщеплення та поведінка тонкого розщеплення. Ми використали ці потенційні моделі в рамках моделі нерелятивістських кварків, щоб представити це дослідження. Ми виявили, що наші очікування узгоджуються з експериментальними даними та іншими теоретичними роботами, а також ми представили нові висновки щодо спектру невидимих станів боттомонію для S, P і D-хвиль боттомонії. І ми очікували інших їхніх характеристик.

Ключові слова: *властивості гіперрозщеплення; тонке розщеплення; ботомонія*

BIOCONVECTION EFFECTS ON NON-NEWTONIAN CHEMICALLY REACTING WILLIAMSON NANOFLUID FLOW DUE TO STRETCHED SHEET WITH HEAT AND MASS TRANSFER[†]

Muhammad Jawad*,a, M. Muti-Ur-Rehmanb, Kottakkaran Sooppy Nisarc,d

aDepartment of Mathematics, The University of Faisalabad, Faisalabad 38000, Pakistan
bDepartment of Mathematics and Statistics University of Agriculture Faisalabad, Faisalabad 38000 Pakistan
cDepartment of Mathematics, College of Science and Humanities in Alkharj, Prince Sattam Bin Abdulaziz University, Alkharj 11942, Saudi Arabia
dSchool of Techanology, Woxsen University-Hyderabad-502345, Telangana State, India
*Correspounding Author E-mai: muhammad.jawad@tuf.edu.pk
Received March 29, 2023; revised April 18, 2023; accepted April 24, 2023

The aim of this paper is to scrutinize the mixed convective flow of Williamson nanofluid in the presence of stretched surface with various physical effects. The impact of Brownian motion and thermophoresis is the part of this investigation. In addition, the features of thermal radiations is considered in energy equation for motivation of problem. Theory of the microorganism is used to stable the model. Mathematical modelling is carried out. Appropriate similarity functions are used to transform the couple of governing PDEs into set of ODEs. Wolfram MATHEMATICA is engaged to solve transformed equations numerically with the help of shooting scheme. The influence of emerging flow parameters like magnetic, thermophoresis, porosity, Péclet and Lewis number on the velocity, temperature, volumetric concentration and density of microorganism distribution are presented in tables and graphs.
Keywords: *Gyrotactic Microorganism; Williamson nanofluid; MHD; Bioconvection; Shooting method.*
PACS: 44.10.+i, 44.05.+e, 44.30.+v, 47.10.ad.

1. INTRODUCTION

Fluid mechanics have two principal types of fluids called Newtonian and non-Newtonian fluid flow belongings of Newtonian and non-Newtonian fluids are not similar. Newtonian fluids are those which satisfy Newton law of viscosity like water, glycerol, alcohol and benzene. Here, the contact between strain rates is explained by taking out the basic model, especially for such liquids that do not obey the Newton law of viscosity. Fluids like toothpaste, cosmetics, butter, ketchup, custard, shampoo, blood, honey, paint are the examples of non-Newtonian fluids in daily life. Because of the complicated and interdisciplinary nature, the study of non-Newtonian fluids has recently involved a lot of attention from researchers. Nanofluids are small-sized solid particles dissolved in conventional processing fluids. Water, glycerol, engine oils, ethylene glycol, and pump oil are conventional processing fluids. Nanoparticles, which are normally recycled in nanofluids are made from various materials, such as metals or non-metals. Choi and Eastman [1] found that by suspending metallic nanoparticles in traditional fluids, the resulting nanofluids have predicted high thermal conductivity. The movement of heat transfer in a fluid will enhance the conduction and convection coefficients. Nanofluid research is becoming more important and effective. Nanofluids are developed to achieve maximal thermal properties at the smallest concentration possible. The production of nanofluids resulted in increased thermal conductivity and improved heat transfer properties. The transmission qualities and heat conduction characteristics of the base fluids, such as organic, refrigerant, and ethylene liquids, are altered by all non-metallic and metallic particles. In fact, while higher thermal conductivity is dependent on nanoparticles, the efficacy of heat transfer enhancement is also dependent on scattered particles, material type, and other parameters. Using additives to improve a base fluid's heat transfer capacity is another option. Nanofluids have a wide variety of applications and they can be used in different sectors, including heat transferring and other cooling applications. In the biological and biomedical sectors, nanofluids have played vital roles for a long time, and their use will be extended to growth. Nanofluids have also been used as detergents and smart fluids. Jawad et al. [2] has inspected that nanofluid is such kinds of hotness move source having nano-particles with shape short 100 (nm). Wen and Ding [3] have found that nanofluids significantly improved convective heat transfer, according to the findings. The improvement was especially noticeable in the entrance region, and it was much greater than the increase in thermal conduction. The classical Such equation was also shown to be ineffective in predicting the heat transfer conduct of nanofluids. The main explanations were proposed to be nanoparticle migration and the commotion of the boundary layer. Bhattacharya *et al.* [4] have evaluated the thermal conductivities of aluminium oxide-water nanofluids at different temperatures and clarify that the enhancement in thermal conductivity is temperature dependent.

Magnetohydrodynamics, also known as hydro-magnetics, is the learning of dynamics of the existence of magnetic properties and the liquid effects that are electrically conducted. Salt water, liquid metals, plasma and electrolytes are known examples of magneto fluids. Alfvén [5], a Swedish physicist, was the first to introduce the MHD fluid flow. Turkyilmazoglu [6] has calculated analytically the magnetohydrodynamic flow and thermal transport features of nanofluid flow across a continually extending or contracting permeable sheet in the presence of temperature and velocity

---

slip. Qayyum *et al.* [7] have observed analytical treatment of MHD radiative flow of tangential hyperbolic nanofluid under the impact of heat generation or absorption. The study's reproduction was based on Newtonian heat and mass conditions. Mohyud-Din *et al.* [8] have presented a revised model for Stokes first issue in nanofluids. At the boundary, this model considers a zero-flux condition. Following the implementation of the similarity transforms, the governing equations were altered into a system of non-linear ordinary differential equations. Majeed *et al.* [9] has concentrated on that Magnetohydrodynamics manages electrically led liquid having attractive properties in like manner of electrolytes, salt water, plasmas, and fluid metals. Nadeem *et al.* [10] have studied the Casson fluid's MHD boundary layer movement across an increasingly permeable shrink sheet.

Williamson [11] concentrated on the progression of pseudoplastic materials and fostered a model to clarify the progression of liquids and gave trial results. In the Williamson model, the compelling consistency ought to be decreased endlessly by raising the shear rate, which is boundless thickness very still and no consistency as the shear rate approaches endlessness. The Williamson liquid model is an essential reenactment of non-Newtonian liquid viscoelastic shear diminishing highlights. Hayat *et al.* [12] have analysed the results of chemically reactive flow of nanomaterial based on Brownian and Thermophoresis movement with a nonlinear bidirectional stretching layer with a constant thickness. Williamson fluid rheological expressions and the optimal homotopy analysis approach were used. Zaman and Gul [13] have examined in the presence of Newtonian conditions, the magnetohydrodynamic (MHD) of Williamson nanofluid bioconvective flow containing microorganisms. The bvp4c technique is used to achieve numerical solutions. Danish *et al.* [14] have explained a new numerical model to analyse the features of activation energy on magnetized Williamson fluid over a section with nonlinear thermal radiation. The Brownian and thermophoresis nanofluid properties have been described using the Buongiorno model. For more details see Refs [15-23].

Kuznetsov [24] were the first to investigate the topic of bioconvection in a suspension containing small solid particles (nanoparticles). To see how minor particles that are denser than water affect the permanence of a motile gyrotactic bacteria suspension in a finite-depth horizontal fluid layer. Bioconvection has the potential to improve mass transport and mixing, particularly in microvolumes, as well as the stability of nanofluids. Thus, a nanofluid and bioconvection combination could be promising for new microfluidic devices. Khan *et al.* [25] have explained the movement over a permeable wedge in the occurrence of viscous dissipation and Joule heating. The nanofluid containing gyrotactic microorganisms was expected to be saturated in the wedge under the effect of magneto-hydrodynamics. The passive control model was used to formulate the problem. Uddin *et al.* [26] have evaluated numerically the impacts of bioconvection on fluid velocity and thermal slips over the flow of nanofluid passing through the horizontal touching sheet. They introduced the first time-similarity solution to nano-bioconvection. The influences of velocity, the bioconvection Lewis number, Peclet number and the bioconvection Peclet number on the governing equations, including local wall mass flux and local Nusselt number, were discussed. Naz *et al.* [27] have reviewed Cross nanofluid with gyrotactic germs, entropy formation and heat and mass transmission. The solutions were obtained using the optimal homotopy analysis technique, and the most important consequences were discussed graphically and numerically. The geometry of flow model is presented in Fig. 1 as:
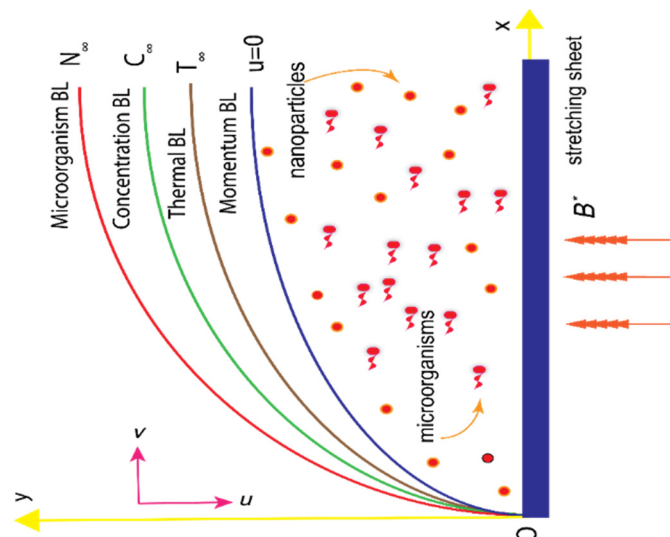

Figure 1. Geometry of physical model

2. PROBLEM STATEMENT

A mathematical study of MHD flow of an incompressible Williamson nanofluid is presented. The two-dimensional fluid flow is passing through porous media and stretched surface. Aman *et al.* [28] work of mixed convection nanofluid flow with gyrotactic microorganisms over extending plate has been considered. The first step is to explore this work and then extending that by observing the consequence of magnetic field, thermal radiation and chemical reaction with compactness of motile microorganisms.

The governing equations [29] are:

$$u_x + v_y = 0 \qquad (1)$$

$$uu_x + vu_y = \nu u_{yy} - \frac{\sigma_e B_0^2 u}{\rho_f} + \Gamma u_y u_{yy} \qquad (2)$$

$$uT_x + vT_Y = \frac{k}{(\rho c)_f}(T_{yy}) + \frac{(\rho c)_p}{(\rho c)_f}\left\{\frac{D_T}{T_\infty}(T_y)^2 + D_B C_y T_y\right\} \qquad (3)$$

$$uC_x + vC_y = D_B C_{yy} + \frac{D_T}{T_\infty}T_{yy} - K_0(C - C_\infty) \qquad (4)$$

$$un_x + vn_y + \frac{bW_c}{C_W - C_\infty}\left[n_y C_{yy}\right] = D_m n_{yy} \qquad (5)$$

Conditions:
The initial and boundary conditions [30] are

$$v = v_0, u = \lambda U_w, T = T_W, C = C_W, N = N_W \text{ at } y = 0,$$

$$u \to 0, T \to T_\infty, C \to C_\infty, N \to N_\infty \text{ as } y \to \infty, \qquad (6)$$

Similarity transformations:

$$u = bxf'(\eta); \; v = -(bv)^{\frac{1}{2}}f(\eta); \; \eta = \sqrt{\frac{b}{v}}y; \; \phi(\eta) = \frac{C - C_\infty}{C_w - C_\infty}; \; \chi(\eta) = \frac{N - N_\infty}{N_w - N_\infty} \; \theta(\eta) = \frac{T - T_\infty}{T_w - T_\infty}.$$

3. NUMERICAL SCHEME: SHOOTING METHOD

The physical aspect of the flow problem under consideration has been investigated by solving the final set of equations, namely (2) to (5) associated with the new boundary conditions (6). The policy of shooting method is specified as next (Fig. 2). The higher order derivatives in the above mentioned are reduced to first order as follows:

$$f'''(\eta) + \lambda f'''(\eta)f''(\eta) + f''(\eta)f(\eta) - f'^2(\eta) - Mf'(\eta) = 0, \qquad (7)$$

$$\theta''(\eta) + Prf(\eta)\theta'(\eta) - 2Pr\theta(\eta) + \frac{Nc}{Le}\phi'(\eta)\theta'(\eta) + \frac{Nc}{(Le)(Nbt)}\theta'^2(\eta) = 0, \qquad (8)$$

$$\phi''(\eta) + \frac{1}{Nbt}\theta''(\eta) + Scf(\eta)\phi'(\eta) - Sc\gamma\phi(\eta) = 0, \qquad (9)$$

$$\chi''(\eta) + Scf(\eta)\chi'(\eta) - Pe[\chi'(\eta)\phi'(\eta) + (\chi(\eta) + \sigma)\phi''(\eta)] = 0. \qquad (10)$$

The higher order equation from (7) to (10) are reduced to first order as

$$f' = u, u' = v, \theta' = w, \phi' = q, \chi' = g,$$

$$v'(1 + \lambda v) + vf - u^2 - Mu = 0, \qquad (11)$$

$$w' + Prfw - 2Pr\theta + \frac{Nc}{Le}qw + \frac{Nc}{(Le)(Nbt)}w^2 = 0, \qquad (12)$$

$$q' + \frac{1}{Nbt}w' + Scfq - Sc\gamma\phi = 0, \qquad (13)$$

$$g' + Scfg - Pe[gq + (\chi + \sigma)q'(\eta)] = 0. \qquad (14)$$

The transformed linearly boundary condition follows that

$$f(0) = S, f'(0) = \lambda, \chi(0) = 1, \theta(0) = 1$$

$$f'(0) = 0, \theta = 0, \phi = 0, \chi = 0 \text{ as } \eta \to \infty \qquad (15)$$

$$\begin{cases} N_b = \dfrac{\tau D_B(C_w - C_\infty)}{\nu}, Nt = \dfrac{\tau D_T(T_w - T_\infty)}{\nu T_\infty}, Sc = \dfrac{\nu}{D_n}, \\[2ex] Pe = \dfrac{bW_c}{D_n}, \sigma = \dfrac{N_\infty}{N_w - N_\infty}, Pr = \dfrac{\nu}{\alpha}, \alpha = \dfrac{k}{(\rho c)_f}, \gamma = \dfrac{K_0}{a}, Le = \dfrac{\nu}{D_B}. \end{cases}$$

The dimensionless drag force factor $Cf_x = \frac{2\tau_w}{\rho_f u_w^2}$, the Nusselt amount $Nu_x = \frac{xq_w}{\alpha_f(T_m - T_\infty)}$, local Sherwood amount

$Sh_x = \frac{xq_s}{D_B(C_w - C_\infty)}$ and density of microorganism's amount $Nn_x = \frac{xq_n}{D_n(N_w - N_\infty)}$ on the surface in x −direction are given by

$$(Re_x)^{1/2}Cf_x = \left[f''(0) + \frac{We}{2}f''^2(0)\right], (Re_x)^{-1/2}Nu_x = -\theta'(0), (Re)^{-\frac{1}{2}}Sh_x = -\phi'(0), (Re)^{-1/2}Nn_x = -\chi'(0) \quad (16)$$
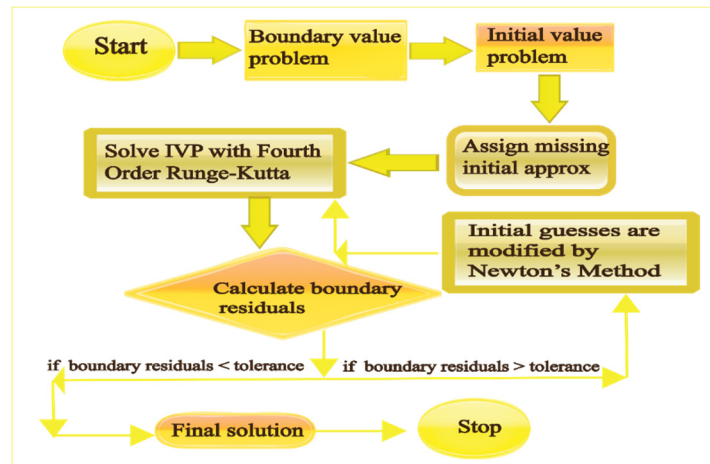
here is Re_x the Reynold amount.

Figure 2. Chart of shooting method steps.

4. CODE VALIDATIONS

Table 1 provides a critical study of the current findings of– $\theta'(0)$ and $-\Phi'(0)$ for the Brownian motion parameter Nbt utilising the bvp4c. The critical study of these numerical findings in Table 1 reveals that the scheme is valid, $M = 0.5$, $\lambda = 0.1$, Pr =7, Nc=σ= 0.3, Pe= Le= Sc=0.2 and $\gamma = 0$. The comparison of findings in Table 1 shows the astonishingly considerable arrangements of the current inquiry with the bvp4c results, which motivates the author to tackle this problem with changes of thermal radiation and chemical reaction effects using a well-known shooting approach.

Table. 1. Comparing of $-\theta'(0)$ and $-\Phi'(0)$ values with Nbt.

Parameter	bvp4c	Present	bvp4c	Present
Nbt	$-\theta'(0)$		$-\Phi'(0)$	
0.1	1.15530	1.15530	0.71014	0.71014
0.2	0.82269	0.82269	0.42568	0.42568
0.3	0.56501	0.56501	0.22571	0.22571
0.4	0.37418	0.37418	0.09420	0.09420
0.5	0.23916	0.23916	0.01731	0.01731

5. RESULT AND DISCUSSION

In the current investigation we analyzed the impact of different parameters graphically on non-layered speed, non-layered liquid temperature, dimensionless liquid focus and non-layered motile microorganism profiles. The principal request arrangement of conditions along with limit and starting conditions is tackled by utilizing the order ND settled on Mathematica. For this, fixed upsides of certain boundaries are picked self-assertively as given in the accompanying: M = 1; S = 2; λ = 1; Sc = 1; σ = 0.1; Nb = 0.5; γ = 0.1; Nt = 0.5; Pe = 1; Pr = 1; Le = 1; Nr = 0.5; Nc = 0.5. Further, in this segment we discussed the graphical consequences of the work of (Aman *et al.* [28]). The first order system of equation (7) to (10) together boundary and initial conditions (15) has been resolved by applying the appreciation ND solve on MATHEMATICA version 11. The computational results for velocity, concentration, temperature, and density function of motile micro-organism have been obtained for several interested parametrical values namely magnetic parameter, the injection/suction parameter, Stretching/Shrinking parameters.

The results have been presented in tabular form in Table 2. The impact of suction/injection at the wall on component of velocity, concentration profile, temperature profile and profile of motile micro-organism.

5.1. Velocity Distribution

In this section, we will confer certain flow parameters that are considered in the velocity contour in the form of schemes. The Hartmann number M, section or injection parameter S are plotted against the velocity function f'. The consequence of the parameter S on the velocity profile f' is shown in Fig. 3. As the parametric value of S increases, the curves show decreasing behavior. The impact of shrinking sheet parameter λ' is described in Figs. 4 and 5.

Table 2. Nusselt number, Sherwood number and local density number at the stretching walls.

M	λ	σ	Pe	S	Pr	Nb	Nc	γ	Le	Sc	$N_u Re_x^{\frac{-1}{2}}$	$S_x Re_x^{\frac{-1}{2}}$	$Nn_x Re_x^{\frac{-1}{2}}$
1.0	0.3	0.2	2.0	1	1.0	0.3	0.3	0.1	0.4	0.4	1.16658	0.56551	4.32922
2.0											1.15122	0.40949	3.21536
3.0											1.07339	0.16074	1.04171
	0.2										0.17513	0.45781	2.94380
	0.6										0.17227	0.44646	2.85186
	0.8										0.16901	0.41386	2.74917
		0.5									1.13332	0.40569	1.36868
		0.9									1.13332	0.40569	1.41038
		1.3									1.13332	0.40569	1.45209
			1.0								1.13733	0.22029	0.43076
			1.5								1.13733	0.22029	0.47949
			2.0								1.13733	0.22029	0.52877
				1							2.16132	1.43886	4.26399
				2							2.16043	1.43679	4.24718
				3							2.15950	1.43468	4.22998
					1.0						0.45076	0.00965	-0.74796
					2.0						0.68382	-0.08265	-1.23761
					3.0						0.84726	-0.07902	-1.04745
						1					1.15747	0.43020	3.19427
						2					0.82403	0.90843	7.04755
						3					0.56578	1.04347	8.14002
							0.5				1.15741	0.43020	3.19439
							1				0.95048	0.10050	0.67047
							1.5				0.86337	0.02480	0.16696
								0.1			1.15751	0.43030	3.19429
								0.5			1.05197	0.48545	3.63175
								1.0			0.99723	0.51465	3.86423
									0.5		1.08466	0.35128	2.43539
									1.0		0.93458	0.66761	5.01486
									1.5		0.83408	0.97853	7.05758
										1	0.82404	0.90851	7.04754
										2	0.89140	0.75772	5.85982
										3	0.92655	0.68163	5.26338
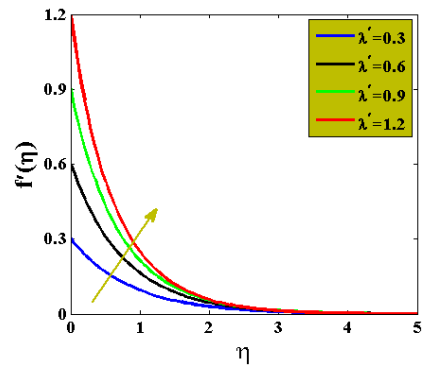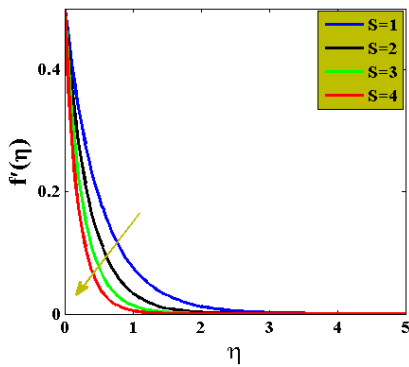
Figure 3. Distribution of velocity profile for some values of S

Figure 4. Distribution of velocity profile for some values of λ'.

The speed of flow is enhanced and reduced for increasing values of λ' and λ respectively. The sense of parameter M on velocity profile of the fluid is demonstrated by Fig. 6.
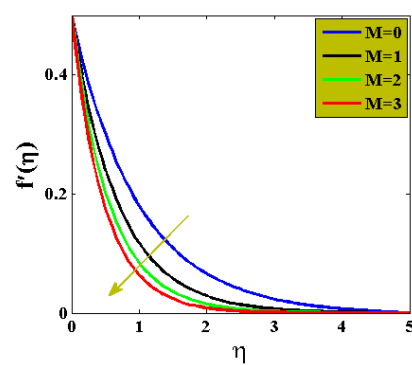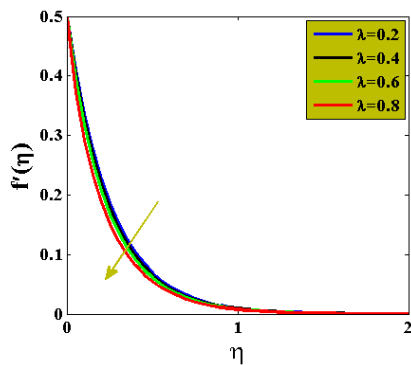
Figure 5. Graph pattern of velocity profile for some values of λ.

Figure 6. Diagram of velocity profile for some values of M.

These curves show reduction in velocity profile with the cumulative values of M. It is because of the cooperation of restricting powers, to be specific Lorentz power, which is expanded. The Lorentz power is a blend of electric and attractive powers on a moving point charge because of electromagnetic fields. Lorentz powers are resistive powers and are associated with attractive numbers. With the augmentation in, Lorentz power supports up, which goes against the fluid stream because of decrease in the speeds.

5.2. Temperature Distribution

In this section, parametrical effects of diffusivity ratio Nbt, Prandtl number $\Pr$, chemical reaction parameter γ, magnetic parameter M, Lewis number Le, suction or injection parameter S, shrinking sheet parameter λ', and parameter of heat capacity Nc are depicted in Figs. 7-13. Behavior of temperature profile with deference to parameter S is represented by Fig. 7. When there is gradual increase in the standards of suction or injection parameter S, curves of temperature profile depict deceleration behavior gradually. Fig. 8 illustrates the behavior regarding magnetic parameter on temperature profile.
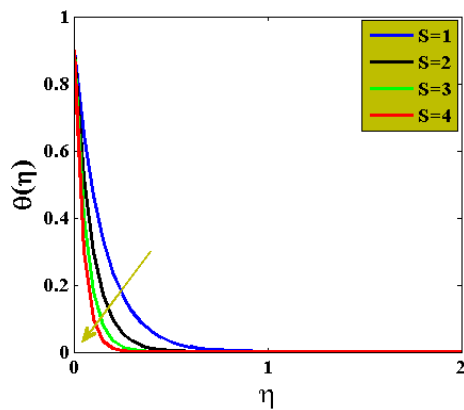
Figure 7. Diagram of temperature profile
for some values of S
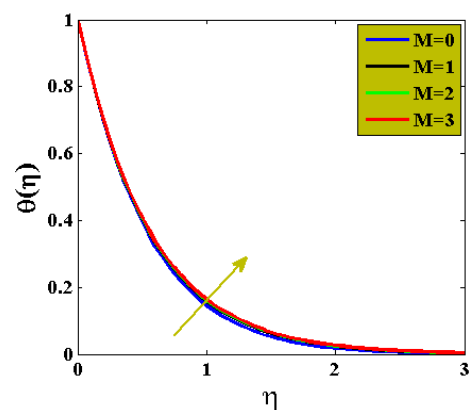
Figure 8. Diagram of temperature profile
for some values of M

The graph curves show significant increment in temperature profile with the increasing values of M. Fig. 9 shows the consequence of shrinking parameter λ' on temperature profile. The decrease in the principles of λ' in the stretching case resulted in reducing the temperature contour θ. Fig. 10 is sketched to analyze the influence of Prandtl number $\Pr$ on temperature profile, while keeping other parameters constant. Deceleration in temperature field was obtained when increment was done in values of $\Pr$.
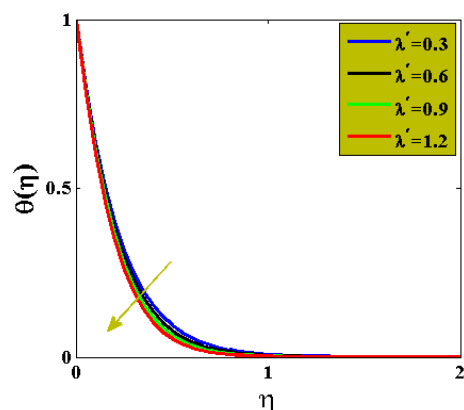

Figure 9. Diagram of temperature profile
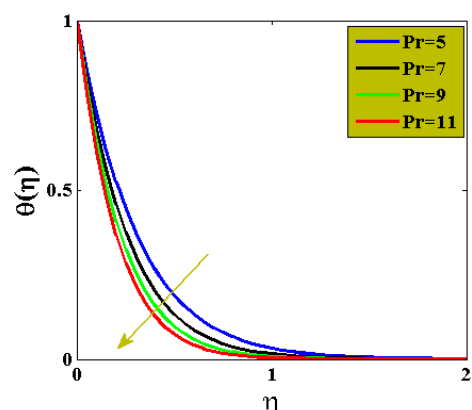for some values of λ'.

Figure 10. Diagram of temperature profile
for some values of Pr.

Fig. 11 is demonstrated to examine the effect of Nc on the temperature profile. When the increment is done in the parametric value of heat capacity ratio, the curves of temperature profile gave an increasing behavior. So, temperature was increased with increasing the heat capacity ratio. Fig. 12 indicates the conduct of temperature profile with respect to parametric values of diffusivity ratio Nbt. When a gradual increment is done in the morals of diffusivity ratio Nbt, deceleration is obtained in the temperature field. Fig. 13 is drawn to summarize the consequence of Lewis number Le on the temperature profile. The curve pattern shows that the increasing Lewis number markedly decreased the temperature profile.
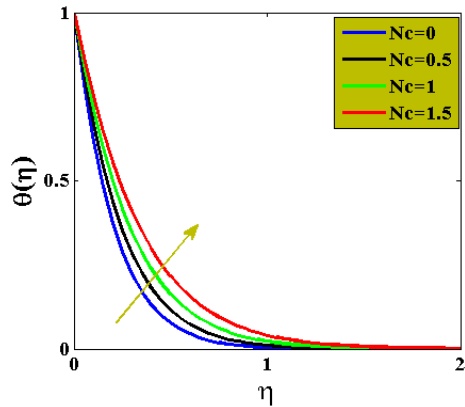
Figure 11. Diagram of temperature profile
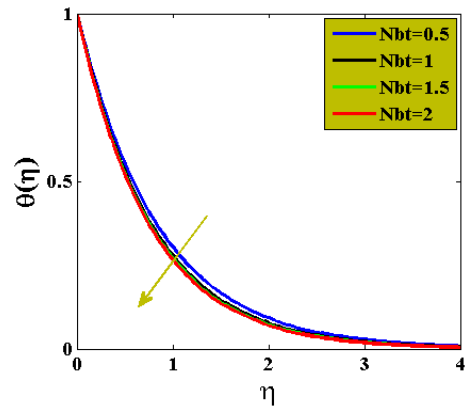for some values of Nc

Figure 12. Diagram of temperature profile
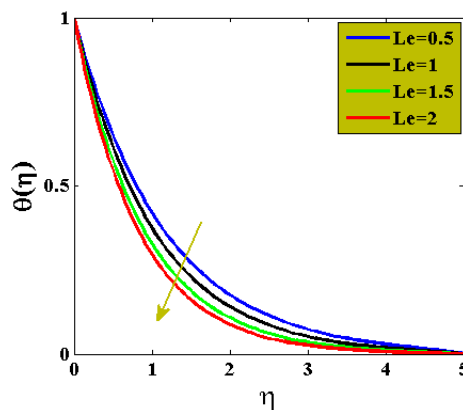for some values Nbt.

Figure 13. Diagram of temperature profile
for some values of Le.

5.3. Concentration Distribution

In this section, influences regarding diffusivity ratio parameter Nbt, chemical reaction parameter γ, magnetic parameter M, suction or injection parameter S, shrinking sheet parameter λ' and Schmidt number Sc are depicted on the concentration profile in Figs. 14-19. Fig. 14 displays the effect of stretching or shrinking sheet parameter on concentration profile. On increasing values of λ', a decreasing behavior of concentration is obtained. In Fig. 15, diffusivity ratio parameter Nbt is depicted to show its behaviour on concentration profile.
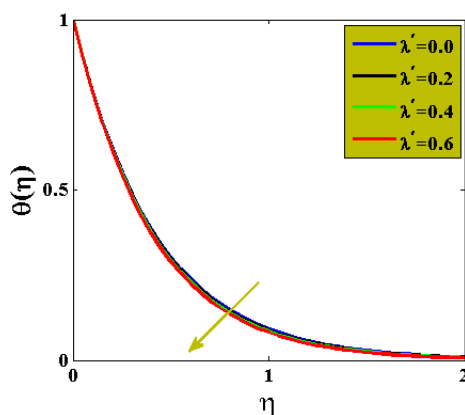

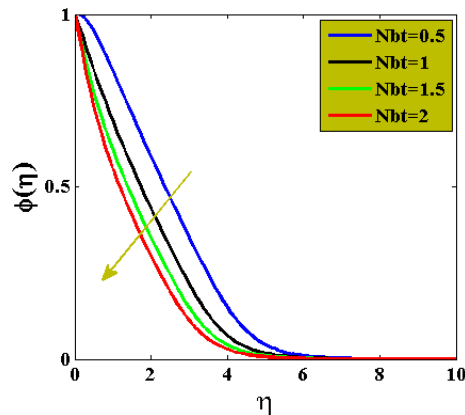**Figure 14.** Diagram of concentration profile
for some values of λ'

Figure 15. Diagram of concentration profile
for some values of Nbt

A significant downfall in the curve of concentration profile is obtained when gradual increase is done in diffusivity ratio parameter Nbt. Behavior of concentration profile regarding Schmidt number Sc is depicted in Fig.16. When parametrical values of Sc are boosted up, a significant decrease is resulted in concentration profile. Schmidt number is ratio between viscosity and molecular diffusion. Impact of chemical reaction parameter γ on concentration profile is depicted in Fig.17.
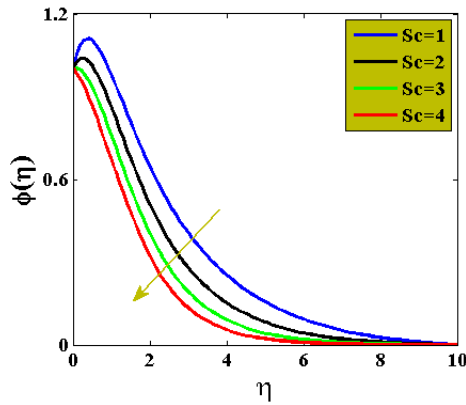
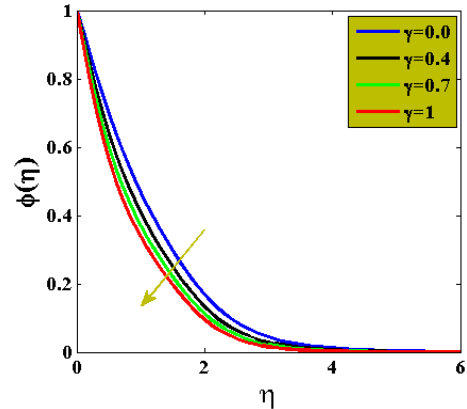**Figure 16.** Diagram of concentration profile for some values of Sc.

Figure 17. Diagram of concentration profile for some values of γ.

Curve of concentration profile of fluid is decreased when chemical reaction parameter γ is increased. The concentration profile curve with respect to magnetic parameter M is demonstrated in Fig. 18. A remarkable increment is resulted in concentration field when magnetic field parameter is increased. The change in concentration profile for some values of suction or injection parameter S is elaborated in Fig. 19. A decreasing behavior of concentration profile of fluid is obtained with increasing values of S.
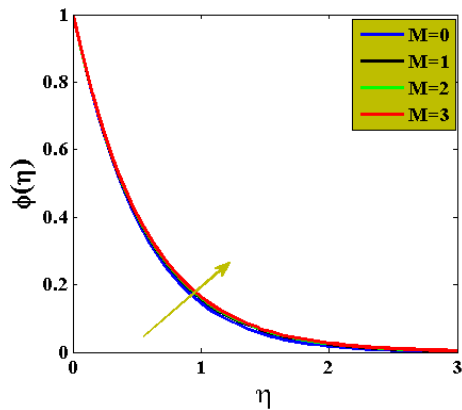

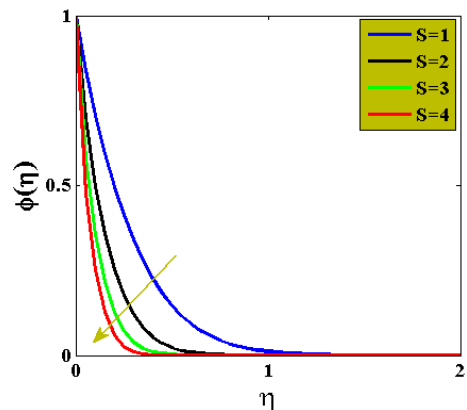**Figure 18.** Diagram of concentration profile for some values of M.

Figure 19. Diagram of concentration profile for some values of S.

5.4. Motile microorganism density Distribution

In this section, effects regarding Schmidt number Sc, Peclet number Pe, σ, and suction or injection parameter S on the density profile of motile micro-organism are discussed in Figs. 20-23. Fig. 20 shows the effect of Peclet number Pe on the density of motile microorganisms. It is observed that increment in the values of Peclet number is caused in increasing the density of motile microorganisms. Fig. 21 shows the effect of parametrical values of suction/injection on the density of motile microorganisms.
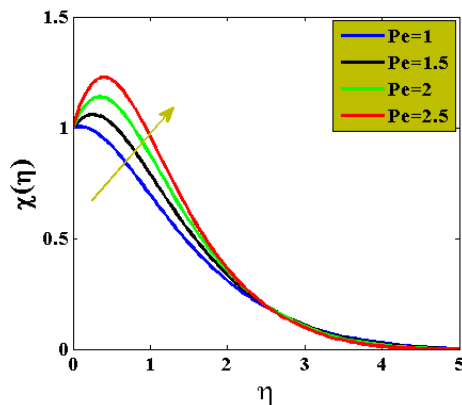

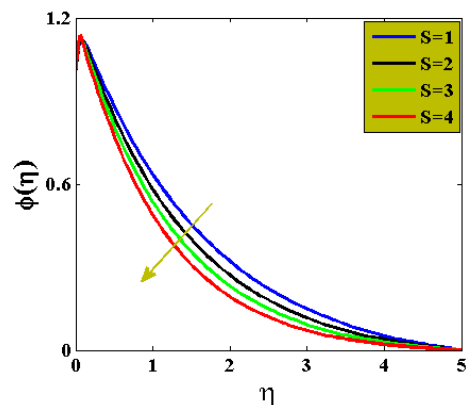**Figure 20.** Diagram of motile microorganism profile for some values of Pe.

Figure 21. Diagram of motile microorganism profile for some values of S.

According to the plot, deceleration in density is attained for increasing values of S. The graph of Schmidt number Sc on motile density profile is displayed in Fig. 22. Density profile of motile microorganisms is decreased for gradual increase in Schmidt number. Effect of dimensionless parameter σ on density of microorganism is presented in Fig. 23. An important growth is observed in density, when dimensionless parameter σ is increased.
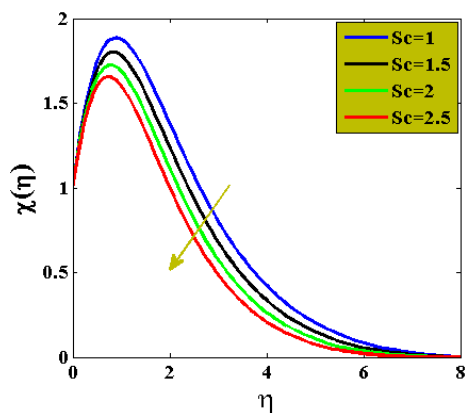

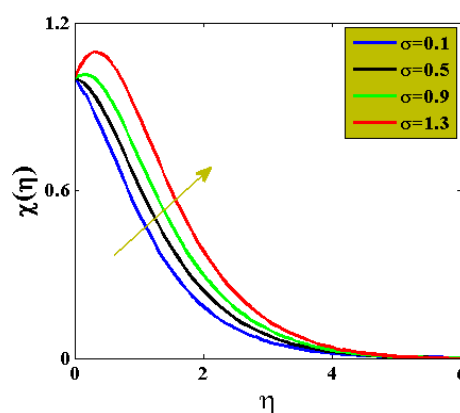**Figure 22.** Diagram of motile microorganism profile for some values of Sc.

Figure 23. Diagram of motile microorganism profile for some values of σ.

6. CONCLUSION

The main objective is to understand the "radiative effects on MHD Williamson nanofluid flow over a porous stretching sheet with gyrotactic microorganism: Buongiorno's model". Furthermore, the impacts of chemical reaction, magnetic effect and density of motile microorganism are under assumption. Firstly, useful dimensionless variables are implemented to alter the system of partial differential equations into system of ordinary differential equations. Later on, the approximate solution of transformed boundary value problem is calculated by using shooting scheme for numerically solution by employing ND solving command on Mathematica software. The effects of different physical parameters on non-dimensional velocity function, temperature profile, mass concentration profile and motile microorganism's density function are observed. The principal revelations of this work are as per the following:

- The effect of attractive field is to diminish every one of the actual amounts of interest, where it affected fundamentally on speed work.
- The speed of nanofluids diminishes by expanding attractions boundary S.
- The temperature nanofluids profile increments by expanding Nc.
- The temperature work for nanofluids diminishes by expanding Prandtl number Pr.
- The concentration function decreases by increasing Nb.
- The concentration function decreases by increasing Sc.
- The microorganism density is increased by collective bio convection Peclet number Pe

The shooting method could be applied to a variety of physical and technical challenges in the future [31-35].

Data Availability
All data generated or analyzed during this study are included in this published article.

Conflict of Interest
The authors announce that no conflict of curiosity exists.

ORCID IDs
Muhammad Jawad, https://orcid.org/0000-0002-9304-615X; M. Muti-Ur-Rehman, https://orcid.org/0009-0008-5572-5208
Kottakkaran Sooppy Nisar, https://orcid.org/0000-0001-5769-4320

REFERENCE
[1] S.U. Choi, and J.A. Eastman, Enhancing thermal conductivity of fluids with nanoparticles, Argonne National Lab., IL (United States), **29**, 99-105 (1995). https://www.osti.gov/biblio/196525
[2] M. Jawad, K. Shehzad, R. Safdar, and S. Hussain, "Novel computational study on MHD flow of nanofluid flow with gyrotactic microorganism due to porous stretching sheet," Punjab University Journal of Mathematics, **52**(12), 43-60 (2020). http://pu.edu.pk/images/journal/maths/PDF/Paper_5_52_12_2020.pdf
[3] D. Wen, and Y. Ding, "Experimental investigation into convective heat transfer of nanofluids at the entrance region under laminar flow conditions," International journal of heat and mass transfer, **47**, 5181-5188 (2004). https://doi.org/10.1016/j.ijheatmasstransfer.2004.07.012
[4] P. Bhattacharya, S. Nara, P. Vijayan, T. Tang, W. Lai, P.E. Phelan, R.S. Prasher, D.W. Song, and J. Wang. "Evaluation of the Temperature Oscillation Technique to Calculate Thermal Conductivity of Water and Systematic Measurement of the Thermal

Conductivity of Aluminum Oxide–Water Nanofluid," American Society of Mechanical Engineers Digital Collection, Heat Transfer, **2**, 51-56 (2004). https://doi.org/10.1115/IMECE2004-60257

[5] H. Alfven, "Existence of electromagnetic-hydrodynamic waves," Nature, **150**, 405-406 (1942). https://doi.org/10.1038/150405d0

[6] M. Turkyilmazoglu, "Exact analytical solutions for heat and mass transfer of MHD slip flow in nanofluids," Chemical Engineering Science, **84**, 182-187 (2012). https://doi.org/10.1016/j.ces.2012.08.029

[7] S. Qayyum, T. Hayat, S.A. Shehzad, and A. Alsaedi, "Mixed convection and heat generation/absorption aspects in MHD flow of tangent-hyperbolic nanoliquid with Newtonian heat/mass transfer," Radiation Physics and Chemistry, **144**, 396-404 (2018). http://dx.doi.org/10.1016/j.radphyschem.2017.10.002

[8] S.T. Mohyud-Din, U. Khan, N. Ahmed, and M.M. Rashidi, "A study of heat and mass transfer on magnetohydrodynamic (MHD) flow of nanoparticles," Propulsion and Power Research, **7**, 72-77 (2018). https://doi.org/10.1016/j.jppr.2018.02.001

[9] A. Majeed, A. Zeeshan, and M. Jawad, "Double stratification impact on radiative MHD flow of nanofluid toward a stretchable cylinder under thermophoresis and Brownian motion with multiple slip," International Journal of Modern Physics B, 2350232, (2023). https://doi.org/10.1142/S0217979223502326

[10] S. Nadeem, R. Ul Haq, and C. Lee, "MHD flow of a Casson fluid over an exponentially shrinking sheet," Scientia Iranica, **19**, 1550-1553 (2012). http://dx.doi.org/10.1016/j.scient.2012.10.021

[11] R.V. Williamson, "The flow of pseudoplastic materials," Industrial & Engineering Chemistry, **21**, 1108-1111 (1929). https://doi.org/10.1021/ie50239a035

[12] T. Hayat, M.Z. Kiyani, A. Alsaedi, M. Ijaz Khan, and I. Ahmad, "Mixed convective three-dimensional flow of Williamson nanofluid subject to chemical reaction," International Journal of Heat and Mass Transfer, **127**, 422-429 (2018). https://doi.org/10.1016/j.ijheatmasstransfer.2018.06.124

[13] S. Zaman, and M. Gul, "Magnetohydrodynamic bioconvective flow of Williamson nanofluid containing gyrotactic microorganisms subjected to thermal radiation and Newtonian conditions," Journal of Theoretical Biology, **479**, 22-28 (2019). https://doi.org/10.1016/j.jtbi.2019.02.015

[14] G.A. Danish, M. Imran, M. Tahir, H. Waqas, M.I. Asjad, A. Akgül, and D. Baleanu, "Effects of Non-Linear Thermal Radiation and Chemical Reaction on Time Dependent Flow of Williamson Nanofluid with Combine Electrical MHD and Activation Energy," Journal of Applied and Computational Mechanics, **7**(2), 546-558 (2021). https://doi.org/10.22055/jacm.2020.35122.2568

[15] V. Kumar, S.K. Singh, V. Kumar, W. Jamshed, and K.S. Nisar, "Thermal and thermo-hydraulic behaviour of alumina-graphene hybrid nanofluid in minichannel heat sink: An experimental study," International Journal of Energy Research, **45**(15), 20700-20714 (2021). https://doi.org/10.1002/er.7134

[16] J. Zhang, S.M. Sajadi, Y. Chen, I. Tlili, and M.A. Fagiry, "Effects of Al_2O_3 and TiO_2 nanoparticles in order to reduce the energy demand in the conventional buildings by integrating the solar collectors a-nd phase change materials," Sustainable Energy Technologies and Assessments, **52**, 102114 (2022). https://doi.org/10.1016/j.seta.2022.102114

[17] I. Tlili, and T. Alharbi, "Investigation into the effect of changing the size of the air quality and stream to the trombe wall for two different arrangements of rectangular blocks of phase change material in this wall," Journal of Building Engineering, **52**, 104328 (2022). https://doi.org/10.1016/j.jobe.2022.104328

[18] X. Qi, M.O. Sidi, I. Tlili, T.K. Ibrahim, M.A. Elkotb, M.A. El-Shorbagy, and Z. Li, "Optimization and sensitivity analysis of extended surfaces during melting and freezing of phase changing materials in cylindrical Lithium-ion battery cooling," Journal of Energy Storage, **51**, 104545 (2022). https://doi.org/10.1016/j.est.2022.104545

[19] J. Alzahrani, H. Vaidya, K.V. Prasad, C. Rajashekhar, D.L. Mahendra, and I. Tlili, "Micro-polar fluid flow over a unique form of vertical stretching sheet: Special emphasis to temperature-dependent properties," Case Studies in Thermal Engineering, **34**, 102037 (2022). https://doi.org/10.1016/j.csite.2022.102037

[20] J. Gao, J. Liu, H. Yue, Y. Zhao, I. Tlili, and A. Karimipour, "Effects of various temperature and pressure initial conditions to predict the thermal conductivity and phase alteration duration of water-based carbon hybrid nanofluids via MD approach," Journal of Molecular Liquids, **351**, 118654 (2022). https://doi.org/10.1016/j.molliq.2022.118654

[21] R.T. Mahmood, M.J. Asad, S.H. Hadri, M.A. El-Shorbagy, A.A.A. Mousa, R.N. Dara, M. Awais, and I. Tlili, "Bioremediation of textile industrial effluents by Fomitopsis pinicola IEBL-4 for environmental sustainability," Human and Ecological Risk Assessment: An International Journal, **29**(2), 285-302, (2023). https://doi.org/10.1080/10807039.2022.2057277

[22] M.K. Nayak, F. Mabood, A.S. Dogonchi, K.M. Ramadan, I. Tlili, and W.A. Khan, "Entropy optimized assisting and opposing non-linear radiative flow of hybrid nanofluid," Waves in Random and Complex Media, 1-22 (2022). https://doi.org/10.1080/17455030.2022.2032474

[23] K.M. Ramadan, O. Qisieh,, and I. Tlili, "Thermal creep effects on fluid flow and heat transfer in a microchannel gas cooling," Proceedings of the Institution of Mechanical Engineers, Part C: Journal of Mechanical Engineering Science, **236**(9), 5033-5047 (2022). https://doi.org/10.1177/09544062211057039

[24] A.V. Kuznetsov, and A.A. Avramenko, "Effect of small particles on this stability of bioconvection in a suspension of gyrotactic microorganisms in a layer of finite depth," International Communications in Heat and Mass Transfer, **31**(1), 1-10 (2004). https://doi.org/10.1016/S0735-1933(03)00196-9

[25] U. Khan, N. Ahmed, and S.T. Mohyud-Din, "Influence of viscous dissipation and Joule heating on MHD bio-convection flow over a porous wedge in the presence of nanoparticles and gyrotactic microorganisms," Springerplus, **5**, 1-18 (2016). https://doi.org/10.1186/s40064-016-3718-8

[26] M.J. Uddin, M.N. Kabir, and O.A. Bég, "Computational investigation of Stefan blowing and multiple-slip effects on buoyancy-driven bioconvection nanofluid flow with microorganisms," International Journal of Heat and Mass Transfer, **95**, 116-130 (2016). https://doi.org/10.1016/j.ijheatmasstransfer.2015.11.015

[27] R. Naz, M. Noor, T. Hayat, M. Javed, and A. Alsaed, "Dynamism of magnetohydrodynamic cross nanofluid with particulars of entropy generation and gyrotactic motile microorganisms," International Communications in Heat and Mass Transfer, **110**, 104431 (2020). https://doi.org/10.1016/j.icheatmasstransfer.2019.104431

[28] F. Aman, W.N.H.W.M. Khazim, and S. Mansur, "Mixed convection flow of a nanofluid containing gyrotactic microorganisms over a stretching/shrinking sheet in the presence of magnetic field," J. Phys.: Conf. Ser. **890**, 012027 (2017). https://doi.org/10.1088/1742-6596/890/1/012027

[29] M. Jawad, F. Mebarek-Oudina, H. Vaidya, and P. Prashar, "Influence of Bioconvection and Thermal Radiation on MHD Williamson Nano Casson Fluid Flow with the Swimming of Gyrotactic Microorganisms Due to Porous Stretching Sheet," Journal of Nanofluids, **11**(4), 500-509 (2022). https://doi.org/10.1166/jon.2022.1863

[30] X. Zhang, D. Yang, M.I.U. Rehman, A. Mousa, and A. Hamid, "Numerical simulation of bioconvection radiative flow of Williamson nanofluid past a vertical stretching cylinder with activation energy and swimming microorganisms," Case Studies in Thermal Engineering, **33**, 101977 (2022). https://doi.org/10.1016/j.csite.2022.101977

[31] M. Jawad, M.K. Hameed, A. Majeed, and K.S. Nisar, "Arrhenius energy and heat transport activates effect on gyrotactic microorganism flowing in maxwell bio-nanofluid with nield boundary conditions," Case Studies in Thermal Engineering, **41**, 102574 (2023). https://doi.org/10.1016/j.csite.2022.102574

[32] M. Jawad, M.K. Hameed, K.S. Nisar, and A.H. Majeed, "Darcy-Forchheimer flow of maxwell nanofluid flow over a porous stretching sheet with Arrhenius activation energy and nield boundary conditions," Case Studies in Thermal Engineering, **44**, 102830 (2023). https://doi.org/10.1016/j.csite.2023.102830

[33] M. Jawad, "Insinuation of Arrhenius Energy and Solar Radiation on Electrical Conducting Williamson Nano Fluids Flow with Swimming Microorganism: Completion of Buongiorno's Model," East European Journal of Physics, (1), 135-145 (2023). https://periodicals.karazin.ua/eejp/article/view/20900/19827

[34] M. Jawad, "A Computational Study on Magnetohydrodynamics Stagnation Point Flow of Micropolar Fluids with Buoyancy and Thermal Radiation due to a Vertical Stretching Surface," Journal of Nanofluids, **12**, 759-766 (2023). https://doi.org/10.1166/jon.2023.1958

[35] A. Majeed, A. Zeeshan, M. Jawad, and M.S. Alhodaly, "Influence of melting heat transfer and chemical reaction on the flow of non-Newtonian nanofluid with Brownian motion: Advancement in mechanical engineering," Proceedings of the Institution of Mechanical Engineers, Part E: Journal of Process Mechanical Engineering, 09544089221145527 (2022). https://doi.org/10.1177/09544089221145527

ВПЛИВ БІОКОНВЕКЦІЇ НА ПОТІК НЕНЬЮТОНІВСЬКОЇ ХІМІЧНО РЕАГУЮЧОЇ НАНОРІДИНИ ВІЛЬЯМСОНА ЧЕРЕЗ РОЗТЯГНУТУ ПОВЕРХНЮ З ТЕПЛО-ТА МАСОПЕРЕНОСОМ

Мухаммад Джавад[a], М. Муті-Ур-Рехман[b], Коттаккаран Суппі Нісар[c,d]

[a]Кафедра математики, Фейсалабадський університет, Фейсалабад 38000, Пакистан
[b]Кафедра математики та статистики Університет сільського господарства Фейсалабад, Файсалабад 38000 Пакистан
[c]Кафедра математики, Коледж природничих і гуманітарних наук, Алхардж, Університет принца Саттама бін Абдулазіза, Алкхардж 11942, Саудівська Аравія

Метою цієї статті є детальне дослідження змішаного конвективного потоку нанорідини Вільямсона за наявності розтягнутої поверхні з різними фізичними ефектами. Вплив броунівського руху та термофорезу є частиною цього дослідження. Крім того, для мотивації проблеми в рівнянні енергії враховуються особливості теплового випромінювання. Для стабільності моделі використовується теорія мікроорганізму. Проведено математичне моделювання. Відповідні функції подібності використовуються для перетворення пари керуючих PDE в набір ODE. Wolfram MATHEMATICA займається чисельним вирішенням трансформованих рівнянь за допомогою схеми зйомки. Вплив параметрів потоку, таких як магнетизм, термофорез, пористість, число Пекле та Льюіса, на швидкість, температуру, об'ємну концентрацію та щільність розподілу мікроорганізмів представлено в таблицях і графіках.

Ключові слова: *гіротаксичний мікроорганізм; нанорідина Вільямсона; МГД; біоконвекція; метод стрільби*

THE EFFECT OF GAS FLOW RATE, EXPOSURE TIMES AND AGEING ON THE PHYSICOCHEMICAL PROPERTIES OF WATER ACTIVATED BY GLOW DISCHARGE PLASMA JET†

Farah A. Naeim*, Hammad R. Humud

Department of Physics, College of Science, University of Baghdad, Baghdad, Iraq
Corresponding author email: farahammar900@gmail.com

The goal of this work is to look into how the glow discharge plasma jet system changes the chemical and physical features of water. In this work, the physical and chemical properties of water were studied by using a plasma jet with Argon gas. 10 cm^3 of distilled water was put in a glass dish with a diameter of 5 cm and a depth of 1 cm. The system was run with an AC voltage of 12 kV and a frequency of 20 kHz, and the exposure time ranged from 1 to 30 minutes. With amounts of 0.7, 1.0, 1.5, and 2.1 l/min, kits made by the American company Bartvation were used to measure the types of reactive oxygen and nitrogen species (RONS) that were formed. The data showed that the levels of NO_2, NO_3, and H_2O_2 were all too high. It gets bigger over time and as the flow rate goes up. The pH goes down with time until it hits 3, and the temperature goes up until it reaches 33°C. However, the pH goes up with storage time, and after 24 hours the water is back to its natural pH of 7. The amount of NO_2, NO_3, in the air goes up a little bit, and then starts to go down rapidly after 6 hours. After 24 hours, it is close to zero. From this, it's clear that the glow discharge plasma jet device can make RONS, which can be used for biological purposes.

Keywords: *Non-Thermal Plasma (NTP); Direct Current (DC); Plasma Activated Water (PAW)*
PACS: 52.25.-b, 52.40.Hf, 52.55.Dy

1. INTRODUCTION

Non-thermal plasma (NTP) is an ionized gas—the fourth state of matter—that generates reactive chemical species, such as reactive oxygen and nitrogen species, electrons, atoms, neutral molecules, charged species, and ultraviolet radiation [1]. NTP can be artificially generated from ambient air or certain gases at atmospheric and low pressures in the presence of a high voltage (~kV) electric current, current (AC), or direct current (DC) can be used for plasma discharge [2]. There are several types of plasma systems suitable for biological and medical applications. The most widely used plasmas are atmospheric pressure dielectric barrier discharges DBD, plasmas jet, and coronary discharges [3,4,5]. One popular technique has been the application of plasma into water to produce plasma-activated water (PAW). The PAW technology has been used in many applications such as disinfection against bacteria, as fertilizer, in chemical reduction, and in water treatment disinfection and sterilization applications, dermatology, cancer treatment, dentistry, anti-fungal treatment, and wound healing. PAW is considered a technology that has various applications, and it is an ecofriendly and cost-effective disinfectant [6]. The key inactivation agents of PAW are the creation of reactive oxygen species (ROS) (atomic oxygen (O), superoxide (O_2-), hydrogen peroxide (H_2O_2), hydroxyl radicals (OH•), and singlet oxygen $^1O_2$ [7], these components have a role later in the process of activating the water. Also, reactive nitrogen species RNS such as NO_2, NO_3 and proxy nitrite will be form [8, 9]. When these compounds reach the surface of the liquid, they will dissolve in the liquid (water) and change its chemical and physical properties. In addition, the non-thermal plasma interaction with the liquid leads to the dissolution of molecules and a very effective layer of electrons. The molecules fragment of the liquid and the interaction of the reactive species of oxygen and nitrogen RNOS with the layer of electrons on the surface of the water leads to an increase in the hydrogen number of the water PH and formation of free radicals that will contribute a lot to the applications of PAW when it is used in the medical or biological field [10]. Non-thermal plasma can be used directly in disinfection and sterilization applications, dermatology, cancer treatment, dentistry, anti-bacterial and anti-fungal treatment, and wound healing [11-14]. They studied compare the exposure of the tooth root canal contaminated with Escherichia coli bacteria to plasma jet and plasma-activated water. The obtained results found that the response of bacteria to treatment with plasma jet is better than treatment with activated water with plasma [15]. Surat Abdul-Kadhim and Hamad R. Hammoud studied Building a plasma jet system for biological purposes. The developed plasma system consists of a power source and a plasma torch. The results showed that the developed plasma is suitable for biological applications [16]. I.E. Vlad et al found that PAW treatment caused a significant reduction in the viability of all bacterial strains tested. The bacterial inhibition effect was found to be dose-dependent, with higher doses resulting in greater inhibition. The authors also investigated the mechanism of action of PAW and found that it induced oxidative stress and DNA damage in the bacteria, leading to their death [17]. Yinglong Li et al utilized a plasma jet device to generate PAW and tested its antimicrobial effect against three strains of bacteria: Streptococcus mutans, Porphyromonas gingivalis, and Candida albicans. The study found that PAW significantly reduced the viability of all three strains of bacteria in a dose-dependent manner [18]. Renwu Zhou et al studied different methods used to generate PAW and the effects of plasma parameters on the generation of reactive species. The authors also discuss the

---

mechanisms of reactive species formation in PAW and their potential biological applications, including disinfection, wound healing, and cancer treatment [19]. Tomy Abuzairi et al studied plasma treatment using atmospheric pressure plasma was demonstrated. Physicochemical properties such as pH, temperature, ORP, and nitrite concentration were assessed. The results suggest that plasma treatment causes acidification on water and generate reactive species, creating an environment suitable for killing bacteria [20]. Rajesh Prakash Guragain et al studied PAW is tested on four seed species: phapar (Fagopyrum esculentum), barley (Hordeum vulgare), mustard (Brassica nigra), and rayo (Brassica juncea). The line-frequency air-operated gliding arc discharge (GAD) system treated DI water for 5- or 10-min. PAW had significantly different physiochemical characteristics than DI water. DI water temperature remained unchanged after GAD exposure. PAW improved all calculated germination parameters compared to the control. They also increased seedling length and vigor [21].

This work will work on developing a glow-discharge plasma jet system. Then a certain amount of water activates after placing it in a suitable container with the two types of plasma. We depend on exposure time, gas type, and flow rate as basic variables. Then we are working to determine the amount of NO_2, NO_3 and H_2O_2 as a function of time and flow rate. The quantitative and qualitative analysis is carried out by means of kits manufactured for this purpose. In addition to PH and water temperature. Then we determine the best conditions to obtain the largest amount of activated water and the highest concentrations of the RONS.

2. EXPERIMENTAL WORKS

The water was irradiated by plasma jet system. Fig. 1 show the system used for the irradiation. The system consists of a power supply capable of supplying a high alternating voltage of up to 12 kV in the form of a sinusoidal wave with a frequency of 20 kHz. The high voltage was connected to an electrode made of aluminum wrapped at the end of a glass tube with inner diameter of 5 mm at a distance of one centimeter from the end of the tube. About 2 cm separates the tube from the water, and the flow is so small that we can't see any swirls on the surface. The second electrode of the system, which was in the form of aluminum plate, was placed under the water container as shown in Fig. 1.

The glass tube at the other end was connected to a bottle of argon gas through a flow rate regulator. 10 cm^3 of distilled water was placed in a container made of glass in the form of a dish with a diameter of 5 cm and a depth of 1 cm. This work was done by a group of researchers, some of whom work on microscopes (meaning spectral studies), some on plasma-activated water (meaning bacteria and viruses), and some on creating plasma systems for activating water. For the purpose of studying the effect of plasma on water, we adopted two variables, the first is the exposure time at intervals, where the longest exposure time was 30 minutes, and the second was the flow rate of argon gas, where the flow rate adopted at 0.7, 1.0, 1.5 and 2.1 l/min. After that, the concentrations of NO_2, NO_3, and H_2O_2 were measured as a function of exposure time and flow rate of argon gas, using special kits for this purpose. The pH and temperature of the water were also measured. The acidity was measured with a pH scale and temperature using an IR thermometer. The concentrations of NO_2, NO_3, H_2O_2 and acidity were also measured after stopping exposure to plasma and for different periods of time in order to determine the effect of storage on the chemical and physical properties of activated water.
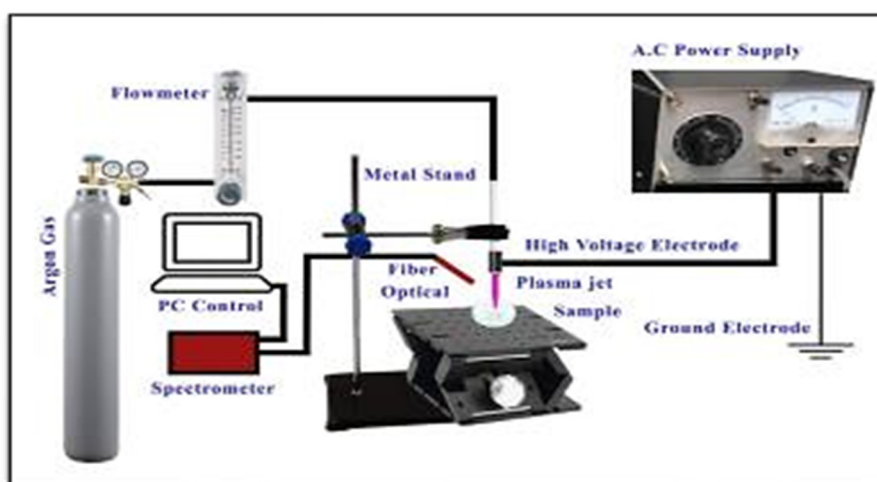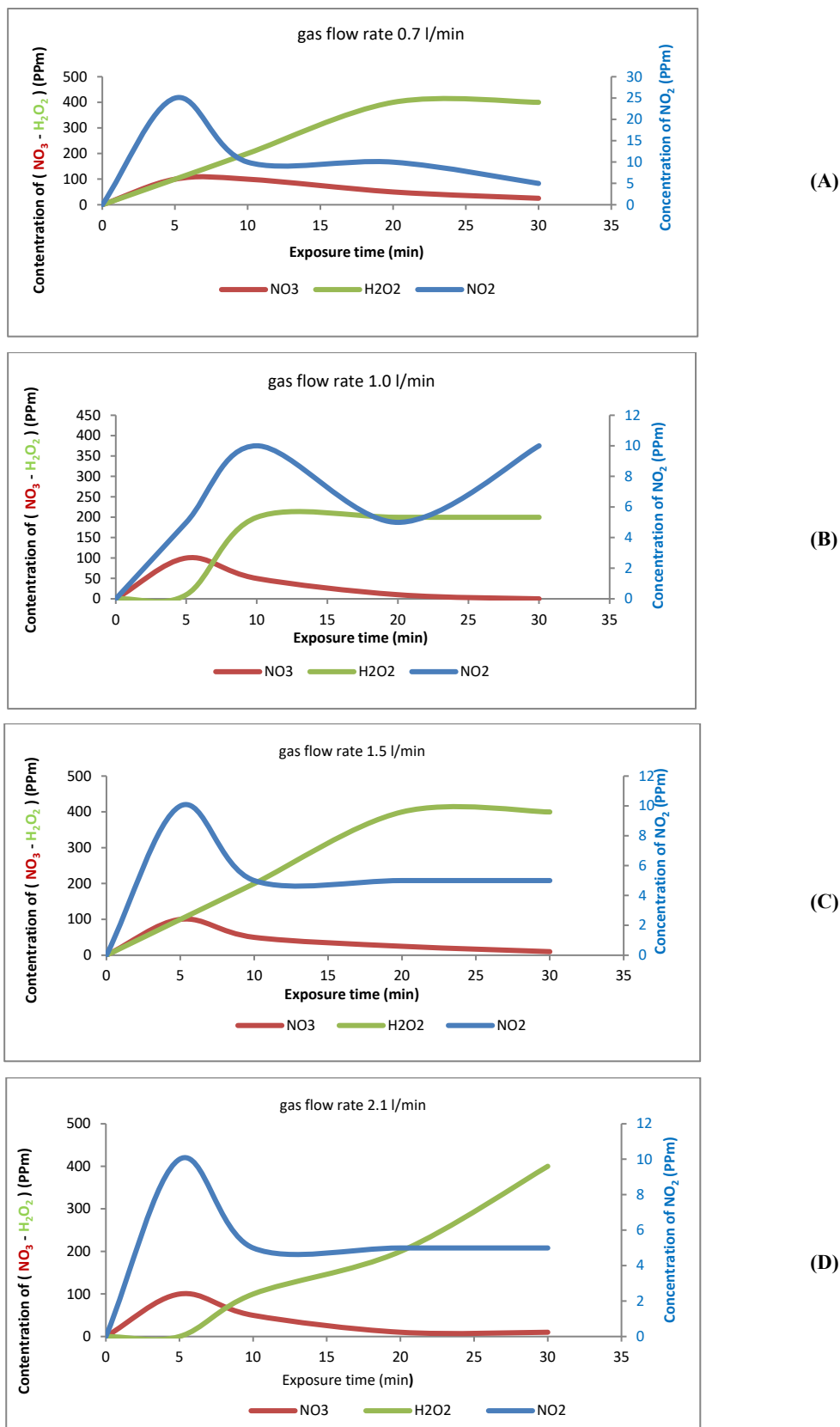

Figure 1. Plasma Jet system at working

3. RESULTS AND DISCUSSION

Fig. 2 shows the relationship between the concentration of NO_2, NO_3, H_2O_2 in units ppm and the exposer time at argon gas flow rate, A – for gas flow rate 0.7 l/min, B – gas flow rate of 1.0 l/min, C – gas flow rate of 1.5 l/min and D – gas flow rate of 2.1 l/min. From Fig. 2 (A, B, C, and D,) we notice that the concentrations of the active species increase dramatically (up and down) with the exposure time.

Figure 2. The relationship between the concentration of NO_2, NO_3, H_2O_2 in unit's ppm and the exposer time at argon gas flow rate: A – for gas flow reat 0.7 l/min, B – gas flow rate of 1.0 l/min, C – gas flow rate of 1.5 l/min, D – gas flow rate of 2.1 l/min.

We notice that each of the concentrations of NO_2, NO_3, and H_2O_2 increases with increasing exposure time, and reaches its highest value at slightly different times. This difference is due to the different in the half-life of these active

species, in addition to that there is conversion between these active species Table 1 shows the total concentrations of NO_2, NO_3 and H_2O_2 for different gas flow rate. From Figure 2A, 2B, 2C, 2D and Table 1A, 1B, 1C and 1D it is clear that the main factors that control the concentrations of the active elements are the exposer time, as the longer the time, the greater the concentration of the active specie, and the best irradiation time is 20 minutes. The second factor is the flow rate. Where the best flow rate is 0.7 l/min where this flow is laminar flow and does not contain swirls. At flow rates greater than 1 L/min, the gas flow velocity becomes greater, and this leads to displacement of atmospheric air located in front of the plasma jet, and thus the percentage of atmospheric gas decreases. The percentage of Ar gas is higher because the system works with Argon gas. The third factor is the different in the half-lives of the NO_2, NO_3, H_2O_2, where the longest-lived is H_2O_2, followed by NO_3, and the shortest-lived is NO_2. The fourth factor is the possibility of converting NO_2 into NO_3 through a series of chemical reactions that are sustained by plasma. From Table 1 we note that the best irradiation time is 20 minutes, as we get at this time the largest amount of active elements. The best flow rate is 0.7 l/min. Where the greater amount of the active species operands 460 ppm, which is the highest quantity for different flow rates. There is currently no method to determine which of these four elements is the most important; nonetheless, we believe that length of exposure time is the most important, followed by the chemical interactions between these concentrations and their transformations.

Table 1. The total concentrations of NO_2, NO_3, H_2O_2 for different gas flow rate values

Gas flow rate 0.7 l/min			
TIME (MIN)	NO₂	NO₃	H₂O₂	total concentrations
0	0	0	0	0
5	25	100	100	225
10	10	100	200	310
20	10	50	400	460
30	5	25	400	430

Gas flow rate 1.0 l/min			
TIME (MIN)	NO₂	NO₃	H₂O₂	total concentrations
0	0	0	0	0
5	5	100	10	115
10	10	50	200	260
20	5	10	200	215
30	10	0	200	210

Gas flow rate 1.5 l/min			
TIME (MIN)	NO₂	NO₃	H₂O₂	total concentrations
0	0	0	0	0
5	10	100	100	210
10	5	50	200	255
20	5	25	400	430
30	5	10	400	415

Gas flow rate 2.1 l/min			
TIME (MIN)	NO₂	NO₃	H₂O₂	total concentrations
0	0	0	0	0
5	10	100	0	110
10	5	50	100	155
20	5	10	200	215
30	5	10	400	415

Fig. 3 shows the relationship between the pH as a function of exposure time. At a flow rate rate 0.7 l/min, 1.0 l/min, 1.5 l/min and 2.1 l/min. From the figure, we notice a decrease in the pH from 7 to 3 during 30 minutes of exposure. And the behavior is similar in the four case of flow. The low PH was due to the treatment of water with plasma, where the treatment leads to the formation of compounds that increase the acidity of the water, such as nitric acid, which results from interaction of NO_3 with hydrogen, which results from the disusation of water by the effect of plasma. Acidic solutions have a high effectiveness in reducing the effectiveness of pathogens.

Fig. 4 shows the relationship between water temperature and plasma exposure time at a flow rate 0.7, 1.0, 1.5 and 2.1 l/min. From the figure, it is clear that there is an increase in the temperature of the water, and that the highest temperature the water reached is about 33°C, as this degree is still not severe and close to the room temperature. We also note that the change in temperature rchanges slightly diffrent with the flow rate.
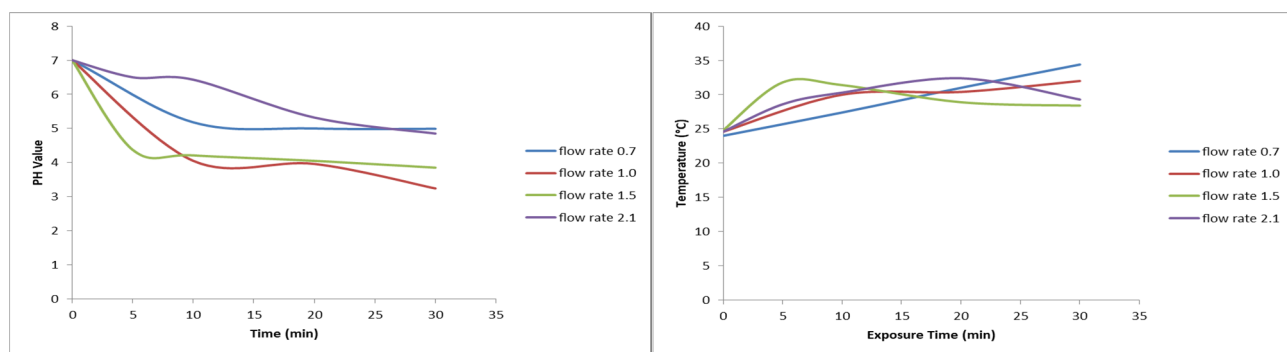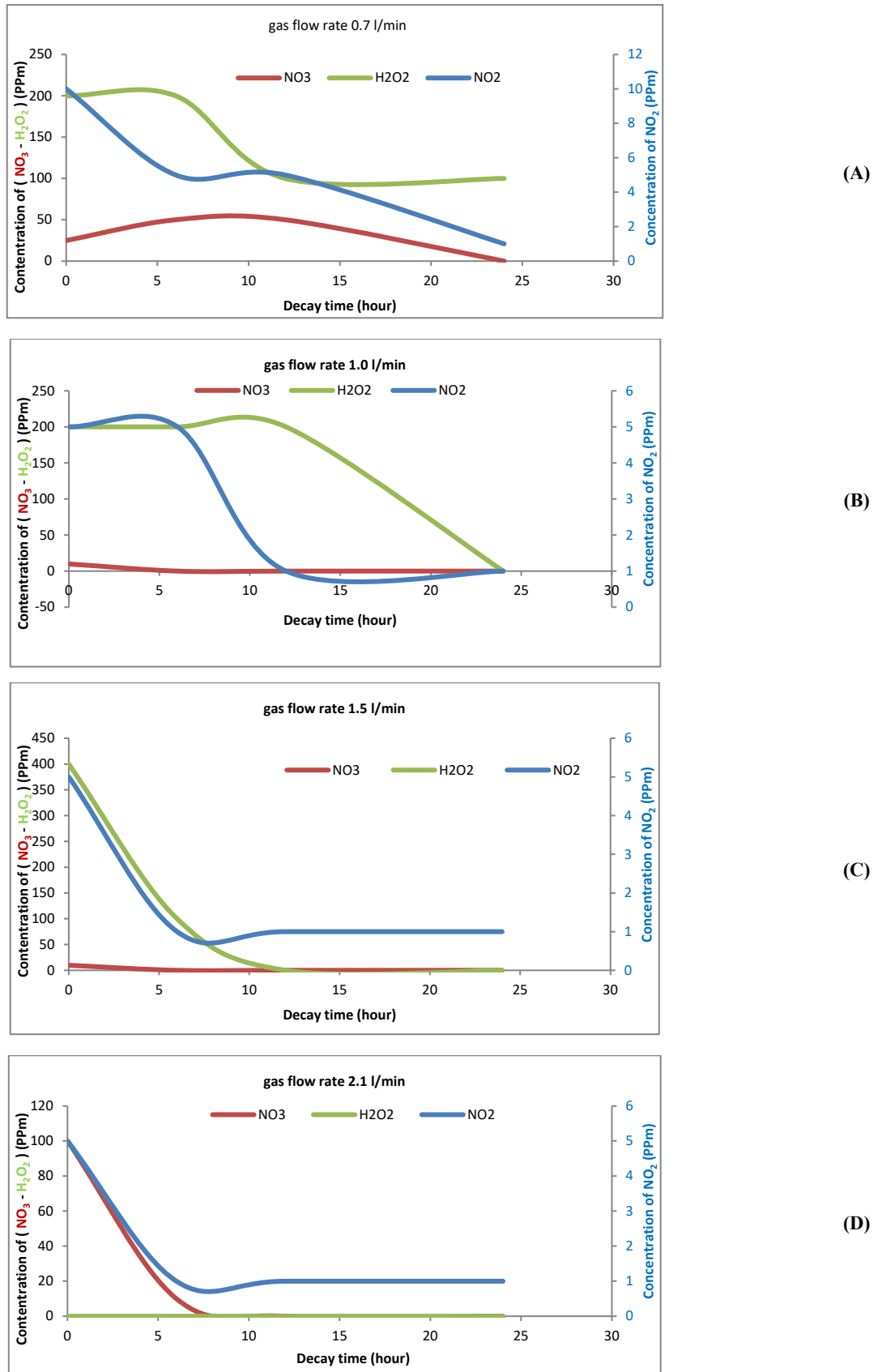
Figure 3. The relationship between the pH and the exposher time time at argon gas flow rate 0.7, 1.0, 1.5 and 2.1 l/min

Figure 4. The relationship between the the water temperture and the exposher time at argon gas flow rate of 0.7, 1.0, 1.5 and 2.1 l/min

Figure 5 shows the relationship between the concentration of NO_2, NO_3 and H_2O_2 in units ppm and the water storage time at different argon gas flow rate. A 0.7 l/min, B 1.0 l/min, C 1.5 l/min, D 2.1 1/min. From the Figure 5 A, B, C, and D, we notice that the concentrations of NO_2, NO_3, H_2O_2 decrease with time, and that the concentrations of these reactive species reach half their concentration after 6 hours of storing at room temperature. As shown in Table (2), we also notice that all reactive species concentration reach small values after 24 hours of storage, and this behavior depends on the half-life time of these reactive species.

Table 2. Total concentrations of NO_2, NO_3, H_2O_2 funtion of storage time for different gas flow rate

	Gas flow rate 0.7 l/min			
TIME (HOUR)	NO_2	NO_3	H_2O_2	total concentrations
0	10	25	200	235
6	5	50	200	255
12	5	50	100	155
24	1	0	100	101

	Gas flow rate 1.0 l/min			
TIME (HOUR)	NO_2	NO_3	H_2O_2	total concentrations
0	5	10	200	215
6	5	0	200	205
12	1	0	200	201
24	1	0	0	1

	Gas flow rate 1.5 l/min			
TIME (HOUR)	NO_2	NO_3	H_2O_2	total concentrations
0	5	10	400	415
6	1	0	100	101
12	1	0	0	1
24	1	0	0	1

	Gas flow rate 2.1 l/min			
TIME (HOUR)	NO_2	NO_3	H_2O_2	total concentrations
0	5	100	0	105
6	1	10	0	11
12	1	0	0	1
24	1	0	0	1

Figure 5. the relationship between the concentration of NO_2, NO_3 and H_2O_2 in units ppm and the water storage time at different argon gas flow rate. A 0.7 l/min, B 1.0 l/min, C 1.5 l/min, D 2.1 1/min.

Fig. 6 shows the relationship between the storage time of the PAW and the PH of the water activated at a flow rate 0.7,1.0,1.5 and 2.1 l/min. It is clear from the figure that the pH increases with the storage time and the water reaches its

natural pH of 7 after 24 hours of storage this is because the reactive species upon stoarge have disappeurel and turned in to more stable elements and thuse the water has returned to its normal state.
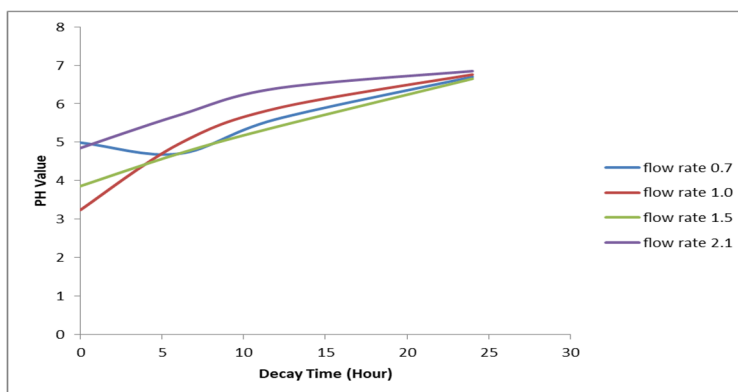

Figure 6. The relationship between the pH and the water storage time for water activated py plasma at argon gas flow rate of 0.7,1.0,1.5 and 2.1 l/min.

4. THE LENGTH OF THE PLASMA JET

It is good and important to know and understand the factors that control the length of a plasma jet to find the benefits of the practical use of a plasma torch. The length of the plasma jet is controlled by examining and measuring the effect of the flow rate of the argon gas. Figure 7 shows the argon gas flow rate on the length of the plasma jet. It was observed that the length of the plasma jet increased with the flow rate and that the flow rate (2.1 l/min) gave the longest length of the plasma jet.
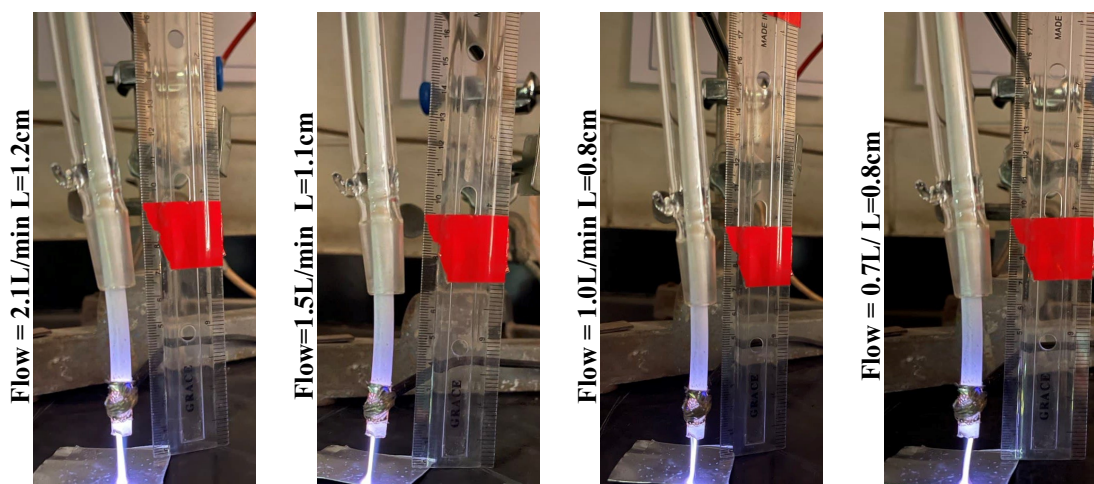

Figure 7. Effect of Ar flow rate on plasma jet length

5. CONCLUSIONS

From this research, it is possible to conclude the possibility of activating water using glow discharge plasma jet. Activating the water leads to the formation of RONS in water such as NO_2, NO_3, and H_2O_2, and the concentration of these species increases with the increase in exposure time and we managed to compute actual concentrations through the use of strips measurements, whereas the majority of our predecessors relied solely on the exposure time of water to plasma . That the main factors that control the concentrations of the active specie are the exposer time, as the longer the time, the greater the concentration of the active specie, and the best irradiation time is 20 minutes. The second factor is the flow rate. Where the best flow rate is 0.7 l/min where this flow is laminar. The third factor is the different in the half-lives of the NO_2, NO_3, H_2O_2, where the longest-lived is H_2O_2, followed by NO_3, and the shortest-lived is NO_2.The fourth factor is the possibility of converting NO_2 into NO_3 through a series of chemical reactions that are sustained by plasma. The best irradiation time is 20 min, as we get at this time the largest amount of active elements. The best flow rate is 0.7 l/min. Where the greater amount of the active species obtained 460 ppm, which is the highest quantity for different flow rates. The best storage time is 6 hours. The water temperature rises to 33°C, and the pH decreases with exposure time. When stored, the pH increases and reaches the same value as before activation after 24 hours. We deduced the half-life, the conversion of NO_3 to NO_2 and the best exposure time to water in plasma, and we found that the water is usable after a 24-hour storage period. Activating water using glow discharge plasma jet. is a simple and environmentally friendly method, so it can be used in medical and biological applications.

ORCID IDs
Farah A. Naeim, https://orcid.org/0009-0001-6471-1077; **Hammad R. Humud,** https://orcid.org/0000-0002-6942-4333;

REFERENCES

[1] A. Fridman, *Plasma Chemistry*, (Cambridge University Press, Cambridge, UK, 2008).

[2] M. Domonkos, P. Tichá, J. Trejbal, P. Demo, "Applications of Cold Atmospheric Pressure Plasma Technology in Medicine, Agriculture and Food Industry," Appl. Sci. **11**, 4809 (2021). https://doi.org/10.3390/app11114809

[3] G. Fridman, A. Shereshevsky, M.M. Jost, A.D. Brooks, A. Fridman, A. Gutsol, V. Vasilets, and G. Friedman, "Floating electrode dielectric barrier discharge plasma in air promoting apoptotic behavior in melanoma skin cancer cell lines," Plasma Chem. Plasma Process, **27**(2), 163-176 (2007). https://doi.org/10.1007/s11090-007-9048-4

[4] M. Laroussi, and T. Akan, "Arc-free atmospheric pressure cold plasma jets: A review," Plasma Process. Polym. 4(9), 777-788 (2007). https://doi.org/10.1002/ppap.200700066

[5] A. Fridman, A. Chirokov, and A. Gutsol, "Non-thermal atmospheric pressure discharges," J. Phys. D. Appl. Phys. **38**(2), R1 (2005). https://doi.org/10.1088/0022-3727/38/2/R01

[6] T. Royintarat, P. Seesuriyachan, D. Boonyawan, E.H. Choi, and W. Wattanutchariya, "Mechanism and optimization of non-thermal plasma-activated water for bacterial inactivation by underwater plasma jet and delivery of reactive species underwater by cylindrical DBD plasma," Curr. Appl. Phys. **19**(9), 1006-1014 (2019). https://doi.org/10.1016/j.cap.2019.05.020

[7] S.G. Joshi, M. Cooper, A. Yost, M. Paff, U.K. Ercan, G. Fridman, G. Friedman, A. Fridman, A.D. Brooks, "Nonthermal dielectric-barrier discharge plasma-induced inactivation involves oxidative dna damage and membrane lipid peroxidation in Escherichia coli," Antimicrob. Agents Chemother. **55**(3), 1053-1062 (2011). https://doi.org/10.1128/AAC.01002-10

[8] P. Lukes, E. Dolezalova, I. Sisrova, and M. Clupek, "Aqueous-phase chemistry and bactericidal effects from an air discharge plasma in contact with water: evidence for the formation of peroxynitrite through a pseudo-second-order post-discharge reaction of H_2O_2 and HNO_2," Plasma Sources Sci. Technol. **23**(1), 15019 (2014). https://doi.org/10.1088/0963-0252/23/1/015019

[9] N.K. Kaushik, B. Ghimire, Y. Li, M. Adhikari, M. Veerana, N. Kaushik, N. Jha, B. Adhikari, et.al., "Biological and medical applications of plasma-activated media, water and solutions," Biol. Chem. **400**(1), 39-62 (2019). https://doi.org/10.1515/hsz-2018-0226

[10] P. Bruggeman, and C. Leys, "Non-thermal plasmas in and in contact with liquids," J. Phys. D. Appl. Phys. **42**(5), 53001 (2009). https://doi.org/10.1088/0022-3727/42/5/053001

[11] M. Moreau, N. Orange, and M.G.J. Feuilloley, "Non-thermal plasma technologies: new tools for bio-decontamination," Biotechnol. Adv. **26**(6), 610-617 (2008). https://doi.org/10.1016/j.biotechadv.2008.08.001

[12] L. Gan, S. Zhang, D. Poorun, D. Liu, X. Lu, M. He, X. Duan, et al., "Medical applications of nonthermal atmospheric pressure plasma in dermatology," JDDG J. der Dtsch. Dermatologischen Gesellschaft, **16**(1), 7-13 (2018). https://doi.org/10.1111/ddg.13373

[13] M. Keidar, D. Yan, I.I. Beilis, B. Trink, and J.H. Sherman, "Plasmas for treating cancer: Opportunities for adaptive and self-adaptive approaches," Trends Biotechnol. **36**(6), 586-593 (2018). https://doi.org/10.1016/j.tibtech.2017.06.013

[14] C. Hoffmann, C. Berganza, and J. Zhang, "Cold Atmospheric Plasma: methods of production and application in dentistry and oncology," Med. Gas Res. **3**(1), 1-15 (2013). https://doi.org/10.1186%2F2045-9912-3-21

[15] T.A. Hameed, and H.R. Hammoud, "Comparison study of plasma-activated water and plasma jet on Escherichia coli bacteria for disinfection of tooth root canal," Iraqi Journal of Science, **64**(12), (2023).

[16] S. Abdul-Kadhim, and H.R. Hammoud, "Development low Temperature non-thermal atmospheric plasma jet sources for the biological applications," Iraqi Journal of Science, **64**(7), (2023).

[17] I.E. Vlad, C. Martin, A.R. Toth, J. Papp, and S.D. Anghel, "Bacterial inhibition effect of plasma activated water," Rom. Rep. Phys. **71**, 602 (2019).

[18] Y. Li, J. Pan, G. Ye, Q. Zhang, J. Wang, J. Zhang, J. Fang, "In vitro studies of the antimicrobial effect of non-thermal plasma-activated water as a novel mouthwash," Eur. J. Oral Sci. **125**(6), 463-470 (2017). https://doi.org/10.1111/eos.12374

[19] R. Zhou et al., "Plasma-activated water: Generation, origin of reactive species and biological applications," J. Phys. D. Appl. Phys. **53**(30), 303001 (2020). https://doi.org/10.1088/1361-6463/ab81cf

[20] T. Abuzairi, S. Ramadhanty, D.F. Puspohadiningrum, A. Ratnasari, N.R. Poespawati, and R.W. Purnamaningsih, "Investigation on physicochemical properties of plasma-activated water for the application of medical device sterilization," AIP Conference Proceedings, **1933**(1), 40017 (2018). https://doi.org/10.1063/1.5023987

[21] R.P. Guragain, H.B. Baniya, B. Shrestha, D.P. Guragain, and D.P. Subedi, "Improvements in germination and growth of sprouts irrigated using plasma activated water (PAW)," Water, **15**(4), 744 (2023). https://doi.org/10.3390/w15040744

ВПЛИВ ШВИДКОСТІ ГАЗУ, ЧАСУ ВПЛИВУ ТА СТАРІННЯ НА ФІЗИКО-ХІМІЧНІ ВЛАСТИВОСТІ ВОДИ, АКТИВОВАНОЇ ПЛАЗМОВИМ СТРУМЕНЕМ ТЛІЮЧОГО РОЗРЯДУ

Фарах А. Найм, Хаммад Р. Хумуд

Факультет фізики, Науковий коледж, Багдадський університет, Багдад, Ірак

Метою цієї роботи є вивчення того, як плазмовий струмень тліючого розряду змінює хімічні та фізичні властивості води. У цій роботі фізико-хімічні властивості води досліджувалися за допомогою плазмового струменя з газом аргон. У скляну посудину діаметром 5 см і глибиною 1 см налили 10 см³ дистильованої води. Система працювала при змінній напрузі 12 кВ і частоті 20 кГц, а час експозиції становив від 1 до 30 хвилин. Для вимірювання типів активних форм кисню та азоту (RONS), які утворюються використовувалися набори, виготовлені американською компанією Bartvation на швидкостях потоку 0,7, 1,0, 1,5 та 2,1 л/хв. Дані показали, що рівні NO₂, NO₃ і H₂O₂ були занадто високими. З часом він стає більшим і швидкість потоку зростає. Рівень pH з часом знижується, поки не досягне 3, а температура підвищується, поки не досягне 33°C. Однак pH підвищується з часом зберігання, і через 24 години вода повертається до свого природного pH 7. Кількість NO₂, NO₃ у повітрі трохи підвищується, а потім починає швидко знижуватися через 6 годин. Через 24 години концентрація близька до нуля. Звідси зрозуміло, що плазмовий струменевий пристрій тліючого розряду може створювати RONS, які можна використовувати для біологічних цілей.

Ключові слова: *нетеплова плазма (НТП), постійний струм (DC), вода, активована плазмою (PAW)*

EXCITON X-RAY INDUCED LUMINESCENCE
OF Y$_2$O$_3$ POLYCRYSTALS SINTERED FROM THE NANOPOWDER†

Evgen Barannik, Sergiy Kononenko, Vitaliy Zhurenko, Oganes Kalantaryan,
Pylyp Kuznietsov
V.N. Karazin Kharkiv National University
4 Svobody Sq., Kharkiv, 61022, Ukraine
Corresponding Author e-mail: v.zhurenko@gmail.com
Received April 15, 2023; revised May 25, 2023; accepted May 28, 2023

The paper is devoted to the changes in the X-ray luminescence spectra of nanoscale Y$_2$O$_3$ ceramics, namely the radiation associated with a self-trapped exciton. Additional heat treatment (annealing) of ceramic samples leads to changes in the exciton band of the spectra. These are a change in the shape and shift of the maximum of this band. Long-term irradiation of the samples by X-ray photons with an energy of 60 keV also led to changes in the exciton band. A theoretical model based on experimental data explains the changes in the spectra. The energy source of luminescence in this case is photoelectrons formed by energetic photons. Traps for these electrons are formed on the surface of submicrocrystals. Changes in the surface-to-volume ratio of crystals, as well as the frequencies of excited phonons and excitons are the basis for changes in the X-ray luminescence spectra of Y$_2$O$_3$ ceramics.
Keywords: *X-ray irradiation; exciton luminescence; yttrium oxide; spectrum; powder sintering*
PACS: 78.55.-m, 78.60.-b

INTRODUCTION

Recently, the number of Y$_2$O$_3$ studies both from a fundamental point of view and with regard to application in important technical tasks, has grown significantly. At first the largest share of yttrium oxide consumed was in the production of such phosphors, which can emit shades of red on electron beam displays (for example, television screens). The scope of other applications is gradually increasing. Yttrium oxide is also used in high-power lasers, in energy-saving white LEDs, to increase the strength and durability of aluminum and magnesium alloys, in specialized types of glass and optical lenses, in various electrical and gas sensors, in high-quality ceramics [1].

Y$_2$O$_3$ ceramics is the basis of a family of phosphors that differ in the elements with which the matrix is doped. In recent years, white light-emitting diodes (W-LED) have replaced traditional light bulbs and fluorescent lamps due to their high luminous efficiency, long working time, energy saving, high reliability, high reproduction index and environmental friendliness [2].

Over the past few decades, mono- and polycrystalline ceramics have been in great demand due to their excellent chemical and physical stability with high transparency over a wide range of wavelengths. They are used for military use and in the semiconductor industry, for example, as components of transparent armor, window domes, and plasma etching chambers [1, 2]. This study focuses on transparent Y$_2$O$_3$ ceramics, which have been attractive as a medium for use in tomorrow's high-power lasers and luminescent materials due to their higher thermal conductivity with lower thermal expansion compared to Y$_3$Al$_5$O$_{12}$ (YAG). Therefore, Y$_2$O$_3$ is selected as the main material for solid-state lasers [3]. Solid-state ceramic lasers have a wide range of applications in industry, medicine and the military. This research paper presents the production of vacuum-sintered Y$_2$O$_3$ ceramics synthesized by the coprecipitation method [3].

New directions of use of this compound should be noted separately. It turned out that the addition of yttrium nanoparticles to lubricants significantly reduces friction in mechanisms and can be recommended as a Lubricant Automotive Application [4].

The luminescence spectra of Y$_2$O$_3$ upon excitation by various types of ionizing radiation are well known. The most powerful band in the spectra is the radiation associated with self-trapped exciton (STE) decay [5]. In our previous work, we presented results clearly indicating that additional annealing leads to changes in luminescence in this wavelength band [6]. In the same works, physical reasons were given that can lead to such an effect.

The purpose of this work is the theoretical reasoning of changes in the luminescence spectra of Y$_2$O$_3$, which are associated with additional heat treatment of the samples.

YTTRIUM OXIDE SAMPLES FOR EXPERIMENTATION

Experimental studies of Y$_2$O$_3$ exciton luminescence induced by 60 keV X-ray photons were carried out with the samples prepared by sintering technique. The detail description of the experiment and the sample preparation procedure one can find in our previous works [6-7]. The samples were ceramics with the shape of round plates (with a diameter of 10.0 mm and a thickness of 3 mm) with a fine-grained nanoscale structure. They were made from ITO LUM nanopowder by sintering

of compacted pellets for one hour in atmospheric conditions at a temperature of 1500°C. Some of ceramics were additionally annealed at a temperature of 1000°C for 10 hours. The results of the study of these samples using an SEM- and XRD-diagnostics, given in previous works, did not reveal any difference in the structure of annealed and unannealed polycrystals. As can be seen from SEM-image on Fig. 1, the sample consists of randomly arranged sub-microcrystals of Y₂O₃. It can be seen that there are significant cavities between the crystals, which can influence a luminescence.
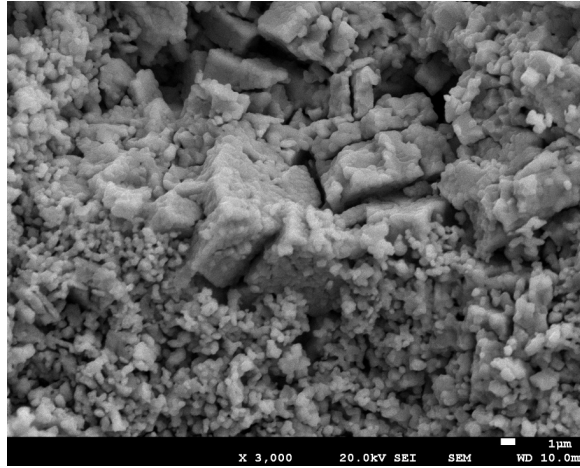
**Figure 1.** SEM-image of fresh cleavage for Y₂O₃ sintered at T = 1500°C

The main energy channel of luminescence in this case is production of photoelectrons by X-ray photons with subsequent conversion of their energy into luminescent radiation at transitions in crystals. The ratio between the volume of the crystals in the sample and the cavities (surfaces of the crystals) is important for the luminescence output.

EXCITON BAND LUMINESCENCE SPECTRA

It was previously shown [7] that after annealing of yttrium oxide polycrystals, the luminescence spectra due to STE recombination shifted to the long-wavelength region. This conclusion was made on the basis of the fact that the maximum of the band of the annealed sample is shifted towards longer wavelengths as compared to the case of the unannealed sample. Figure 2 shows the typical normalized luminescence spectra $S(\varepsilon)$ in the energy range from 2.762 eV (450 nm) to 4.972 eV (250 nm), which corresponds to exciton luminescence, for two Y₂O₃ samples that differ in additional annealing at 1000°C for 10 hours.
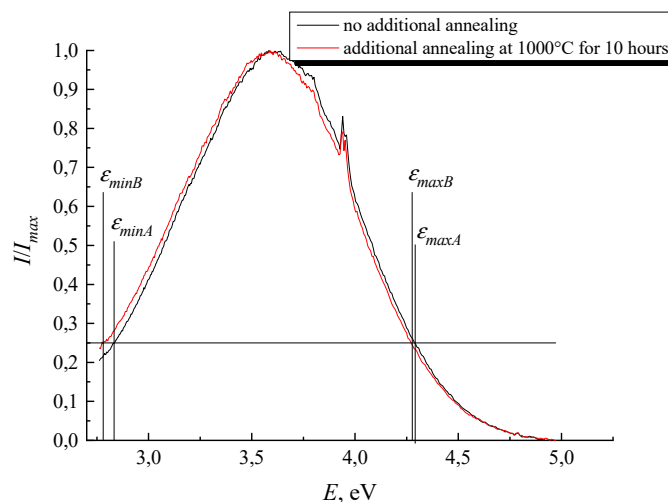
Figure 2. Normalized luminescence spectra for two Y₂O₃ samples sintered at T=1500°C for 1 hour without additional annealing (*A*) and with annealing at T=1000°C for 10 hours (*B*).

As can be seen from the figure, the long-wave shift occurs both for the long-wave limit of the luminescence photon spectrum (with photon energy ε_{min} at the level of –12 dB) and for the short-wave limit (with photon energy ε_{max}). The calculated average photon energies lead to the same conclusion about the long-wavelength shift in the spectra for the samples with additional annealing:

$$\bar{\varepsilon} = \int_{\varepsilon_{min}}^{\varepsilon_{max}} \varepsilon S(\varepsilon) d\varepsilon \left\{ \int_{\varepsilon_{min}}^{\varepsilon_{max}} S(\varepsilon) d\varepsilon \right\}^{-1}$$

Table 1 shows the corresponding values of the average photon energy of exciton luminescence for the samples being studied.

Table 1. The average photon energy of exciton luminescence

No	Preparation technology of Y_2O_3 sample	$\bar{\varepsilon}$, eV	ε_{min}, eV	ε_{max}, eV
1	Sintering at T=1500°C for 1 hour without additional annealing	3.5072	2.8379	4.2862
2	Sintering at T=1500°C for 1 hour with additional annealing at T=1000°C for 10 hours	3.4738	2.7746	4.2715

A similar effect of reducing the energy and frequency of radiation photons in Y_2O_3 with a decrease in temperature was described in detail in [8]. According to the developed theory, upon cooling, the stiffness of the crystals increases and thus the frequency of optical phonons, which are associated with excitons, increases. At the same time, the energy of the ground state of the exciton increases in proportion to the phonon energy $\hbar\omega_u$ of its own optical mode as follows: $E_u = S_u\hbar\omega_u$. The energy of the excited state defines the absorption properties of Y_2O_3 whereas the energy of ground state is responsible for the energy of photons at emission:

$$\varepsilon = \hbar\omega = E_0 - S_u\hbar\omega_u, \tag{1}$$

here E_0 is the energy at the bottom of excited state. As a result, changes in the phonon energy $\hbar\omega_u$ results in a small shift of the exciton spectrum into the long-wavelength region [8-10].

According to recent studies, annealing affects the composition, microstructure, and mechanical properties of not only single crystals, but also Y_3O_2 films [11-14]. Therefore, the reason for the decrease in radiation energy can be, as in the case of cooling, an increase in the stiffness of microcrystals, which leads to an increase in the phonon frequency ω_u of the optical mode. The formula for the relative change in phonon frequency follows directly from the expression (1) for relaxation energy

$$\frac{\Delta\omega_u}{\omega_u} = \frac{\hbar\Delta\omega}{S_u\hbar\omega_u}$$

where $\hbar\Delta\omega$ is the change in energy of luminescent radiation photons. Using the data of table 1, we get $\Delta\omega_u/\omega_u = 2.2\times10^{-2}$.

## TIME DEPENDENCE OF THE LUMINESCENCE

During the long-term continuous X-ray irradiation of yttrium oxide samples, the intensity of luminescence decreases sharply at first, but eventually reaches a plateau. As it is shown on Fig. 3, this feature applies to both additionally annealed and unannealed samples. As a matter of fact, the curve presented on this figure represents the dependence of exciton luminescence on the radiation dose of continuous irradiation.

Note that to plot the curves of the dependence of the exciton luminescence intensity on the irradiation time, we used data on the intensity level at a wavelength of λ=350 nm, which corresponds to the luminescence photon energy of 3.56 eV. The reason is that the maximum of the luminescence spectrum associated with excitons did not change during the irradiation time and was always close to this value.
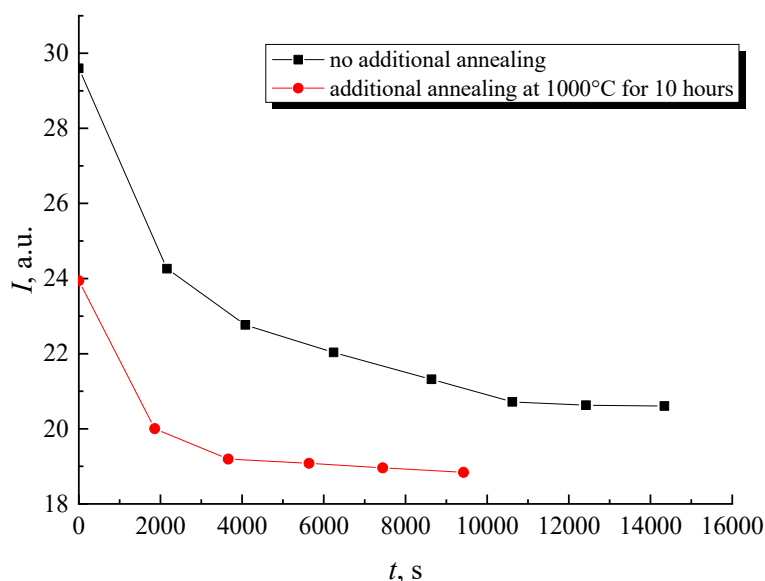
Figure 3. The dependence of luminescence intensity at λ=350 nm (photon energy of 3.56 eV) for two Y_2O_3 samples sintered at T=1500°C for 1 hour without additional annealing and with annealing at T=1000°C for 10 hours on the time of X-ray irradiation

The decrease of luminescence spectral intensity with exposure time is shown on Fig. 4. Table 2 presents the numerical values of the luminescence level, which corresponds to the spectral maximum for each of the spectra presented on Fig. 3. The average time interval between experimental data points of the spectra (cyclic scanning with dose accumulation) is about 1800 seconds.
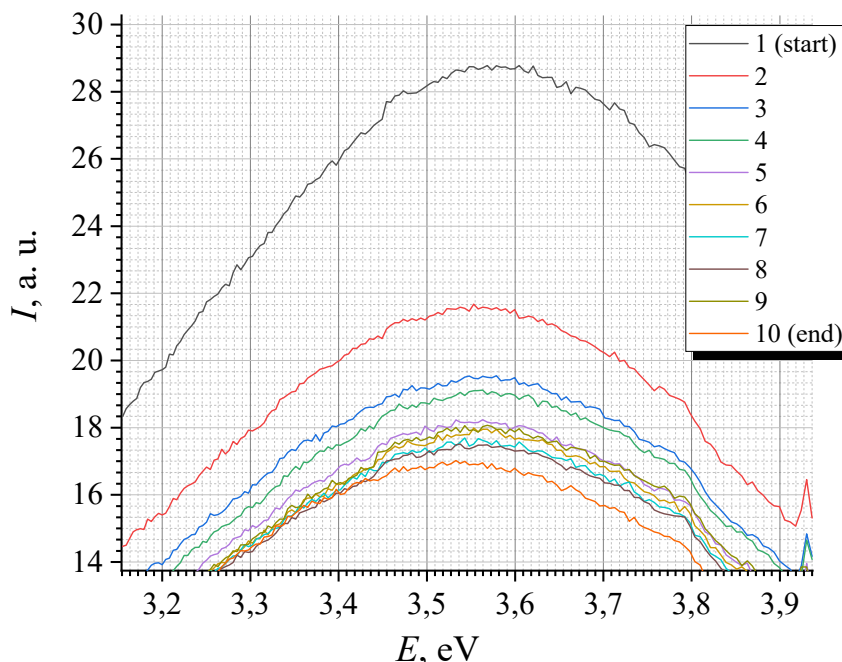
Figure 4. Decrease of exciton luminescence with irradiation cycle (time) for Y$_2$O$_3$ sample
sintered at 1500°C for 1 hour without additional annealing

**Table 2.** The parameters of exciton intensity maxima

The number of cycle scanning	Photon energy at maximum, eV	Luminescence intensity at maximum, a. u.
1	3.59	28.77
2	3.56	21.59
3	3.56	19.52
4	3.56	19.12
5	3.56	18.16
6	3.56	17.95
7	3.56	17.68
8	3.56	17.48
9	3.56	18.03
10	3.54	16.94

The experimental dependences of luminescence intensity at λ=350 nm (photon energy of 3.56 eV) for both types of Y$_2$O$_3$ samples (see Fig. 3) were analyzed and treated by Origin program fitting procedure. The best match of the experimental data on the dynamics of the luminescence intensity with the fitting results can be achieved when using the time dependence with two exponentials:

$$I(t) = I_0 - I_1 - I_2 + I_1 e^{-b_1 t} + I_2 e^{-b_2 t} = I_0 - I_1(1 - e^{-b_1 t}) - I_2(1 - e^{-b_2 t}).$$

It was suggested in [7] that the luminescence level decrease is caused by the presence of traps for photoelectrons. The results of the fitting can be interpreted by the presence of two types of traps, each of which is characterized by its capacities I_1, I_2 and the relaxation rates of trapped electrons b_1 and b_2. I_0 is initial value of the luminescence intensity at $t = 0$, which decreases at $t \to \infty$ to the smallest value due to the filling of traps. At the same time, the inequality must be fulfilled.

After termination of X-ray irradiation, the traps must be emptied, that is, the concentration of captured electrons in the traps must gradually decrease to zero. The emptying rate is determined by the same constants $b_{1,2}$ as the relaxation rate, since the emptying process is the inverse of the trap filling process. As a result, even after a short-term termination of X-ray irradiation for 10-20 minutes upon further resumption of irradiation, a partial recovery of the luminescence level is observed, as shown, for example, for the sample without annealing on Fig. 5. This means that in this case the dependence of the luminescence intensity on the irradiation dose ceases to be a monotonic time function.
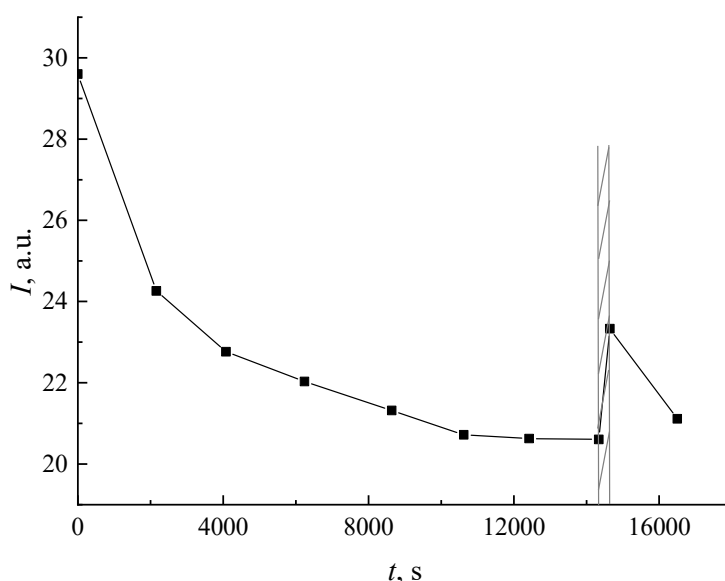
Figure 5. Recovery of the luminescence level upon continuation of irradiation after a brief shutdown of X-ray irradiation for Y_2O_3 sample without additional annealing. The time interval without X-ray exposure is shaded.
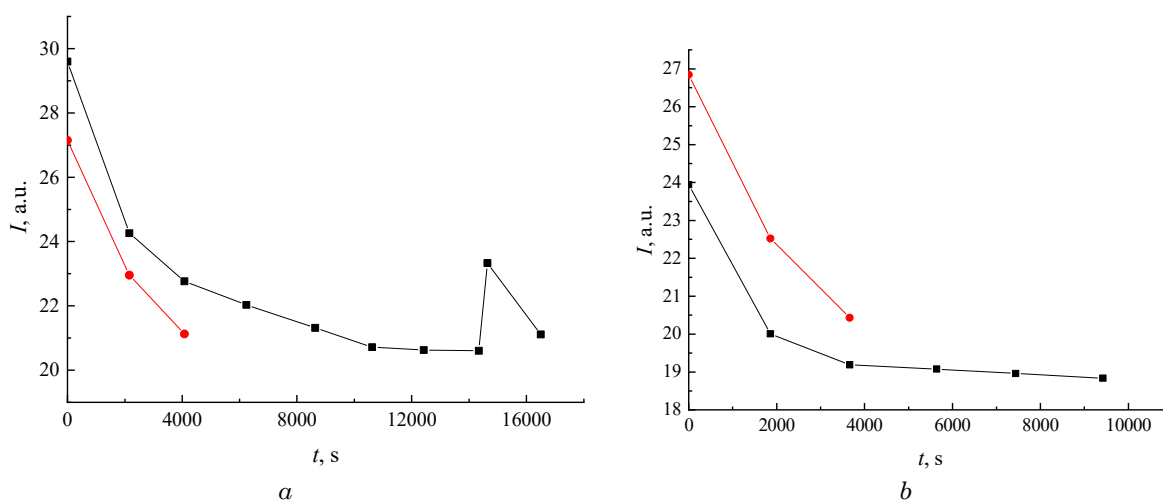
Figure 6. Recovery of the luminescence level upon resumption of irradiation after a long termination of X-ray irradiation in the Y_2O_3 samples: *a* is without additional annealing, *b* is additionally annealed (squares correspond to first X-ray exposure, circles – the second repeated exposure after X-ray termination).

Moreover, the recovery of the luminescence level appears to be greater the longer the time of its absence. This is associated with a higher level of trap emptying, since at $t \to \infty$ the concentration of trapped electrons must decrease to zero. As shown on Fig. 6a, after a long termination of X-ray irradiation for the sample without annealing, there is an almost complete recovery of the luminescence intensity (see table 3). In the case of the annealed sample after long termination of X-ray irradiation, even some increase in the exciton luminescence intensity was observed during re-irradiation, as shown on fig. 6b and Table 3.

Table 3. The exciton luminescence intensity at maximum

Technique of sample preparation	The maximum intensity at the first exposure, a. u.	The maximum intensity at the second exposure, a. u.
No additional annealing	29.6003	27.1511
Additional annealing	23.9435	26.8464

CONCLUSIONS

The paper presents the theoretical model of exciton luminescence of Y_2O_3 ceramics sintered from nanopowder. The samples were sintered at a temperature of 1500°C for 1 hour, then some of them were removed from the furnace, and the others were additionally annealed at a temperature of 1000°C for 10 hours. Luminescence was excited by continuous X-ray radiation with energy of 60 keV.

It is shown that the effect of additional heat treatment on the luminescence spectrum in the STE region can be explained by the changes in the coupling of excitons with phonons. An increase in the frequency of phonons, which leads to a decrease in the energy of photons of STE luminescent radiation, is calculated.

The experimental results for long-term irradiation indicated a significant role of photoelectron traps formed between the surfaces of submicrocrystals in Y$_2$O$_3$ samples. The intensity of luminescence initially decreases quite rapidly, but over time exponentially reaches a plateau. Temporary termination of X-ray irradiation leads to the disappearance of luminescence, and then, when turned on, its intensity becomes greater than it was at the plateau. This effect is associated with the gradual capture of photoelectrons by the traps until they are completely filled, as a result of which the luminescence level reaches a plateau. The traps should be emptied after the X-ray radiation has stopped. When the X-ray is turned on again, they are again filled with photoelectrons, which in turn leads to a decrease in the level of exciton luminescence.

ORCID IDs
Evgen Barannik, https://orcid.org/0000-0002-3962-9960; **Sergiy Kononenko**, https://orcid.org/0000-0001-6060-2589;
Vitaliy Zhurenko, https://orcid.org/0000-0002-4738-094X; **Oganes Kalantaryan,** https://orcid.org/0000-0002-5625-6908;
Pylyp Kuznietsov, https://orcid.org/0000-0001-8477-1395

REFERENCES
[1] H. Tripathi, S. Kumar, Sh. Kumari, S. Bhardwaj, A. Gupta, and J. Sharma, Materials Today: Proceedings, (2023). https://doi.org/10.1016/j.matpr.2023.02.352 (in press).
[2] D.R. Taikar, Journal of Alloys and Compounds, **828**, 154405 (2020), https://doi.org/10.1016/j.jallcom.2020.154405
[3] Hyeon-Myeong Oh, Young-Jo Park, Ha-Neul Kim, Jae-Woong Ko, Hyun-Kwuon Lee, Ceramics International, **47**(4), 4681 (2021). https://doi.org/10.1016/j.ceramint.2020.10.035
[4] Tóth, Álmos D., Ádám I. Szabó, Máté Zs. Leskó, Jan Rohde-Brandenburger, and Rajmund Kuti, Lubricants, **10**(2), 28 (2022). https://doi.org/10.3390/lubricants10020028
[5] A. Lushchik, M. Kirm, Ch. Lushchik, I. Martinson, and G. Zimmerer, Journal of Luminescence, **87**, 232 (2000). https://doi.org/10.1016/S0022-2313(99)00271-9
[6] S. Kononenko, E. Barannik, V. Zhurenko, O. Kalantaryan, V. Chishkala, R. Skiba, S. Lytovchenko, in: *2022 IEEE 12th International Conference Nanomaterials: Applications & Properties (NAP), Krakow, Poland,* pp. NRA09-1-NRA09-4 (2022), https://doi.org/10.1109/NAP55339.2022.9934259
[7] O. Kalantaryan, S. Kononenko, E. Barannik, V. Zhurenko and V. Chishkala, in: *2021 IEEE 11th International Conference Nanomaterials: Applications & Properties (NAP)*, (2021), pp. 1-4. https://doi.org/10.1109/NAP51885.2021.9568608
[8] A. Konrad, U. Herr, R. Tidecks, F. Kummer, and K. Samwer, Journal of Applied Physics, **90**, 3516 (2001). https://doi.org/10.1063/1.1388022
[9] A. Kuznetsov, V. Abramov, N. Rooze, and T. Savikhina, Letters to Journal of Experimental and Theoretical Physics, **28**, 602 (1978) (in Russian).
[10] A. Kuznetsov, V. Abramov, and T. Uibo, Optical Spectroscopy, **58**, 369 (1985) (in Russian).
[11] Y. Mao, J. Engels, A. Houben, M. Rasinski, J. Steffens, A. Terra, Ch. Linsmeier, and J.W. Coenen, Nuclear Materials and Energy, **10**, 1 (2017). http://dx.doi.org/10.1016/j.nme.2016.12.031
[12] S.R. Sung. Ch. Zhu, and R. Miller, NASA Technical Memorandum, 212625 (2004), http://gltrs.grc.nasa.gov
[13] Sh. Xu, Zh. Yao, J. Zhou, Ch. Fang, Materials Letters, **186**, 349 (2017). https://doi.org/10.1016/j.matlet.2016.10.045
[14] P.F. Yu, K. Zhang, S.X. Du, P. Ren, M. Wen, W.T. Zheng, Materials Science Forum, **898**, 1516 (2017). https://doi.org/10.4028/www.scientific.net/msf.898.1516

ЕКСИТОННА ЛЮМІНЕСЦЕНЦІЯ ПОЛІКРИСТАЛІВ Y₂O₃, ЩО СПЕЧЕНІ З НАНОПОРОШКУ
Є. Баранник, С. Кононенко, В. Журенко, О. Калантар'ян, П. Кузнєцов
Харківський Національний університет ім. В.Н. Каразіна
61022, Україна, м. Харків, пл. Свободи, 4

Стаття присвячена вивченню змін у рентгенлюмінесцентних спектрах нанорозмірної кераміки Y₂O₃, а саме випромінення, що пов'язане з самозахопленим екситоном. Додаткова теплова обробка (відпал) зразків кераміки призводить до змін у екситонній смузі спектрів. Це зміна форми та зсув максимуму цієї смуги. Довготривале опромінення зразків рентгенівськими фотонами з енергією 60 кеВ також призводило до змін у екситонній смузі. Теоретична модель, яка базується на експериментальних даних, пояснює зміни у спектрах. Енергетичним джерелом люмінесценції у цьому випадку є фотоелектрони утворені енергійними фотонами. На поверхні субмікрокристалів утворюються пастки для цих електронів. Зміни у співвідношенні поверхні з об'ємом кристалів, а також частот збуджених фононів та екситонів є базою для змін у спектрах рентгенолюмінесценції кераміки Y₂O₃.
Ключові слова: *рентгенівське опромінення, екситонна люмінесценція, оксид ітрію, спектр, спікання порошку*

Ігор Євгенійович Гаркуша
(до 60-річчя від дня народження)

12 травня виповнюється шістдесят років видатному фахівцю в галузі фізики плазми Ігорю Євгенійовичу ГАРКУШІ. Ігор Гаркуша є випускником кафедри фізики плазми фізико-технічного факультету Харківського університету 1986 року, доктором фізико-математичних наук, професором, академіком НАНУ, лауреатом Державної премії України в галузі науки і техніки. Він є заступником генерального директора Національного наукового центру. З 2010 він викладає в університеті, з 2018 року – завідує кафедрою прикладної фізики та фізики плазми університету. З 2021 року він є членом Наглядової ради Благодійної організації "Благодійний Фонд Випускників Фізико-Технічного Факультету Харківського Університету".

І. Є. Гаркуша народився 1963 року в м. Люботин Харківської області. Він закінчив з відзнакою Харківський державний університет в 1986 р. і протягом багатьох років веде науково-педагогічну діяльність у Харківському національному університеті. Під його керівництвом, починаючи з 1991 р., виконано десятки дипломних і курсових робіт студентами фізико-технічного факультету.

Починаючи з 2010 р. і по теперішній час І. Є Гаркуша веде викладацьку діяльність в якості професора за сумісництвом на кафедрі фізичних технологій, а згодом, на кафедрі прикладної фізики та фізики плазми фізико-технічного факультету, де читає курс лекцій "Плазмодинаміка та плазмові технології" студентам п`ятого курсу кафедр прикладної фізики та фізики плазми, а також кафедри матеріалів реакторобудування та фізичних технологій.

І.Є. Гаркуша активно співпрацює з викладачами університету в науковій сфері, внаслідок чого опубліковано низку спільних статей у провідних наукових журналах. Бере участь в організації міжнародних наукових конференцій і шкіл, що проводяться на базі університету, є членом редколегії журналу «East European Journal of Physics», що видається в ХНУ ім. В.Н. Каразіна. І.Є. Гаркуша є членом Спеціалізованої вченої ради Д 64.051.12 ХНУ імені В.Н. Каразіна МОН України для захисту дисертацій на здобуття наукового ступеня доктора та кандидата фізико-математичних наук зі спеціальностей «01.04.08- фізика плазми» та «01.04.16 - фізика ядра, елементарних частинок і високих енергій». Підготував двох докторів та трьох кандидатів наук за спеціальністю «фізика плазми».

Він очолює філію кафедри фізики плазми ХНУ в ННЦ ХФТІ, сприяє успішному виконанню переддипломної та дипломної практики студентів університету в Інституті фізики плазми та їх подальшому працевлаштуванню. Протягом багатьох років філія кафедри прикладної фізики та фізики плазми працює в інституті фізики плазми ННЦ ХФТІ. Цей механізм дає можливість науковцям ННЦ ХФТІ, як роботодавцям, брати безпосередню участь у вдосконаленні навчальних планів і програм з урахуванням сучасних проривних наукових напрямів і потреб академічних інститутів, розподіляти студентів на всі види практик, залучати для підготовки кадрів найсучасніше наукове, вимірювальне та діагностичне обладнання, готувати спільно з викладачами ФТФ навчальні посібники. В якості директора інституту фізики плазми брав активну участь в акредитації та оцінюванні освітньої програми «прикладна фізика та наноматеріали» в Каразінському університеті. Викладачі ХНУ ім. В. Н. Каразіна проходять підвищення кваліфікації в ІФП ННЦ ХФТІ.

І. Є. Гаркуша зробив суттєвий внесок у розвиток експериментальної бази сучасної фізики плазми, створення цілої низки новітніх плазмових установок: сильнострумові квазістаціонарні та імпульсні прискорювачі плазми, магнітоплазмовий компресор для отримання потужного випромінювання в діапазоні екстремального ультрафіолету, розробку та практичну реалізацію концепції квазістаціонарних плазмових прискорювачів нового покоління, розвиток сучасних методів діагностики плазми. Ці експериментальні установки світового рівня активно залучені до освітнього процесу та практичних занять студентів магістратури ФТФ.

Творча діяльність І. Є. Гаркуші знайшла відображення в одній монографії, шістнадцяти патентах та понад 375 публікаціях, що широко цитуються в провідних міжнародних наукових виданнях. Індекс Хірша в базі Скопус складає 24. Його роботи цитовані 1651 раз.

У межах освітніх програм підготовки магістрів та аспірантів з фізики плазми суттєву увагу приділено також інтеграції до європейського навчального простору, залучення лабораторної бази європейських університетів-партнерів для підготовки студентів Каразінського університету. Доступ до сучасного коштовного та навіть унікального експериментального обладнання є необхідною складовою для підготовки студентів і майбутніх дослідників. Так, наприклад, за ініціативи І. Є. Гаркуші та його зусиллями в березні 2019 р. студенти ФТФ у

межах навчального курсу з утримання плазми здійснювали дистанційне керування в режимі реального часу роботою токамака «GOLEM» у Чеському технічному університеті в Празі. Працюючи з Харкова, вони здійснили 55 плазмових розрядів за різного тиску газоподібного водню та часу затримки запалювання. Після обробки здобутих результатів вимірювань параметрів плазми сучасними діагностичними засобами студенти доповіли їх на спільному семінарі. Наразі здобуті наукові результати у вигляді спільної статті опубліковані в Українському фізичному журналі.

Аспіранти Каразінського на регулярній основі беруть участь у загальноєвропейських освітніх заходах. Прикладом цьому є «European PhD event», що проводиться щороку, і де аспіранти доповідають про свої наукові здобутки та мають можливість спілкування з колегами з інших університетів. Крім того, І. Є. Гаркуша залучений до спільного оцінювання рівня підготовки аспірантів у різних закладах і формування рекомендацій щодо структури освітніх програм.

І. Є. Гаркуша був головою оргкомітету відомої серії міжнародних конференцій-шкіл з фізики плазми та керованого термоядерного синтезу, що проводились кожні два роки, починаючи з 1998 в Алушті, а з 2014 в Харкові, за участю провідних фахівців світу та широкого загалу студентів і в яких Каразінський університет спільно з ННЦ ХФТІ був організатором.

Багато зусиль було спрямовано І. Є. Гаркушею для успішного залучення українських науковців і освітян до Європейської програми Горизонт-2020, зокрема набуття асоційованого членства в науково-освітній програмі Євратом. Він є головою Української ланки в EUROfusion, у складі якої є три інститути Національної академії наук України та три провідні університети. Каразінський університет є унікальним прикладом залучення коштів Євросоюзу для розвитку вищої освіти в Україні в галузі фізики керованого термоядерного синтезу у межах Програми Євратом Горизонт-2020, і, зокрема, робочого пакету «Освіта» європейського консорціуму EUROfusion. Участь в освітній програмі Євратом буде подовжено і в наступній рамковій програмі Горизонт Європа (2021-2027).

Наукова громадськість, друзі та колеги Ігоря Євгенійовича щиро вітають його з 60-річчям і бажають йому невичерпних життєвих сил та плідного довголіття на науковій та просвітницькій нивах України.

*М.О. Азарєнков, І.О. Афанасьєва, Є.О. Баранник, Ю.А. Бережной, В.М. Береснєв, О.А. Бізюков, І.О. Гірка,
М.І. Гришанов, І.Б. Денисенко, А.М. Кондратенко, О.Ю. Корчин, П.Е. Кузнецов, В.М. Куклін,
В.Т. Лазурик, С.В. Литовченко, В.О. Лісовський, В.П. Олефір, І.М. Середа,
К.М. Середа, Ю.В. Слюсаренко, В.І. Ткаченко, В.М. Трусова,
М.Ф. Шульга, М.М. Юнаков*

INSTRUCTIONS FOR PREPARING MANUSCRIPT IN THE EAST EUROPEAN JOURNAL OF PHYSICS

Name A. Author[a]*, Name B. Co-Author(s)[b]†

[a]Affiliation of first author
[b]Affiliation of second author (if different from the first Author)
*Corresponding Author: corresponding_authors@mail.com
†E-mail: co_authors@mail.com

Each paper must begin with an abstract. The abstract should be typed in the same manner as the body text (see below). Please note that these Instructions are typed just like the manuscripts should be. The abstract must have at least **250-300 words**, supplying general information about the achievements, and objectives of the paper, experimental technique, methods applied, significant results and conclusions. Page layout: the text should be printed on the paper **A4** format, at least **5 pages**, with margins of: **Top - 3, Bottom, Left and Right - 2 cm**. The abstract, keywords should be presented **in English** (only for foreign authors), **and Ukrainian**. The text should be prepared in "**doc", "docx" or LaTeX** format (EEJP Template).

Keywords: there, must, be, 5-10 keywords
PACS: specify PACS code(s) here

INSTRUCTIONS

The text should be typed as follows:
• **title**: Times New Roman, 11 pt, ALL CAPS, bold, 1 spacing, centred;
• **authors**: name, initials and family names; Times New Roman, 11 pt, bold, 1 spacing, centred;
• **affiliation(s)**: Times New Roman, 9 pt, italic, 1 spacing, centred;
• **abstract**: Times New Roman, 9 pt, 1 spacing, justified;
• **body text**: Times New Roman, 10 pt, 1 spacing, justified; paragraphs in sections should be indented right (tabulated) for 0.75 cm;
• **section titles**: Times New Roman, 10 pt, bold, 1 spacing, centred, without numbering, one line should be left, blank above section title;
• **subsection titles**: Times New Roman, 10 pt, bold, 1 spacing, centred, without numbering in accordance to the section (see below), one line should be left blank above subsection title;
• **figure captions**: width of the figure should be 85 or 170 mm, Figures should be numbered (**Figure 1**.) and titled below Figures using sentence format, Times New Roman, 9 pt, 1 spacing, centred (if one line) or justified (if more than one line); one line should be left blank below figure captions;
• **table captions**: width of the table should be 85 or 170 mm, Tables should be numbered (**Table 1.**) and titled above tables using sentence format, Times New Roman, 10 pt, 1 spacing, left, Tables should be formatted with a single-line box around the outside border and single ruling lines between rows and columns; one line should be left blank below tables;
• **equations**: place equations centred, numbered in Arabic: (1), flush right, equations should be specially prepared in **MathType** or "**Microsoft Equation**", Times New Roman, 10 pt.

Additional Instructions

Numerated figures and tables should be embedded in your text and placed after they are cited. Only sharp photographs and drawings are acceptable. Letters in the figures should be 3 mm high. The figures should be presented in one of the following graphic formats: jpg, gif, pcx, bmp, tif.

REFERENCES

List of References must contain **at least 30% of articles published over the past 5 years** and **no more than 30% of links to their own work**. Cite References by number in AIP style (https://aip.scitation.org/php/authors/manuscript). Numbering in the order of referring in the text, e.g. [1], [2-5], etc. References should be listed in numerical order of citation in the text at the end of the paper (justified), Times New Roman, 9 pt, 1 spacing.

Journal Articles
[1]   T. Mikolajick, C. Dehm, W. Hartner, I. Kasko, M.J. Kastner, N. Nagel, M. Moert, and C. Mazure, Microelectron. Reliab. **41**, 947 (2001), https://doi.org/10.1016/S0026-2714(01)00049-X.
[2]   S. Bushkova, B.K. Ostafiychuk, and O.V. Copaiev, Physics and Chemistry of Solid State. **15**(1), 182 (2014), http://page.if.ua/uploads/pcss/vol15/!1501-27.pdf. (in Ukrainian)
[3]   M. Yoshimura, E. Nakai, K. Tomioka, and T. Fukui, Appl. Phys. Lett. **103**, 243111 (2013), http://dx.doi.org/10.7567/APEX.6.052301

E-print Resourses with Collaboration Research or Preprint
[4]   M. Aaboud et al. (ATLAS Collaboration), Eur. Phys. J. C, **77**, 531 (2017), http://dx.doi.org/10.1140/epjc/s10052-017-5061-9
[5]   Sjöstrand et al., *Comput. Phys. Commun.* **191,** 159 (2015), https://doi.org/10.1016/j.cpc.2015.01.024
[6]   Boudreau, C. Escobar, J. Mueller, K. Sapp, and J. Su, (2013), http://arxiv.org/abs/1304.5639

Books
[7]   S. Inoue, and K.R. Spring, *Video Microscopy*: *The fundamentals*, 2nd ed. (Plenum, New York, 1997), pp. 19-24.
[8]   I. Gonsky, T.P. Maksymchuk, and M.I. Kalinsky, *Біохімія Людини [Biochemistry of Man],* (Ukrmedknyga, Ternopil, 2002), pp. 16. (in Ukrainian)

Edited Books
[9]   Z.C. Feng, editor, *Handbook of Zinc Oxide and Related Materials: Devices and Nano Engineering, vol. 2*, (CRC Press/Taylor & Francis, Boca Raton, FL, 2012)

Book Chapters
[10] P. Blaha, K. Schwarz, G.K.H. Madsen, D. Kvasnicka, and J. Luitz, in: *WIEN2K, An Augmented Plane Wave Plus Local Orbitals Program for Calculating Crystal Properties,* edited by K. Schwarz (Techn. Universität Wien, Austria, 2001).
[11] M. Gonzalez-Leal, P. Krecmer, J. Prokop, and S.R. Elliot, in: *Photo-Induced Metastability in Amorphous Semiconductors*, edited by A.V. Kolobov (Wiley-VCH, Weinheim, 2003), pp. 338-340.
[12] A. Kochelap, and S.I. Pekar, in: *Теория Спонтанной и Стимулированной Хемилюминесценции Газов [Theory of Spontaneous and Stimulated Gas Chemiluminescence]* (Naukova dumka, Kyiv, 1986), pp. 16-29. (in Russian)

Conference or Symposium Proceedings
[13] C. Yaakov, and R. Huque, in: *Second International Telecommunications Energy Symposium Proceedings*, edited by E. Yow (IEEE, New York, 1996), pp. 17-27.
[14] V. Nikolsky, A.K. Sandler, and M.S. Stetsenko, in: *Автоматика-2004: Матеріали 11 Міжнародної Конференції по Автоматичному Управлінню [Automation-2004: Materials of the 11th International Conference on Automated Management]* (NUHT, Kyiv, 2004), pp. 46-48. (in Ukrainian)

Patent
[15] I.M. Vikulin, V.I. Irha, and M.I. Panfilov, Patent Ukraine No. 26020 (27 August 2007). (in Ukrainian)

Thesis / Dissertation
[16] R.E. Teodorescu, Ph.D. dissertation, The George Washington University, 2009.

Special Notes
1. Use International System of Units (SI system). 2. It is undesirable to use acronyms in the titles. Please define the acronym on its first use in the paper. 3. Refer to isotopes as ^{14}C, ^{3}H, ^{60}Co, etc.

Наукове видання

СХІДНО-ЄВРОПЕЙСЬКИЙ ФІЗИЧНИЙ ЖУРНАЛ
Номер 2, 2023

EAST EUROPEAN JOURNAL OF PHYSICS
No 2, 2023

Збірник наукових праць
англійською та українською мовами